

Doctoral thesis

Doctoral theses at NTNU, 2022:304

Maren Marie Sjaastad Andreassen

Multimodal Imaging-derived Biomarkers for Early Detection and Personalized Treatment of Breast Cancer

NTNU
Norwegian University of Science and Technology
Thesis for the Degree of
Philosophiae Doctor
Faculty of Medicine and Health Sciences
Department of Circulation and Medical Imaging



Norwegian University of
Science and Technology

Maren Marie Sjaastad Andreassen

Multimodal Imaging-derived Biomarkers for Early Detection and Personalized Treatment of Breast Cancer

Thesis for the Degree of Philosophiae Doctor

Trondheim, December 2022

Norwegian University of Science and Technology
Faculty of Medicine and Health Sciences
Department of Circulation and Medical Imaging



Norwegian University of
Science and Technology

NTNU

Norwegian University of Science and Technology

Thesis for the Degree of Philosophiae Doctor

Faculty of Medicine and Health Sciences

Department of Circulation and Medical Imaging

© Maren Marie Sjaastad Andreassen

ISBN 978-82-326-5677-6 (printed ver.)

ISBN 978-82-326-5933-3 (electronic ver.)

ISSN 1503-8181 (printed ver.)

ISSN 2703-8084 (online ver.)

Doctoral theses at NTNU, 2022:304

Printed by NTNU Grafisk senter

Acknowledgements

I would first like to thank my supervisors Dr. Neil Jerome and Prof. Tone Frost Bathen. I want to thank Neil for his guidance and for contributing to my education in the MRI field. Tone has demonstrated to me how to take our work from the lab and use it to improve patient care. Despite her busy schedule, her door is always open. I would like to thank Prof. Steinar Lundgren for attributing clinical aspects to this thesis. I would also like to express my gratitude to Pål Erik Goa. He has been generous with his time and energy and has been instrumental in all the work included in this thesis.

This thesis would not have been possible without the fruitful collaboration with Prof. Rebecca Rakow-Penner and Prof. Anders M. Dale at the Center for Multimodal Imaging and Genetics (CMIG) at UCSD, USA. I would like to thank Rebecca for her mentorship and the countless hours spent at the lab; she managed to make them both scientifically educational and fun. Her work ethic has been truly inspirational, and she has demonstrated how to successfully fulfill a combined clinical and academic career path. Anders has shared greatly of his knowledge, and I am truly grateful to have had the opportunity to benefit from his world-leading analytical and methodological expertise in addition to his attention to detail and quality. It has also been a joy working alongside Dr. Ana Rodriguez-Soto on our projects and her guidance has been truly appreciated. Thank you for all the scientific input to Prof. Tyler Seibert and Dr. Christopher Conlin. Lastly, I would like to thank the Fulbright Scholarship Program for the financial support that made this collaboration possible.

All the great colleagues at the MR Cancer Group have provided a constant source of support and friendship. Leslie, Liv, Igor, Debbie, Hanna-Maja, Mohammed, Daniel, Christina, Kaia, Gabriel, and Chris, thank you for making my experience in the lab so great. Additionally, thank you to the “Forskerlinje” program for funding and for Ana Bofin, May Karin Dyrendahl, and Cecilie Nordvik for making the administrative aspects painless. Lastly, thank you to the Faculty of Medicine and Health Sciences at NTNU for funding the finalization of this PhD.

Sammendrag

Dynamisk kontrastforsterket Magnetisk Resonans (MR) avbildning (DCE) er en veletablert klinisk metode for oppdagelse og karakterisering av brystkreft. Men DCE har flere begrensninger og det er derfor behov for å utvikle nye metoder for nøyaktig oppdagelse av kreft og skille det fra omkringliggende friskt brystvev uten bruk av intravenøs kontrast. Diffusjonsvektet MR (DWI) er en metode som reflekterer underliggende vevsstruktur ved å detektere diffusjon av vannmolekyler, uten å bruke kontrast. DWI har vist stort potensiale i brystkreft, blant annet for vurdering av behandlingsrespons ved beregning av kvantitative diffusjonsegenskaper. Men et stort problem ved dagens DWI metoder er at de er avhengig av å bruke DCE til å identifisere tumor.

Oppgavens hovedmål var å utforske alternative MR-baserte metoder for deteksjon og responsevaluering av neoadjuvant behandling av brystkreft: hybrid positron emisjon tomografi og MR (PET/MR) og avansert DWI (Restriction Spectrum Imaging (RSI)). For å overføre RSI til klinisk bruk var det nødvendig å undersøke de underliggende diffusjonsegenskapene i brystvev. Dette gjorde vi ved å tilpasse signalet fra alt brystvev, både friskt vev og kreft. RSI ble også brukt for å vurdere behandlingsrespons av neoadjuvant behandling.

Resultatene viser at en ny semi-automatisk segmenteringsmetode basert på PET-signalet i stor grad detekterer det samme tumorarealet som DCE, og diffusjonsparameterne som avledes for å beskrive behandlingsrespons er like for de to metodene. Videre tyder funnene på at optimalisering av RSI gjør det mulig å filtrere ut diffusjonssignal fra normalt brystvev, og metoden kan derfor benyttes til å detektere brystkreftvev og skille det fra det omkringliggende friske brystvevet. RSI modellen viste også et lovende potensial for å evaluere behandlingsrespons allerede 3 uker etter behandlingsstart. RSI viste dessuten tilsvarende nøyaktighet som DCE i å vurdere gjenværende kreftvev etter fullført neoadjuvant behandling.

Metodene som er beskrevet i denne oppgaven viser at brystkreft kan detekteres uten bruk av intravenøst, gadoliniumbasert kontrastmiddel, og det er spesielt lovende at RSI modellen kan benyttes på tvers av ulike institusjoner, med bruk av ulike MR-skannere og varierende opptaksprotokoller. Det ser også ut til at den optimaliserte RSI modellen kan måle respons på neoadjuvant behandling av brystkreft i tidlig fase, noe som er viktig for bedre klinisk vurderingsgrunnlag og for å muliggjøre persontilpasset behandling.

*Ovennevnte avhandling er funnet verdig til å forsvares offentlig
for graden PhD i Medisinsk teknologi
Digital disputas finner sted
fredag 2. desember*

Summary

Accurate segmentation of cancer from surrounding healthy breast tissues in magnetic resonance imaging (MRI) without intravenous administration of contrast agents, is a question of wide interest. Current standard-of-care dynamic contrast-enhanced MRI (DCE) depends on Gadolinium contrast. Diffusion-weighted MRI (DWI) avoids the use of contrast since it is able to report on tissue microstructure by detecting diffusion of water molecules and has shown large potential in several breast cancer settings, including assessment of treatment response. However, the current application of DWI for quantitative studies requires radiologists to manually define tumors based on DCE, prior to transferring the defined regions of interest (ROIs) to the DWI image space for analysis.

In this thesis, we investigated alternative methods to DCE for breast tumor definition and neoadjuvant treatment response evaluation: simultaneous positron emission tomography and MRI (PET/MRI), and optimizing an advanced DWI model, Restriction Spectrum Imaging (RSI), for use in the breast. Since meaningful assessment by the RSI model requires knowledge about the underlying breast diffusion properties, we investigated the optimal fitting of diffusion signal for all voxels in cancer and healthy breast tissues. Furthermore, the optimized RSI model was applied for neoadjuvant treatment response evaluation.

We found that tumor definition using our novel semi-automatic PET/MRI segmentation method, GMM-PET, mimics results normally attained through DCE by successfully tracking the same changes in functional parameters for assessment of neoadjuvant treatment. Secondly, optimal fitting of diffusion signal for all voxels in cancer and healthy breast tissues resulted in a three-component RSI model, with globally-determined component-specific apparent diffusion coefficients (*ADCs*) that decomposed the diffusion signal to correspond to major anatomical components in healthy breast tissues. These results were then applied for optimized discrimination of cancer from healthy breast tissues directly on DWI images, which yielded the derived RSI parameter, C_1C_2 that showed highly promising discriminatory performance superior to conventional DWI estimates. The three-component RSI model was further used to develop an automatic tissue classifier (RSI classifier) that was able to assess treatment response after only 3 weeks of neoadjuvant treatment and was found to have similar accuracy to DCE in assessing residual tumor post-therapy.

Our novel methodologies, GMM-PET and three-component RSI model-derived C_1C_2 parameter, can detect breast cancer without the use of Gadolinium contrast. Of particular interest, the highly promising diagnostic performance of C_1C_2 was determined using data acquired across different sites, scanners, and imaging acquisition protocols. This suggests a readily available clinical utility that may reduce the need to pre-identify lesions on non-diffusion modalities altogether. The finding that the automatic RSI classifier can assess early response to neoadjuvant treatment is important for improved clinical decision-making to enable tailored treatment regimens.

List of papers

Paper I

Semi-automatic segmentation from intrinsically-registered 18F-FDG-PET/MRI for treatment response assessment in a breast cancer cohort: comparison to manual DCE-MRI

Andreassen MMS, Goa PE, Sjøbakk TE, Hedayati R, Eikesdal HP, Deng C, Østlie A, Lundgren S, Bathen TF, Jerome NP.

MAGMA. 2020 Apr;33(2):317-328. doi: 10.1007/s10334-019-00778-8. Epub 2019 Sep 27. PMID: 31562584

Paper II

Characterization of the diffusion signal of breast tissues using multi-exponential models

Rodríguez-Soto AE*, Andreassen MMS*, Fang LK, Conlin CC, Park HH, Ahn GS, Bartsch H, Kuperman J, Vidić I, Ojeda-Fournier H, Wallace AM, Hahn M, Seibert TM, Jerome NP, Østlie A, Bathen TF, Goa PE, Rakow-Penner R, Dale AM.

Magn Reson Med. 2022, Apr;87(4):1938-1951. doi: 10.1002/mrm.29090. Epub 2021 Dec 14. PMID: 34904726

*Shared first authorship

Paper III

Discrimination of Breast Cancer from Healthy Breast Tissue Using a Three-component Diffusion-weighted MRI Model

Andreassen MMS*, Rodríguez-Soto AE*, Conlin CC, Vidić I, Seibert TM, Wallace AM, Zare S, Kuperman J, Abudu B, Ahn GS, Hahn M, Jerome NP, Østlie A, Bathen TF, Ojeda-Fournier H, Goa PE, Rakow-Penner R#, Dale AM#.

Clin Cancer Res. 2021 Feb 15;27(4):1094-1104. doi: 10.1158/1078-0432.CCR-20-2017. Epub 2020 Nov 4.

PMID: 33148675

*Shared first authorship #Shared last authorship

Paper IV

Restriction Spectrum Imaging with elastic image registration for automated evaluation of early response to neoadjuvant therapy in breast cancer

Andreassen MMS, Tong MW, Loubrie S, Fang L, Seibert TM, Wallace AM, Zare S, Ojeda-Fournier H, Kuperman J, Hahn M, Jerome NP, Bathen TF, Rodríguez-Soto AE, Dale AM, Rakow-Penner R

Unpublished manuscript

List of abbreviations

ADC – Apparent diffusion coefficient

Au – Arbitrary unit

AUC – Area under the curve

BI-RADS – Breast Imaging-Reporting and Data System

BPE – Background parenchymal enhancement

CNR – Contrast-to-noise ratio

DCE – Dynamic contrast-enhanced imaging

DCIS – Ductal carcinoma in situ

DKI – Diffusion kurtosis imaging

DWI – Diffusion-weighted imaging

EUSOMA – European Society of Breast Cancer Specialists

EUSOBI – European Society of Breast Imaging

EPI – Echo planar imaging

ER – Estrogen receptor

FAP1 – Fibroblast-activation protein inhibitor

FOV – Field of view

GRAPPA – Generalized autocalibrating partial parallel acquisition

HER2 – Human epidermal growth factor receptor 2

HER2-E – Human epidermal growth factor receptor 2-enriched subtype

IVIM – Intravoxel incoherent motion

LABC – Locally-advanced breast cancer

LCIS – Lobular carcinoma in situ

MUSE – Multiplexed sensitivity-encoding

MRI – Magnetic resonance imaging

NAC – Neoadjuvant chemotherapy

NME – Non-mass enhancement

NST – Invasive carcinoma of no special type

PET – Positron emission tomography

PET/CT – Simultaneous positron emission tomography and computed tomography

PET/MRI – Simultaneous positron emission tomography and magnetic resonance imaging

pCR – Pathological complete response

PgR – Progesterone receptor

PDF – Probability density function
PE – Phase encoding
RF – Radiofrequency
ROC – Receiver operating characteristic
ROI – Region of interest
RPG – Reverse polarity gradient
RSI – Restriction Spectrum Imaging
SNR – Signal-to-noise ratio
TDLU – Terminal duct lobular units
TE – Echo time
TR – Repetition time
¹⁸F-FDG – Fluorodeoxyglucose F 18
¹⁸F-FES – Fluoroestradiol F 18
⁶⁸Ga – Gallium 68

Table of Contents

1. Introduction	15
2. Background	17
2.1 Breast anatomy and function	17
2.2 Epidemiology	19
2.3 Diagnosis	19
2.4 Breast cancer stratification	20
2.4.1 Pathology and subtypes.....	20
2.4.2 Stages.....	21
2.5 Prognosis	23
2.6 Locally-advanced breast cancer (LABC)	23
2.7 Treatment response endpoint: pathological complete response (pCR)	24
2.8 Physical basis of MRI	24
2.9 Radiological assessment of breast cancer; mammography, ultrasound, MRI	26
2.9.1 Indications for breast MRI.....	27
2.9.2 Standard breast MRI acquisition.....	27
2.9.3 Breast Imaging-Reporting and Data System (BI-RADS).....	28
2.10 Novel MRI Methods – DWI	30
2.10.1 Biophysical background and DWI acquisition.....	30
2.11 Models of diffusion signal decay	33
2.11.1 Modeling low and mid b-values.....	34
2.11.2 Modeling high b-values.....	35
2.12 DWI in the breast	40
2.13 MRI during neoadjuvant therapy	41
2.14 Physical basis of positron emission tomography (PET)	43
2.15 PET/MRI in the breast	44
3. Aims	45
4. Materials and methods	47
4.1 Patient cohorts	47
4.1.1 Longitudinal PET/MRI cohort (paper I).....	47
4.1.2 Baseline high b-value MRI cohort 1 (papers II and III).....	48
4.1.3 Baseline high b-value MRI cohort 2 (papers II and III).....	48
4.1.4 Longitudinal high b-value MRI cohort (paper IV).....	48
4.2 PET/MRI and MRI acquisition	50
4.2.1 PET/MRI acquisition (paper I).....	50
4.2.2 MRI acquisition (papers II-IV).....	50
4.3 Image preparation	50
4.4 Segmentation	52
4.4.1 Manual segmentation.....	52
4.4.2 Semi-automated PET/MRI segmentation (paper I).....	53
4.5 DWI analysis	53

4.5.1 Conventional DWI analysis (papers I–IV).....	53
4.5.2 Multi-component partial volume modeling of DWI signal decay (papers II–IV).....	54
4.5.3 Development of an automatic RSI tissue classifier for neoadjuvant therapy response evaluation (paper IV).....	55
4.5.4 Conventional imaging metrics during neoadjuvant treatment (papers I and IV).....	56
4.5.5 Response definition (papers I and IV).....	56
4.5.6 Assessment of contrast-to-noise ratio (CNR) (paper II).....	58
4.6 Statistical analysis	58
4.6.1 Longitudinal metric and spatial concordance assessment (paper I)	58
4.6.2 SNR and determination of DWI data goodness-of-fit (paper II).....	58
4.6.3 Discrimination between cancer and healthy breast tissues (papers II and III)	58
4.6.4 Response prediction (paper IV).....	59
5. Summary of papers	61
5.1 Paper I.....	61
5.2 Paper II	62
5.3 Paper III.....	64
5.4 Paper IV	65
6. Discussion.....	67
6.1 GMM-PET ROI metrics mimic conventional treatment measures (area, ADC) derived from manual DCE (paper I).....	68
6.2 Spatial concordance between PET-derived segmentation and manual DCE (paper I).....	68
6.3 GMM-PET segmentation compared to conventional DCE in a neoadjuvant setting (paper I)	69
6.4 Institutional differences in diffusion signal (paper II).....	70
6.5 Three-component RSI model reveals the diffusional composition of breast tissues (paper II).....	71
6.6 Three-component RSI model better fit breast diffusion data (paper II).....	71
6.7 Application of the three-component RSI model allows for biophysical characterization of breast tissues (paper II).....	73
6.8 Discrimination between cancer and healthy breast tissues with RSI C_1C_2 (paper III).....	77
6.9 C_1C_2 discriminatory performance in comparison to conventional DWI (paper III)	79
6.10 C_1C_2 discriminatory performance in comparison to DCE (paper III)	80
6.11 C_1C_2 in comparison to other high b-value models (paper III).....	81
6.12 RSI classifier for longitudinal response assessment compared to DCE (paper IV)	81
6.13 RSI classifier for longitudinal response assessment compared to DWI (paper IV)	83
6.13.1 ROI definition	84
6.13.2 ADC calculation.....	86
6.14 Signal-to-noise (SNR)	86

6.15 Limitations	88
6.16 Future implications of hybrid PET/MRI and the three-component RSI model ..	92
7. Conclusion	99
8. References	101
9. Papers	113

1. Introduction

Breast cancer is the leading cause of cancer death in women worldwide ¹, and is the most frequent female malignancy both globally ¹ and in Norway ². Breast cancer prognosis is highly dependent on the cancer stage at the time of diagnosis; the 5-year relative survival rate is 92.1 % for the entire patient group, reduced to 79.4 % for more severe cancer stages ². For high-risk patients (stage III; 10.4 % of breast cancer population) ², tumor downstaging by neoadjuvant medical therapy prior to surgical removal is critical to allow breast-conserving surgery and ameliorate their poor prognosis ³.

The European Society of Breast Cancer Specialists (EUSOMA) breast cancer working group of 2010 has urged the investigation of magnetic resonance imaging (MRI) as a potential source of non-invasive biomarkers for the prediction of treatment response ⁴. Alongside MRI, simultaneous positron emission tomography (PET) and MRI (PET/MRI) is a recent technology with significant potential in many aspects of breast cancer practice, including diagnostics, staging, and neoadjuvant response evaluation ⁵. Early and accurate detection of non-responders is key to discontinuing ineffective treatment and embarking on alternative treatment regimens. The multi-modal physiological tumor characterization that can be obtained with PET/MRI suggests clinical utility in this setting, although this is not yet well-explored. Thus, one focus of this thesis was to optimize MRI-derived predictive biomarkers for improved treatment response evaluation of breast cancer in a neoadjuvant chemotherapy (NAC) setting.

Dynamic contrast-enhanced imaging (DCE) is the most sensitive breast cancer detection tool ⁶⁻¹⁰. However, DCE is limited by conflicting results regarding specificity ⁷⁻¹¹, dependency on expert radiologist readers, additional costs, and the use of Gadolinium-based contrast agents that are linked to deposition in the brain ¹². In addition to PET/MRI, another alternative to DCE is diffusion-weighted MRI (DWI), an imaging technique that does not require an extrinsic contrast agent, but where image contrast is sensitized to water diffusion in tissue via application of pulsed magnetic field gradients. In its simplest form, diffusion information from DWI can be quantified by the calculation of the conventional apparent diffusion coefficient (*ADC*), a robust biomarker that is reduced in tumor tissue and which has shown a greater specificity than conventional MRI for distinguishing between *pre-identified* malignant and benign lesions ¹³⁻¹⁵. However, DWI is underexplored for discriminating cancer tissue from all other breast

tissues, an application that would increase the clinical utility of DWI in a range of breast cancer evaluation settings. To reach this goal, the diffusional composition of cancer and healthy breast tissues must be explored. Thus, another focus of this thesis was to determine the diffusion profile of breast tissue by application of advanced diffusion models. This will lay the foundation to explore the ability of diffusion models, optimized for breast application, to distinguish cancer from healthy breast tissues. The development of advanced DWI methods is important for the overall goal of improved conspicuity of cancer relative to background breast tissue, which is fundamental for the real-world application of any oncological imaging technique.

2. Background

2.1 Breast anatomy and function

The breasts are two prominences located ventral to the pectoral muscles of the torso (Figure 1). Each breast is organized into ~20 milk-producing units called lobes. Furthermore, each lobe is organized into smaller clusters of glands called lobules with a primary functional unit called terminal duct lobular unit (TDLU) ¹⁶ (Figure 2A). TDLUs consist of clusters of highly specialized glands that produce milk, and a small segment of the duct (terminal duct) that transports milk from the glands. When breast cancer develops, it most frequently arises from TDLUs ¹⁷. From the TDLUs, the milk is transported through a network of ducts to the nipple where it secretes through holes in the surface of the breast. The nipple lies within an area of pigmented skin called the areola ¹⁸.

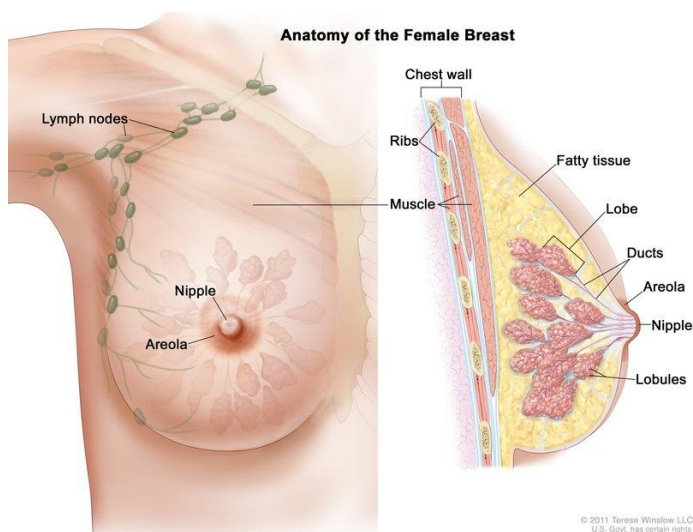


Figure 1. Breast anatomy. © 2011 Terese Winslow LLC, U.S. Govt. has certain rights.

The major components of healthy breast tissues are fatty tissue, glandular tissue, and fibrous tissue. Fibrous tissue is a specialized connective tissue that surrounds and supports glands and ducts in the TDLUs. Fatty tissue lies in between the lobes and encloses the breast and provides isolation ¹⁸. Fatty tissue is primarily made up of adipocytes which typically contain a large lipid

droplet, occupying > 90 % of the cell volume, leaving a small rim of water-containing cytoplasm (Figure 2B). On average, fatty tissue consists of ~ 85 % lipids and ~ 15 % water ¹⁹. This means that healthy breast tissues are an admixture of fibrous, glandular, and fatty tissue rather than distinctly separate areas of different healthy tissue types. The fibrous and glandular tissue is collectively known as fibroglandular tissue, and this term will be used throughout this text.

The breast also includes a network of blood and lymph vessels. The main blood supply of the breasts comes from the thoracoacromial and internal mammary arteries. Lymphatic vessels drain the breast to internal mammary and axillary lymph nodes. Lymphatic spread to these lymph nodes is the most frequent route of metastasis in breast cancer ¹⁸.

The relative composition of fatty and fibroglandular tissue varies greatly among women and throughout a woman's lifetime. Healthy breast tissues are targets for sex hormones ²⁰, and their size and contribution thus fluctuate throughout female hormonal changes such as menstruation, pregnancy, lactation, and menopause. After menopause healthy breast tissue becomes increasingly fatty and less fibroglandular. Radiologic evaluation of the breasts therefore includes categorization of the general breast composition concerning fatty and fibroglandular tissue: breast density (mammography) and amount of fibroglandular tissue and degree of background parenchymal enhancement (BPE) on MRI.

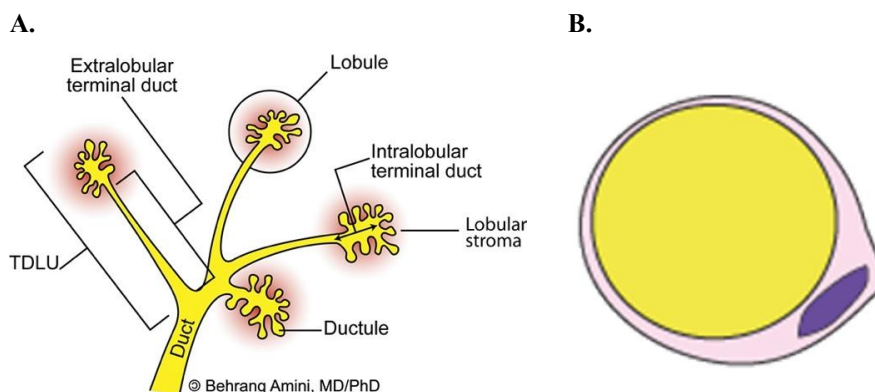


Figure 2. A. Terminal duct lobular unit (TDLU). B. Adipocytes. Illustration 2A. is from © Behrang Amini, MD/PhD published under the creative commons license CC BY-NC-SA 3.0 (<https://creativecommons.org/licenses/by/3.0/deed.no>).

2.2 Epidemiology

Breast cancer is the most frequent female malignancy both globally ¹ and in Norway ²; in Norway, one in every 11 women will develop breast cancer by the age of 80 years. The risk of developing breast cancer increases with age, where women over the age of 50 are primarily affected, and the mean age for diagnosis is 62 years ². Conversely, men are rarely affected by breast cancer; of the 3455 new cases recorded in Norway in 2020, only 31 were men. In addition, there is a clear trend towards an increase in the diagnosis of disease over the past years, with only 1235 women receiving the diagnosis in 1970 (Figure 3) ². Alongside improved diagnostics and treatment, one important contributing factor is the Norwegian public x-ray mammography screening program which was introduced in 1996 for women in the age group 50–69. Similarly, there has been a clear increase in survival rates, and mortality has slightly decreased (Figure 3) ².

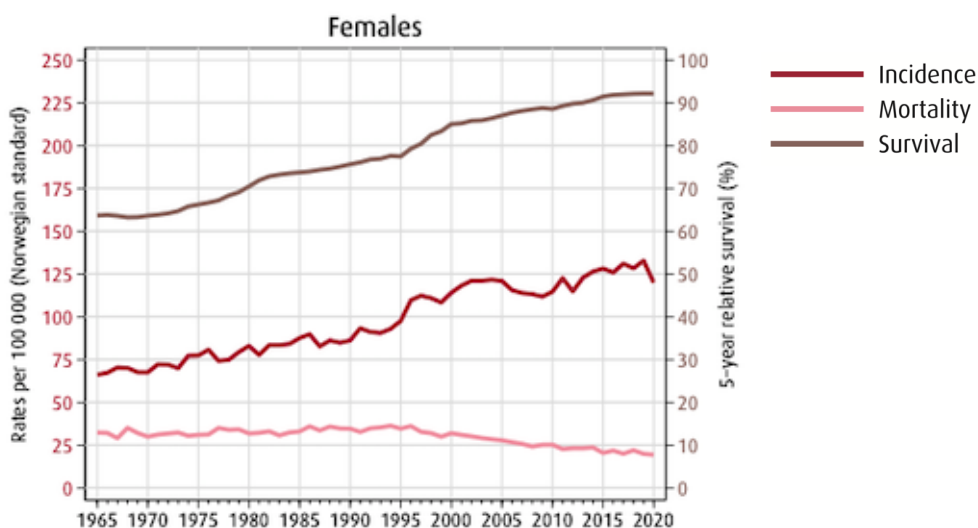


Figure 3. Trends in incidence and mortality rates and 5-year relative survival proportions in Norway. *Adapted from ² with permission.*

2.3 Diagnosis

In Norway, breast cancer is diagnosed by “triple diagnosis” which consists of clinical palpation of the breast, radiological assessment, and histopathologic analysis of core needle biopsy ²¹. This is performed by a multidisciplinary team: clinical palpation by a breast and endocrine

surgeon, radiological assessment (see 2.9) by a radiologist, and histopathological analysis of the biopsy by a pathologist.

2.4 Breast cancer stratification

Breast cancer is a heterogeneous disease and can be stratified based on pathological characteristics into subtypes and stages (extent of spread). These stratifications are the basis for treatment recommendations and follow-up.

2.4.1 Pathology and subtypes

Most invasive breast cancers are carcinomas, which are cancers that develop from epithelial cells. Once abnormal cells spread and invade surrounding fibrous and fatty tissue the lesion is considered cancerous. Following the new WHO guidelines¹⁷ from 2012, invasive carcinoma of no special type (NST) is the new term for what was previously described as “invasive ductal carcinoma”. The justification for this change in terminology is related to the current thinking that carcinomas arise from the TDLUs which makes the term “ductal” misleading²². NST is the most common type of invasive breast carcinomas and makes up 70–80 % of all cases¹⁷, while invasive lobular carcinomas are the second most common type (10–20 %). In situ lesions are pre-cancerous lesions where abnormal cells have not yet invaded surrounding fibrous and fatty tissues; these are ductal carcinoma in situ (DCIS) and lobular carcinoma in situ (LCIS).

Breast cancer may furthermore be sub-classified into subtypes based on gene expression profiling, yielding five subtypes: luminal A, luminal B, human epidermal growth factor receptor 2-enriched (HER2-E), basal-like (basal), and normal-like²³. Luminal A is the most common, then luminal B, basal, and HER2-E in primary breast cancer²⁴; the normal-like subtype is rarely used and will not be discussed in further detail. Each subtype has a characteristic gene expression profile with a distinct receptor- and cell proliferation marker (Ki67)-signature linked to it. Since the receptor profiling, with expression of estrogen receptor (ER), progesterone receptor (PgR), and human epidermal growth factor receptor 2 (HER2) are targets for standard-of-care treatment regimens, these subtypes are vital for treatment decision-making and are known to correlate with clinical outcome²⁵. The Prosigna gene profile test is now approved for gene profiling in the clinic in Norway²¹.

Luminal A and luminal B are both hormone-receptor positive (ER positive and/or PgR positive) while the majority are HER2 negative ²⁶. The main difference between the two luminal subtypes is the proliferation rate, where luminal A has lower levels of Ki67 and is thus more slowly growing, which is linked to a slightly better prognosis and longer relapse-free survival compared to luminal B. HER2-E cancers are generally hormone negative (ER and PgR negative), HER2 positive, and have higher Ki67 levels, though there is some variability within the subtype. Lastly, the basal subtype is triple-negative for the majority of tumors within this subtype, which means that it is negative for all receptors (ER, PgR, and HER2 negative) and has the poorest prognosis ²⁵. Both the hormone-positive luminal A and luminal B are targets for endocrine therapy while HER2-E are targets for HER2-targeted therapies such as trastuzumab. In most cases, chemotherapy is indicated for all subtypes except luminal A ²⁷; thus, one of the most clinically important aspects of gene profiling is identifying luminal A cancer.

2.4.2 Stages

Breast cancer extent of spread is graded through the globally recognized standard TNM classification system for solid tumors and is used to guide patient management and evaluate prognosis ²⁸. The system classifies the extent of cancer spread by the size and local invasion of the primary tumor (“T”), the involvement of regional lymph nodes (“N”), and the presence of distant metastasis (“M”). In breast cancer, four stages with increasing extent of spread are derived from the TNM classification: stage I, stage II, stage III, and stage IV; details are given in given in Table 1 and Figure 4.

Breast cancer stage	TNM code	Definition
Stage I	T1N0M0	Primary tumor size <2 cm. No involvement for regional lymph nodes or presence of distant metastasis.
Stage II	T0-2N1M0	Primary tumor size <2 cm with involvement of movable ipsilateral axillary lymph nodes.
	T2N0M0	Primary tumor size 2-5 cm without involvement of lymph nodes.
Stage III	T3N0M0	Primary tumor size >5 cm without involvement of lymph nodes.
	T0-2N2M0	Primary tumor size 2-5 cm with involvement of ipsilateral axillary lymph nodes which are knitted to each other or surrounding tissue or ipsilateral mammaia interna lymph nodes.
	T3N1-2M0	Primary tumor size >5 cm with involvement of movable ipsilateral axillary lymph nodes, ipsilateral axillary lymph nodes which are knitted to each other or surrounding tissue or ipsilateral mammaia interna lymph nodes.
	T4N0-2M0	Primary tumor of any size with local growth into the skin or chest wall.
Stage IV	T0-4N3M0	Primary tumor of any size with more widespread regional lymph node involvement, including ipsilateral infra- or supraclavicular lymph nodes or involvement of both ipsilateral axillary lymph nodes and ipsilateral mammaia interna lymph nodes.
	T1-4N0-3M1	Presence of distant metastasis. Primary tumor of any size and regional lymph node involvement of any kind.

Table 1. Staging of breast cancer based on TNM-classification. Rows marked in orange are defined as primary inoperable ²¹.

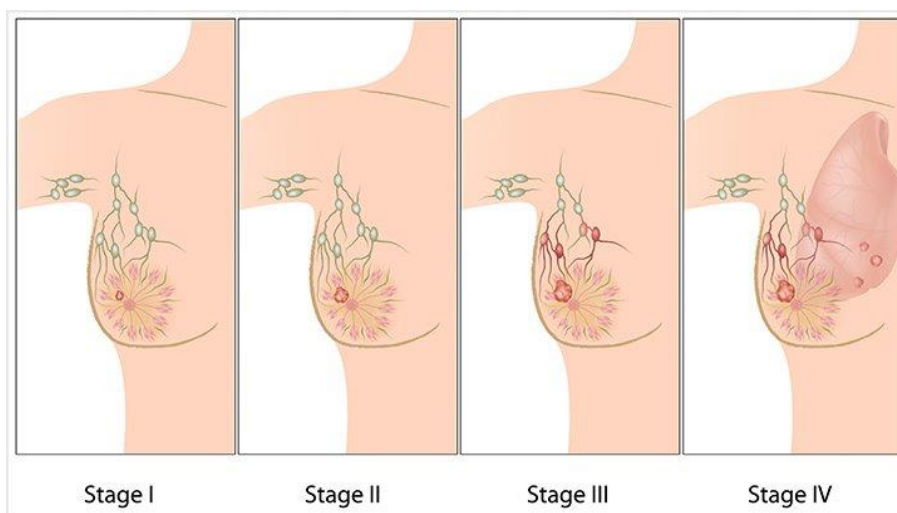


Figure 4. Four stages with increasing extent of spread: stage I, stage II, stage III, and stage IV. The image was obtained from ²⁹.

2.5 Prognosis

Breast cancer is the leading cause of female cancer-related death globally ¹ and primary reason for years of life lost for women up to 65 years in Norway ³⁰. The prognosis of breast cancer has improved over the last decades, and the 5-year survival rate for the entire patient group in 2016–2020 has reached 92.1 %, largely due to early diagnosis as a result of the mammography screening program, in addition to improved treatment regimens and diagnostics. However, the prognosis is highly dependent on the cancer stage at the time of diagnosis; the 5-year survival rate relative to the general population for stage I cancer is 100.5 %, for stage II is 96.1 %, but only 79.4 % for stage III and 33.9 % for IV. Consequently, different patient management is required for the different stages, where locally-advanced breast cancer (LABC, see 2.6) is a group that requires extra treatment efforts ²¹.

Given the relatively high overall prognosis, many women live on after breast cancer treatment. There has been an increased focus on the side effects these women face, such as chronic fatigue, premature menopause, infertility, osteoporosis, and sexual dysfunction, according to Patient Reported outcome Measures and Patient Reported Experience Measures ³¹.

2.6 Locally-advanced breast cancer (LABC)

LABC is defined as large cancers with a primary tumor size > 5 cm (T3), local infiltration of skin or muscle (T4), or locally-advanced lymph node involvement (N2–3). In the TNM classification system, the term is used for stage III tumors (10.4 % of breast cancer population) ², and large stage II tumors (T3N0M0), defined as primarily inoperable (Table 1). Thus, LABC occurs in a heterogeneous group of breast cancer patients with variable prognosis, as T3 tumors have a considerably better prognosis compared to T4. Stage III cancers make up a small group of all breast cancer patients (approximately 10 %) ². Contrary to standard patient care, tumor downstaging by neoadjuvant medical therapy before surgery is used to make tumors operable or enable breast-conserving surgery, control micrometastasis, and aid as an *in vivo* drug-sensitivity test bed ^{32,33} (Figure 5). The neoadjuvant treatment regimen is assessed individually for each patient, where subtype/receptor status are main determinants for treatment choice. Most patients receive NAC, but endocrine therapy can be an alternative for selected subtypes (Luminal A) ²¹. One key aspect of neoadjuvant therapy regimens is that they are adaptive, meaning that treatment selection is tailored during therapy. Thus, assessment of the efficiency

of therapy is crucial to guide therapy selection. Ideally, predicting response as early as possible may help tailor treatment regimens for the best patient outcome.

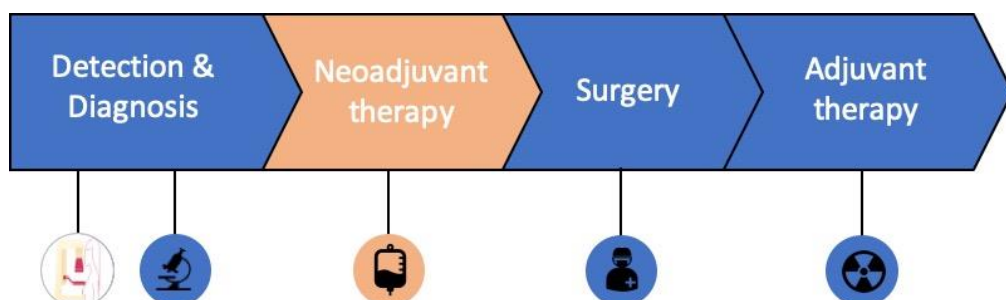


Figure 5. Schematic figure of work-up and patient care for locally-advanced breast cancer (LABC). Detection and diagnosis, surgery, and neoadjuvant therapy are standard-of-care for all breast cancers (except stage IV), while neoadjuvant therapy (orange) is indicated for LABC only.

2.7 Treatment response endpoint: pathological complete response (pCR)

Another goal of neoadjuvant therapy is pathological complete response (pCR), defined as no remaining tumor tissue in breast and lymph nodes as measured by post-surgical pathology. pCR is the most used endpoint to evaluate response to neoadjuvant therapy. A large meta-analysis by Cortazar et al. concluded that pCR correlates with improved survival and a reduced chance of breast cancer recurrence³⁴. Though the field of genetic sequencing has massive ongoing experimental trials associating specific genes to chemoresistance, the *in vivo* association is still limited and has to this date not produced any predictive factors assessed in clinical care³⁵. Consequently, a major field of interest is to be able to predict pCR through MRI-derived predictive biomarkers. The EUSOMA breast cancer working group of 2010 urged for further investigation of MRI as a source of potential non-invasive biomarkers in response prediction⁴. This has become a major field of interest. Such predictive biomarkers may guide treatment switching, expedite surgical intervention for responders, and select correct treatment regimens to avoid unnecessary toxic side effects.

2.8 Physical basis of MRI

MRI is an imaging modality that allows the formation of images from the interaction of certain atomic nuclei with magnetic fields. In particular, hydrogen atoms (protons) that are abundant

in the human body, predominantly as part of a water molecule (H_2O) in soft tissue, are visible by MR since they possess a spin angular momentum $\frac{1}{2}$. When the patient is positioned in the MRI scanner, the protons are exposed to the main magnetic field B_0 , (Figure 6A), the proton spin eigenstates adopt an equilibrium state with a slight net magnetic alignment M_0 (Figure 6B) and have known resonant precession frequency (determined by B_0 and the nucleus type) in the radiofrequency (RF) range. During an imaging sequence, RF pulses applied to the system temporarily disrupt the equilibrium (Figure 6C), leading to a precessing magnetic signal that induces a voltage in receiver coils placed around the patient in the transverse plane (and which are also used for the RF transmission) (Figure 6D). This induced voltage is the MR signal, which decays as the protons return to their equilibrium state through various simultaneous relaxation processes (see below). The MR signal can be spatially encoded in order to give images by modulating the RF frequency and phase of particular spin locations across the object through the use of linear magnetic field gradients along chosen axes, which also enable the selective excitation of particular slices through the patient.³⁶ The specific details of MR image generation, as well as echo planar imaging (EPI) sequences and diffusion encoding, are well-established³⁶ and beyond the scope of this introduction. Only standard imaging sequences were used in this thesis.

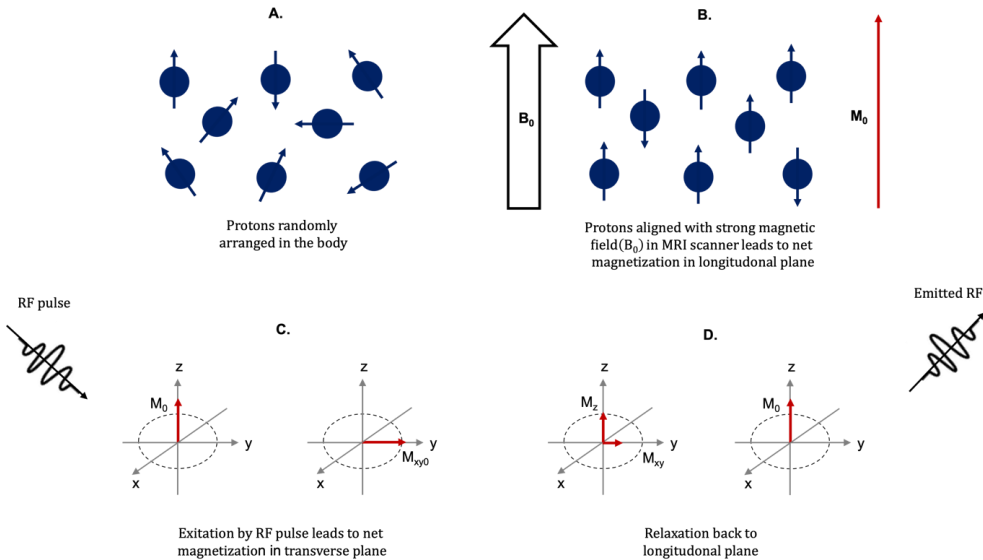


Figure 6A–D. Basic principles of MRI signal generation. The MR signal arises from a slight net alignment with the stationary field B_0 , and this net magnetization interacts with an RF pulse to disturb the equilibrium. Once disturbed, any transverse magnetization precesses around B_0

and induces an RF signal in the receiver coil. RF; radiofrequency. *Adapted and modified from* ³⁷ *with permission.*

Two basic MR sequence parameters which influence the overall image contrast in the MRI acquisition protocol are the repetition time (TR) and the echo time (TE). TR is the time between the delivery of consecutive RF excitation pulses, while TE is the time between the RF pulse and the resulting echo signal from the protons. The choice of TR and TE are important because they allow time for different relaxation processes of the excited protons, governed by time constants T1 and T2. Both are exponential decay time constants; T1 is associated with the return to equilibrium with the B₀ magnetic field, and T2 describes the decay of the observable signal. These processes reflect the local spin environment, and so T1 and T2 relaxation times will vary among different tissue types, resulting in contrast between different tissues in the acquired images (on top of the underlying density of proton spins in each location). Choice of TR and TE can thus be tuned to reveal useful anatomical information; in addition to these intrinsic contrast mechanisms, and of relevance to the work in this thesis, tissue contrast in MRI can also be generated through the diffusion of water molecules (see below) ³⁶.

2.9 Radiological assessment of breast cancer; mammography, ultrasound, MRI

A variety of radiological tools are used for breast cancer detection and follow-up. X-ray *mammography* is the primary screening tool for the general population where the goal is early detection of early-stage disease to reduce breast cancer mortality. However, mammography has several limitations including low positive predictive value ^{38,39}, alongside the personal, health care, and societal impact of false results. Moreover, mammography primarily detects slowly growing low-grade and in situ cancers ⁴⁰. Both WHO ⁴¹ and the European Commission Initiative on Breast Cancer ⁴² strongly recommends systematic mammography screening for women in the age group 50–69 years in well-resourced countries with a health care system able to implement large-scale population-based screening programs. Together with several European countries, Norway has followed these recommendations; screening was introduced in 1996 for the age group 50–69 years every other year ²¹. Moreover, screening guidelines for ages 40–44 years, 45–49 years, and 70–74 years vary for the European Commission Initiative on Breast Cancer ⁴² and WHO ⁴¹. In the US, the Society of Breast Imaging and The American

College of Radiology recommends annual mammography screening already at the age of 40 and without an upper age limit unless severe comorbidities limit life expectancy⁴³.

Additionally, *ultrasound* may be used as a complement to mammography and is especially useful in younger women whose breasts are filled with abundant glandular tissue making mammographs difficult to interpret, so-called dense breast. Similar approaches are used for follow-up after primary treatment for the detection of cancer recurrence. Breast *MRI* is shown to have the highest sensitivity for breast cancer detection^{6-9,44,45} and is shown to detect more clinically-relevant tumors⁴⁰. Nevertheless, conventional breast MRI is considered too expensive, time-consuming, and inaccessible for mainstream screening of the general population but has indications in several other settings.

2.9.1 Indications for breast MRI

According to the American College of Radiology, current indications for breast MRI include preoperative evaluation of the extent of disease for selected patient groups (staging), assessment of treatment response for patients undergoing neoadjuvant therapy, and surveillance of high-risk patients with $\geq 20\%$ lifetime risk of breast cancer⁴⁶. MRI has proven to be the best available modality for assessment of treatment response to neoadjuvant therapy and is indicated for a patient with LABC or stage T2 disease receiving neoadjuvant therapy⁴⁷ (see below). Additional indications are assessment of occult breast cancer in the setting of axillary lymphatic metastatic disease of unknown primary origin if mammography and ultrasound are negative and problem-solving if mammography and ultrasound show inconclusive results. These indications are mimicked in the 2021 guidelines from the Norwegian Directorate of Health²¹. In the Norwegian guidelines, screening of high-risk patients includes women with highly penetrant gene mutations such as BRCA1 and BRCA2, who are recommended to have annual screening with combined mammography and MRI from the age of 25 (MRI only from 20 years of age for TP53 mutation carriers).

2.9.2 Standard breast MRI acquisition

The current standard MRI breast tumor evaluation protocol (Figure 7) includes T2- and T1-weighted images, DWI and DCE. The T2-series displays the anatomy of the breast well and can therefore detect areas of suspected malignancy. The definition of tumor on DCE images is

governed by leaking of gadolinium contrast through pathological vessels that are abundant in tumor tissue owing to malignancy-related angiogenesis. The DCE acquisition consists of a baseline pre-contrast T1-weighted image prior to contrast injection followed by 6 post-contrast images acquired 1 minute apart. This lengthy acquisition of 7 minutes is required to generate kinetic enhancement curves which are critical for tumor assessment through the Breast Imaging-Reporting and Data System (BI-RADS) (see below). Though not yet a part of the standardized BI-RADS reporting system, DWI is becoming a part of standard breast MRI acquisition at many sites ⁴⁸.

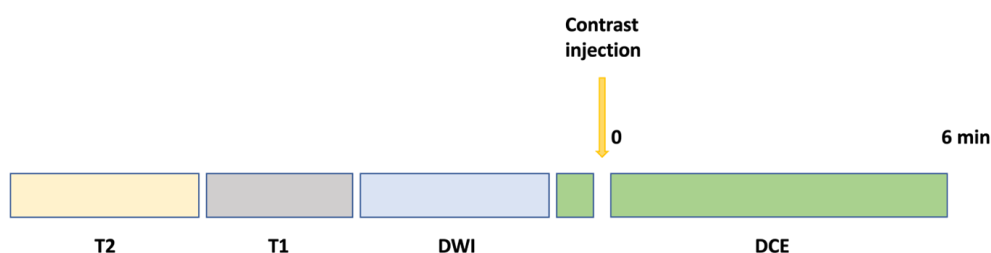


Figure 7. Schematic of clinical breast MRI protocol at St. Olavs Hospital, Trondheim., Norway. DCE; Dynamic contrast-enhanced imaging. DWI; Diffusion weighted imaging. T1: T1-weighted imaging. T2; T2-weighted imaging.

2.9.3 Breast Imaging-Reporting and Data System (BI-RADS)

BI-RADS ⁴⁹ is a standardized breast imaging reporting system for mammography, breast ultrasound, and breast MRI used by radiologists. BI-RADS for breast MRI assesses both the general breast composition and breast lesions and provides final assessment categories yielding the likelihood of cancer and proper management and follow-up. Here the main aspects of BI-RADS for breast MRI are described.

General breast composition

Breast composition is categorized into four categories based on the amount of fibroglandular tissue; almost entirely fat, scattered fibroglandular tissue, heterogeneous fibroglandular tissue, and extreme amount of fibroglandular tissue. Approximately 50 % of women have almost entirely fatty breast tissue or scattered fibroglandular tissue ⁵⁰. In addition, the degree of BPE on DCE is classified into four categories: minimal, mild, moderate, and marked. Assessment of breast composition is important because macroscopic tumor environment may confound lesion detection and categorization. For example, patients who present with moderate and

marked BPE on DCE are associated with both false positive ⁵¹ and false negative ⁵² interpretations.

Lesion assessment

Based on a combination of morphological and functional assessment criteria of breast lesions on MRI, BI-RADS provides a final assessment yielding the likelihood of cancer. Lesion interpretation is based on two basic steps: 1) lesion identification and 2) lesion classification. Lesion identification is based on the initial enhancement on DCE; if no lesion is found, a BI-RADS score of 1 is given. Furthermore, if a lesion is identified, it must be classified as benign or malignant. Lesions on MRI can be divided into three types which are described with different morphological assessment criteria: a focus (too small to be characterized), mass enhancement (lesion occupying a three-dimensional space), and non-mass enhancement (NME), meaning diffusely infiltrating lesion with unclear margins). Mass enhancement lesions are described by the morphological characteristics of shape, margin, and internal enhancement pattern, while NME is described by distribution pattern and internal enhancement pattern.

Furthermore, enhancement kinetics curves on DCE give a functional measure common for all lesion types ⁵³. The enhancement kinetics curves are defined by an initial phase and a delayed phase following administration of Gadolinium contrast. The initial phase may have a “slow”, “medium” or “fast” curve, while the delayed phase may show “persistent”, “plateau” or “wash-out”. A slow or medium enhancement in the initial phase followed by a persistent enhancement in the late phase is common in benign lesions. Contrary, a rapid initial phase followed by wash-out or plateau is indicative of malignant lesions.

It is the combined morphological and functional criteria that determine cancer suspicion: a round and well-circumscribed mass lesion with a medium initial phase curve followed by a persistent enhancement kinetic curve would most likely be interpreted as a benign finding, while similar morphological features combined with a rapid initial phase curve followed by wash-out enhancement kinetic curve is more indicative of cancer. MRI BI-RADS categories lesions from 0 to VI where 0 indicates additional imaging needed, I–V increasing likelihood of cancer, and VI known biopsy-proven cancer.

BI-RADS pitfalls

The BI-RADS classification system is conducted subjectively by a radiologist and there is no decision tree guiding clinical decision-making, making it prone to interobserver variability. An only fair interobserver agreement has been demonstrated for BPE rating ⁵⁴. For lesion classification, studies have shown moderate to a substantial interobserver agreement for most morphological characteristics ^{54,55}. However, there was only a slight agreement on lesion kinetics ⁵⁴, moderate agreement for NME compared to mass lesions ⁵⁵, and considerable disagreement regarding patient follow-up ⁵⁴.

Moreover, BI-RADS is dependent on DCE, which has several limitations such as low specificity ranging from 61 to 81 % ^{6-9,44,45}, concerns regarding contrast allergy, and potential brain deposition of Gadolinium with unknown sequela ¹². Gadolinium contrast is also contraindicated in patients with renal failure and pregnant women ⁵⁶. Moreover, there is a large overlap between kinetic curves and the different lesion types ⁵⁷. Thus, improvements in screening technology and methodology are essential for implementing precision treatment and can have a significant impact on health care. This has created a setting for the exploration of alternative techniques.

2.10 Novel MRI Methods – DWI

DWI is an MRI method that does not require exogenous contrast and yields quantitative information on tissue microstructure by being sensitive to Brownian motion (random movement) of water molecules through the application of the varying degree of pulsed field gradients.

2.10.1 Biophysical background and DWI acquisition

Diffusion of water molecules in biological tissue can be categorized as *free*, *hindered*, or *restricted* diffusion according to a component model of water diffusion (may also be referred to as a “compartment model”) ⁵⁸. Free diffusion is the random, isotropic Gaussian diffusion seen in pure solutions. Hindered and restricted diffusion refer to observably non-Gaussian diffusion, which is predominately defined in extracellular space by tortuosity of cell packing density and intracellular diffusion, respectively. The scalar distance water travels is defined by the diffusion time from the sequence parameters and may be quantified by DWI techniques.

As hypercellular tumors have increased restricted intracellular water, DWI has become an increasingly used tool for oncological imaging⁵⁹. Conventional DWI (ADC model, see below) typically measures the hindered and restricted diffusion collectively. Stronger diffusion weighting, by application of higher b -value (see below) regimens, is required to sensitize DWI to restricted components where the water has very short diffusion distances. DWI techniques may also reflect geometric information, but since it is not specifically relevant to the work in this thesis it will not be elaborated on in any further detail.

The conventional DWI acquisition protocol is based on the Stejskal-Tanner pulse sequence, which is a single-shot spin-echo sequence with an additional diffusion gradient pulse before and after the 180-degree refocusing pulse⁶⁰. The diffusion pulses are applied for a duration δ with a gradient strength G and time separation Δ (diffusion time) and enable measurement of length scale water diffusion properties (Figure 8). The diffusion gradient pulses are normally applied in a minimum of three orthogonal directions to reflect overall diffusion. An important term in DWI is the b -value which describes the degree of applied diffusion weighting. The diffusion weighting increases with increasing b -value, given as;

$$b = G^2 \cdot \gamma^2 \cdot \delta^2 \left(\Delta - \frac{\delta}{3} \right) \quad (1)$$

where b is the b -value given in s/mm^2 , γ is the gyromagnetic ratio of the nucleus (for MRI, water protons). Thus, the diffusion weighting can be increased by increasing diffusion duration δ or time Δ , and/or gradient strength G .

The purpose of the first pulse is to encode the physical position of the water molecules along the gradient pulse direction. This is done by adding phase increments to water molecule spins with increasing magnitude along the gradient field direction and is thus called the dephasing pulse. The second pulse (rephasing pulse) is applied after the spin echo pulse (which inverts the phase offsets) with the same gradient strength as the dephasing pulse and adds phase increments in the same way. Water molecules that change physical position between the diffusion pulses, i.e. during the duration Δ , will experience mismatched phase increments from the pulses owing to their changed position, and so will not be properly rephased by the rephasing pulse. This results in a signal at readout that is reduced proportionally with the

diffusion distance of water during time Δ , and thus the signal from free diffusion will be relatively decreased compared to hindered and restricted diffusion.

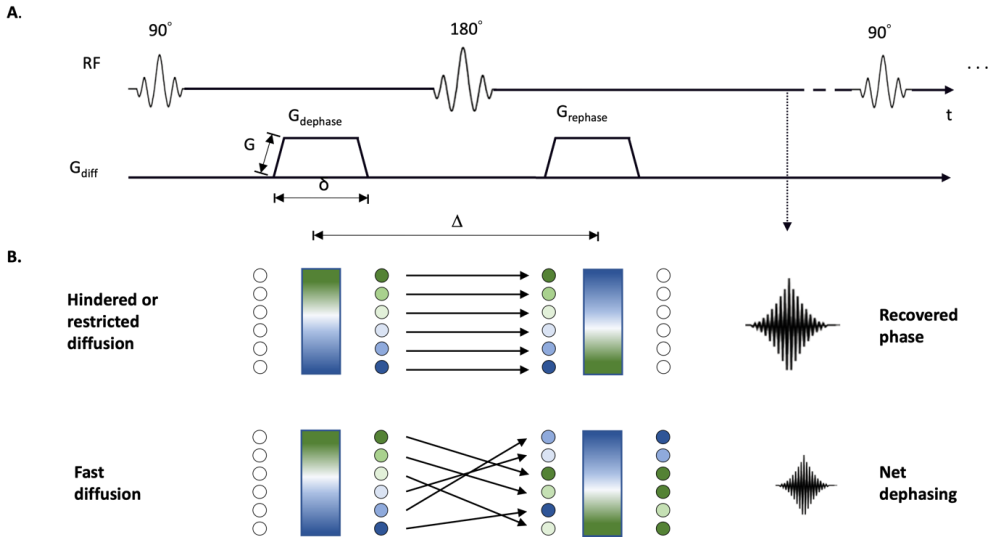


Figure 8. Illustration of A. basic principles of diffusion-weighted imaging (DWI) acquisition and B. one-dimensional schematic of net dephasing dependent on spin motion. A. Two symmetric diffusion pulses (G_{diff}), dephasing pulse ($G_{dephase}$) and rephasing pulse ($G_{rephase}$), are applied before and after the 180-degree radiofrequency pulse (RF), respectively. They are each applied for the duration δ and strength G , with the duration Δ apart. B. The diffusion pulses affect free diffusion spins and hindered/restricted diffusion spins differently. G_{diff} adds additional phase (blue and green being +/- additions to the static magnetic field), the amount defined by the spin location along the gradient pulse direction (here given up/down). Free diffusion spins change position between diffusion pulses, leading to net dephasing as these spins are not being rephased properly by $G_{rephase}$ and consequently lose readout signal. Hindered and restriction diffusion, however, remain in roughly the same location, which means that the dephasing from $G_{dephase}$ will be directly reversed by $G_{rephase}$. Thus, hindered and restricted diffusion results in an increased readout signal relative to free diffusion. Details of hindered and restricted diffusion are given in Figure 11. *Adapted and modified from ³⁷ and ⁶¹ with permission.*

The DWI signal in an image voxel (S_{DWI}) at a given b -value is typically described as:

$$S_{DWI} = S_0 \cdot e^{-b \cdot ADC} \quad (2)$$

where S_0 is the signal at $b = 0 \text{ mm}^2/\text{s}^2$, and ADC is the conventional apparent diffusion coefficient that quantifies this mono-exponential description. However, an important aspect of

the Stejskal-Tanner sequence, which is not explicit in the above formula that assumes the b -value is the only variable in the DWI acquisition, is that the signal is also T2-weighted, owing to the spin echo readout, which means that signal intensity on DWI is determined by both the intrinsic transverse relaxation time T2 and diffusion properties of the tissue. Additionally, proton density ρ also influences the diffusion signal. An alternative way of expressing the diffusion signal more clearly demonstrating the T2 and proton density effects is therefore:

$$S_{DWI} = S_{\rho} \cdot e^{-TE/T2_{eff}} \cdot e^{-b \cdot ADC} \quad (3)$$

where S_{ρ} is the total available signal for the given proton density ρ , TE is the echo time, and $T2_{eff}$ is the effective T2 relaxation time in a given voxel. For the remainder of this thesis, T2 effects on diffusion signal refer to $T2_{eff}$. As the TR is typically very long in diffusion acquisitions (5000–15000 ms), T1 influence is negligible. TE is typically 60–120 ms, which means that tissue with long T2 relaxation will have a proportionately high signal in the diffusion-weighted image, an effect known as “T2 shine-through”. Conventionally this has been regarded as an unwanted diffusion image contamination⁶² and, by calculating parametric ADC maps from multiple diffusion weightings with identical TR and TE , both T2- and proton density-influence is purposely removed to solely quantify diffusion properties.

2.11 Models of diffusion signal decay

There are many ways to model the diffusion signal on DWI, which may rely on different assumptions about underlying water diffusion in biological tissue. Firstly, the models differ in the range of b -values used to fit the model, which ultimately decides what aspect of physiology the models study. Low and mid b -values, up to approximately 1000 s/mm², are used to quantify free and hindered diffusion, as well as fast-flowing vascular fluid. On the other side, higher b -values are needed to probe the restricted diffusion within hypercellular tumors. Secondly, while some models are purely mathematical, such as kurtosis (see below), some multi-component models aim to provide information on underlying microstructure by explicitly modelling the diffusion of water in distinct components. These more biophysical models have become an emerging standard in several imaging domains⁶³⁻⁶⁷.

2.11.1 Modeling low and mid b -values

In its simplest form, the diffusion signal can be modeled as described in equations 2 and 3 by application of two or more separate b -values which allows for the calculation of ADC ⁶⁸ as a quantifiable diffusion measure. This model explicitly assumes a single Gaussian process, or random model of diffusion behavior (i.e. isotropic unrestricted diffusion), which manifests as a mono-exponential signal decay across b -values. However, water diffusion in biological tissue is a complex phenomenon influenced by tissue microstructure such as cell membranes and perfusion which in turn may influence diffusion signal decay. The ADC model thus does not separately account for signal originating from hindered and restricted diffusion components, and so fitting a mono-exponential is an oversimplification of the true signal curve in the presence of these effects. This has motivated the development of more advanced diffusion models to describe the diffusion signal decay across b -values more fully

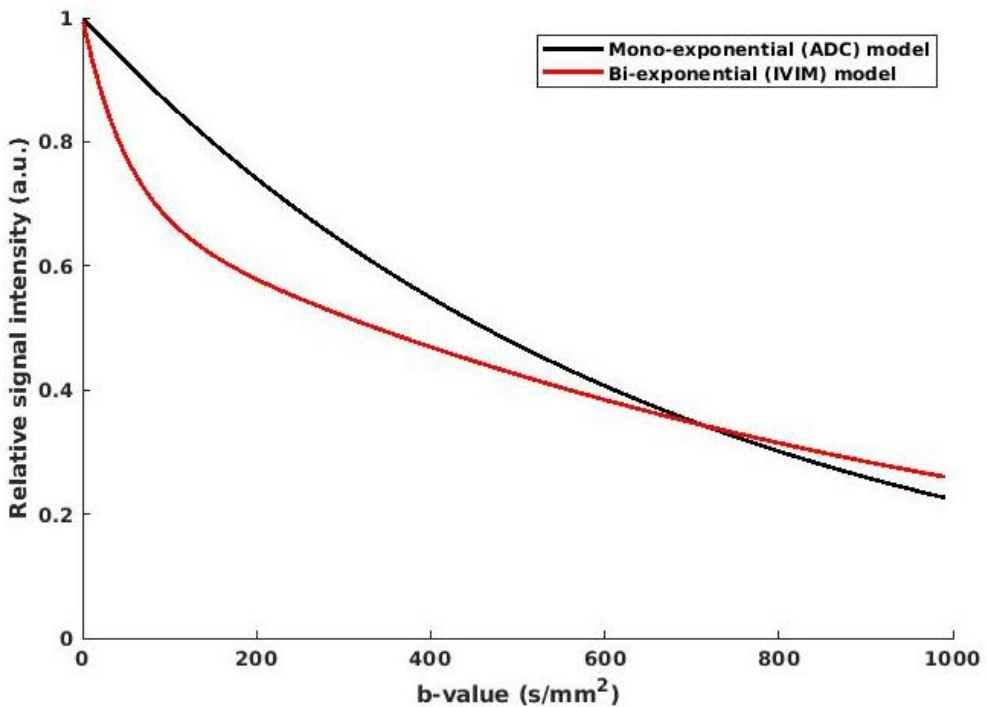


Figure 9. Illustration of signal over low and mid b -value ranges, here displaying up to 1000 s/mm^2 . Mono-exponential (ADC model) and bi-exponential (IVIM model) are displayed; note the deviation of IVIM model from the Gaussian ADC model. Parameters used for the simulation were $ADC = 0.0015 \text{ mm}^2/s$ for ADC model, and $f = 0.3$, $D = 0.001 \text{ mm}^2/s$, and $D^* = 0.02 \text{ mm}^2/s$ for IVIM model. Note that the curves are for illustration purposes only and effects are exaggerated. a.u.; arbitrary unit. IVIM; intravoxel incoherent motion.

Intravoxel incoherent motion (IVIM) model

The intravoxel incoherent motion (IVIM) model is a DWI model that was first proposed by Denis Le Bihan in the 1980s⁶⁸. IVIM assumes two primary types of diffusion in biological tissue; “true” Gaussian diffusion within the extracellular matrix, and microscopic diffusion of capillary blood flow which manifests as an accelerated diffusion process (pseudodiffusion) given the right assumptions. This is mathematically expressed as a two-component model that assumes a bi-exponential signal decay across b -values, where each element represents a distinct tissue component with its own signal decay quantified with a corresponding diffusion coefficient. In the low b -value range, commonly less than 200 s/mm², the faster pseudodiffusion component of the signal is effectively removed, while the true diffusion component signal, from free and hindered diffusion, remains up to and through the mid b -value ranges (typically up to 600–1000 s/mm²)⁶⁸. The overall curve is therefore non-Gaussian, and the signal decay is given as:

$$S_{DWI} = S_0[f \cdot e^{-b(D+D^*)} + (1 - f) \cdot e^{-bD}] \quad (4)$$

where f is the pseudodiffusion fraction, D^* is the pseudodiffusion coefficient corresponding to this component, and D is the “true” apparent diffusion coefficient (equivalent to ADC in the absence of a perfusion influence). In this fitting, the diffusion coefficients D and D^* are free parameters, and the equation becomes non-linear (cannot be linearized using a log transform in the way equation 2 can) and the signal fractions for each component are mutually dependent (summing to 1). The IVIM model also normalizes by S_0 which includes the T2- and proton density-weighting of diffusion signal, similar to ADC calculation (equation 3). Owing to the increased complexity, and the fast-decaying pseudodiffusion component of the model, to successfully fit a diffusion signal with the IVIM equation (equation 4), five or more b -values are typically used (though a minimum of three can yield a simplified version). Figure 9 shows example diffusion signal decay curves simulated for typical values of the ADC and IVIM models, and the behavior at small b -values can be clearly seen; where there is significant perfusion or flow component of the diffusion signal, the IVIM model may be more appropriate.

2.11.2 Modeling high b -values

Higher b -value ranges are needed to accurately probe the very short diffusion distances of the restricted intracellular water component. This is the aim of several DWI models because

hypercellular tumors have increased restricted intracellular water volumes, described below and with illustrative simulated curves shown in Figure 10.

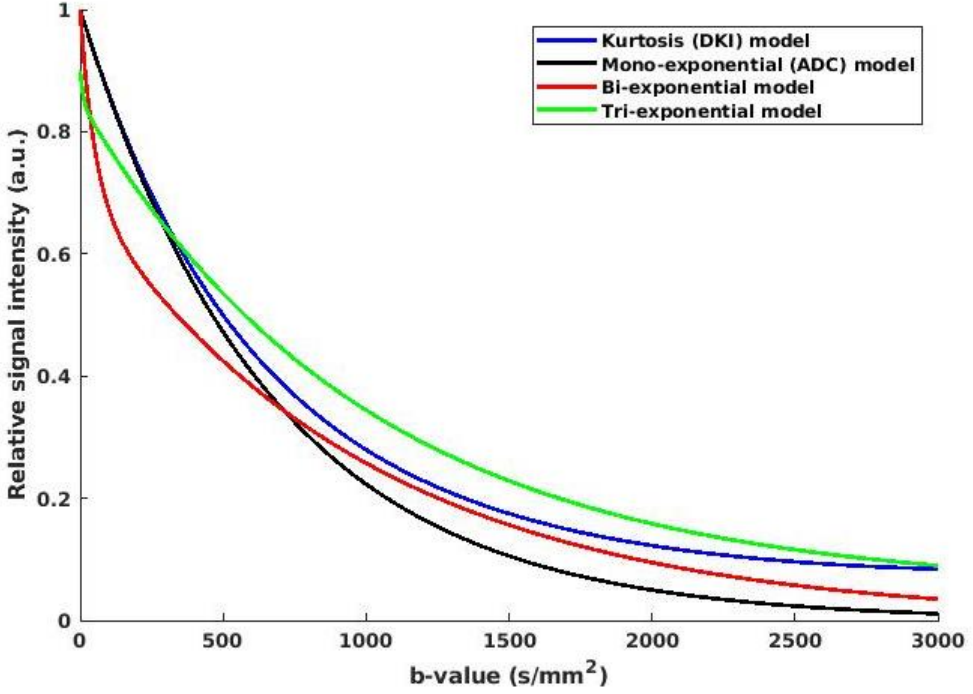


Figure 10. Illustration of signal over high b -value ranges, here displaying up to 3000 s/mm^2 . Mono-exponential (ADC model), multi-component model (here displayed with $K = 2$, bi-exponential, and $K = 3$, tri-exponential) and kurtosis (DKI) model. Parameters used for the simulation was $ADC = 0.0015 \text{ mm}^2/\text{s}$ for ADC model, $D_k = 0.0015 \text{ mm}^2/\text{s}$ and $K_{app} = 0.6$ for DKI model, $C_{1,2} = 0.3$, $C_{2,2} = 0.7$, $ADC_{1,2} = 0.02 \text{ mm}^2/\text{s}$ and $ADC_{2,2} = 0.001 \text{ mm}^2/\text{s}$ for bi-exponential model, and $C_{1,3} = 0.05$, $C_{2,3} = 0.8$, $C_{3,3} = 0.05$, $ADC_{1,3} = 0.1 \text{ mm}^2/\text{s}$, $ADC_{2,3} = 0.001 \text{ mm}^2/\text{s}$ and $ADC_{3,3} = 0 \text{ mm}^2/\text{s}$ for tri-exponential model. Note that the curves are for illustration purposes only and effects are exaggerated. a.u.; arbitrary unit. DKI; diffusion kurtosis imaging.

Diffusion kurtosis imaging (DKI)

The diffusion kurtosis imaging (DKI) representation⁶⁹ is an entirely mathematical representation of diffusion signal that quantifies the deviation from mono-exponential decay through the apparent kurtosis coefficient (K_{app}):

$$S_{DWI} = S_0 [e^{-b(D_k + \frac{1}{6}b^2 \cdot D_k^2 \cdot K_{app})}] \quad (5)$$

where D_k is the diffusion coefficient. As in IVIM, the DKI model includes the overall signal intensity term S_0 which separates the T2- and proton density-weighting of the diffusion signal.

Restriction spectrum imaging (RSI)

Restriction Spectrum Imaging (RSI) ^{64,70,71} is a multi-component model applied in several organs. Multi-component models in general deal with a higher b -value range, and therefore also a different biophysical model (i.e. sensitized to restricted diffusion, Figure 11); several are higher-order models (ie. increased number of diffusion components), and there are other individual variations such as different normalization schemes compared to IVIM.

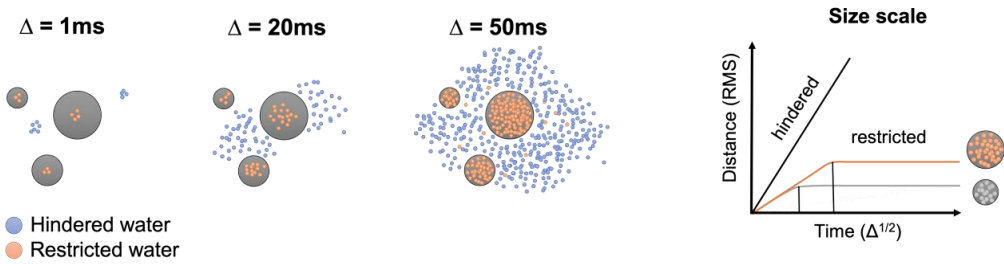


Figure 11. Model of water diffusing in tissue over increasing diffusion times. Hindered diffusion (blue) is predominately defined in extracellular space and restricted diffusion (orange) refers to intracellular diffusion. With increasing diffusion times, restricted diffusion is confined in intracellular space by the cell membrane while hindered diffusion moves in extracellular space. This means that restricted diffusion has a very short diffusion distance (Root Mean Square, RMS) relatively to hindered diffusion. Several diffusion models aim to isolate the signal from restricted diffusion. *Adapted and modified from ⁷² with permission.*

One key element of RSI is that the ADC of each expected component is fixed at a predetermined value, and not left as a free variable in the fitting process. This means that the variation in magnitude of each component arising from the curve fitting is interpreted as a variation in the signal contribution of each tissue component. Mathematically, fixing component ADC s means that the multi-component equation becomes linear, which ensures rapid fitting of diffusion signal that is essential for clinical application (fitting component ADC s for multiple components and voxels can become prohibitively time-consuming) ⁵⁸. As a general formula, the RSI model can be expressed as:

$$S_{DWI} = \sum_i^K N[C_{i,K} \cdot e^{-bADC_{i,K}}] \quad (6)$$

where K is the number of components, $C_{i,K}$ is the unit-less signal contribution of a given component i to the overall signal, $ADC_{i,K}$ is the component apparent diffusion coefficient of a given component i , and N is the normalization factor. This means that $K = 2$ is a bi-exponential or a two-component model, and $K = 3$ is a tri-exponential. Given the similarity in nomenclature, note that we distinguish between 1) *ADC* in italic which refers to the calculated, conventional, mono-exponential diffusion parameter (as previously described) and 2) ADC in a normal font that refers to the conventional, mono-exponential ADC model (equation 2), while we specify that $ADC_{i,K}$, also in italic, refers to the component ADCs from the multi-component partial volume model (equation 6). By convention, the components are ordered from the lowest to the highest diffusion coefficient. This means that $ADC_{1,3}$ refers to the slowest diffusion coefficient in a tri-exponential model.

Signal normalization in RSI

Note that $\sum_i^K [C_{i,K}] \propto \rho \cdot \exp(-TE/T2_{\text{eff}})$, where ρ represents the proton density and $T2_{\text{eff}}$ the effective T2 relaxation constant in a given voxel. Normalization by a constant N (which varies in magnitude among studies) rather than by S_0 means that signal contributions $C_{i,K}$ are still reflective of T2- and proton density-contribution while simultaneously addressing different overall image intensity scaling. This differs from all other models discussed previously, which normalizes by S_0 instead. One major benefit of DWI normalization by S_0 is that proton density and $T2_{\text{eff}}$ effects are separated from diffusion effects, making biophysical interpretation of signal fractions easier. However, the major downside is that the resulting parametric maps typically are noisy, making it difficult to visually distinguish tumors from surrounding normal tissue. The main rationale to keep proton density and $T2_{\text{eff}}$ in RSI is to generate visually distinct tumors that are superimposed from surrounding tissue.

RSI in brain and prostate

In the RSI model, the number of components K and the corresponding component ADCs are set empirically according to the organ. RSI was originally developed in the brain. As the brain is anatomically complex including white matter tracts, the RSI model in the brain accounts for both isotropic and anisotropic diffusion ⁷¹. The model yields information on anisotropic diffusion by sampling b -values in multiple directions and modelling the signal to cylindrical tissue elements in multiple directions. In addition to the anisotropic RSI outputs, isotropic diffusion is accounted for by modeling entirely restricted diffusion ($ADC = 0 \text{ mm}^2/\text{s}$) and

entirely free water ($3 \times 10^{-3} \text{ mm}^2/\text{s}$). Together, this resulted in an eight-component model of isotropic and anisotropic diffusion components. The model yields parametric “cellularity maps” by primarily weighting the isotropic restricted diffusion component. This is used for oncological imaging (gliomas, lymphomas, and metastatic tumors were studied) and has shown increased tumor conspicuity between tumor and nontumor tissue⁷¹. Furthermore, it has shown highly sensitive in monitoring brain tumors undergoing treatment⁷¹. Thus, RSI has proved useful for oncological use in the brain, and one would expect that the RSI signal in brain tumors would exhibit similar diffusion characteristics to breast tumors, as both locations can have hypercellular tumors that are hypothesized to have increased restricted diffusion. The detailed information on anisotropic diffusion is not expected to be significant for application in the breast and will not be considered in this work.

Since normal brain tissue mainly consists of nerve- and glial cells, vastly different from normal breast tissue, discussion of the RSI signal in non-cancerous brain tissue will not be covered in this thesis. On the other hand, discussion of RSI signal in normal tissue is more relevant in the prostate, which is more similar to the breast anatomically, consisting of glandular and connective tissue. Unlike the brain, the RSI model used for the prostate is simpler, only containing isotropic diffusion components. RSI model in the prostate was originally based on a two-component model (i.e. $K = 2$) with the two components corresponding to restricted and free water diffusion^{63,73,74}, similar to the isotropic components in the brain RSI model. This two-component model has proved to discriminate between cancer and healthy prostate tissue^{63,73,75}. In an optimized prostate RSI model⁷⁶ fitting the diffusion signal from the entire prostate, including both cancerous and healthy tissue, a four-component model was demonstrated to be the best fit. In this higher-order model, the DWI signal is further decomposed into component C_1 ($5.2 \times 10^{-4} \text{ mm}^2/\text{s}$) representing restricted diffusion, C_2 ($1.9 \times 10^{-3} \text{ mm}^2/\text{s}$) hindered diffusion of extracellular extravascular space, and C_3 ($3.0 \times 10^{-3} \text{ mm}^2/\text{s}$) free diffusion. C_4 ($3.0 \times 10^{-2} \text{ mm}^2/\text{s}$) accounts for rapid pseudodiffusion but is not precisely estimated as there were no non-zero b -values below $200 \text{ s}/\text{mm}^2$.

One would expect that the diffusion signal would be distributed similarly in the breast. However, one major difference is that breast tissue is more complex, containing fatty tissue intermixed with glandular tissue. Fatty tissue consists of $\sim 85\%$ lipids and $\sim 15\%$ water, where common fat suppression techniques are designed to suppress the lipid component⁷⁷. The RSI model has not previously been studied in tissues containing fatty tissue. A study by Baron et

al. reported diffusion coefficients close to zero in fat-suppressed healthy breast tissues⁷⁸ which suggests that the signal from the water component in fatty tissue (separate from the suppressed signal from the fat itself) remains on conventional DWI. Thus, one would assume that RSI in the breast would be more complex than in the prostate, since we hypothesize that restricted diffusion also is present in healthy fatty tissue, in addition to cancerous tissue.

2.12 DWI in the breast

The European Society of Breast Imaging (EUSOBI) international breast DWI working group recently issued consensus guidelines importance of a systematic approach to DWI standardization for clinical breast MRI⁴⁸. As previously described, lesion interpretation on breast MRI by BI-RADS is based on two basic steps: 1) lesion identification and 2) lesion classification. Various commonly explored diffusion models such as ADC, DKI, and IVIM have demonstrated comparable ability to DCE in discriminating between *pre-identified* benign and malignant lesions in small regions of interest (ROIs) in the breast⁷⁹⁻⁸⁵, i.e. lesion classification (step 2). Recently, a study by Clauser et al. demonstrated that ADC may help downgrade lesions classified as BI-RADS 4 on breast DCE-MRI, resulting in reducing unnecessary biopsies with one-third⁸⁶. However, DWI is still not optimized for lesion identification (step 1) in the breast and is currently not included in BI-RADS. Thus, a central focus of this work was lesion identification. Conventional DWI measures of malignant lesions are commonly measured by summary statistics of diffusion parameters assessed within ROIs manually defined by a radiologist; there is no standard protocol for this tumor segmentation, and different approaches can significantly influence resulting diffusion parameters⁸⁷. Given that direct tumor segmentation of DWI may be confounded by noise and lack of conspicuity, tumor ROIs are commonly delineated on DCE images before being transferred to DWI. The definition of tumor on DCE images is thus governed by leakage of gadolinium contrast through pathological vessels, and therefore, linked to vascularity, whereas diffusion changes, reflecting cellularity, do not necessarily coincide⁸⁸.

Moreover, DWI would increase its clinical utility and practicality in a variety of breast cancer applications ranging from cancer screening to treatment evaluation, if it could also discriminate cancer from all healthy breast tissues and thus be used for lesion segmentation. Healthy breast tissues consist of a varying degree of admixtures of fatty and fibroglandular tissues⁸⁹, and fatty and fibroglandular tissues are mixed within a voxel on DWI⁷⁷. This makes the characterization

of healthy breast tissue problematic on DWI. Conventional DWI analysis of the signal from small healthy breast tissues ROIs ⁹⁰⁻⁹³ do not capture heterogenous intravoxel tissue environment of the breast and are biased by ROI placement. Thus, advanced imaging techniques are needed to fully explain the heterogenous breast tissue environment at a voxel-wise level including the hyper-restricted water component in the intravoxel fatty tissue.

As previously described, RSI and other multi-component partial volume models are not yet well investigated in the breast. Initial results have been demonstrated by Vidić et al. ⁸³, showing that the magnitude of the slowest signal fraction in a two-component model, where component *ADCs* were not fixed and the signal was normalized by S_0 , was excellent (area under the curve, AUC = 0.99) in discriminating between pre-identified benign and malignant breast lesions, although this study did not explore higher-order models (with an increasing number of terms) or investigate optimal component *ADCs* for both cancer and healthy breast tissues, which is important for improved characterization of all breast tissues towards the goal of increasing the discriminatory performance of DWI for better lesion identification. This is a requirement for the assessment of breast cancer with multi-component partial volume models such as RSI and is another central focus of this thesis.

The lack of standardization and reproducibility of conventional breast DWI estimates (such as *ADC*) across scanners and sites is a known challenge and improvement is an area of widespread interest ⁴⁸. Therefore, in this thesis, we aim to develop generalizable methods that can be easily implemented across scanner platforms.

2.13 MRI during neoadjuvant therapy

MRI has become an important part of the routine patient management for patients receiving neoadjuvant therapy and is indicated before (baseline) and after neoadjuvant therapy (Figure 5). Baseline assessment by MRI is performed with two objectives, tumor staging and disease prognosis estimation, while post-neoadjuvant therapy MRI is used for evaluation of residual disease. In addition, an area of scientific evaluation is the use of MRI for objective response assessment during therapy to assess efficacy; at an early and mid-treatment time point (Figure 12) ⁹⁴.

Tumor size reduction is monitored by manually assessing the diameter of the largest central slice by DCE, based on the RECIST treatment response criteria for solid tumors ⁹⁵. However, changes in size may take several weeks before it is detected by DCE, potentially delaying clinical decision-making. Furthermore, DCE-based RECIST has conflicting results regarding residual cancer detection specificity ⁹⁶ and requires expert radiologist readers to manually delineate tumor tissue at each time point. Thus, improvement of radiological response assessment tools in all these time points have a large potential for improved patient care.

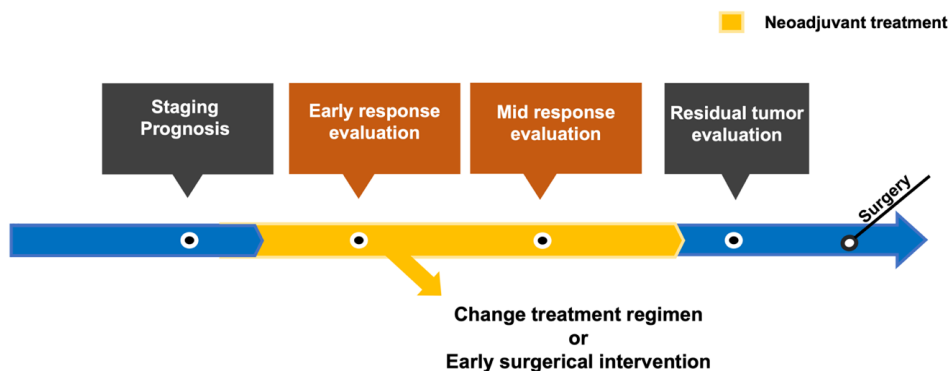


Figure 12. MRI during neoadjuvant therapy. Pre and post-therapy time points (grey) are standard-of-care, while early and mid-treatment response assessments (orange) are an area of scientific evaluation.

Clinical trials as a test bed for new MRI treatment assessment biomarkers

I-SPY (and the following ISPY-2 trial) is a large, multi-center clinical trial that uses serial investigative MRI assessments during therapy of LABC (pre-therapy, early-therapy, mid-therapy, post-therapy) to quantify tumor response. At the early therapy time point, the standard longest diameter of manual DCE had an AUC of predicting pCR at 0.64; AUC increased to 0.70 using a threshold-based DCE model (functional tumor volume, FTV) ⁹⁷.

DWI is sensitive to early treatment-induced changes and has shown associations with therapy outcomes ^{98,99}. However, the clinical standard DWI model, ADC, also uses time-consuming manual tumor delineation approaches ¹⁰⁰ and may be confounded by treatment-related changes such as edema. In the I-SPY trial ¹⁰⁰, the AUC for prediction of response by standard ADC was reported as low as 0.53 for the early-treatment time point (increased to 0.60 for the mid-treatment time point). This calls for the exploration of alternative DWI techniques.

RSI estimates of cellularity are shown to be directly related to histopathological tumor cellularity in preclinical models ^{58,101} and the human prostate ^{73,75,102}. Additionally, RSI is effective for treatment response assessment for glioma ^{58,103} but has not yet been evaluated for treatment response assessment in the breast. We hypothesize that an RSI classifier with elastic image registration can both assess early response to treatment significantly better than conventional DWI and DCE-based RECIST and increase residual cancer detection specificity.

2.14 Physical basis of positron emission tomography (PET)

Positron emission tomography (PET) ¹⁰⁴ is a molecular imaging modality that uses injected tracers to visualize specific metabolic processes in the body. A PET tracer is made up of a biologically active molecule that is tagged by an unstable isotope that emits gamma rays through positron emission and annihilation. A commonly used tracer is Fluorodeoxyglucose (¹⁸F-FDG), which comprises a glucose analog coupled with the position-emitting radionuclide fluorine-18. Thus, when ¹⁸F-FDG is injected intravenously into the bloodstream and taken up by glucose membrane transporters. Once inside the cell, the tracer characteristics prohibit it from being fully metabolized in the regular glucose metabolism pathway. Thus, ¹⁸F-FDG accumulates in the cell and functions as a glucose marker (Figure 13A). The PET detector panel is equipped with gamma-cameras that detect the gamma-rays emitted from the tracer, which enables the location of areas of increased glucose uptake (in the case of ¹⁸F-FDG) (Figure 13B). Since cancer cells are known to have increased glucose metabolism, PET can therefore be used for the detection of cancerous cells.

The PET imaging system is typically coupled with another imaging system to secure anatomical reference and attenuation correction. Traditionally, PET has been acquired with computer tomography (PET/CT), which means exposure to large doses of ionizing x-rays which are known to damage the body. However, simultaneous PET/MRI is a more recent technology that has superior soft tissue definition. PET/MRI examinations allow simultaneous collection of structural, functional, and metabolic imaging properties in the same spatial and temporal domain. MRI complements PET's ability to visualize glucose metabolism by reflecting other hallmarks of cancer ¹⁰⁵, including invasion and metastatic propensity (by DWI) and increased angiogenesis (DCE).

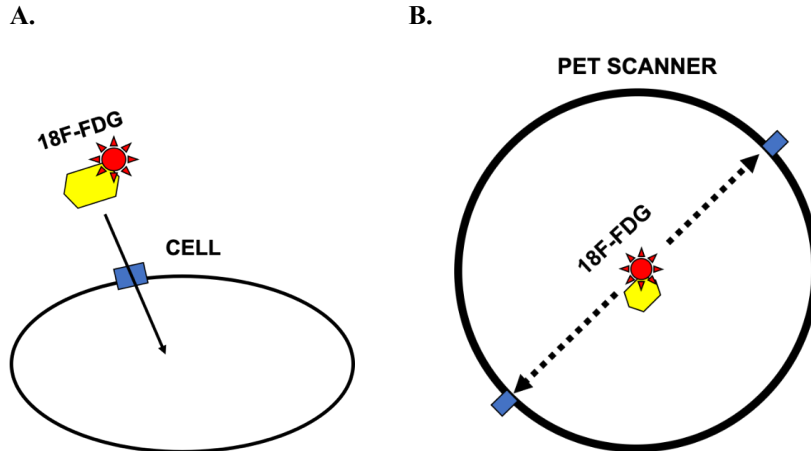


Figure 13. A. Fluorodeoxyglucose F 18 (^{18}F -FDG) tracer uptake in the cell through glucose membrane transporters. The tracer accumulates in the cell and functions as a glucose marker. B. Positron emission tomography (PET) scanner detects the gamma-rays emitted from the tracer through gamma-cameras, which enables the location of areas of increased glucose uptake.

2.15 PET/MRI in the breast

PET/MRI is not a part of the standard radiological assessment of breast cancer in the US ¹⁰⁶ or Norway ²¹, but has potential in a range of breast cancer practices, such as diagnostics, staging, and neoadjuvant response evaluation ⁵. Several studies report correlations between standardized uptake values (SUV) from ^{18}F -FDG-PET and *ADC* in malignant tissue ¹⁰⁷⁻¹⁰⁹, indicating that intrinsically-registered ^{18}F -FDG uptake may provide an alternative approach to manually drawn DCE ROI for breast lesion characterization in conventional DWI analysis ¹⁰⁸. Another focus of this thesis was to investigate the reliability of deriving conventional longitudinal diffusion imaging characteristics from ^{18}F -FDG uptake during neoadjuvant treatment compared to manual DCE.

3. *Aims*

The overall goal of the thesis was to explore the potential role of DWI and PET/MRI as alternatives to conventional DCE for the assessment of breast cancer in a screening and treatment response monitoring setting. The main aim of the thesis was two-fold; the first was to explore the use of PET/MRI to derive simple treatment monitoring measures of longitudinal scans in breast cancer neoadjuvant treatment evaluation. The second was to explore diffusion properties of cancer and healthy breast tissues using a multi-component partial volume model acquired at high b -values to develop and optimize an RSI model to discriminate between breast cancer and healthy breast tissues, and to monitor neoadjuvant treatment response.

The **specific aims** were to:

1. Investigate the reliability of deriving conventional longitudinal diffusion imaging characteristics from ^{18}F -FDG uptake during neoadjuvant treatment compared to manual DCE using PET/MRI (paper I).
 - a. Hypothesis: ^{18}F -FDG uptake during neoadjuvant treatment by using PET/MRI is as reliable as manual DCE to derive conventional imaging characteristics.
2. Explore the diffusion properties of breast cancer and healthy breast tissues by optimizing the number of components and corresponding component ADC s for the breast RSI model (paper II).
 - a. Hypothesis: An optimized RSI model will better characterize diffusion in breast tissue than conventional diffusion imaging.
3. Evaluate the ability of the optimized three-component RSI model to discriminate between breast cancer and healthy breast tissues (paper III).
 - a. Hypothesis: Optimizing RSI can discriminate between breast cancer and healthy breast tissues with acceptable AUC and false positive rate.
4. Evaluate the ability of a three-component RSI model to automatically assess response to neoadjuvant treatment (paper IV).
 - a. Hypothesis: Optimized RSI can detect response to NAC earlier than conventional diffusion imaging.

4. Materials and methods

4.1 Patient cohorts

The materials included in this thesis consisted of three distinct breast cancer patient cohorts from two separate sites, where image acquisition was performed on different scanners with unique acquisition protocols, including one cohort of longitudinal PET/MRI scans of patients receiving neoadjuvant therapy. The unique characteristics of the acquired data allowed for testing of a range of research questions as well as exploration of model robustness across patients, scanners, acquisition protocols, and sites.

Written informed consent was obtained from all patients at both sites. The studies were approved by local institutional review boards and conducted in accordance with the Declaration of Helsinki. Handling of sensitive personal data followed the relevant regulations at all sites. The patient cohorts are described in further detail below.

4.1.1 Longitudinal PET/MRI cohort (paper I)

This prospective study was approved by the Regional Committee for Medical and Health Research Ethics (REC) in Western Norway (# 2015/1493) and was performed at St. Olavs Hospital, Trondheim, Norway. A total of 24 patients (median age 53 years, range 37–74) with pathology-proven, invasive breast cancers > 4 cm or LABC (i.e., cT2–4N0–3) were recruited; this minimum tumor size was an inclusion criterion for recruitment to the phase II PETREMAC trial (Clinicaltrials.gov #[NCT02624973](https://clinicaltrials.gov/ct2/show/study/NCT02624973)), where lesions of this size are targets for neoadjuvant chemotherapy. The recruitment started in February 2017 and ended in November 2018. The patients underwent individualized neoadjuvant therapy based on ER, PgR, HER2, and TP53 mutation status. The treatment was primarily endocrine. Tumor categorization was done by histopathologic analysis of core needle or open incisional biopsies.

Patients were examined with ¹⁸F-FDG-PET/MRI scans, at baseline and up to four scanning sessions during neoadjuvant treatment. This resulted in 53 data sets overall; 24 untreated lesions, and 29 treated lesions.

4.1.2 Baseline high b-value MRI cohort 1 (papers II and III)

The study was approved by the local Institutional Review Board and performed at the University of California San Diego (UCSD), CA, USA. Ninety-five patients with pathology-proven breast cancer with no cytotoxic regimens, chemotherapy, or ipsilateral radiation therapy for this malignancy prior to a single MRI scanning were eligible for this prospective study. The recruitment of patients began in December 2015 and ended in June 2019. In total, 14 patients were excluded from the study; nine patients had contralateral cancer or mastectomy, one patient had no visible cancerous tissue on DWI, and in four patients image quality was insufficient from low signal-to-noise ratio (SNR) ($n = 2$), poor fat saturation ($n = 1$), or severe image distortion ($n = 1$), resulting in 81 patients (median age 51 years, range 20–84). Due to data availability at the time of analysis, only a subset of 49 patients were included in paper II, while the whole patient cohort was included in paper III (Figure 14). Tumor categorization was done by histopathologic analysis of core needle or open incisional biopsies.

4.1.3 Baseline high b-value MRI cohort 2 (papers II and III)

The study was approved by the REC in Central Norway (# 2011/568) and performed at St. Olavs Hospital, Trondheim, Norway. Twenty-five patients (median age 53 years, range 29–75) in this prospective study underwent a single MRI scan. The recruitment of patients began in August 2014 and ended in August 2016. Tumor categorization was done by histopathologic analysis of core needle or open incisional biopsies. Inclusion criteria and tumor categorization were similar to those of the baseline high b -value MRI cohort 1; for more details, see the inclusion of malignant lesions from Vidić et al.⁸³.

4.1.4 Longitudinal high b-value MRI cohort (paper IV)

A subset ($n = 31$) of patients from the baseline high b -value MRI cohort 1 received additional longitudinal MRI scans after the baseline scan. These were participants in a prospective phase II clinical trial at the UCSD site who underwent multi- b -value DWI acquisition (b -values = 0, 500, 1500, and 4000 s/mm², see detailed information below). Trial criteria included biopsy-proven invasive breast cancer ≥ 2.5 cm (defined on imaging/clinical examination) who indicated to undergo neoadjuvant therapy. For a summary of analysis sets from the UCSD site for papers II–IV, see Figure 14.

Patients underwent MRI at four time points to evaluate response to treatment: baseline (pre-treatment), early-treatment (3 weeks), mid-treatment (12 weeks), and post-treatment (Figure 16). Furthermore, 17 patients received all four scans. In total, four patients were excluded from the study due to low image quality, and for three patients, individual scans were excluded due to major patient movement ($n = 1$) and low image quality ($n = 2$). This led to 27 patients (median age 47 years, range 20–68). This led to pre-treatment ($n = 27$), early-treatment ($n = 22$), mid-treatment ($n = 19$) and post-treatment ($n = 27$).

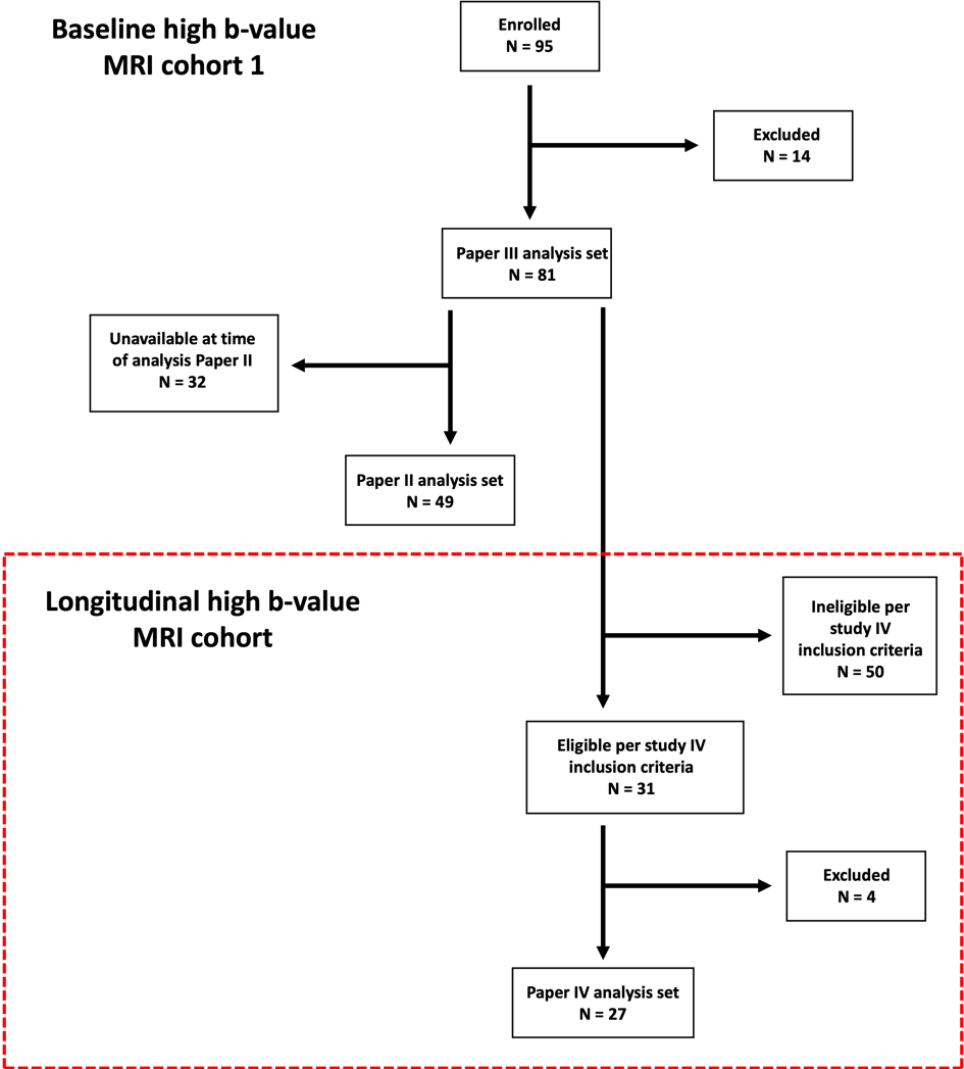


Figure 14. Summary of UCSD cohorts: baseline high b -value MRI cohort 1 (paper II and III) and longitudinal high b -value MRI cohort (paper IV).

4.2 PET/MRI and MRI acquisition

This section details the PET/MRI and MRI acquisitions for the different papers presented. The longitudinal PET/MRI cohort (paper I) includes a PET/MRI data acquisition cohort, while the following papers examined cohorts where high b -value diffusion data were acquired for baseline (papers II and III) and longitudinal studies (paper IV). The details are given below and are summarized in Table 2.

4.2.1 PET/MRI acquisition (paper I)

Patients in the longitudinal PET/MRI cohort (paper I) underwent simultaneous PET/MRI on a 3T Biograph mMR scanner (Siemens Healthcare, Erlangen, Germany), 75 min after ^{18}F -FDG injection. MRI acquisition utilized a designated 4-channel breast coil with a bilateral axial imaging plane and utilized an extended imaging protocol including Dixon, T2, DWI, and DCE. DCE parameters included: 3D FLASH sequence, transverse orientation, TR = 5.88 ms, TE = 2.21 ms, resolution $0.7 \times 0.7 \times 2.5$ mm, 72 slices, flip angle 15° , 1 baseline, and 7 post-contrast sequences, time resolution 1 min. DWI parameters are given in Table 2.

4.2.2 MRI acquisition (papers II-IV)

MRI data were acquired on a 3T GE scanner (MR750, DV25–26, GE Healthcare, Milwaukee, United States) and an 8-channel breast array coil with a bilateral axial imaging plane for the baseline high b -value MRI cohort 1, while patients from the baseline high b -value MRI cohort 2 were imaged with a 3T Siemens scanner (Skyra, VD13–E11, Siemens Healthcare, Erlangen, Germany) and a 16-channel breast array coil with a unilateral sagittal imaging plane. Differences in scanner and pulse sequence parameters across sites were used to determine that the discriminatory potential of the three-component RSI model is robust for data collected in different scanners and pulse sequence parameters. In addition to Gadolinium DCE and T2-images, both datasets included high b -value DWI acquisition, summarized in Table 2.

4.3 Image preparation

Corrections for eddy current artifacts, motion⁶⁴, and geometric distortion¹¹⁰ were applied to all DWI data. DWI data were averaged across directions for each b -value. Noise correction¹¹¹ was performed for decreasing signal-to-noise ratio with increasing b -value (papers II–IV). In

paper II, data quality before fitting was evaluated by averaging the signal of cancer and fibroglandular ROIs divided by the standard deviation of a background ROI outside the breast at each b -value.

Resampling of the data was performed for papers I and IV only. For paper I, all images were resampled to DWI resolution, while for paper IV, all images were resampled to DCE resolution. PET attenuation correction was performed on the scanner ¹¹², and standardized uptake values (SUV) were normalized against body weight and dose. Image preparation and lesion segmentation processes for paper I are summarized in Figure 15.

Parameter	Longitudinal PET/MRI cohort	Baseline high b -value MRI cohort 1/ Longitudinal high b -value MRI cohort	Baseline high b -value MRI cohort 2
Paper	I	II, III, IV	II, III
Scanner	3T Biograph mMR, Siemens	3T MR750, DV25–26, GE Healthcare	3T Skyra, VD13–VE11, Siemens
Coil	4-channel breast coil	8-channel breast coil	16-channel breast coil
Imaging plane	Axial	Axial	Sagittal, single breast
TE (ms)	77	82	88
TR (ms)	9000	9000	10600 (n = 15) 11800 (n = 10)
FOV (mm²)	380 × 190	160 × 320 (reduced FOV)	180 × 180
Acquisition matrix	192 × 96	48 × 96	90 × 90
Reconstruction matrix	192 × 96	128 × 128	90 × 90
Voxel size (mm³)	2.0 × 2.0 × 2.5	2.5 × 2.5 × 5.0	2.0 × 2.0 × 2.5
b-values (no. of diffusion directions) (s/mm²)	0, 50 (3), 120 (3), 200 (3), 400 (3), 700 (3)	0, 500 (6), 1500 (6), 4000 (15)	0, 200 (6), 600 (6), 1200 (6), 1800 (6), 2400 (6), 3000 (6)
b-values utilized for ADC calculation (s/mm²)	200, 400, 700	0, 500	0, 200, 600
Phase encoding direction	Anterior/Posterior	Anterior/Posterior	Anterior/Posterior
Parallel imaging	GRAPPA (reduction factor, R = 2)	none	GRAPPA (reduction factor, R = 2)

Table 2. Summary of diffusion parameters for all patient cohorts. *ADC*; Apparent diffusion coefficient. FOV; Field of view. GRAPPA; Generalized autocalibrating partial parallel acquisition. TE; Echo time. TR; Repetition time.

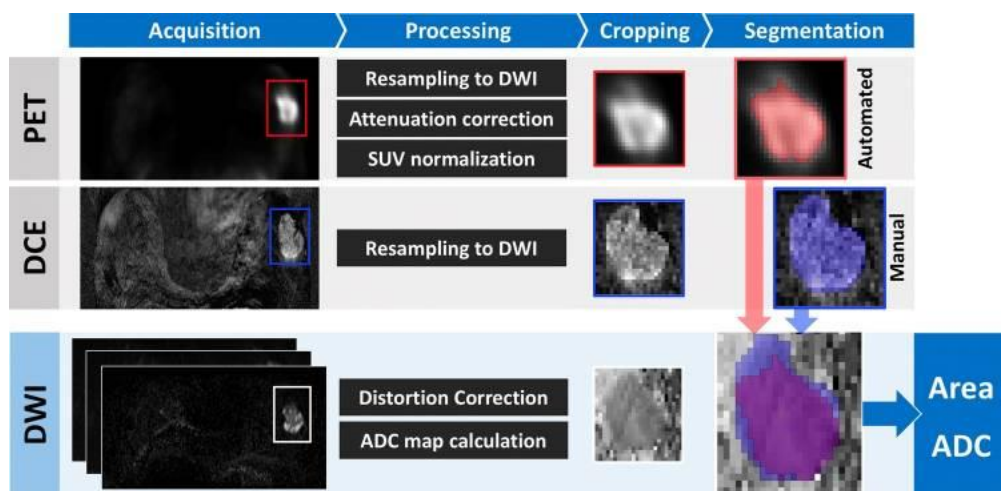


Figure 15. Image preparation and lesion segmentation for paper I. Images were downsampled to diffusion-weighted imaging (DWI) space. Positron emission tomography (PET) images were attenuation-corrected and went through standardized uptake values (SUV) normalization. Apparent diffusion coefficient (ADC) maps were generated from distortion-corrected DWI images. Tumor segmentation was performed by Gaussian mixture modeling (GMM) segmentation on cropped PET images, and manually on DCE images. The resulting regions of interest (ROIs) were transferred to the ADC maps for the derivation of tumor area and mean ADC . Adapted from ¹¹³ with permission.

4.4 Segmentation

4.4.1 Manual segmentation

All manual lesion segmentation was performed under the supervision of and validated by, two breast radiologists, one at each site (St. Olavs Hospital and UCSD). ROIs were drawn for the lesions corresponding to pathology-proven cancer: single central slice defined on DCE (denoted “manual DCE” for paper I) and full-volume cancer ROIs defined on DWI (denoted “cancer ROI” for papers II–IV). Control ROIs were defined to include all representative healthy breast tissue for pre-treatment images for papers II–IV; control ROIs were defined slightly differently for axial MRI images (baseline high b -value MRI cohort 1 and longitudinal high b -value MRI cohort) compared to sagittal images (baseline high b -value MRI cohort 2) owing to the presence/absence of the contralateral breast in the image. For axial images, control ROIs were defined using a semi-automatic approach. First, a rectangular box was placed around the entire healthy contralateral breast, then the healthy breast was masked using

intensity thresholding and 3D connected components. For sagittal images containing only the single breast, control ROIs were drawn in a cancer-free region at least 10 mm away from the cancer ROI. Further differentiation of control ROIs into fibroglandular ROIs and fatty tissue ROIs were performed for paper II. ROIs were generated by thresholding $b = 0 \text{ s/mm}^2$ volume within the initial control ROI.

4.4.2 Semi-automated PET/MRI segmentation (paper I)

Gaussian mixture modeling (GMM-PET)

For paper I, a rectangular region containing the visible lesion was manually cropped from the SUV map (corresponding to the single central slice of enhancing tumor on DCE). An algorithm using default k-means++¹¹⁴ initialization and an assumption of three Gaussian distribution classes was used, returning an assignment for each voxel based on the highest probability¹¹⁵ of belonging to each class, given as: tumor (highest intensity), ‘non-tumor’ background (lowest intensity), and unknown (intermediate intensity). To compromise between accuracy and avoid overestimation from partial volume effects, voxels classed as ‘unknown’ were considered non-tumor, defining the tumor class threshold (and therefore the tumor ROI) as the intersection of tumor and unknown class distributions. User input is thus limited to initial region cropping.

Thresholding-based PET segmentation

Two common simple thresholding-based PET segmentation methods, a fixed threshold of 2.5 ($SUV_{2.5}$) and 42 % of the maximum SUV ($SUV_{42\%}$)¹¹⁶, were also performed to provide a comparison with GMM-PET (paper I).

4.5 DWI analysis

4.5.1 Conventional DWI analysis (papers I–IV)

ADC maps were calculated using a mono-exponential model (equation 2) for all papers; although included b -values varied between papers. For paper I, perfusion-insensitive ADC maps were calculated using b -values 200–700 s/mm^2 . For papers II–IV that acquired higher b -values, only the lower b -values $< 1000 \text{ s/mm}^2$ were used: 0–500 s/mm^2 for baseline high b -

value MRI cohort 1, and 0–600 s/mm² for high b -value MRI cohort 2. Inclusion of b -values < 200 s/mm² made these maps sensitive to any perfusion effects present.

In addition, the non-noise-corrected maximum b -value image (DWI_{\max}) and K_{app} from DKI (equation 5) for b -values < 2000 s/mm² were estimated for paper III. DWI_{\max} was acquired at $b = 4000$ s/mm² for the baseline high b -value MRI cohort 1 and $b = 3000$ s/mm² for the baseline high b -value MRI cohort 2.

4.5.2 Multi-component partial volume modeling of DWI signal decay (papers II–IV)

The DWI signal from all available b -values was modeled as a multi-exponential model (equation 6). For papers II and III, all voxels were normalized to the 98th percentile of intensity within the entire $b = 0$ s/mm² image, indicated by N . To improve normalization across time points for longitudinal scans, we further normalized output $C_{i,k}$ maps by the 95th percentile of the intensity of the computed geometric mean of the resulting $C_{1,3}$ and $C_{2,3}$ maps of the three-component RSI model (described in detail below) of the control ROI for each patient for paper IV.

In paper II, the goal was to determine the optimal number of components (K) and the corresponding global component $ADCs$ ($ADC_{i,k}$) for use in describing voxels including cancer and healthy breast tissues across patients and sites. This was done by globally fitting DWI signal by a simplex search fitting method with non-negativity constraints¹¹⁷ for all voxels within cancer and control ROIs from baseline high b -value MRI cohort 1 and 2 simultaneously. Fitting was performed for $K = 2$ and $K = 3$, i.e. due to previous results in breast assuming two components⁸³ and *a priori* assumption of three breast components due to the heterogeneous breast tissue environment. This fitting regimen is fundamentally different from conventional voxel-wise fitting approaches where the component $ADCs$ is determined for each voxel independently. Note that there is a slight discrepancy in terminology between the attached papers in this thesis compared to the terminology given here: component $ADCs$ ($ADC_{i,k}$) were denoted $D_{i,N}$ in paper II and component signal contributions for the three-component model ($C_{i,3}$) were denoted C_1 in paper III since signal contributions for $K = 2$ were not assessed in this paper. Also in paper III, the three-component RSI model was only referred to as the “three-component model”. Furthermore, in paper IV, the “RSI classifier” refers to the tumor classifier based on the $C_{1,3}$ and $C_{2,3}$ derived from the three-component RSI model.

Once global optimal component $ADC_{i,K}$ were determined, they were incorporated into equation 6 to generate signal contribution ($C_{i,K}$) maps. This was done for both of the examined models ($K = 2$ and $K = 3$) for paper II; however, for paper III, only $K = 3$ and the corresponding component $ADC_{i,3}$ were used, yielding the following equation derived from equation 6:

$$S_{DWI}(b) = N [C_{1,3} \cdot e^{-b \cdot ADC_{1,3}} + C_{2,3} \cdot e^{-b \cdot ADC_{2,3}} + C_{3,3} \cdot e^{-b \cdot ADC_{3,3}}] \quad (7)$$

using the same parameter definitions as described for equation 6. This was done because $K = 3$, i.e. a tri-exponential model, was shown to represent the best fit in paper II. The model yielded the following component ADC values used as fixed values in this analysis: $ADC_{1,3} = 0 \text{ mm}^2/\text{s}$, $ADC_{2,3} = 1.4 \times 10^{-3} \text{ mm}^2/\text{s}$ and $ADC_{3,3} = 10.2 \times 10^{-3} \text{ mm}^2/\text{s}$. Note that these initial ADC s given in paper II preprint¹¹⁸ are slightly different than the final ADC s reported in paper II (see below), although with no practical consequence. The use of $ADC_{1,3} = 0 \text{ mm}^2/\text{s}$ means this component behaves not as a distinct exponential as in other tissues^{58-60,95} but as a constant offset ($C_{1,3}$). Hence, we use the term “three-component” RSI model for the fitted model instead of “tri-exponential”. In paper III, the resulting parametric maps were generated from equation 7: $C_{1,3}$, $C_{2,3}$, and their product $C_1 C_2$.

4.5.3 Development of an automatic RSI tissue classifier for neoadjuvant therapy response evaluation (paper IV)

To create a ‘global’ tissue classifier applicable across all patients and time points included in the study, the first two components of the three-component RSI model ($C_{1,3}$ and $C_{2,3}$) were selected, as these demonstrated excellent discrimination of cancer from healthy breast tissue in paper III (see results below). Joint $C_{1,3}, C_{2,3}$ probability density functions (PDFs) for cancer and control ROIs were calculated for all patients simultaneously at the pre-treatment time point, generating a lookup table of the posterior probability of cancer, given $C_{1,3}$ and $C_{2,3}$ measurements for any voxel. This was used to create voxel-wise probability maps for each individual patient at each time point.

Estimation of longest tumor dimension: the cancer ROI at the pre-treatment time point was uniformly expanded by 1 cm to generate a tumor-containing region and used for analysis using the voxel-wise probability maps (Figure 16). The largest single connected component within

the tumor-containing region on the voxel-wise probability maps was identified to give the longest diameter (in cm). To account for tumor growth outside of the initial tumor-containing region, any components connected to the tumor-containing region above a threshold of 0.4 on voxel-wise probability maps were also included in the tumor definition per time point. Using the pre-treatment tumor-containing region for all time points was possible since an elastic registration procedure had been applied to register all images to the pre-treatment time point¹¹⁹. This approach limits the required user input to a single manual definition of cancer ROI and a semi-automatic definition of control ROI at the pre-treatment time point.

4.5.4 Conventional imaging metrics during neoadjuvant treatment (papers I and IV)

For paper I, cancer ROIs for the lesion within the chosen central slice, derived from both manual DCE and GMM-PET were transferred to *ADC* maps and used to estimate the tumor ROI area (cm²) and the ROI mean *ADC* value. This was performed for all untreated and treated lesions to evaluate the performance and concordance of these biomarkers. Response to treatment was not assessed.

For paper IV, the longest diameter of the cancer ROI (in cm) was manually defined on post-contrast DCE for each individual time point. The largest conglomerate of connected lesions was used for cases with several cancer lesions. In addition, *ADC* maps were longitudinally registered using an elastic registration technique to the pre-treatment time point, thus transferring the pre-treatment cancer region across all time points. The mean *ADC* value was assessed within the pre-treatment cancer ROI for each time point. This approach thus avoids the time-consuming and technically difficult manual delineation of a tumor undergoing treatment, reducing it to a single diameter measurement.

4.5.5 Response definition (papers I and IV)

Definition of response to treatment was primarily relevant for paper IV since paper I did not consider response assessment. There were several definitions of response to treatment used: the primary endpoint was pCR, defined as no residual invasive disease in either breast or axillary lymph nodes after neoadjuvant therapy (ypT0/is, ypN0) with or without the presence of DCIS¹²⁰. Assessment of pCR was performed by examination of histological specimen post-

surgically. Patients were categorized into pCR and non-pCR groups. The pathological response was considered the true response definition.

As a sub-analysis, early response was also assessed based on imaging data, using a definition of a $\geq 30\%$ decrease from pre-treatment size (in accordance with RECIST criteria) at the early-treatment time point, and which persisted at the mid-treatment time point. This is referred to as ‘early imaging response’, and was assessed for RSI and DCE measurements (giving ΔRSI and ΔDCE respectively). The change in mean ADC (ΔADC) was also calculated as a reference. Early imaging response to treatment was assessed for patients who underwent all four scans ($n = 17$).

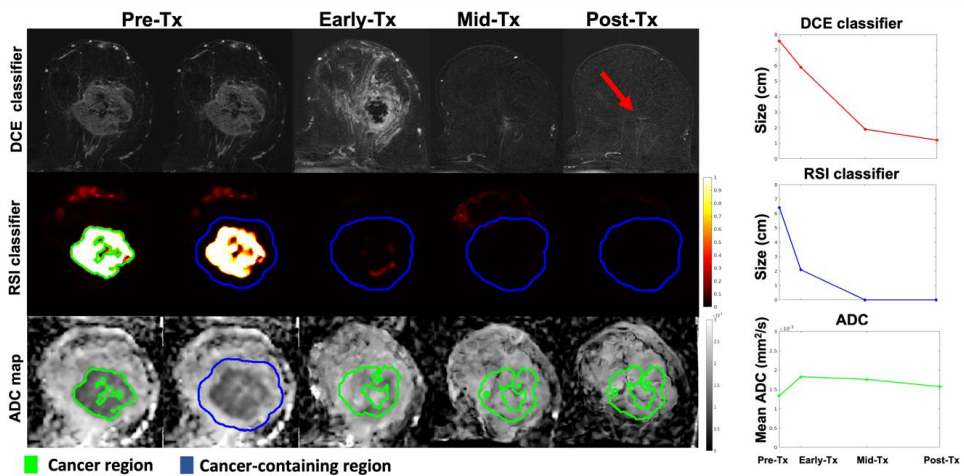


Figure 16. Dynamic contrast-enhanced (DCE) images, Restriction Spectrum Imaging (RSI) classifier, and apparent diffusion coefficient (ADC) maps across all imaging time points for a subject with no remaining tumor tissue on final post-surgical pathology. The cancer region is given in green and the dilated cancer-containing region is given in blue. Note that the RSI classifier is well-defined within the cancer ROI at the pre-treatment time point (green). For all time points, the largest diameter is given for the DCE and RSI classifier, and the mean ADC value of the cancer ROI. The RSI classifier captured a more dramatic response to treatment at the early-treatment time point compared to the DCE classifier. As expected, ADC increased as a response to treatment. RSI classifier showed no remaining cancer at the post-treatment time point, while there was still some indication of remaining tumor left within the tumor bed at the post-treatment time point for the DCE classifier (red arrow). Tx; treatment. *Adapted from* ¹²¹ *with permission.*

4.5.6 Assessment of contrast-to-noise ratio (CNR) (paper II)

To assess the conspicuity of lesions in the parametric maps, the contrast-to-noise ratio (CNR) was estimated for all RSI outputs ($C_{i,K}$), DCE, and ADC maps by dividing the averaged signal from cancer ROI by the averaged signal from the fibroglandular ROI.

4.6 Statistical analysis

4.6.1 Longitudinal metric and spatial concordance assessment (paper I)

Performance of the three PET segmentation techniques in reference to manual DCE ROIs was measured using the Dice similarity coefficient¹²², and center-of-gravity displacement (CoG). Tumor area and ADC values from the different segmentation methods were compared using a paired t -test, and Pearson's test for correlation. A two-sample t -test was used to assess the difference between the untreated ($n = 24$) and treated cohort ($n = 29$) for all metrics.

4.6.2 SNR and determination of DWI data goodness-of-fit (paper II)

To investigate the robustness of RSI to SNR, we performed our fitting analysis using only data of b -values ≤ 1500 s/mm² and found that the estimated $ADC_{i,K}$ were the same as in the original analysis.

The relative fitting residual (the percent variance of the difference between the measured signal and the model-predicted signal) and Bayesian information criterion (BIC) were computed for each model to determine how well the different models describe breast DWI data. BIC is reported as the difference in BIC ($\Delta BIC = BIC_{bi} - BIC_{tri}$), where a lower BIC value implies a better fitting of the data. Relative fitting residuals were also assessed for the ADC model (mono-exponential, conventional) for comparison to conventional DWI estimates.

4.6.3 Discrimination between cancer and healthy breast tissues (papers II and III)

Kolmogorov-Smirnov test was used to examine data normality, and related-samples Friedman's one-way analysis of variance by ranks test was used to identify significant

differences in CNR across diffusion components and tissues (cancer and fibroglandular). The level of significance was set to 0.05.

The discriminatory performance between cancer and control ROIs was assessed for the parameters C_1C_2 , $C_{1,3}$, $C_{2,3}$, DWI_{\max} , ADC , and K_{app} . Because there were ~ 52 times more healthy breast tissue voxels than cancer voxels, performance in discriminating between cancer and healthy breast tissues was examined for all voxels by the expected false positive rate given the sensitivity of 80 % (FPR_{80}). In addition, the conventional performance measure of receiver operating characteristic (ROC) AUC, sensitivity, specificity, and accuracy were estimated.

Further statistical tests aiming to identify differences between signal contributions ($C_{i,k}$) across models and tissues were investigated as a preliminary measure to characterize the signal contributions outputs as part of paper II and are not discussed in more detail here.

4.6.4 Response prediction (paper IV)

At the early, mid, and post-treatment time points, the ROC AUC was computed to assess the ability of ΔRSI , ΔDCE , and ΔADC to predict non-pCR in cases with all four scans ($n = 17$). At the post-treatment time point using all cases ($n = 27$), sensitivity, specificity, and accuracy for the prediction of non-pCR were assessed and were calculated for absolute values for RSI, DCE, and mean ADC . For all analysis, we estimated the ability to detect residual tumor tissue (i.e. positive was defined as a patient with remaining tumor tissue, non-pCR). For the primary analysis, we used an *a priori* assumption that an increase in mean ADC and a decrease in RSI and DCE size represents a response to treatment in line with clinical practice¹⁰⁰. Diagnostic sensitivity and specificity between techniques were compared by McNemar's test, while DeLong's test was used to compare ROC curves. After observing the results from primary analysis, we also performed secondary analysis with inverted ADC model classification (assuming a decrease in ADC represented response).

5. Summary of papers

5.1 Paper I

This paper aimed to investigate the reliability of PET/MRI-derived biomarkers using semi-automated GMM segmentation on PET/MRI images, against conventional manual tumor segmentation on DCE images.

The study included twenty-four breast cancer patients who underwent PET/MRI (following ^{18}F -FDG injection at baseline and during neoadjuvant treatment, yielding 53 data sets (24 untreated, 29 treated). Two-dimensional tumor segmentation was performed manually on DCE images (manual DCE) and using a GMM with corresponding PET images (GMM-PET). Tumor area and mean *ADC* derived from both segmentation methods were compared, and spatial overlap between the segmentation was assessed with Dice similarity coefficient and center-of-gravity displacement.

No significant differences were observed between mean *ADC* and tumor area derived from manual DCE segmentation and GMM-PET. There was a strong positive correlation between the resulting metrics from manual DCE and GMM-PET for *ADC* mean for untreated lesions and treated lesions ($r = 0.895$, $p < 0.001$), and tumor area from untreated ($r = 0.870$, $p < 0.0001$) and treated ($r = 0.928$, $p < 0.001$) lesions. The mean Dice score for GMM-PET was 0.770 and 0.649 for untreated and treated lesions, respectively.

Using PET/MRI, tumor area and mean *ADC* value estimated with a GMM-PET can replicate manual DCE tumor definition from MRI for monitoring neoadjuvant treatment response in breast cancer.

5.2 Paper II

This paper aimed to determine the number of discernible diffusion components and optimal component ADC s for the RSI model for breast.

A total of 49 women with breast cancer without any prior neoadjuvant treatment underwent multi- b -value DWI. The DWI signal was described using a linear combination of multiple exponential components (either two or three). A set of fixed component ADC values was estimated to fit across all voxels in cancer and control ROIs. Later, the signal contributions of each diffusion component were estimated using these fixed component ADC values. Relative fitting residuals and Bayesian information criterion were assessed. CNR between cancer and fibroglandular tissue in RSI-derived signal contribution maps was compared to DCE imaging.

The relative fitting residuals of ADC model, and bi- ($K = 2$) and tri-exponential ($K = 3$) models for cancer ROIs were 3.3 %, 1.0 %, and 0.3 % for cancer ROIs, respectively, and 2.1 %, 1.6 %, and 1.0 % for control ROIs, respectively. Note that residuals were the smallest for the tri-exponential model. Furthermore, ΔBIC of 74 was estimated between the bi- and tri-exponential models (i.e. $BIC_{bi} > BIC_{tri}$); both of these results indicate that a tri-exponential model is better suited for describing breast DWI data, and that adding a third component is supported by the data. Estimated component ADC s for the bi-exponential model were $ADC_{1,2} = 2.8 \times 10^{-5}$ and $ADC_{2,2} = 2.4 \times 10^{-3}$ mm^2/s , while component ADC s for the tri-exponential model were $ADC_{1,3} = 1.6 \times 10^{-17}$, $ADC_{2,3} = 1.5 \times 10^{-3}$ and $ADC_{3,3} = 10.8 \times 10^{-3}$ mm^2/s . For the tri-exponential model, the slowest component ADC is far smaller than can be quantified accurately; thus, in this model $ADC_{1,3}$ was set to 0 mm^2/s , effectively replacing the slowest diffusion component with a constant offset term ($C_{1,3}$). As noted above, the term “tri-exponential” is therefore replaced with “three-component”. The signal contributions for cancer and fibroglandular tissue ROIs were not significantly different ($p > 0.05$) when estimated using $ADC_{1,3} = 1.6 \times 10^{-17}$ and $ADC_{1,3} = 0$ mm^2/s in the three-component RSI model. The RSI-derived signal contributions of the slower diffusion components were larger in tumors than in fibroglandular tissues. Further, the CNR and specificity at 80 % sensitivity of DCE and a subset of RSI-derived maps were equivalent.

The breast DWI signal was best described using a three-component RSI model. Tumor conspicuity in breast RSI model parameter maps is comparable to that of DCE without the use of exogenous contrast.

5.3 Paper III

The aim of this paper was to explore the voxel-wise ability to distinguish cancer from healthy breast tissue using signal contributions from the three-component RSI model.

Patients with pathology-proven breast cancer from two datasets ($n = 81$ and $n = 25$) without any prior neoadjuvant treatment underwent multi- b -value DWI. The three-component RSI signal contributions $C_{1,3}$ and $C_{2,3}$ and their product, C_1C_2 , and signal fractions $F_{1,3}$, $F_{2,3}$, and F_1F_2 were compared with the image defined on maximum b -value (DWI_{\max}), conventional ADC , and K_{app} . The ability to discriminate between cancer and healthy breast tissue was assessed by the false-positive rate given a sensitivity of 80 % (FPR_{80}) and ROC AUC.

Mean FPR_{80} for both datasets was 0.016 [95 % confidence interval (CI), 0.008–0.024] for C_1C_2 , 0.136 (95 % CI, 0.092–0.180) for $C_{1,3}$, 0.068 (95 % CI, 0.049–0.087) for $C_{2,3}$, 0.462 (95 % CI, 0.425–0.499) for F_1F_2 , 0.832 (95 % CI, 0.797–0.868) for $F_{1,3}$, 0.176 (95 % CI, 0.150–0.203) for $F_{2,3}$, 0.159 (95 % CI, 0.114–0.204) for DWI_{\max} , 0.731 (95 % CI, 0.692–0.770) for ADC , and 0.684 (95 % CI, 0.660–0.709) for K_{app} . Mean ROC AUC for C_1C_2 was 0.984 (95 % CI, 0.977–0.991).

The C_1C_2 parameter of the three-component RSI model yields clinically useful discrimination between cancer and healthy breast tissue, superior to other DWI methods and obviating the need for pre-defining lesions. This novel DWI method may serve as a non-contrast alternative to standard-of-care DCE.

5.4 Paper IV

This study aimed to evaluate early response detection and residual cancer detection with an RSI-based tumor classifier with elastic image registration compared to the conventional manual DCE and diffusion imaging.

Twenty-seven patients (median age 47 years, range 20–68) with breast cancer underwent multi-parametric 3T MRI (including multi-*b*-value diffusion acquisition) at four time points to evaluate response to neoadjuvant treatment. Response to treatment was determined by pCR. In addition to standard manual measurement on DCE images, longitudinally-registered diffusion images were used to generate an RSI classification. The absolute post-treatment tumor size for DCE and RSI, and the mean *ADC* value at the post-treatment time point, were used to determine residual cancer detection correlation with pCR. Response to treatment during treatment was assessed by the percent change in tumor size from pre-treatment for each time point for DCE (ΔDCE) and RSI (ΔRSI) and the change in mean *ADC* from pre-treatment time point (ΔADC).

Sensitivity, specificity, and accuracy for absolute post-treatment tumor size were 0.88 (0.64–0.99), 0.70 (0.35–0.93) and 0.81 (0.61–0.94) for the DCE classifier; 0.71 (0.44–0.90), 0.90 (0.56–1.00) and 0.78 (0.58–0.91) for the RSI classifier; and 0.71 (0.44–0.90), 0.50 (0.19–0.81) and 0.63 (0.42–0.81) for the ADC model. McNemar’s test did not show significant differences between any modalities. *ROC AUC* for change in tumor size from pre-treatment for early, mid and post-treatment time points were 0.64 (0.36–0.91), 0.71 (0.45–0.96) and 0.80 (0.59–1.00) for the ΔDCE classifier; 0.73 (0.48–0.97), 0.62 (0.34–0.90) and 0.76 (0.52–0.99) for the ΔRSI classifier; and 0.56 (0.27–0.85), 0.39 (0.10–0.69) and 0.44 (0.14–0.74) for ΔADC . DeLong’s test for comparison of ROC curves for early, mid and post-treatment time points between ΔDCE , ΔRSI , and ΔADC were all non-significant.

The ΔADC AUC values < 0.5 revealed unexpected behavior from the ADC classification. *Sensitivity, specificity, and accuracy* for the inverted ADC classification were 1.00 (0.81–1.00), 0.20 (0.03–0.56), 0.71 (0.50–0.86) and the AUCs were 0.44 (0.14–0.74), 0.61 (0.32–0.89) and 0.56 (0.25–0.84) for early, mid and post-treatment time points, respectively.

The automatic RSI classifier showed nearly the same accuracy as manual DCE but was able to predict non-pCR after only 3 weeks of neoadjuvant treatment and may complement DCE in assessing residual tumor post-therapy. This is important for cost-efficient evaluation of neoadjuvant breast cancer treatment and improved clinical decision-making to enable tailored treatment regimens.

6. Discussion

The main results of this thesis demonstrate the feasibility of PET/MRI and advanced DWI as alternatives to the current clinical standard of using DCE for locating and defining breast cancer lesions. Tumor definition is the basis of breast cancer evaluation in any clinical setting, ranging from screening to treatment monitoring, and the application of DWI as a quantitative metric currently depends on pre-identifying tumors on DCE prior to transferring them to the DWI image space for quantitative analysis.

The work in this thesis addresses this issue in different ways. Firstly, paper I indicates that our novel PET/MRI semi-automatic segmentation technique (GMM-PET) is reliable in deriving functional parameters for monitoring neoadjuvant treatment response. Secondly, higher-order multi-component DWI models applied to data acquired across higher b -value ranges were investigated (papers II–IV), where the optimal fitting of diffusion signal decay from cancer and healthy breast tissues resulted in a three-component RSI model with globally-determined component $ADCs$ (paper II). The three-component RSI model decomposes the diffusion signal to correspond to major anatomical components in healthy breast tissues and lays the foundation for optimizing tissue discrimination on DWI through the derived RSI parameter C_1C_2 (paper III). The highly promising discriminatory performance of RSI C_1C_2 suggests clinical utility and improved conspicuity of cancer relative to surrounding healthy breast tissues, which may reduce the need to pre-identify lesions on non-diffusion modalities altogether. The RSI parameter C_1C_2 was further applied in a longitudinal dataset (paper IV) and was able to predict non-pCR in early-phase (just after 3 weeks of neoadjuvant treatment) and was more specific than manual DCE in the late-phase assessment of residual tumor post-therapy. This is important for cost-efficient evaluation of neoadjuvant breast cancer treatment and improved clinical decision-making to enable tailored treatment regimens. All these results lay the foundation for quantitative frameworks specific to pathology and a comprehensive model for diffusion in the breast which may complement imaging gold-standard DCE in clinical BI-RADS assessment.

6.1 GMM-PET ROI metrics mimic conventional treatment measures (area, ADC) derived from manual DCE (paper I)

The main finding of paper I is that tumor area and mean *ADC* values derived from GMM-PET matched those derived from conventional manual DCE. The *ADC* values were not significantly different from GMM-PET compared to manual DCE, although *ADC* metrics are known to be significantly influenced by the segmentation method^{87,123}. In line with a previous study by Byun et al.¹⁰⁸, our study also demonstrates strong, positive correlations between tumor *ADC* values derived from PET (GMM-PET in our case) and manual DCE segmentation. Though Byun et al.¹⁰⁸ use a similar approach for deriving *ADC* measures in breast carcinomas, their method is based on sequential ¹⁸F-FDG-PET/CT acquisition which requires an additional registration process. Simultaneous PET/MRI as used in this work has intrinsic voxel correspondence, and we therefore argue that our results confer greater confidence. Thus, successful analysis by GMM-PET may yield clinical utility as an accurate assessment of *ADC* metrics is considered increasingly important in a neoadjuvant treatment response setting^{98,100,124}.

6.2 Spatial concordance between PET-derived segmentation and manual DCE (paper I)

In paper I, GMM-PET recapitulated manual DCE definitions significantly better than the commonly used threshold methods *SUV*_{2.5}, for both treated and untreated lesions, and *SUV*_{42%} for untreated lesions. GMM-PET successfully estimated tumor area in well-known problem cases such as tumors with heterogeneous uptake and high-intensity tumors relative to their immediate surroundings^{125,126}, although GMM-PET did not perform better than *SUV*_{42%} in untreated lesions. A limit of all adaptive and data-driven algorithms that are sensitive to the uptake range^{127,128}, including GMM-PET and *SUV*_{42%}, is that the decreasing tumor ¹⁸F-FDG uptake range during successful treatment¹²⁹ leads to overestimations of tumor size as maximum SUV (*SUV*_{max}) becomes smaller and eventually approaches background levels. One solution to this might be algorithm-based approaches such as gradient methods^{126,130} which have also been recommended¹¹⁶. However, there is a trade-off between data-driven segmentation, requiring minimal user input, and more advanced methods that need increased user input. For this study, we focused on limiting user input for increased clinical practicality and efficiency and did not investigate gradient methods further.

6.3 GMM-PET segmentation compared to conventional DCE in a neoadjuvant setting (paper I)

GMM-PET segmentation gives good spatial concordance with manual DCE segmentation for untreated breast cancer lesions. However, segmentation performance was significantly poorer for treated lesions, indicated by a lower Dice score and higher CoG. It is well-known that therapy affects tumor vascularity¹³¹, and the tumor may become more diffuse as ¹⁸F-FDG uptake is substantially reduced by treatment, thus increasing GMM-PET segmentation variability. It is worth noting that this is not unique to the technique in this study; the reduction of DCE contrast in treated tumors also makes tumor definition more challenging for the conventional approach. This is clearly illustrated by a recent study by Choi et al. who demonstrated that 48.3 % of breast cancer patients who were radiologically defined as treatment responders on DCE after NAC (i.e. no enhancing lesion left) had residual tumor at surgery¹³². It is known that residual tumors with low tumor grade and hormone receptor positive subtypes are most commonly missed on DCE¹³³ and thus these tumors should be interpreted with more caution before surgery. When it comes to tumor biology, the formerly known lobular carcinomas are more likely to have the largest discrepancy in tumor size post-therapy¹³⁴ and to have positive margins at the time of surgery. In our study, we did not consider tumor grade, subtype, or tumor biology¹³⁵. However, it should be noted that several treated lesions with poor spatial concordance are cases where tumor definition on manual DCE was difficult due to low enhancement on DCE. This might suggest that the definition of tumor on DCE in our study, which was not blinded to the pathological results, may have biased the results. This is especially important as both modalities are dependent on sufficient blood flow for contrast and tracer uptake, meaning that the treatment effect on tumor vascularity may have influenced both manual DCE and GMM-PET segmentation. It is an area of future interest to investigate how these are affected differently during treatment.

Our results illuminate the concordance between ROIs derived from different imaging modalities, and as such allow for investigation of the spatial relationship between functional information arising from PET, DWI, and DCE and the tissue characteristics these modalities are sensitized to. The relationship between glucose metabolism (PET) and pharmacokinetic parameters from DCE was not further investigated in this study, but holds potential for increased utility of response assessment in a neoadjuvant treatment setting, as discussed in section 6.16.

The correlation between glucose metabolism (PET) and diffusion quantification (ADC) was not assessed in the current study. However, it has been demonstrated that the correlation between the two biomarkers is relatively weak. SUV and ADC are independently associated with treatment response¹³⁶ and the ratio between the two is useful for assessing response to therapy¹³⁷. This means that similarly to PET and DCE, PET and diffusion imaging may offer complementary information for the assessment of treatment response. Furthermore, change in both SUV and ADC through the course of treatment is associated with disease-free survival¹³⁸. Altogether, all these findings support the assertion that clinical decision-making will benefit from the integration of information from two modalities that are based on distinctly different biophysical properties. In addition, it illustrates PET/MRI's ability to assess a range of biomarkers, which may help increase the knowledge of cancer biology and ultimately lead to increased diagnostic accuracy.

6.4 Institutional differences in diffusion signal (paper II)

We included data from two sites (baseline high b -value MRI cohort 1 and baseline high b -value MRI cohort 2) with different MRI scanners and acquisition parameters to increase the generalizability of the RSI model (paper II). This yielded slightly different estimated component ADC values of the two- and three-component RSI model between sites. $ADC_{1,2}$ is lower than can be meaningfully quantified for both sites. $ADC_{2,2}$, $ADC_{2,3}$, and $ADC_{3,3}$ were higher for baseline high b -value MRI cohort 2 compared to high b -value MRI cohort 1. We hypothesize that this is attributed to the difference in TE between sites; baseline high b -value MRI cohort 1 had a TE of 82 ms, while TE was 88 ms for baseline high b -value MRI cohort 2. Given T2 values of cancer and fibroglandular tissue of 68 ms and 46 ms respectively, the signal decay due to T2 effects is in the same region, resulting in ~ 70–85 % decay to T2 effects across sites and tissues, but will certainly influence the overserved signal. Another important aspect is the inclusion of more non-zero b -values below 500 s/mm² for baseline high b -value MRI cohort 2, which lead to a better characterization of the signal curve at this b -value interval. However, the slight difference in component ADC values did not affect output signal contributions for tumor ROIs; this suggests the joint RSI model is generalizable and can be applied to data acquired across scanners and acquisition parameters (within a certain range).

6.5 Three-component RSI model reveals the diffusional composition of breast tissues (paper II)

The application of optimized models allows for the examination of the diffusion profile of cancer and healthy breast tissues. By visual examination of the resulting signal contribution ($C_{i,K}$) maps we see that different signal contributions highlight different anatomical regions. Across both models, cancer showed elevated signal from the slowest components ($C_{1,K}$). For the bi-exponential model, $C_{1,2}$ highlights cancer, fatty tissue, and fibroglandular tissue, whereas $C_{2,2}$ has elevated signal from cancer, fibroglandular tissue, and vascular flow (and possibly fluid in ducts and glands). The three-component RSI model, however, better separates tissue types with $C_{1,2}$ highlighting cancer and fatty tissue, $C_{2,3}$ highlighting cancer and fibroglandular tissue, while $C_{3,3}$ highlighting vascular flow/fluid in ducts and glands. This separation of breast anatomy is not previously demonstrated by other DWI models.

6.6 Three-component RSI model better fit breast diffusion data (paper II)

The three-component RSI model has a lower BIC and lower fitting residuals compared to the bi-exponential model, which suggests that three components provide a better characterization of diffusion signal in the breast. However, in the study by Vidić et al. which examined several mathematical signal representations, the Padé approximation demonstrated the best data fit of the diffusion signal from malignant and benign lesions modeled for b -values up to 3000 s/mm^2 ⁸³. Interestingly, several other models, such as the bi-exponential model, had a higher discriminatory performance between malignant and benign lesions, indicating that discrimination performance is not precisely tied to the quality of curve fit⁸³. Though our studies are not directly comparable, since the tri-exponential model and healthy breast tissue fitting were not explored in that study, it illustrates the balance between *a priori* assumptions and biophysical interpretability when modeling diffusion signal. The Padé approximation is an example of an entirely mathematical representation without any assumptions about underlying tissue microstructure, thus limiting the possibility for biophysical interpretation (as well as spurious over-interpretation). In our study, the aim was to limit the number of model assumptions while simultaneously conserving biophysical interpretation, which resulted in a three-component RSI model that demonstrated both goodness of fit of diffusion signal and the ability for biophysical interpretation of output model parameters.

The application of the three-component RSI model in the current work yields global component *ADCs* that present the best fit across all training voxels, which explicitly includes both cancer and healthy breast tissues. The inclusion of all breast tissue voxels in the fitting is different than for other commonly investigated models for healthy breast tissues such as IVIM⁹¹ (equation 4), *ADC*^{78,112} (equation 2), and the DKI model¹³⁹ (equation 5). Previous studies investigating cancerous and healthy breast tissues using the IVIM⁹¹, *ADC*^{78,112}, and DKI¹³⁹ models have been performed by signal averaged across entire (pre-identified) ROIs and not on a voxel-wise basis, and purposely avoid the inclusion of fatty tissue. Thus, these studies are not able to reflect the spatial information included in the image; applying our analysis on a voxel-wise basis allows the three-component RSI model to capture the unique breast tissue environment, including the admixture of fatty tissue and fibroglandular tissue. Note that we included fitting analysis without fatty tissue voxels, further discussed in section 6.7.

Once component *ADCs* across all breast voxels were determined, these values were fixed and incorporated into the three-component RSI model for generating signal contribution ($C_{1,K}$) maps from the different components. Fixing component *ADCs* is beneficial for several reasons, and is fundamentally different from common diffusion fitting methods such as in the IVIM model, where component *ADCs* are left free and determined for each voxel individually. Firstly, fixing component *ADCs* allows for a computationally-efficient linear analysis with only one unknown per voxel per signal component, i.e. the signal contribution, and avoids overfitting. Contrary to a fully-independent model fitting per voxel, this enables more stable estimates. This is particularly important when fitting higher-order models. Secondly, it simplifies the biophysical interpretation of the signal contribution as being the individual weighting of a given diffusion component (with a corresponding component *ADC*) from the total diffusion signal. Thus, comparisons across patients and sites are more easily done, which is essential for the development of effective imaging biomarkers.

6.7 Application of the three-component RSI model allows for biophysical characterization of breast tissues (paper II)

Application of the three-component RSI model allows for examination of the diffusion profile of cancer and healthy breast tissues, where different anatomical tissue types are distinguishable using the different components, and can be tied to biophysical behavior. $C_{1,3}$ is determined using $ADC_{1,3} = 0$ mm²/s and highlights cancer and fatty tissue; $C_{2,3}$ with $ADC_{2,3} = 1.4 \times 10^{-3}$ mm²/s highlights cancer and fibroglandular tissue, while $C_{3,3}$ with $ADC_{3,3} = 10.2 \times 10^{-3}$ mm²/s highlights areas with fast apparent diffusion representing vascular flow and fluid in ducts and glands. Thus, $C_{1,3}$ represents restricted diffusion, $C_{2,3}$ hindered diffusion and $C_{3,3}$ pseudodiffusion. Note that $C_{3,3}$ was the only signal contribution that was not sensitive to cancer. Thus, the three-component RSI model reveals the diffusion signal heterogeneity in breast tissues and can decompose diffusion signal by signal contributions corresponding to basic breast tissue components of fatty tissue, fibroglandular tissue, and fast vascular flow/fluid in ducts and glands.

The two fastest signal components $C_{2,3}$ and $C_{3,3}$ are on the same length scale as the two biophysical components probed by low to mid b -value regimen in the bi-exponential IVIM model ¹⁴⁰ (equation 4), described by D^* (pseudodiffusion coefficient) and D (“true” apparent diffusion coefficient), respectively. Thus, $C_{2,3}$ may similarly represent the hindered diffusion of the extracellular space in fibroglandular tissues, where the $ADC_{2,3}$ value is consistent with previous studies of fibroglandular tissue specimen ^{93,141}. Furthermore, $C_{3,3}$ can be related to the signal contribution from flow in vessels with diffusion coefficient values typically ~10 times higher than fibroglandular tissue diffusion times ^{140,142}. The percent diffusion signal associated with this normalized signal fraction component is described by the $f_{3,3} = 22$ % in our study. This is higher than what is commonly reported for breast cancer lesions using the IVIM model ⁹⁰. A source of this discrepancy may be due to the different number of diffusion components compared to IVIM. In addition, it is important to note that the pseudodiffusion component cannot be precisely estimated in our dataset since one of the two datasets used for fitting, baseline high b -value MRI cohort 1, did not include any non-zero b -values below 500 s/mm².

When a bi-exponential model is applied to data from a higher b -value range (b -values > 1000 s/mm²), there is a shift in diffusion coefficient and the corresponding biophysical interpretation. Several studies have shown that the slowest diffusion coefficient in a high b -value bi-

exponential model, ADC_{slow} , is $\sim 0.5 \times 10^{-3} \text{ mm}^2/\text{s}$ and the fastest diffusion coefficient, ADC_{fast} , is $\sim 2.0 \times 10^{-3} \text{ mm}^2/\text{s}$ ^{83,92,141}. The length scale of ADC_{fast} is therefore in between the D (and $ADC_{2,3}$) and D^* (and $ADC_{3,3}$) which suggests that it is a mixture of contributions from two biophysical components including hindered fibroglandular tissue diffusion and pseudodiffusion. This is apparent in our study where $C_{2,2}$ (with $ADC_{2,2} \sim ADC_{\text{fast}}$) was elevated in both perfused and fibroglandular tissues. Moreover, the slowest component with ADC_{slow} is conventionally attributed to restricted intracellular diffusion which characterizes hypercellular tumors; the low diffusion distances of this tissue component are not well probed without high b -values regimes. In our study, $C_{1,2}$ was elevated in cancer and fibroglandular tissue, but also in fatty tissue, with $ADC_{1,2}$ that was approximately tenfold shorter than conventional ADC_{slow} (discussed in detail below). Thus, the bi-exponential model applied to higher b -values appears to combine several biophysical components, and our results suggest that higher-order models (i.e. three components) are needed to further decompose diffusion signal into more meaningful biophysical components related to the complex breast tissue environment.

The tri-exponential model component ADC s vary depending on the tissues included in the analysis, and so it is important to make the distinction of what these values represent. When Nakagawa et al. fit a tri-exponential model at high b -values (up to $2500 \text{ s}/\text{mm}^2$) for pre-identified malignant lesions, that is without including any non-lesion voxels, it resulted in the following mean diffusion coefficients: slow restricted (D_s) = $0.85 \times 10^{-3} \text{ mm}^2/\text{s}$, fast free diffusion (D_f) = $2.16 \times 10^{-3} \text{ mm}^2/\text{s}$, perfusion-related diffusion (D_p) = $14.81 \times 10^{-3} \text{ mm}^2/\text{s}$ ¹⁴³. The two fastest diffusion coefficients, D_f and D_p , are on comparable length scales to $ADC_{2,3}$ and $ADC_{3,3}$, respectively, and may be roughly attributed to the same biophysical components. However, the slowest diffusion coefficient D_s is similar to ADC_{slow} from the bi-exponential model ^{83,92,141} and is markedly higher than $ADC_{1,3} = 0 \text{ mm}^2/\text{s}$ in our study. We attribute this to the control ROIs which were not included in the study by Nakagawa et al. ¹⁴³ or the bi-exponential fits ^{83,92,141}. However, stronger conclusions from our study cannot be drawn without histological tissue samples.

For completeness, we also performed RSI model fitting where we excluded the majority of visible fatty tissue voxels. The main difference in resulting component ADC s were in $ADC_{3,3}$; $ADC_{3,3} = 7.2 \times 10^{-3} \text{ mm}^2/\text{s}$ excluding fatty tissue, $ADC_{3,3} = 10.8 \times 10^{-3} \text{ mm}^2/\text{s}$ including fatty tissue. On the contrary, $ADC_{1,3}$ is lower when including fatty tissue; this is not surprising as the

highly restricted diffusion of fatty tissue generates low diffusion coefficients. Thus, we hypothesize that the increased $ADC_{3,3}$ when excluding fatty tissue indicates that pseudodiffusion evolves at a slower rate when fatty tissue is excluded. However, note that our fibroglandular tissue ROIs excluding fatty tissue did not account for intravoxel fatty tissue within fibroglandular tissue. This may be a contributing factor to why fibroglandular tissue also experiences restricted diffusion, though the amount of water experiencing restricted diffusion appears to be higher in tumor tissue.

IVIM is a commonly used multi-component model in the breast. Even though we use an extended b -value range compared to what is commonly used for IVIM analysis, we acknowledge above that $C_{2,3}$ and $C_{3,3}$ may reflect the same biophysical components as the IVIM model. One could therefore argue that the three-component RSI model presented in this paper is similar to the IVIM model with an additional offset ($C_{1,3}$) accounting for the hyper-restricted water component in fatty tissue and tumors which manifests in the high b -value range. Additional differences between the three-component RSI model and IVIM include: fitting regimen across both cancer and non-cancer voxels (three-component RSI) rather than in a pre-identified ROI (IVIM), using fixed component ADC s (three-component RSI) rather than fitted variables (IVIM), and describing the signal with three components (three-component RSI) rather than two (IVIM). In addition, one fundamental difference between the three-component RSI model and IVIM is the normalization method, where IVIM normalizes by S_0 to eliminate proton density- and T2-weighting. By doing this, the signal fractions of each component in the IVIM model add up to 1 and are mutually dependent. However, $C_{1,3}$, $C_{2,3}$, and $C_{3,3}$ are not normalized by S_0 , and all components are thus scaled to individual proton density-weightings and are influenced by the T2-relaxation of the individual components. The importance of proton density- and T2-weighting for breast tissue discrimination will be described in further detail below.

While the biophysical interpretation of $C_{2,3}$ and $C_{3,3}$ are well-described in the literature as the focus of the IVIM model, diffusion signal from suppressed fatty tissue and its diffusion properties are not well-known. It is important to note that using a fixed $ADC_{1,3} = 0$ mm²/s does not mean that there is no diffusion at all; instead, it reflects the fact that this diffusion coefficient was too slow to be quantified in our experimental setup using long TEs. We hypothesize that the very slow diffusion properties of $C_{1,3}$, modeled with $ADC_{1,3} = 0$ mm²/s, may arise from extremely restricted cell environments such as the water within the thin cytoplasmic membrane

in adipocytes and intracellular structures in cancer cells. This conclusion is also presented in a study by Baron et al. who reported diffusion coefficients close to zero in normal breast tissues⁷⁸. However, unsuppressed fatty tissue, i.e. diffusion signal from the lipid component of adipocytes which fat suppression techniques target, has been reported to have low diffusion coefficients as well¹⁴⁴. Thus, another possible explanation is that our diffusion data was not adequately fat suppressed, which is a common hypothesis for explaining the hyper-restricted diffusion signal from fatty tissue^{78,145}. We did not perform any quantitative investigation of the fat suppression (by SPAIR and FatSat) in this study, but all diffusion images in this study were visually inspected by an experienced breast radiologist and only included if they were defined as adequately fat suppressed. Furthermore, $C_{1,3}$ was found to be sensitive to cancer, which does not contain fatty tissue. Thus, we believe that the included data was sufficiently fat suppressed and that the hyper-restricted signal from $C_{1,3}$ has biophysical importance and relates to water within adipocytes and intracellular structures in cancer cells. This can also be seen as the persistent signal intensity from suppressed fatty breast tissue at very high b -values. However, noise, which we attempted to account for by assuming a Rician noise distribution¹¹¹, may have been a partial contributor to the $C_{1,3}$ signal. The initial RSI model in the brain uses $ADC = 0 \text{ mm}^2/\text{s}$ for the slowest component⁷¹, and previous studies suggest that this component account for the diffusion of intracellular water^{101,146}. In the most recent RSI model in the prostate, the ADC of the slowest component was also estimated to be $0 \text{ mm}^2/\text{s}$ ⁷⁶, meaning that this observation is not unique to the breast. This is different from previous prostate RSI models^{63,66,73,75} where the slowest component was not zero. This might suggest that an $ADC = 0 \text{ mm}^2/\text{s}$ better represents the restricted diffusion component than previous models that may include tortuous extracellular or hindered diffusion¹⁴⁶.

Regardless of the specific origin of hyper-restricted diffusion signal from fatty tissue, it is problematic in breast DWI for several reasons. Firstly, hyper-restricted diffusion from fatty tissue confounds the detection of restricted intracellular diffusion that characterizes hypercellular tumors^{63-67,83}. In most body sites, such as the prostate, this would not be particularly problematic because subcutaneous fatty tissue can be easily distinguished from parenchymal tissue where tumors arise. However, the unique tissue microstructure of normal breast tissues, where fibroglandular tissue is admixed with fatty tissue, creates a fatty tissue signal on DWI⁷⁷ at an intravoxel level.

The results from paper II suggest that the three-component RSI model is useful in the characterization of all breast tissue, both cancer and healthy breast tissues when the component ADC s are determined from training data containing these tissues. Building on these findings, we evaluated the three-component RSI model using a more clinically relevant approach by assessing discriminatory performance of parameters derived from the three-component model in paper III.

6.8 Discrimination between cancer and healthy breast tissues with RSI C_1C_2 (paper III)

The results from paper III show that cancer can be non-invasively discriminated from healthy breast tissues using the compound parameter C_1C_2 derived from the three-component RSI model. C_1C_2 achieved very low false positive rates while detecting 80 % or more of the defined cancer voxels, as defined by FPR_{80} mean = 0.016, 95 % CI = 0.008–0.024. The discriminatory power of C_1C_2 was superior to that of signal contributions considered independently, conventional DWI-estimates (ADC), and other methods, including DKI (K_{app}) and DWI_{max} . Moreover, the C_1C_2 approach was performed at two different sites, scanners, and acquisition protocols, suggesting the generalizability of model parameters with potential for real-world applications.

The high discriminatory performance of C_1C_2 is derived from the nature of the three-component RSI model; as healthy breast tissues consist of an admixture of fat and fibroglandular tissue, it is essential to be able to discriminate cancer from all healthy breast tissues, including the hyper-restricted water component in fatty tissue. We show that the $C_{1,3}$ is high in fatty tissue, while $C_{2,3}$ is low. Conversely, the $C_{2,3}$ is high in fibroglandular tissue, while $C_{1,3}$ is low. Both signal contributions are sensitive to the restricted diffusion from the intracellular cancer tissue. Thus, by computing the product of the two (C_1C_2), we can better suppress signal from both normal fatty tissue and fibroglandular tissue, which have low values in at least one contribution, while preserving the signal from cancer tissue (Figure 17). $C_{3,3}$ is not included because it is sensitive to perfusion in vessels and fluid in ducts and glands, but not cancer. Thus, using the RSI-derived C_1C_2 approach may account for women with varying degrees of admixed fatty tissue.

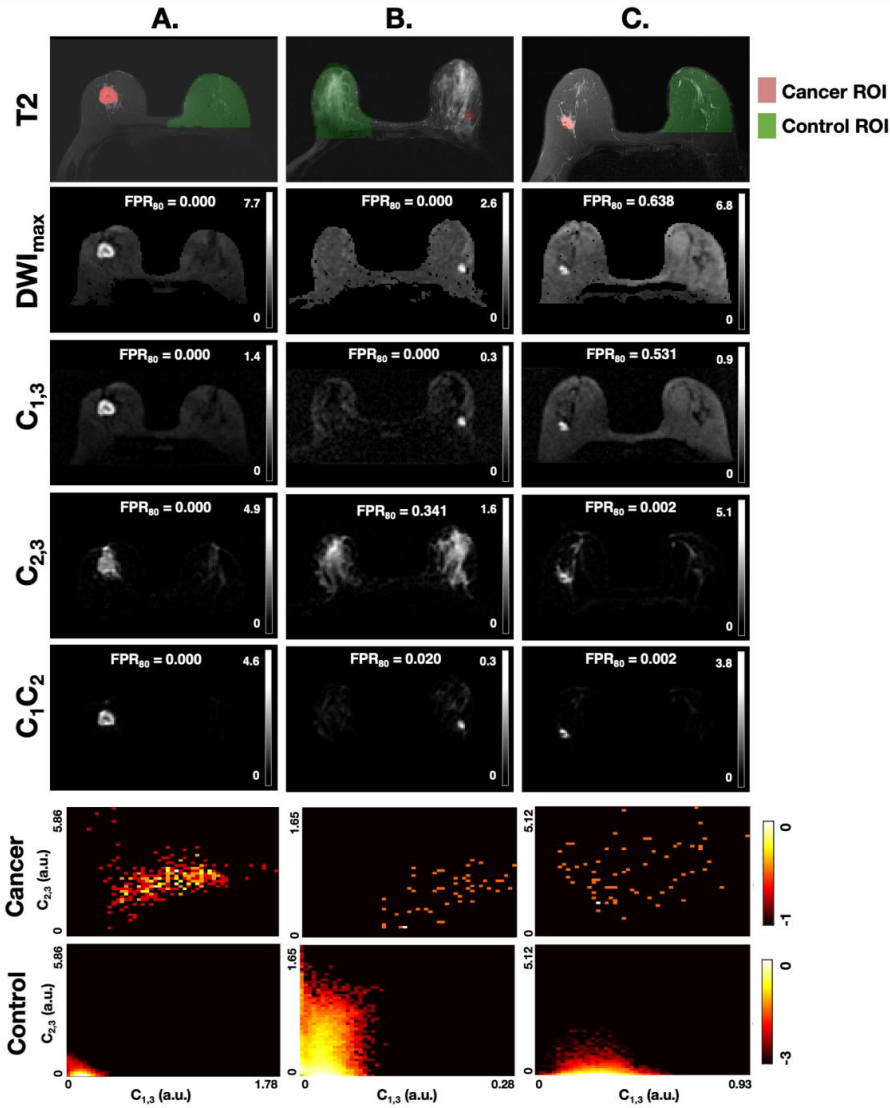


Figure 17. Parameter maps for maximum b -value image (DWI_{max}), Restriction Spectrum Imaging (RSI) signal contribution maps for $C_{1,3}$, $C_{2,3}$, C_1C_2 (labelled with the false-positive rate given the sensitivity of 80 %, FPR_{80}), T2 images with cancer (red) and control (green) region of interest (ROI) overlay for three representative cases. FPR_{80} varies depending on the composition of healthy breast tissue in relation to the magnitude of $C_{1,3}$ and $C_{1,3}$ in cancer. A. Mixed tissue composition with cancer high on both dimensions. B. Abundant fibroglandular tissue and high $C_{1,3}$ -magnitude of cancer. C. Abundant fatty tissue and high $C_{2,3}$ -magnitude of cancer. a.u.; arbitrary unit. *Adapted and modified from* ¹⁴⁷ *with permission.*

Another important aspect that contributes to the high discriminatory performance is the normalization method that retains T2- and proton density-contribution to the DWI signal. On conventional DWI, T2-effects on DWI signal are removed to derive pure diffusion parameters⁶². As can be seen for conventional ADC and signal fractions (f), these maps are visually more noisy than corresponding signal contributions ($C_{i,K}$) in paper II. The non-normalized signal contributions ($C_{i,K}$) from the three-component RSI model retain contribution from voxel-wise proton density and T2, and visually we see tumor tissue superimposed on the background. The increased discriminatory effect of signal contributions ($C_{i,K}$) is unsurprising as T2-relaxation is known to be slower in cancer¹⁴⁸ compared to healthy breast tissues¹⁴⁹, and hypercellular cancerous lesions are likely to have higher water concentration, and therefore proton density, compared to normal breast tissues. This is also reflected by the higher CNR comparable to DCE of signal contributions ($C_{i,K}$) compared to ADC and signal fractions in paper II. Thus, long T2 and high proton density together with restricted diffusion of cancerous lesions lead to a high discriminatory performance. The difference in magnitude in signal intensity between fibroglandular tissue and cancer due to T2 effects in our data can be estimated to be approximately 13 %, assuming T2 of 46 ms for fibroglandular tissue and 68 ms for cancer¹⁵⁰, with the TE in our acquisition protocol. These effects are therefore quantitatively larger than the difference due to diffusion, yielding approximately 5% difference for b -values 500 and 1500 s/mm² and 1–2 % for b -value of 4000 s/mm² when assuming ADC values from our cohort (1.1×10^{-3} mm²/s for fibroglandular tissue and 0.93×10^{-3} mm²/s). The importance of T2 and proton density has also been shown in separating benign and malignant breast lesions, where S_0 , the calculated signal at $b = 0$ s/mm² (which has no diffusion weighting), yielded a relatively high AUC of 0.85⁸³.

6.9 C_1C_2 discriminatory performance in comparison to conventional DWI (paper III)

We hypothesize that contributing factors to the poor discriminatory performance of the ADC model (ADC) and DKI (K_{app}) include the hyper-restricted water component within adipocytes in fatty tissue, and the elimination of proton density- and T2-effects that contribute to discriminatory performance. In this study there was a large variation of the FPR_{80} discriminatory performance of ADC and DKI across cases; though the performance was around 0.2 in selected cases, the overall performance was no better than chance. We argue that our

voxel-level assessment of discriminatory performance better reflects healthy breast tissue heterogeneity including admixture of fatty and fibroglandular tissue. This means that previous studies that have demonstrated significant differences between cancer and healthy breast tissues in signal-averaged ROIs by ADC^{78,112} and DKI¹³⁹ are not directly comparable to the FPR₈₀ results in this study. Conversely, DWI_{\max} shares the same basic properties as C_1C_2 (diffusion-, proton density- and T2-weighting) and performs much better than ADC and DKI, giving several cases with perfect discriminatory performance. However, DWI_{\max} is also influenced by the hyper-restricted water in fatty tissue, resulting in worse performance than C_1C_2 on average. C_1C_2 better accounts for all healthy breast tissues including water in fatty tissue. This is a major advantage compared DWI_{\max} and the other DWI estimates, as fatty tissue is a major component of healthy breast tissues⁵⁰ and is admixed with fatty tissue on a voxel-level on DWI.

It is well-known that ADC, DKI, and other DWI-based models can discriminate between benign and malignant lesions with pre-identified ROIs, an assessment that was not within the scope of this study. Vidić et al.⁸³ demonstrated that ADC (ADC) and DKI (K_{app}) had a nearly perfect discriminatory performance of 0.96 and 0.99, respectively, suggesting potential utility for quantitative breast lesion characterization. However, because C_1C_2 is insensitive to the majority of healthy breast tissues and highlights potential pathology, we propose it as an imaging tool with the potential of cancer detection within an image, with the further possibility of lesion classification in conjunction with more conventional, quantitative diffusion analysis.

6.10 C_1C_2 discriminatory performance in comparison to DCE (paper III)

For RSI-derived C_1C_2 to be a non-invasive alternative to DCE for breast cancer detection, it will ideally have comparable or better sensitivity and specificity. Previous studies have shown that DWI improves detection specificity^{79,151}, which is beneficial as the results of lesion-level DCE specificity range from 72 to 97 %⁷⁻¹¹. The high performance of discriminating cancer from all other healthy breast tissues in comparison to other DWI-based methods is highly promising and may suggest comparable clinical utility to DCE. C_1C_2 may be particularly useful in improving DCE specificity, such as when DCE demonstrates false positives in patients with moderate or marked background parenchymal enhancement⁵¹. Ultimately, successful analysis using C_1C_2 has the potential to remove the need to administer Gadolinium contrast entirely, and consequently preclude any accumulation of Gadolinium in the brain¹². Contrast-free

breast-MRI scans would also benefit pregnant women and patients with renal failure, where Gadolinium contrast is contraindicated ⁵⁶.

6.11 C_1C_2 in comparison to other high b -value models (paper III)

Various diffusion methods aim to isolate the signal from the slowly diffusing water component in cancer tissue by utilizing high b -values ^{63-67,80-83}. Advanced, multi-component models have been developed to probe the microstructure in the brain and prostate, including RSI ^{63,64}, the VERDICT model ⁶⁵, and the hybrid multidimensional MR imaging model ⁶⁷. A key difference comparing the hybrid multidimensional MR imaging model to RSI and VERDICT is that the hybrid multidimensional MR imaging model does not use fixed component ADC s, but determines the component ADC for each voxel independently, making a comparison of corresponding signal contributions across patients difficult. However, though these *a priori* assumptions about underlying microstructure allow for biophysical interpretability, they may also lead to over-interpretation. Another difference is that, unlike RSI and VERDICT, the hybrid multidimensional MR imaging model incorporates multi-echo information not available in our study, meaning that the intrinsic T2-relaxation time of each component, which may vary between components, is included in the model. Moreover, as previously discussed, the T2- and proton density-effects seen in RSI are removed from the other two modeling approaches, potentially reducing cancer conspicuity. Although the other multi-component models have shown promising results as cancer biomarkers in the prostate, for example, the unique tissue admixture of fibroglandular and fatty tissue in healthy breast tissues suggests that these results may be limited in the breast. It should also be noted that DKI also uses high b -values to isolate the restricted water signal from cancer, where the derived parameter K_{app} has proven potential utility in the breast in discriminating *pre-identified* malignant and benign lesions ⁸⁰⁻⁸². However, this is not a multi-component model, but rather a purely mathematical representation of diffusion data.

6.12 RSI classifier for longitudinal response assessment compared to DCE (paper IV)

Our study shows that the RSI classifier, based on $C_{1,3}$ and $C_{2,3}$ of the three-component RSI model, shows promise for detecting early response to treatment, with significant changes in the RSI measurement detected after only three weeks of neoadjuvant breast cancer therapy. In the

later phase of treatment, the automatic RSI classifier showed nearly the same accuracy as DCE with manually-defined ROIs, but does not require any user input beyond the pre-treatment MRI scan. The RSI classifier was (non-significantly) more specific for assessing residual tumor post-therapy than DCE. The promising results from the development of this advanced DWI classifier invite further study that can potentially lay the foundation for a quantitative, easily implemented, and cost-efficient response assessment framework that may complement standard DCE in the evaluation of neoadjuvant breast cancer treatment, thus improving clinical decision-making for enabling tailored treatment regimens.

The improved predictive performance at the early-treatment time point is probably due to the RSI classifier's quantification of tumor cellularity, in contrast to DCE which is based on tumor vascular perfusion. The RSI classifier is sensitive to slow diffusion within hypercellular tumors while simultaneously suppressing signal from healthy fatty and fibroglandular breast tissue¹⁴⁷. Thus, the RSI classifier reflects the decrease in cellularity through the course of neoadjuvant therapy, consistent with RSI's known estimation of tumor cellularity across organs^{58,73,75,101,102}. This may help resolve early phase diagnostic challenges of tumors that regress with diffuse cell loss rather than direct tumor shrinkage, meaning little or no change in overall tumor size on DCE.

Early-phase treatment response assessment is important for clinical decision-making and may enable tailored treatment regimens, and the current findings of detecting response after only three weeks by ΔRSI yield valuable information on *in vivo* treatment efficacy at an early time point. Establishing early response status may allow for non-responding patients in adaptive treatment regimens to switch to alternative treatment regimens pre-surgery. This allows for the planning of additional systemic therapy for non-responders after surgery which is known to improve survival^{152,153}. On the other hand, establishing early complete responders may facilitate de-escalated treatment strategies such as shortened treatment regimens¹⁵⁴, thus avoiding unnecessary chemotherapy with toxic side effects.

The RSI classifier is informative of tumor cellularity also in the later phase of therapy, which is important as post-therapy cellularity is associated with overall patient survival¹⁵⁵. However, RSI did not reflect post-therapy size especially well, contributing to the low sensitivity for detection of remaining tumor tissue post-therapy. Thus, DCE-based methods are likely to continue to have a more prominent role than the RSI classifier in the context of e.g. surgical

planning, where the exact extent of tumor borders must be precisely determined. The RSI classifier may yet have a role in complementing DCE in this setting since it suggested a higher specificity than seen for DCE measures post-therapy.

The RSI classifier automatically estimates tumor volume through elastic image registration to the pre-treatment time point. This is an advantage compared to conventional MRI which uses manually defined lesions for each time point. Automatic assessment is particularly useful in a treatment setting as defining the tumor is especially difficult when the tumor shrinks in size and may be affected by treatment and procedure-related changes. These results also add to current literature demonstrating that DWI-based response assessment may precede changes in tumor size measured by DCE ⁹⁸. RSI performed better than the longest diameter of manual DCE which had an AUC of predicting pCR at the early time point of 0.64 in the ISPY trial ⁹⁷; AUC increased to 0.70 using a threshold-based DCE model (functional tumor volume, FTV).

6.13 RSI classifier for longitudinal response assessment compared to DWI (paper IV)

Our results complement existing literature on DWI as a response biomarker following neoadjuvant therapy in breast cancer. However, in our study the ADC model failed to provide useful results; in particular, the AUC for ADC was < 0.5 and therefore suggested the reverse hypothesis (decrease in *ADC* equals response to treatment) at the mid or late-treatment timepoints. This is contrary to the expected behavior from the literature ^{97-100,156,157} and it is therefore likely that our study was not well suited to assess the predictive value of ADC. This may have several reasons, outlined below. Nevertheless, there are conflicting results in the literature regarding the predictive value of ADC; while several single-center trials have reported that ADC is predictive of response in the early phase ^{157 98,99}, the multi-center I-SPY trial ¹⁰⁰ and a recent 2022 study by Almutlaq et al. ¹⁵⁶ showed a low predictive value of ADC at this time point, similar to our results. However, at the mid-treatment time point, the AUC is increased to 0.60 in the multi-center I-SPY trial ¹⁰⁰, while the study by Almutlaq et al. ¹⁵⁶ did not demonstrate response prediction.

6.13.1 ROI definition

Cancer ROI definition in our study was performed by manual delineation on the site of visible cancer tissue of the pre-treatment raw DWI image with expert radiologist validation. This ROI was applied to *ADC* maps for all time points after being registered to the pre-treatment time point images. *ADC* mean was calculated within the cancer ROI; the rationale for this approach was to avoid time-consuming and technically difficult manual delineation of a tumor undergoing treatment and to avoid a substantial increase or decrease in the number of analyzed voxels across time points depending on tumor response. Manual delineation directly on *ADC* maps, as done in the multi-center I-SPY trial¹⁰⁰, also requires high-quality images, a known issue for diffusion imaging. However, using the same cancer ROI for all treatment time points will necessarily include some non-tumor tissue in the *ADC* mean calculation at early, mid and post-treatment time points, to a varying degree dependent on the true tumor decrease in size. Conversely, the entire tumor will on the other hand not be included in the ROI for cases with tumor progression, although in this case the *ADC* mean value might arguably be representative of the tumor within the cancer ROI. In addition, potential inclusion of necrotic tumor tissue might have influenced results, although this is a form of response to which *ADC* is sensitive. ROI-definition is a fundamental aspect of quantitative imaging analysis, and *ADC* mean calculation will be sensitive to ROI delineation, because the surrounding healthy tissue may have different diffusion properties;⁸⁷ inclusion of fatty tissue will decrease the resulting value, while inclusion of fibroglandular tissue will increase the value, in addition to variability within the tumor as well. Thus, surrounding healthy tissue in combination with tumor changes may have contributed to the unexpected *ADC* model behavior in this study, as well as any imperfect registration that will effectively alter the shape or location of the ROI.

There is a large variability in the literature in regards to whether necrotic areas are included in the ROI, or if the ROI was defined by viable tissue only. Necrosis of the center of the tumor occurs when a fast-growing tumor outgrows its vascular supply. Such lesions are suggested to be more aggressive, hypoxic, and treatment-resistant¹⁵⁸. Necrotic areas have high intensity on *ADC* maps and will influence the resulting *ADC* mean. In the study by Bedair et al.¹⁵⁷ where the *ADC* model predicted response during early-phase treatment, care was taken to avoid necrotic regions so that only viable tumor tissue was left for analysis. Since the same cancer ROIs were used for all time points in our study, both necrotic tissue of the tumor and healthy tissue were included in the ROI at early, mid, and post-treatment time points, thus an increase

in ADC mean in a non-responding case can be interpreted as arising from confounding necrotic tissue, seen in Figure 18 for early and mid-treatment time point. However, exclusion of necrotic tissue was also done by Almutlaq et al.¹⁵⁶ and I-SPY trial¹⁰⁰, where ADC was not predictive for the early-treatment time point. Thus, other factors seem also to influence the results.

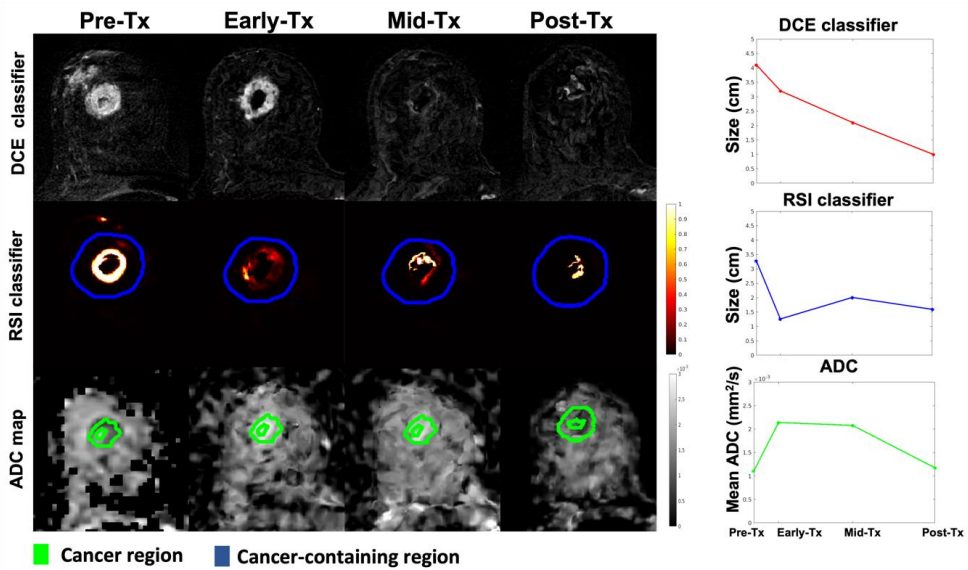


Figure 18. Dynamic contrast-enhanced (DCE) images, Restriction Spectrum Imaging (RSI) classifier, and apparent diffusion coefficient (ADC) maps across all imaging time points for a subject with remaining tumor tissue on final post-surgical pathology (non-responder). The cancer region (green) is given for ADC maps and the dilated cancer-containing region (blue) is given for RSI. For all time points, the largest diameter is given for DCE and RSI classifier, and the mean ADC value of the cancer ROI. ADC maps, particularly for early and mid-treatment (Tx) time points are heavily influenced by necrotic tissue, leading to an increase in mean ADC within the cancer ROI.

In our study, we performed the analysis with an *a priori* assumption that an increase in ADC represents a response to treatment in line with current practice. ROC AUC results for the ADC model for mid and post-treatment time points were < 0.5 , indicating that ADC was negatively predictive of response. This finding is unexpected and has to our knowledge not been observed in prior ADC breast studies. Biologically, a decrease in ADC with response might suggest fibrosis/dehydration in the extracellular space. However, the common assumption is that the tumor is replaced with fibroglandular tissue, which will increase ADC .

6.13.2 ADC calculation

Another factor that might have influenced the results is how the *ADC* mean value was calculated. In our study, the *ADC* maps were generated first, then the *ADC* mean was extracted from the maps. However, EUSOBI⁴⁸ recommends calculating the mean *ADC* by first averaging signal intensities rather than averaging voxels across the *ADC* map so that the output is less affected by noise¹⁵⁹. Also, the choice of *b*-values is important. We used *b*-values < 1000 s/mm², ie. 0 and 500 s/mm². However, the influence of pseudodiffusion is particularly prominent for *b*-values < 200 s/mm², and these *b*-values are therefore commonly eliminated to avoid this effect. Since our dataset focused on high *b*-values acquired for RSI, it did not contain a range of low *b*-values which have been used in comparable studies¹⁰⁰, thus, the ability to accurately estimate *ADC* values may have been limited,

It is well-known that there are challenges with DWI acquisition and image quality that might also have affected the results. In a recent multi-center study, quality assessment excluded 30 % of data;¹⁶⁰ several lesions were considered non-evaluable due to factors such as image quality, limited lesion contrast, and partial volume effects. The diagnostic performance of the calculated *ADC* mean was reduced from AUC 0.75 to AUC 0.61 when all lesions (including non-evaluable) were included in the analysis, which is a notable difference. In our study, DWI data were quality controlled, however, images in our study were generally quite noisy and proved difficult to use for manual ROI delineation directly, one of the reasons for our ROI strategy that may have influenced the results.

6.14 Signal-to-noise (SNR)

It is a well-known issue that DWI signal at high *b*-values can approach the image noise floor, as a result of noise having a Rician (non-normal) distribution that cannot take negative values; this is especially relevant for RSI as it requires the use of higher *b*-values. In paper II, the regional SNR of cancer ROIs vs. healthy breast tissue was ≥ 20 . There is no common consensus on the ideal SNR for DWI breast application⁴⁸, though an SNR ≥ 20 has been suggested as adequate for conventional DWI parameters¹⁶¹ since at these values noise can be assumed to be Gaussian in nature (and thus does not influence the outcome of diffusion model fitting).

From the literature, one would expect mean *ADC* values (mono-exponential) of $0.9\text{--}1.3 \times 10^{-3}$ mm²/s for malignant lesions⁴⁸, which is in line results of papers I and III where mean *ADC*

values are given. However, on a voxel level, we see that negative ADC values occur, as can be seen in Figure 4 in paper III. Negative ADC values are biophysically impossible since diffusion processes *must* cause a signal decay across increasing b -values. The negative values are nevertheless correct mathematically, and arise from data with low SNR where voxel values are close to zero, and as a result of noise the signal at $b = 500 \text{ s/mm}^2$ is higher than at $b = 0 \text{ s/mm}^2$ (example in Figure 19). The presence of negative ADC voxels is not unusual in DWI studies, and can be used as an indicator of data quality; their direct effect on result is often ameliorated by use of summary statistics (i.e. taking the mean value). In one case, observed in Figure 6 in the paper I erratum, where the mean value itself is negative. This specific case was due to a gross misplacement of the ROI owing to a large patient movement between acquisition of DCE (where the ROI was drawn) and DWI data. For the conclusions of paper I, the GMM-PET ROI was derived from the PET data acquired concurrently with the DCE data, and so while the ADC values are incorrect, the fact that both ROI methods return the *same* negative mean ADC still supports the conclusion that the methods agree.

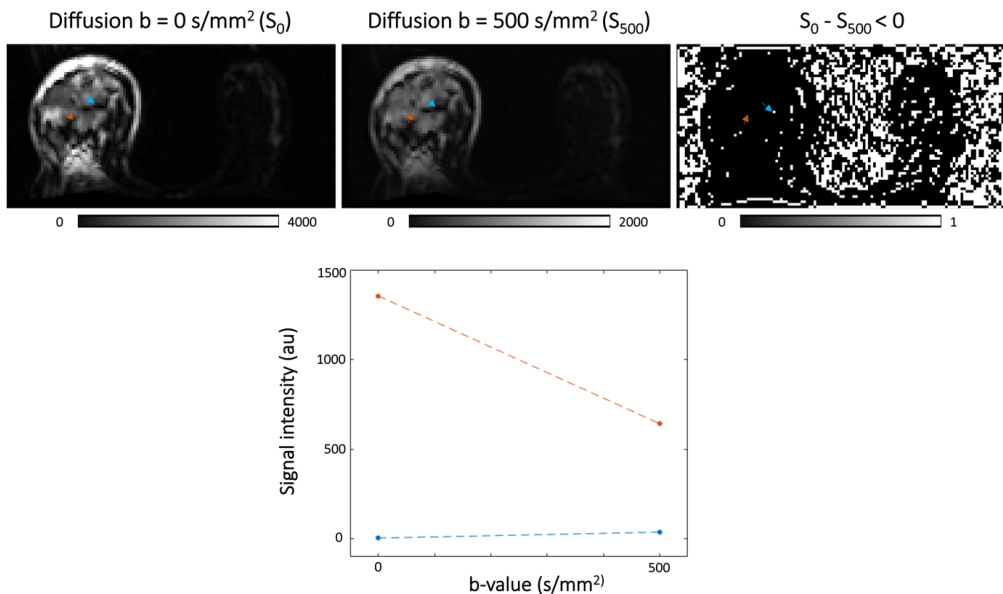


Figure 19. Figure illustrating voxel-level signal-to-noise (SNR) issues at $b = 0 \text{ s/mm}^2$ (S_0) and at $b = 500 \text{ s/mm}^2$ (S_{500}). A signal decay across b -values is biophysically expected for diffusion data (red arrow and graph). In cases with poor SNR, the signal at S_0 is zero or close to zero and $S_0 - S_{500} < 0$ (blue arrow and graph), which will lead to nonsensical apparent diffusion coefficient (ADC) map calculation. *Courtesy of S. Loubrie.*

6.15 Limitations

There were some limitations to the work carried out in this thesis. For paper I, our GMM-PET methodology depended on some simple user input for the selection of the initial tumor-containing region which, if performed poorly, might introduce errors as increased tracer uptake is less specific to disease than the manual DCE definition used for region placement in our study¹⁶². Further optimization to minimize or ultimately remove all user-dependency, unbiased by DCE, is needed to evaluate if PET data can act as a proxy for (manual) tumor definition using DCE. Furthermore, this work was a proof-of-concept study that demonstrates that PET/MRI fits within the existing RECIST treatment response criteria⁹⁵ framework, where tumor size reduction is assessed by the diameter of one single slice on DCE. However, this conventional size assessment is both quite limited and specific, and more extensive MRI metrics can retain much more detailed information about tumor response over time, so the comparison to RECIST is not necessarily the most appropriate endpoint. Lastly, though our results demonstrate the feasibility of GMM-PET treatment response assessment in the neoadjuvant setting, we did not explicitly measure how the novel method would impact clinical decision-making.

Given the similarities in the included patient cohorts and methodology in papers II and III, the limitations for these papers are naturally interrelated. Firstly, one limitation concerned the definition of control ROIs; although we ensured that control ROIs were verified as radiologically cancer-free, based on MRI review by expert breast radiologists at both sites, we cannot know if occult cancer may have been included in the control ROIs. In the bilateral baseline high b -value cohort 1 we further ensured cancer-free contralateral control ROIs by excluding all cases with pathology-proven contralateral cancer. However, since baseline high b -value cohort 2 was unilateral, the control ROIs were defined in the same breast as the cancer, meaning that this cohort may have been particularly prone to potential cancer influence. This also made the size of control regions dependent on the extent of cancer and thus more variable from case to case. It should also be noted that the RSI model was not fully independent of DCE since the ROIs were guided by all images in the MRI acquisition including DCE. While yielding component ADC s generalizable across sites, scanners, acquisition protocols, and patients, the biophysical meaning of signal contributions was only derived by visual inspections of images and correlating to corresponding anatomical structures and not by histopathological analysis. The detailed relationship between the three-component RSI model

and breast microstructure remains to be studied, as it has been for the bi-exponential model^{93,141}. We would also like to note that the main rationale for combining two datasets from different scanners and clinical settings was to show clinical robustness.

There were also some limitations specific to paper III. Firstly, there were some false positives on the derived RSI parameter C_1C_2 , such as the hyperintense signal from the interface between fatty and fibroglandular tissue. Secondly, it is also apparent this paper did not consider the final steps on how to generate a “lesion ROI” once positive voxels are identified by C_1C_2 , though this was partly addressed in paper IV as the “RSI classifier”. Also, we do not know how C_1C_2 performs in discriminating between benign and malignant lesions. All these issues illustrate that further development of the three-component RSI breast model is warranted, and is an area of interest for future improvement that could extend the use of the method. Additionally, detection performance is commonly evaluated at the lesion level. The voxel-wise false positive rate, FPR_{80} , that was used as a performance measure in this study, does not give an absolute measure comparable to other literature. However, all voxels in the entire image are used in breast cancer examination, and therefore we argue that such a measure is useful from a radiologist’s perspective.

There were some limitations for paper IV. First, the sample size for this longitudinal study of serial MRI is not large. There were 27 patients included, where 17 had all four scans in the study protocol; validation in a larger cohort would be a necessary extension of this work to confirm and validate the results of the method in longitudinal data. In addition, the RSI classifier was automatic except for the definition of cancer for the pre-treatment ROI, which was propagated to other time points through registration, and ideally, this would be made part of the automated process. However, tumors that receive NAC are generally large tumors (> 4 cm) and are easy to detect on pre-treatment MRI scans, while the time-consuming step of delineating tumors in post-treatment scans is automatic. The results warrant replication in independent samples. Another element is the definition of pCR, where we allowed for remaining DCIS in our definition. We argue that from an oncologist’s point of view, this definition can be justified since there is no difference in disease-free survival between patients with residual DCIS compared to patients with no residual invasive or in situ disease¹⁶³. Here, the focus is on the change in tumor size through the course of disease. However, from a surgeon’s perspective, the extent of all tumor tissue post-therapy, including DCIS, is important to assess to achieve the goal of free resection margin when performing breast-conserving

surgery. This might warrant separate strategies for early and late-phase response to neoadjuvant therapy (Figure 20). Moreover, we did not correct for overall differences in signal intensity for the RSI classifier across time points. This is an area of interest for future method development. Lastly, limitations of the ADC methodology applied in our study may have underestimated the prediction performance in the primary analysis. This may have given RSI an advantage compared to ADC, which may have inflated the difference, as discussed in detail above.

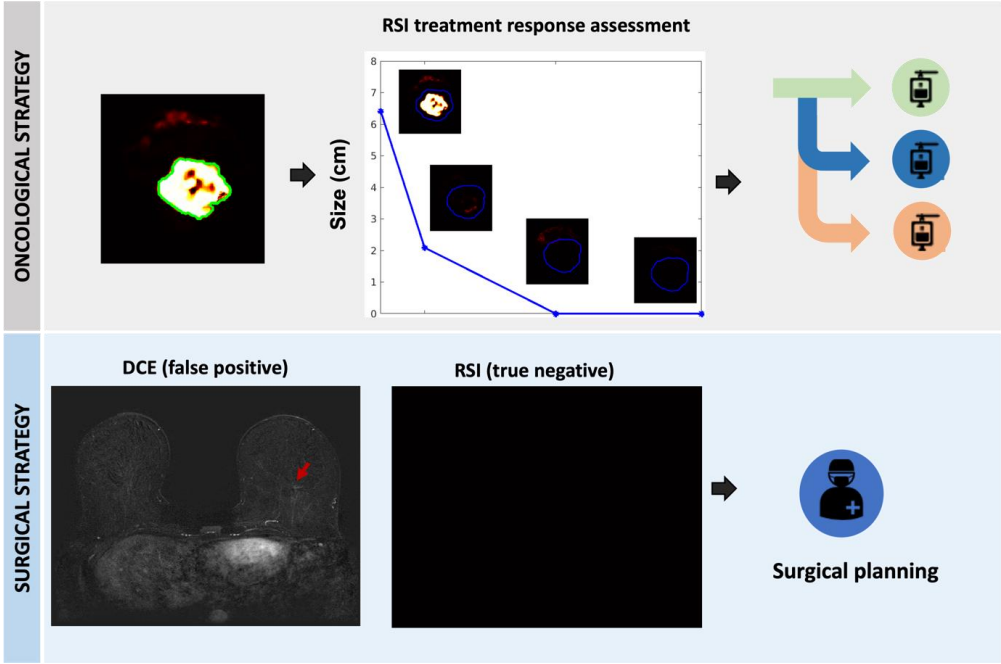


Figure 20. Separate strategies for assessment of neoadjuvant therapy for oncological and surgical intervention, given for a patient with invasive carcinoma of no special type (NST) experiencing complete pathological response (pCR) post-therapy, including no remaining ductal carcinoma in situ (DCIS). Oncological strategy: First, the tumor must be defined at pre-therapy. Treatment response may be assessed automatically through neoadjuvant therapy by the Restriction Spectrum Imaging (RSI) classifier. This may give real-time information on *in vivo* treatment efficacy which may guide clinical decision-making. Surgical strategy: Together with imaging gold-standard dynamic contrast-enhanced imaging (DCE), RSI may help aid for assessment of residual tumor post-therapy. RSI has high specificity and may compliment DCE, especially in cases where DCE represents false positive cases. This may help guide surgical planning. However, the RSI classifier is not optimized for the assessment of DCIS.

Lastly, technical limitations such as poor image quality and low spatial resolution have hindered widespread use of DWI and are relevant for all papers in this thesis. This is illustrated

by a recent multi-center study that excluded 30 % of DWI data were excluded after quality control ¹⁶⁰. While DCE has excellent spatial resolution, it is limited in standard DWI. Improvement of spatial resolution is therefore important for DWI to act as a reliable diagnostic tool. There are several multi-shot strategies available to improve resolution such as multiplexed sensitivity-encoding (MUSE) ¹⁶⁴, and readout-segmented EPI ¹⁶⁵. With a DWI resolution of $2.5 \times 2.5 \times 5.0 \text{ mm}^3$ and $2.0 \times 2.0 \times 2.5 \text{ mm}^3$ in the studies in this thesis both RSI and conventional ADC will likely miss small malignant lesions ($\leq 12 \text{ mm}$ in size), which is a well-known limitation for breast DWI ¹⁶⁵⁻¹⁶⁷. The patient cohorts in paper II–III were heterogeneous, with a large range of tumor volumes (mean = 10.6 cm^3 , range = $0.2\text{--}105.9 \text{ cm}^3$), not reflective of the typical patient pool in the screening or surveillance setting that normally have smaller lesions. Thus, the promising discriminatory results of these papers are important for the feasibility of large-scale studies for validation in routine breast cancer detection in a real-world screening population (including healthy controls), which was not performed as part of this thesis.

Moreover, one major image quality issue of DWI is B_0 inhomogeneities in EPI acquisitions which can cause warping. There are several technical advances to overcome this. Reduced field of view (FOV) reduces EPI readout time, thus limiting spin dephasing that causes B_0 inhomogeneities. While reduced FOV corrects for distortion prospectively, retrospective approaches are also possible. One such approach is reverse polarity gradient (RPG) ¹¹⁰ where an additional diffusion volume is acquired for the opposite phase encoding (PE) direction to leverage the symmetry of distortions. This method has been applied across several body sites ^{168,169} including breast ^{170,171}. Both reduced FOV and RPG have been applied for several datasets in this thesis to limit distortion. More advanced DWI acquisition and post-processing techniques may improve image quality and sensitivity in cancer detection to a sufficient standard.

6.16 Future implications of hybrid PET/MRI and the three-component RSI model

Over the past years, there has been an increased interest in radiological tools for breast cancer detection and follow-up without the use of administering MRI contrast agents⁴⁸. Avoiding the use of Gadolinium contrast is beneficial to decrease both scan time and cost. Contrast-free MRI is relevant both for the screening and the neoadjuvant treatment setting. Both the DWI-based RSI acquisition and post-processing and PET/MRI technology, neither requiring Gadolinium contrast, are readily available and thus implementable for clinical application.

In paper I, we exploit the major advantage of PET/MRI systems, where simultaneously acquired PET and MR data gives intrinsic registration of multi-modal data with voxel-level correspondence, without additional registration processes that generally involve user input or additional processing¹⁷². Benefits of a data-driven, semi-automated GMM-PET approach include faster segmentation processes and thus reduced radiologist workload, and reduced interobserver variability¹⁷³. However, to entirely eliminate manual input for clinical use¹⁷⁴, automated initialization of GMM-PET should be further explored and optimized.

There are growing public concerns regarding the unknown long-term health effects from the Gadolinium accumulation in the brain after repeated DCE scans¹⁷⁵. This is especially relevant in the high-risk breast cancer screening population where young and asymptomatic women receive annual MRIs including DCE from the age of 25. Though the risk-benefit for women with a 20 % or greater lifetime risk of breast cancer favors the use of DCE¹⁷⁵, we argue that precautionary measures are warranted.

¹⁸F-FDG-PET/MRI can also be considered in the screening setting. PET/MRI has proven useful for screening of (for example) marrow infiltrative malignancies such as leukemia or lymphoma¹⁷⁶. However, PET/MRI requires extensive patient preparation (including fasting, antidiabetic medication restrictions, etc.), as well as high costs, and as its core method of operation requires application of a radioactive tracer, which ultimately limits its use as a practical screening tool. In addition, PET/MRI infrastructure is limited; in Norway, PET/MRI machines are only located in major cities. Considering all these factors, PET/MRI is likely not a cost-effective alternative that can be implemented on a broad scale for screening purposes.

In contrast to the screening setting, PET/MRI may have a more prominent role in the neoadjuvant treatment response assessment setting. While the analysis in this study did not consider patient response and the potential influence of clinical decision-making, our patient cohort provided a variety of treatments and responses in which to test the GMM-PET methodology, including cases where response included an almost total loss of detectable disease. Results from a meta-analysis of 13 studies with a head-to-head comparison of PET/CT and DCE showed that PET/CT had higher sensitivity and DCE had higher specificity in predicting residual tumor after neoadjuvant therapy ¹⁷⁷. Though this study investigated PET/CT and not PET alone, it illustrates that the modalities may have complementary properties which may benefit from being combined. This has been demonstrated in a study by Cho et al. where combining a set of qualitative and quantitative DCE and PET metrics yielded increased neoadjuvant treatment response prediction specificity compared to a single modality assessment ¹⁷⁸. This illustrates the potential synergistic effects of PET/MRI, which is an excellent example of improved results when combining two complementary modalities. It is likely these complementary and synergetic effects that justify the use of PET/MRI in the neoadjuvant treatment setting. However, as previously mentioned, the limited availability of PET/MRI systems and the additional cost of PET tracer, and the associated radiation dose, are also important practical considerations for implementation in clinical practice.

Moreover, the development of new targeted PET tracers beyond ¹⁸F-FDG paves the way for the increased utility of PET, PET/CT, and PET/MRI systems. Of particular interest, Gallium 68 (⁶⁸Ga)-labeled fibroblast-activation protein inhibitor (FAPI), which targets cancer-associated fibroblasts that upregulate FAPI, and has higher lesion uptake compared to reported values of PET gold standard ¹⁸F-FDG ¹⁷⁹. Another promising tracer, Fluoroestradiol F 18 (¹⁸F-FES), targets ER expressed in ER-positive breast cancer ¹⁸⁰. This holds potential for non-invasive “scan and treat” strategies for patients undergoing endocrine therapy. Such strategies are especially useful in a metastatic setting where sampling tissue biopsies may be technically difficult.

PET/MRI is not routinely used as a diagnostic imaging tool for breast cancer, but has demonstrated increased clinical utility compared to PET/CT and/or conventional MRI in several settings, such as breast lesions characterization by multiparametric MRI including DCE, DWI, and 3d 1H-MRSI ¹⁸¹, axillary lymph node assessment ¹⁸²⁻¹⁸⁴, and whole-body staging ^{116,185} which may be particularly useful for LABC which requires accurate TNM

staging, but this was beyond the scope of this thesis. The staging setting may be another scenario where the use of PET/MRI may be warranted to combine PET and MRI examinations that are indicated for distinct purposes. Here, MRI alone is more sensitive for T staging than PET/CT^{183,186,187} or PET alone for multifocality¹⁸², while PET/CT is known to have higher sensitivity for axillary lymph node assessment¹⁸²⁻¹⁸⁴.

Paper I used the PET/MRI data as a test-bed for multi-modal imaging and concordance of different modalities with the assumption that DWI needs a high-contrast modality, PET, to guide tumor segmentation. Simultaneously, results from paper III demonstrated that DWI, when acquired at higher b -value ranges and fitted using a model developed on all breast tissues, is excellent at discriminating cancer from surrounding healthy breast tissues through the RSI parameter C_1C_2 . A future area of interest is therefore to investigate concordance in segmentations between GMM-PET, manual DCE, and the derived RSI parameter C_1C_2 .

In paper II we determined the best model fit for the signal from all voxels for cancer and control ROIs from two sites simultaneously. The resulting three-component RSI model and corresponding component ADC s are, theoretically, generalizable across sites, scanners, and acquisition protocols, which is a known challenge for conventional DWI⁴⁸ and an essential criterion for the development of effective imaging biomarkers for clinical use. The clinical feasibility of the three-component RSI model was demonstrated by the very high discriminatory performance of the derived RSI parameter C_1C_2 (paper III). The relatively simple computational demand needed to derive the C_1C_2 parameter does not impede its inclusion in the BI-RADS classification system, which is known to have variable interobserver variability^{54,55} in both assessments of lesions and breast composition and is dependent on DCE. In both cases, alternative strategies for breast lesion segmentation and concurrent classification have the potential to augment, or fundamentally change the role of MRI in breast cancer patient management, and strongly argue for their place in further research.

In a recent review by Amornsiripanitch et al.¹⁸⁸, the authors conclude that contrast-free MRI with DWI shows promising sensitivity and specificity based on several recent blinded reader studies. In general, the readers in the studies visually evaluated a contrast-free MRI, typically consisting of T1- and T2 sequences and DWI images including ADC maps and raw b -value images (maximum b -value ranging from 600 to 1000 s/mm^2), for the presence of cancer. The studies mimicked a true screening setting by also including healthy controls or asymptomatic

patients. Though promising results, in the reader studies directly comparing conventional DWI to DCE for detection of cancer, DWI had lower sensitivity than DCE¹⁸⁹⁻¹⁹¹. One contributing factor is likely DWI's reduced performance for small lesions (≤ 12 mm in size)¹⁶⁵⁻¹⁶⁷ which may be due to technical limitations of DWI as discussed previously.

The RSI model may play a role in the setting of contrast-free MRI for screening of women with high risk for breast cancer as an alternative to DCE. Though not directly comparable to the blinded contrast-free MRI reader studies from Amornsiripanitch et al.¹⁸⁸, the C_1C_2 parameter of the three-component RSI model had a higher discriminatory performance than both *ADC* maps and raw *b*-value images (maximum *b*-value ranging from 3000 to 4000 s/mm²) in our studies. Discriminatory performance is indicative of lesion visibility superimposed from surrounding healthy tissue for radiologists, and thus we argue that the RSI model may improve DWI in contrast-free MRI. Another potential use could be as a first screening tool to detect lesions specific for pathology for all women in the screening group. The goal of the primary scan would be to select patients with suspicious findings for a follow-up full MRI including DCE, rather than screening all patients with DCE primarily. This might decrease the number of DCE scans and consequently the costs and potential health risks that follow repeated DCE scans. However, though RSI acquisition and post-processing utilize methods to correct for distortions, RSI faces the same technical limitations as conventional DWI and there is currently no data supporting that RSI will improve performance in small lesions.

Contrast-free MRI may also serve as an alternative to or as an addition to routine mammography screening of the general population (women with low to moderate risk for breast cancer) that receive annual mammography (from the age of 40 to 50 depending on the country)^{41 21 43 42}. High costs, as well as incapability and lengthy scan time of DCE, limits widespread use in this large group of women. Recent studies^{191,192} have shown that contrast-free MRI including DWI provides higher sensitivity than mammography for the detection of breast cancer and improved sensitivity when combining both modalities¹⁹². The RSI model may play a role in contrast-free screening also in this group. However, studies designed to evaluate RSI in screening populations are needed before clinical use of RSI-based contrast-free screening can be advocated.

In the discussion of MRI scan duration, it should be noted that while conventional DCE has lengthy scan times, there is a large body of work supporting abbreviated DCE protocols having

similar diagnostic qualities as conventional DCE ¹⁹³. A recent randomized screening trial including 1444 women with dense breasts found that 7 additional invasive cancers per 1000 women were detected with abbreviated DCE compared to digital breast tomosynthesis ¹⁹⁴. The suggested protocols may substantially decrease scan times, either as part of full diagnostic protocols including conventional T2 and STIR (10 min) ¹⁹⁵ or stripped down to only pre-contrast T1 and the first post-contrast T1 series (3 min) ¹⁹⁶. In comparison, a standard clinical protocol with full DCE, T1, and T2 takes approximately 17 minutes ¹⁹⁶, 20 min including conventional DWI. Using the baseline high *b*-value MRI cohort 2 as an example cohort, the RSI scan time including *b*-values = 0, 200, 600, 1200, 1800, 2400, and 3000 s/mm² was approximately 8 minutes, equivalent to conventional DCE. However, it should be noted that this is an excessive research protocol with six non-zero *b*-values, while RSI only requires three non-zero *b*-values. Thus, there is a large potential for optimized *b*-value protocols with improved scan time efficiency. Also, it should be noted that DWI often requires additional anatomical images such as T2. Thus, contrast-free DWI with anatomical images will likely reduce scan times compared to a full diagnostic protocol including conventional DCE, but not compared to abbreviated DCE that is currently not a part of the standard clinical protocol.

Paper IV suggests that the three-component RSI model also has potential value in longitudinal response evaluation. Specifically, we have generated a classifier (RSI classifier) based on the $C_{1,3}$ and $C_{2,3}$ parameters of the three-component RSI model that seems to detect early response to treatment, with significant changes detected after only three weeks of neoadjuvant breast cancer therapy. This is important for clinical decision-making when creating and optimizing tailored treatment regimens. This also means that the RSI classifier yields valuable information on *in vivo* treatment efficacy. In the later phase of treatment, the RSI classifier showed nearly the same accuracy as manual DCE with non-significantly better specificity. The classifier uses elastic image registration to allow propagation of a single manual ROI before being analyzed with the RSI model, potentially relieving radiologists' workload. The RSI classifier signals a new way of utilizing DWI in the breast. As other models (ADC, DKI, IVIM) use calculated metrics from ROIs, RSI can be used to quantify tumor size. This is attributed to the very good discrimination between tumors and healthy tissue. The potential for diffusion imaging as a compliment or alternative to contrast MRI is large. Contrast-free MRI in the neoadjuvant setting could be advantageous to allow for more frequent monitoring, especially in the early-treatment stage, in addition to potentially being time- and cost-saving.

The three-component RSI model may be useful for oncological application in other body sites, particularly sites prone to fatty tissue. The highly promising diagnostic properties of this advanced DWI classifier warrants large-scale studies for validation in routine breast cancer detection and follow-up in comparison to DCE.

After scientific validation of the three-component RSI model in larger cohorts, the MRI acquisition protocol and post-processing are ready for clinical implementation. The RSI model may be suitable for implementation in current breast MRI protocols as a post-processing stream on clinical MR scanners or as functionality available in imaging analysis software packages. In the longitudinal setting, the RSI classifier uses an effective rapid longitudinal registration¹¹⁹ incorporating the pre-treatment MRI scan and requires only a small amount of user input. These factors are important for the implementation of RSI in standard-of-care breast MRI, and also in the treatment follow-up setting.

7. Conclusion

The potential implications of the current findings in relation to improved imaging technology and analysis in breast cancer are large, and the results from this thesis demonstrate that PET/MRI and advanced DWI models are tools to investigate basic biophysical characteristics of breast cancer such as increased metabolism (PET) and decreased diffusion (DWI), without additional scan time.

This thesis shows that PET/MRI, using a semi-automated GMM segmentation strategy, provides basic treatment response metrics that can replicate DWI results derived from the manual definition of ROIs on DCE (paper I), which is the current gold standard in any breast cancer evaluation setting. This was performed in a neoadjuvant treatment setting. This proof-of-concept study illustrates the benefits of the PET/MRI methodology for a broader assessment of morphological and metabolic features and has the potential to guide clinical decision-making.

Moreover, the application of an advanced DWI multi-component model resulted in an optimized three-component RSI model with fixed ADC s (paper II). The model decomposes the diffusion signal into meaningful biophysical components and is developed using image voxels in both cancer and healthy breast tissues, and is conducted across patients, sites, scanners, and acquisition protocols.

The ability of the optimized three-component RSI model (paper II) to discriminate between breast cancer and healthy breast tissues was evaluated (paper III). The derived parameter C_1C_2 had a high discriminatory performance between cancer and healthy breast tissue. The highly promising discriminatory performance is applicable for lesion detection and segmentation, effectively suppressing background breast tissue and potentially reducing the need for pre-identified lesions required by conventional DWI analysis, thus serving as an alternative to segmentation using DCE.

Finally, the ability of the three-component RSI model to assess neoadjuvant treatment response was evaluated in a longitudinal setting (Paper IV). The established automatic quantification classifier (RSI classifier) performed reasonably well compared to gold-standard DCE measures for the detection of treatment response. In addition, the RSI classifier showed potential for

detection of response after only three weeks of neoadjuvant breast cancer therapy. The RSI classifier may also complement DCE for assessing residual tumor post-therapy.

Overall, the multimodal imaging-derived biomarkers investigated in this thesis may help to improve early detection and personalized treatment of breast cancer, with beneficial personal, health care, and societal impact.

8. References

1. Sung H, Ferlay J, Siegel RL, et al: Global Cancer Statistics 2020: GLOBOCAN Estimates of Incidence and Mortality Worldwide for 36 Cancers in 185 Countries. *CA Cancer J Clin* 71:209-249, 2021
2. Cancer Registry of Norway: Cancer in Norway 2020 - Cancer Incidence, mortality, survival and prevalence in Norway Oslo, Norway, 2020
3. Kuerer BHM, Newman LA, Smith TL, et al: Clinical Course of Breast Cancer Patients With Complete Pathologic Primary Tumor and Axillary Lymph Node Response to Doxorubicin - Based Neoadjuvant Chemotherapy. *Journal of clinical Oncology* 17:460-469, 2017
4. Sardanelli F, Boetes C, Borisch B, et al: Magnetic resonance imaging of the breast : Recommendations from the EUSOMA working group. 6, 2010
5. Plecha DM, Faulhaber P: PET/MRI of the breast. *Eur J Radiol* 94:A26-a34, 2017
6. Lehman CD, Blume JD, Weatherall P, et al: Screening women at high risk for breast cancer with mammography and magnetic resonance imaging. *Cancer* 103:1898-905, 2005
7. Kuhl CK, Schrading S, Leutner CC, et al: Mammography, breast ultrasound, and magnetic resonance imaging for surveillance of women at high familial risk for breast cancer. *J Clin Oncol* 23:8469-76, 2005
8. Kriege M, Brekelmans CTM, Boetes C, et al: Efficacy of MRI and mammography for breast-cancer screening in women with a familial or genetic predisposition. *The New England journal of medicine* 351:427-437, 2004
9. Leach MO, Boggis CR, Dixon AK, et al: Screening with magnetic resonance imaging and mammography of a UK population at high familial risk of breast cancer: a prospective multicentre cohort study (MARIBS). *Lancet* 365:1769-78, 2005
10. Saadatmand S, Geuzinge HA, Rutgers EJT, et al: MRI versus mammography for breast cancer screening in women with familial risk (FaMRIsc): a multicentre, randomised, controlled trial. *Lancet Oncol* 20:1136-1147, 2019
11. Peters NH, Borel Rinkes IH, Zuithoff NP, et al: Meta-analysis of MR imaging in the diagnosis of breast lesions. *Radiology* 246:116-24, 2008
12. Gulani V, Calamante F, Shellock FG, et al: Gadolinium deposition in the brain: summary of evidence and recommendations. *Lancet Neurol* 16:564-570, 2017
13. Guo Y, Cai Y-Q, Cai Z-L, et al: Differentiation of clinically benign and malignant breast lesions using diffusion-weighted imaging. *Journal of magnetic resonance imaging* 16:172-8, 2002
14. Leong KM, Lau P, Ramadan S: Utilisation of MR spectroscopy and diffusion weighted imaging in predicting and monitoring of breast cancer response to chemotherapy. *J Med Imaging Radiat Oncol* 59:268-77, 2015
15. Tozaki M: Characterizing Breast Lesions. *American Journal of Radiology*:840-849, 2009
16. Russo J, Russo IH: Development of the human breast. *Maturitas* 49:2-15, 2004
17. James D. Brierley MKG, Christian Wittekind: TNM Classification of Malignant Tumours (ed 8.). Oxford; Hoboken, NJ, John Wiley & Sons, 2017
18. Institute NC: SEER Training: Breast Anatomy, 2012
19. Protection ICoR: ICRP Publication 23, Reference Man: Anatomical, Physiological, and Metabolic Characteristics, 1975

20. Brisken C, O'Malley B: Hormone action in the mammary gland. *Cold Spring Harb Perspect Biol* 2:a003178, 2010
21. Nasjonalt handlingsprogram med retningslinjer for diagnostikk, behandling og oppfølging av pasienter med brystkreft. Oslo, Helsedirektoratet, 2021
22. Dickie L. J, CH., Adams, S., Negoita, S.: *Solid Tumor Rules*. National Cancer Institute. Rockville, MD 20850, 2019
23. Perou CM, Sorlie T, Eisen MB, et al: Molecular portraits of human breast tumours. *Nature* 406:747-52, 2000
24. Cejalvo JM, Martínez de Dueñas E, Galván P, et al: Intrinsic Subtypes and Gene Expression Profiles in Primary and Metastatic Breast Cancer. *Cancer Res* 77:2213-2221, 2017
25. Sorlie T, Perou CM, Tibshirani R, et al: Gene expression patterns of breast carcinomas distinguish tumor subclasses with clinical implications. *Proc Natl Acad Sci U S A* 98:10869-74, 2001
26. Prat A, Perou CM: Deconstructing the molecular portraits of breast cancer. *Mol Oncol* 5:5-23, 2011
27. Goldhirsch A, Wood WC, Coates AS, et al: Strategies for subtypes--dealing with the diversity of breast cancer: highlights of the St. Gallen International Expert Consensus on the Primary Therapy of Early Breast Cancer 2011. *Ann Oncol* 22:1736-47, 2011
28. Amin MB, Greene FL, Edge SB, et al: The Eighth Edition AJCC Cancer Staging Manual: Continuing to build a bridge from a population-based to a more "personalized" approach to cancer staging. *CA Cancer J Clin* 67:93-99, 2017
29. Hælle T: Breast Cancer Stages: What do They Mean?, in Health E (ed): *Everyday Health*. Everyday Health, Everyday Health, 2018
30. Movik E HV, Norderhaug IN, Klemp M.: Helseøkonomisk analyse av bevacizumab+paclitaxel sammenlignet med paclitaxel alene som førstelinjebehandling ved metastatisk brystkreft, in Kunnskapssenteret (ed). <https://www.fhi.no/publ/eldre/helseokonomisk-analyse-av-bevacizumabpaclitaxel-sammenlignet-med-paclitaxel/>, 2009
31. Krefregisteret: Resultater og forbedringstiltak fra Nasjonalt kvalitetsregister for brystkreft, 2020
32. Makhoul I, Kiwan E: Neoadjuvant systemic treatment of breast cancer. *J Surg Oncol* 103:348-57, 2011
33. Miller E, Lee HJ, Lulla A, et al: Current treatment of early breast cancer: adjuvant and neoadjuvant therapy. *F1000Res* 3:198, 2014
34. Cortazar P, Zhang L, Untch M, et al: Pathological complete response and long-term clinical benefit in breast cancer: the CTNeoBC pooled analysis. *Lancet* 384:164-72, 2014
35. Lønning PE, Knappskog S: Mapping genetic alterations causing chemoresistance in cancer: identifying the roads by tracking the drivers. *Oncogene* 32:5315-5330, 2013
36. Catherine Westbrook CKR, John Talbot: *MRI in practice* (ed 4th), Wiley-Blackwell, 2011
37. Nketiah GA: *Magnetic Resonance Imaging for Improved Prostate Cancer Diagnosis*. Doctoral thesis, Department of Circulation and Medical Imaging. Trondheim, Norwegian University of Science and Technology (NTNU), 2018
38. Roman M, Hubbard RA, Sebuodegard S, et al: The Cumulative Risk of False-Positive Results in the Norwegian Breast Cancer Screening Program : Updated Results. *European Journal of Radiology*, 2013

39. Kramer BS, Welch HG, Prorok PC, et al: Breast-Cancer Tumor Size, Overdiagnosis, and Mammography Screening Effectiveness. *The New England journal of medicine* 375:1438-1447, 2016
40. Sung JS, Stampler S, Brooks J, et al: Breast Cancers Detected at Screening MR Imaging and Mammography in Patients at High Risk: Method of Detection Reflects Tumor Histopathologic Results. *Radiology* 280:716-22, 2016
41. Organization WH: WHO Position Paper on Mammography Screening. Geneva, 2014
42. Schünemann HJ, Lerda D, Quinn C, et al: Breast Cancer Screening and Diagnosis: A Synopsis of the European Breast Guidelines. *Ann Intern Med* 172:46-56, 2020
43. Monticciolo DL, Malak SF, Friedewald SM, et al: Breast Cancer Screening Recommendations Inclusive of All Women at Average Risk: Update from the ACR and Society of Breast Imaging. *J Am Coll Radiol* 18:1280-1288, 2021
44. Kuhl CK: Current status of breast MR imaging. Part 2. Clinical applications. *Radiology* 244:672-91, 2007
45. Sardanelli F, Podo F, D'Agnolo G, et al: Multicenter comparative multimodality surveillance of women at genetic-familial high risk for breast cancer (HIBCRIT study): interim results. *Radiology* 242:698-715, 2007
46. Radiology ACo: ACR PRACTICE PARAMETER FOR THE PERFORMANCE OF CONTRAST-ENHANCED MAGNETIC RESONANCE IMAGING (MRI) OF THE BREAST, 2018
47. Croshaw R, Shapiro-Wright H, Svensson E, et al: Accuracy of clinical examination, digital mammogram, ultrasound, and MRI in determining postneoadjuvant pathologic tumor response in operable breast cancer patients. *Ann Surg Oncol* 18:3160-3, 2011
48. Baltzer P, Mann RM, Iima M, et al: Diffusion-weighted imaging of the breast—a consensus and mission statement from the EUSOBI International Breast Diffusion-Weighted Imaging working group. *European radiology* 30:1436-1450, 2020
49. Morris EA CC, Lee CH, : ACR BI-RADS® Magnetic Resonance Imaging. Reston, VA, American College of Radiology, 2013
50. American College of Radiology: Breast density: breast cancer screening. https://www.acr.org/-/media/ACR/Files/Breast-Imaging-Resources/Breast-Density-bro_ACR_SBI.pdf, Accessed March 20, 2020
51. Giess CS, Raza S, Birdwell RL: Patterns of nonmasslike enhancement at screening breast MR imaging of high-risk premenopausal women. *Radiographics* 33:1343-60, 2013
52. Shimauchi A, Jansen SA, Abe H, et al: Breast cancers not detected at MRI: review of false-negative lesions. *AJR Am J Roentgenol* 194:1674-9, 2010
53. Agrawal G, Su M-Y, Nalcioglu O, et al: Significance of breast lesion descriptors in the ACR BI-RADS MRI lexicon. *Cancer* 115:1363-1380, 2009
54. Grimm LJ, Anderson AL, Baker JA, et al: Interobserver Variability Between Breast Imagers Using the Fifth Edition of the BI-RADS MRI Lexicon. *American Journal of Roentgenology* 204:1120-1124, 2015
55. El Khoury M, Lalonde L, David J, et al: Breast imaging reporting and data system (BI-RADS) lexicon for breast MRI: Interobserver variability in the description and assignment of BI-RADS category. *European Journal of Radiology* 84:71-76, 2015
56. (RSNA) TRSoNA: RSNA Statement on Gadolinium-Based MR Contrast Agents Updated 5/6/2019, 2019
57. Schnall MD, Blume J, Bluemke DA, et al: Diagnostic architectural and dynamic features at breast MR imaging: multicenter study. *Radiology* 238:42-53, 2006

58. White NS, McDonald C, Farid N, et al: Diffusion-weighted imaging in cancer: physical foundations and applications of restriction spectrum imaging. *Cancer Res* 74:4638-52, 2014
59. Messina C, Bignone R, Bruno A, et al: Diffusion-Weighted Imaging in Oncology: An Update. *Cancers (Basel)* 12, 2020
60. Stejskal EO, Tanner JE: Spin Diffusion Measurements: Spin Echoes in the Presence of a Time-Dependent Field Gradient. *The Journal of Chemical Physics* 42:288-292, 1965
61. Jerome NP, Caroli A, Ljimani A: Renal Diffusion-Weighted Imaging (DWI) for Apparent Diffusion Coefficient (ADC), Intravoxel Incoherent Motion (IVIM), and Diffusion Tensor Imaging (DTI): Basic Concepts. *Methods Mol Biol* 2216:187-204, 2021
62. Provenzale JM, Engelter ST, Petrella JR, et al: Use of MR exponential diffusion-weighted images to eradicate T2 "shine-through" effect. *AJR Am J Roentgenol* 172:537-9, 1999
63. Rakow-Penner RA, White NS, Parsons JK, et al: Novel technique for characterizing prostate cancer utilizing MRI restriction spectrum imaging: proof of principle and initial clinical experience with extraprostatic extension. *Prostate Cancer Prostatic Dis* 18:81-5, 2015
64. White NS, McDonald CR, Farid N, et al: Diffusion-weighted imaging in cancer: Physical foundations and applications of restriction spectrum imaging. *Cancer Research* 74:4638-4652, 2014
65. Panagiotaki E, Chan RW, Dikaios N, et al: Microstructural characterization of normal and malignant human prostate tissue with vascular, extracellular, and restricted diffusion for cytometry in tumours magnetic resonance imaging. *Invest Radiol* 50:218-27, 2015
66. Karunamuni RA, Kuperman J, Seibert TM, et al: Relationship between kurtosis and bi-exponential characterization of high b-value diffusion-weighted imaging: application to prostate cancer. *Acta Radiologica* 59:1523-1529, 2018
67. Chatterjee A, Bourne RM, Wang S, et al: Diagnosis of Prostate Cancer with Noninvasive Estimation of Prostate Tissue Composition by Using Hybrid Multidimensional MR Imaging: A Feasibility Study. *Radiology* 287:864-873, 2018
68. Le Bihan D, Breton E, Lallemand D, et al: MR imaging of intravoxel incoherent motions: application to diffusion and perfusion in neurologic disorders. *Radiology* 161:401-7, 1986
69. Jensen JH, Helpert JA, Ramani A, et al: Diffusional kurtosis imaging: the quantification of non-gaussian water diffusion by means of magnetic resonance imaging. *Magn Reson Med* 53:1432-40, 2005
70. White NS, McDonald CR, Farid N, et al: Improved conspicuity and delineation of high-grade primary and metastatic brain tumors using "restriction spectrum imaging": quantitative comparison with high B-value DWI and ADC. *AJNR Am J Neuroradiol* 34:958-64, s1, 2013
71. White NS, Leergaard TB, D'Arceuil H, et al: Probing tissue microstructure with restriction spectrum imaging: Histological and theoretical validation. *Hum Brain Mapp* 34:327-46, 2013
72. White N, Dale, Anders M. (La Jolla, CA, US): MEASURING BIOLOGICAL TISSUE PARAMETERS USING DIFFUSION MAGNETIC RESONANCE IMAGING. United States, THE REGENTS OF THE UNIVERSITY OF CALIFORNIA (Oakland, CA, US), 2012

73. McCammack KC, Schenker-Ahmed NM, White NS, et al: Restriction spectrum imaging improves MRI-based prostate cancer detection. *Abdom Radiol (NY)* 41:946-53, 2016
74. Geith T, Biffar A, Schmidt G, et al: Physiological Background of Differences in Quantitative Diffusion-Weighted Magnetic Resonance Imaging Between Acute Malignant and Benign Vertebral Body Fractures: Correlation of Apparent Diffusion Coefficient With Quantitative Perfusion Magnetic Resonance Imaging Using the 2-Compartment Exchange Model. *J Comput Assist Tomogr* 39:643-8, 2015
75. Liss MA, White NS, Parsons JK, et al: MRI-Derived Restriction Spectrum Imaging Cellularity Index is Associated with High Grade Prostate Cancer on Radical Prostatectomy Specimens. *Front Oncol* 5:30, 2015
76. Conlin CC, Feng CH, Rodriguez-Soto AE, et al: Improved Characterization of Diffusion in Normal and Cancerous Prostate Tissue Through Optimization of Multicompartmental Signal Models. *J Magn Reson Imaging* 53:628-639, 2021
77. Partridge SC, Singer L, Sun R, et al: Diffusion-weighted MRI: influence of intravoxel fat signal and breast density on breast tumor conspicuity and apparent diffusion coefficient measurements. *Magn Reson Imaging* 29:1215-21, 2011
78. Baron P, Dorrius MD, Kappert P, et al: Diffusion-weighted imaging of normal fibroglandular breast tissue: influence of microperfusion and fat suppression technique on the apparent diffusion coefficient. *NMR Biomed* 23:399-405, 2010
79. Chen X, Li WL, Zhang YL, et al: Meta-analysis of quantitative diffusion-weighted MR imaging in the differential diagnosis of breast lesions. *BMC Cancer* 10:693, 2010
80. Nogueira L, Brandao S, Matos E, et al: Application of the diffusion kurtosis model for the study of breast lesions. *Eur Radiol* 24:1197-203, 2014
81. Wu D, Li G, Zhang J, et al: Characterization of breast tumors using diffusion kurtosis imaging (DKI). *PLoS One* 9:e113240, 2014
82. Christou A, Ghiatas A, Priovolos D, et al: Accuracy of diffusion kurtosis imaging in characterization of breast lesions. *Br J Radiol* 90:20160873, 2017
83. Vidic I, Egnell L, Jerome NP, et al: Modeling the diffusion-weighted imaging signal for breast lesions in the $b = 200$ to 3000 s/mm² range: quality of fit and classification accuracy for different representations. *Magn Reson Med*, 2020
84. Luo J, Hippe DS, Rahbar H, et al: Diffusion tensor imaging for characterizing tumor microstructure and improving diagnostic performance on breast MRI: a prospective observational study. *Breast Cancer Res* 21:102, 2019
85. Iima M, Kataoka M, Kanao S, et al: Intravoxel Incoherent Motion and Quantitative Non-Gaussian Diffusion MR Imaging: Evaluation of the Diagnostic and Prognostic Value of Several Markers of Malignant and Benign Breast Lesions. *Radiology* 287:432-441, 2018
86. Clauser P, Krug B, Bickel H, et al: Diffusion-weighted Imaging Allows for Downgrading MR BI-RADS 4 Lesions in Contrast-enhanced MRI of the Breast to Avoid Unnecessary Biopsy. *Clin Cancer Res* 27:1941-1948, 2021
87. Bickel H, Pinker K, Polanec S, et al: Diffusion-weighted imaging of breast lesions: Region-of-interest placement and different ADC parameters influence apparent diffusion coefficient values. *Eur Radiol* 27:1883-1892, 2017
88. Kim TH, Yoon JK, Kang DK, et al: Correlation Between F-18 Fluorodeoxyglucose Positron Emission Tomography Metabolic Parameters and Dynamic Contrast-Enhanced MRI-Derived Perfusion Data in Patients with Invasive Ductal Breast Carcinoma. *Ann Surg Oncol* 22:3866-72, 2015

89. Ghosh K, Brandt KR, Reynolds C, et al: Tissue composition of mammographically dense and non-dense breast tissue. *Breast Cancer Res Treat* 131:267-75, 2012
90. Liu C, Liang C, Liu Z, et al: Intravoxel incoherent motion (IVIM) in evaluation of breast lesions: comparison with conventional DWI. *Eur J Radiol* 82:e782-9, 2013
91. Bokacheva L, Kaplan JB, Giri DD, et al: Intravoxel incoherent motion diffusion-weighted MRI at 3.0 T differentiates malignant breast lesions from benign lesions and breast parenchyma. *Journal of magnetic resonance imaging : JMRI* 40:813-823, 2014
92. Jin YN, Zhang Y, Cheng JL, et al: Monoexponential, Biexponential, and stretched-exponential models using diffusion-weighted imaging: A quantitative differentiation of breast lesions at 3.0T. *J Magn Reson Imaging* 50:1461-1467, 2019
93. Egnell L, Vidic I, Jerome NP, et al: Stromal Collagen Content in Breast Tumors Correlates With In Vivo Diffusion-Weighted Imaging: A Comparison of Multi b-Value DWI With Histologic Specimen From Benign and Malignant Breast Lesions. *J Magn Reson Imaging*, 2019
94. Thomas E, Holmes FA, Smith TL, et al: The use of alternate, non-cross-resistant adjuvant chemotherapy on the basis of pathologic response to a neoadjuvant doxorubicin-based regimen in women with operable breast cancer: long-term results from a prospective randomized trial. *J Clin Oncol* 22:2294-302, 2004
95. Eisenhauer EA, Therasse P, Bogaerts J, et al: New response evaluation criteria in solid tumours: revised RECIST guideline (version 1.1). *Eur J Cancer* 45:228-47, 2009
96. Gu YL, Pan SM, Ren J, et al: Role of Magnetic Resonance Imaging in Detection of Pathologic Complete Remission in Breast Cancer Patients Treated With Neoadjuvant Chemotherapy: A Meta-analysis. *Clin Breast Cancer* 17:245-255, 2017
97. Hylton NM, Blume JD, Bernreuter WK, et al: Locally advanced breast cancer: MR imaging for prediction of response to neoadjuvant chemotherapy--results from ACRIN 6657/I-SPY TRIAL. *Radiology* 263:663-672, 2012
98. Pickles MD, Gibbs P, Lowry M, et al: Diffusion changes precede size reduction in neoadjuvant treatment of breast cancer. *Magn Reson Imaging* 24:843-7, 2006
99. Jensen LR, Garzon B, Heldahl MG, et al: Diffusion-weighted and dynamic contrast-enhanced MRI in evaluation of early treatment effects during neoadjuvant chemotherapy in breast cancer patients. *J Magn Reson Imaging* 34:1099-109, 2011
100. Partridge SC, Zhang Z, Newitt DC, et al: Diffusion-weighted MRI Findings Predict Pathologic Response in Neoadjuvant Treatment of Breast Cancer: The ACRIN 6698 Multicenter Trial. *Radiology* 289:618-627, 2018
101. Hope TR, White NS, Kuperman J, et al: Demonstration of Non-Gaussian Restricted Diffusion in Tumor Cells Using Diffusion Time-Dependent Diffusion-Weighted Magnetic Resonance Imaging Contrast. *Front Oncol* 6:179, 2016
102. Yamin G, Schenker-Ahmed NM, Shabaik A, et al: Voxel Level Radiologic-Pathologic Validation of Restriction Spectrum Imaging Cellularity Index with Gleason Grade in Prostate Cancer. *Clin Cancer Res* 22:2668-74, 2016
103. Daghighi S, Bahrami N, Tom WJ, et al: Restriction Spectrum Imaging Differentiates True Tumor Progression From Immune-Mediated Pseudoprogression: Case Report of a Patient With Glioblastoma. *Front Oncol* 10:24, 2020
104. Bailey DLDWTPVMNM: Positron Emission Tomography: Basic Sciences. Secaucus, NJ, Springer-Verlag, 2005
105. Hanahan D, Weinberg RA: Hallmarks of cancer: the next generation. *Cell* 144:646-74, 2011

106. Lehman CD: ACR practice parameter for the performance of contrast-enhanced magnetic resonance imaging (MRI) of the breast. Available at: https://www.acr.org/~media/ACR/Documents/PGTS/guidelines/MRI_Breast.pdf?db=web 1076:1-9, 2013
107. Nakajo M, Kajiya Y, Kaneko T, et al: FDG PET/CT and diffusion-weighted imaging for breast cancer: prognostic value of maximum standardized uptake values and apparent diffusion coefficient values of the primary lesion. *Eur J Nucl Med Mol Imaging* 37:2011-20, 2010
108. Byun BH, Noh WC, Lim I, et al: A new method for apparent diffusion coefficient measurement using sequential (18)F-FDG PET and MRI: correlation with histological grade of invasive ductal carcinoma of the breast. *Ann Nucl Med* 27:720-8, 2013
109. Kitajima K, Yamano T, Fukushima K, et al: Correlation of the SUVmax of FDG-PET and ADC values of diffusion-weighted MR imaging with pathologic prognostic factors in breast carcinoma. *Eur J Radiol* 85:943-9, 2016
110. Holland D, Kuperman JM, Dale AM: Efficient correction of inhomogeneous static magnetic field-induced distortion in Echo Planar Imaging. *Neuroimage* 50:175-83, 2010
111. Gudbjartsson H, Patz S: The Rician distribution of noisy MRI data. *Magn Reson Med* 34:910-4, 1995
112. Martinez-Moller A, Souvatzoglou M, Delso G, et al: Tissue classification as a potential approach for attenuation correction in whole-body PET/MRI: evaluation with PET/CT data. *J Nucl Med* 50:520-6, 2009
113. Andreassen MMS, Goa PE, Sjobakk TE, et al: Semi-automatic segmentation from intrinsically-registered 18F-FDG-PET/MRI for treatment response assessment in a breast cancer cohort: comparison to manual DCE-MRI. *Magma*, 2019
114. Arthur D, Vassilvitskii S: k-means++: the advantages of careful seeding. Presented at the Proceedings of the eighteenth annual ACM-SIAM symposium on Discrete algorithms, New Orleans, Louisiana, 2007
115. Geoff McLachlan DP: *Finite Mixture Models*. New York, Wiley, 2000
116. Im HJ, Bradshaw T, Solaiyappan M, et al: Current Methods to Define Metabolic Tumor Volume in Positron Emission Tomography: Which One is Better? *Nucl Med Mol Imaging* 52:5-15, 2018
117. Partridge SC, McDonald ES: Diffusion weighted magnetic resonance imaging of the breast: protocol optimization, interpretation, and clinical applications. *Magn Reson Imaging Clin N Am* 21:601-24, 2013
118. Rodriguez-Soto AE, Andreassen MMS, Conlin CC, et al: Characterization of the Diffusion Signal of Breast Tissues using Multi-exponential Models. *medRxiv:2020.04.27.20082271*, 2020
119. Tong M, Rodríguez-Soto AE, Andreassen MMS, et al: Fast Longitudinal Image REgistration (FLIRE) for Breast MRI, International Society of Magnetic Resonance Medicine Vancouver, Canada 2021
120. U.S. Food and Drug Administration (FDA) . Guidance for industry: pathological complete response in neoadjuvant treatment of high-risk early-stage breast cancer: use as an endpoint to support accelerated approval.,
121. Andreassen MMS, Tong MW, Loubrie S, et al: Restriction Spectrum Imaging with elastic image registration for automated evaluation of early response to neoadjuvant therapy in breast cancer, 2022
122. Dice LR: Measures of the Amount of Ecologic Association Between Species. *Ecology* 26:297-302, 1945

123. Nogueira L, Brandao S, Matos E, et al: Region of interest demarcation for quantification of the apparent diffusion coefficient in breast lesions and its interobserver variability. *Diagn Interv Radiol* 21:123-7, 2015
124. Chu W, Jin W, Liu D, et al: Diffusion-weighted imaging in identifying breast cancer pathological response to neoadjuvant chemotherapy: A meta-analysis. *Oncotarget* 9:7088-7100, 2018
125. Daisne JF, Duprez T, Weynand B: Tumor volume in pharyngolaryngeal squamous cell carcinoma: comparison at CT, MR imaging, and FDG PET and validation with surgical specimen. *Radiology* 233:93, 2004
126. Sridhar P, Mercier G, Tan J, et al: FDG PET metabolic tumor volume segmentation and pathologic volume of primary human solid tumors. *AJR Am J Roentgenol* 202:1114-9, 2014
127. Burger IA, Vargas HA, Apte A, et al: PET quantification with a histogram derived total activity metric: superior quantitative consistency compared to total lesion glycolysis with absolute or relative SUV thresholds in phantoms and lung cancer patients. *Nucl Med Biol* 41:410-8, 2014
128. Burger IA, Casanova R, Steiger S, et al: 18F-FDG PET/CT of Non-Small Cell Lung Carcinoma Under Neoadjuvant Chemotherapy: Background-Based Adaptive-Volume Metrics Outperform TLG and MTV in Predicting Histopathologic Response. *J Nucl Med* 57:849-54, 2016
129. Schelling M, Avril N, Nahrig J, et al: Positron emission tomography using [(18)F]Fluorodeoxyglucose for monitoring primary chemotherapy in breast cancer. *J Clin Oncol* 18:1689-95, 2000
130. Werner-Wasik M, Nelson AD, Choi W: What is the best way to contour lung tumors on PET scans? Multiobserver validation of a gradient-based method using a NSCLC digital PET phantom. *Int J Radiat Oncol Biol Phys* 82:1164, 2012
131. Muz B, de la Puente P, Azab F, et al: The role of hypoxia in cancer progression, angiogenesis, metastasis, and resistance to therapy. *Hypoxia (Auckl)* 3:83-92, 2015
132. Choi WJ, Kim HH, Cha JH, et al: Complete response on MR imaging after neoadjuvant chemotherapy in breast cancer patients: Factors of radiologic-pathologic discordance. *Eur J Radiol* 118:114-121, 2019
133. De Los Santos JF, Cantor A, Amos KD, et al: Magnetic resonance imaging as a predictor of pathologic response in patients treated with neoadjuvant systemic treatment for operable breast cancer. Translational Breast Cancer Research Consortium trial 017. *Cancer* 119:1776-83, 2013
134. McGuire KP, Toro-Burguete J, Dang H, et al: MRI staging after neoadjuvant chemotherapy for breast cancer: does tumor biology affect accuracy? *Ann Surg Oncol* 18:3149-54, 2011
135. O'Connor DJ, Davey MG, Barkley LR, et al: Differences in sensitivity to neoadjuvant chemotherapy among invasive lobular and ductal carcinoma of the breast and implications on surgery-A systematic review and meta-analysis. *Breast* 61:1-10, 2021
136. Miyake KK, Nakamoto Y, Kanao S, et al: JOURNAL CLUB: Diagnostic Value of 18F-FDG PET/CT and MRI in Predicting the Clinicopathologic Subtypes of Invasive Breast Cancer. *American Journal of Roentgenology* 203:272-279, 2014
137. Rakheja R, Chandarana H, DeMello L, et al: Correlation between standardized uptake value and apparent diffusion coefficient of neoplastic lesions evaluated with whole-body simultaneous hybrid PET/MRI. *AJR Am J Roentgenol* 201:1115-9, 2013
138. Baba S, Isoda T, Maruoka Y, et al: Diagnostic and Prognostic Value of Pretreatment SUV in 18 F-FDG/PET in Breast Cancer: Comparison with Apparent Diffusion

Coefficient from Diffusion-Weighted MR Imaging. *Journal of Nuclear Medicine* 55:736-742, 2014

139. Zhou WP, Zan XY, Hu XY, et al: Characterization of breast lesions using diffusion kurtosis model-based imaging: An initial experience. *J Xray Sci Technol* 28:157-169, 2020

140. Sigmund EE, Cho GY, Kim S, et al: Intravoxel incoherent motion imaging of tumor microenvironment in locally advanced breast cancer. *Magn Reson Med* 65:1437-47, 2011

141. Tamura T, Usui S, Murakami S, et al: Comparisons of multi b-value DWI signal analysis with pathological specimen of breast cancer. *Magnetic Resonance in Medicine* 68:890-897, 2012

142. Cho GY, Gennaro L, Sutton EJ, et al: Intravoxel incoherent motion (IVIM) histogram biomarkers for prediction of neoadjuvant treatment response in breast cancer patients. *European journal of radiology open* 4:101-107, 2017

143. Nakagawa M, Miyati T, Hayashi T, et al: [Triexponential diffusion analysis in invasive ductal carcinoma and fibroadenoma]. *Nihon Hoshasen Gijutsu Gakkai Zasshi* 70:199-205, 2014

144. Steidle G, Eibofner F, Schick F: Quantitative diffusion imaging of adipose tissue in the human lower leg at 1.5 T. *Magn Reson Med* 65:1118-24, 2011

145. Mlynarska-Bujny A, Bickelhaupt S, Laun FB, et al: Influence of residual fat signal on diffusion kurtosis MRI of suspicious mammography findings. *Scientific reports* 10:13286-13286, 2020

146. White NS, Dale AM: Distinct effects of nuclear volume fraction and cell diameter on high b-value diffusion MRI contrast in tumors. *Magn Reson Med* 72:1435-43, 2014

147. Andreassen MMS, Rodríguez-Soto AE, Conlin CC, et al: Discrimination of breast cancer from healthy breast tissue using a three-component diffusion-weighted MRI model. *Clin Cancer Res*, 2020

148. Liu L, Yin B, Geng DY, et al: Changes of T2 Relaxation Time From Neoadjuvant Chemotherapy in Breast Cancer Lesions. *Iran J Radiol* 13:e24014, 2016

149. Rakow-Penner R, Daniel B, Yu H, et al: Relaxation times of breast tissue at 1.5T and 3T measured using IDEAL. *Journal of Magnetic Resonance Imaging* 23:87-91, 2006

150. Chen Y, Panda A, Pahwa S, et al: Three-dimensional MR Fingerprinting for Quantitative Breast Imaging. *Radiology* 290:33-40, 2019

151. Tsushima Y, Takahashi-Taketomi A, Endo K: Magnetic resonance (MR) differential diagnosis of breast tumors using apparent diffusion coefficient (ADC) on 1.5-T. *J Magn Reson Imaging* 30:249-55, 2009

152. Masuda N, Lee SJ, Ohtani S, et al: Adjuvant Capecitabine for Breast Cancer after Preoperative Chemotherapy. *N Engl J Med* 376:2147-2159, 2017

153. von Minckwitz G, Huang CS, Mano MS, et al: Trastuzumab Emtansine for Residual Invasive HER2-Positive Breast Cancer. *N Engl J Med* 380:617-628, 2019

154. van der Voort Aea
Image-guided de-escalation of neo-adjuvant chemotherapy in HER2-positive breast cancer: the TRAIN-3 study (TRAIN-3). *ClinicalTrials.gov Identifier: NCT03820063*.

<https://clinicaltrials.gov/ct2/show/NCT03820063>

Date accessed: October 1, 2021

155. Ogston KN, Miller ID, Payne S, et al: A new histological grading system to assess response of breast cancers to primary chemotherapy: prognostic significance and survival. *Breast* 12:320-7, 2003

156. Almutlaq ZM, Wilson DJ, Bacon SE, et al: Evaluation of Monoexponential, Stretched-Exponential and Intravoxel Incoherent Motion MRI Diffusion Models in Early Response Monitoring to Neoadjuvant Chemotherapy in Patients With Breast Cancer-A Preliminary Study. *J Magn Reson Imaging*, 2022
157. Bedair R, Priest AN, Patterson AJ, et al: Assessment of early treatment response to neoadjuvant chemotherapy in breast cancer using non-mono-exponential diffusion models: a feasibility study comparing the baseline and mid-treatment MRI examinations. *Eur Radiol* 27:2726-2736, 2017
158. Li SP, Padhani AR, Makris A: Dynamic contrast-enhanced magnetic resonance imaging and blood oxygenation level-dependent magnetic resonance imaging for the assessment of changes in tumor biology with treatment. *J Natl Cancer Inst Monogr* 2011:103-7, 2011
159. Iima M, Partridge SC, Le Bihan D: Six DWI questions you always wanted to know but were afraid to ask: clinical relevance for breast diffusion MRI. *Eur Radiol* 30:2561-2570, 2020
160. Whisenant JG, Romanoff J, Rahbar H, et al: Factors Affecting Image Quality and Lesion Evaluability in Breast Diffusion-weighted MRI: Observations from the ECOG-ACRIN Cancer Research Group Multisite Trial (A6702). *J Breast Imaging* 3:44-56, 2021
161. Celik A: Effect of imaging parameters on the accuracy of apparent diffusion coefficient and optimization strategies. *Diagn Interv Radiol* 22:101-7, 2016
162. Adejolu M, Huo L, Rohren E, et al: False-positive lesions mimicking breast cancer on FDG PET and PET/CT. *AJR Am J Roentgenol* 198:W304-14, 2012
163. Jones RL, Lakhani SR, Ring AE, et al: Pathological complete response and residual DCIS following neoadjuvant chemotherapy for breast carcinoma. *Br J Cancer* 94:358-62, 2006
164. Hu Y, Ikeda DM, Pittman SM, et al: Multishot Diffusion-Weighted MRI of the Breast With Multiplexed Sensitivity Encoding (MUSE) and Shot Locally Low-Rank (Shot-LLR) Reconstructions. *J Magn Reson Imaging* 53:807-817, 2021
165. Yang ZL, Hu YQ, Huang J, et al: Detection and Classification of Breast Lesions With Readout-Segmented Diffusion-Weighted Imaging in a Large Chinese Cohort. *Front Oncol* 11:636471, 2021
166. Daimiel Naranjo I, Lo Gullo R, Saccarelli C, et al: Diagnostic value of diffusion-weighted imaging with synthetic b-values in breast tumors: comparison with dynamic contrast-enhanced and multiparametric MRI. *Eur Radiol* 31:356-367, 2021
167. Pinker K, Moy L, Sutton EJ, et al: Diffusion-Weighted Imaging With Apparent Diffusion Coefficient Mapping for Breast Cancer Detection as a Stand-Alone Parameter: Comparison With Dynamic Contrast-Enhanced and Multiparametric Magnetic Resonance Imaging. *Invest Radiol* 53:587-595, 2018
168. Digma LA, Feng CH, Conlin CC, et al: Correcting B(0) inhomogeneity-induced distortions in whole-body diffusion MRI of bone. *Sci Rep* 12:265, 2022
169. Rakow-Penner RA, White NS, Margolis DJA, et al: Prostate diffusion imaging with distortion correction. *Magn Reson Imaging* 33:1178-1181, 2015
170. Teruel JR, Fjøsne HE, Østlie A, et al: Inhomogeneous static magnetic field-induced distortion correction applied to diffusion weighted MRI of the breast at 3T. *Magnetic Resonance in Medicine* 74:1138-1144, 2015
171. Rodríguez-Soto AE, Fang LK, Holland D, et al: Correction of Artifacts Induced by B(0) Inhomogeneities in Breast MRI Using Reduced-Field-of-View Echo-Planar Imaging and Enhanced Reversed Polarity Gradient Method. *J Magn Reson Imaging* 53:1581-1591, 2021

172. Riola-Parada C, Garcia-Canamaque L, Perez-Duenas V, et al: Simultaneous PET/MRI vs PET/CT in oncology. A systematic review. *Rev Esp Med Nucl Imagen Mol* 35:306-12, 2016
173. Kim HR, Jung HK, Ko KH, et al: Mammography, US, and MRI for Preoperative Prediction of Extensive Intraductal Component of Invasive Breast Cancer: Interobserver Variability and Performances. *Clin Breast Cancer* 16:305-11, 2016
174. Aristophanous M, Penney BC, Martel MK, et al: A Gaussian mixture model for definition of lung tumor volumes in positron emission tomography. *Med Phys* 34:4223-35, 2007
175. Sardanelli F, Cozzi A, Trimboli RM, et al: Gadolinium Retention and Breast MRI Screening: More Harm Than Good? *AJR Am J Roentgenol* 214:324-327, 2020
176. Eichner R, Essler M, Specht K, et al: PET-MRI hybrid imaging in a rare case of B cell lymphoblastic lymphoma with musculoskeletal manifestation. *Annals of Hematology* 93:501-503, 2014
177. Li H, Yao L, Jin P, et al: MRI and PET/CT for evaluation of the pathological response to neoadjuvant chemotherapy in breast cancer: A systematic review and meta-analysis. *Breast* 40:106-115, 2018
178. Cho N, Im S-A, Cheon GJ, et al: Integrated 18F-FDG PET/MRI in breast cancer: early prediction of response to neoadjuvant chemotherapy. *European Journal of Nuclear Medicine and Molecular Imaging* 45:328-339, 2018
179. Backhaus P, Burg MC, Roll W, et al: Simultaneous FAPI PET/MRI Targeting the Fibroblast-Activation Protein for Breast Cancer. *Radiology* 302:39-47, 2022
180. Chae SY, Ahn SH, Kim SB, et al: Diagnostic accuracy and safety of 16 α -[(18)F]fluoro-17 β -oestradiol PET-CT for the assessment of oestrogen receptor status in recurrent or metastatic lesions in patients with breast cancer: a prospective cohort study. *Lancet Oncol* 20:546-555, 2019
181. Pinker K, Bogner W, Baltzer P, et al: Improved differentiation of benign and malignant breast tumors with multiparametric 18fluorodeoxyglucose positron emission tomography magnetic resonance imaging: a feasibility study. *Clin Cancer Res* 20:3540-9, 2014
182. Taneja S, Jena A, Goel R, et al: Simultaneous whole-body 18F-FDG PET-MRI in primary staging of breast cancer: a pilot study. *Eur J Radiol* 83:2231-2239, 2014
183. Grueneisen J, Nagarajah J, Buchbender C, et al: Positron Emission Tomography/Magnetic Resonance Imaging for Local Tumor Staging in Patients With Primary Breast Cancer: A Comparison With Positron Emission Tomography/Computed Tomography and Magnetic Resonance Imaging. *Invest Radiol* 50:505-13, 2015
184. Goorts B, Voo S, van Nijnatten TJA, et al: Hybrid (18)F-FDG PET/MRI might improve locoregional staging of breast cancer patients prior to neoadjuvant chemotherapy. *Eur J Nucl Med Mol Imaging* 44:1796-1805, 2017
185. Catalano OA, Daye D, Signore A, et al: Staging performance of whole-body DWI, PET/CT and PET/MRI in invasive ductal carcinoma of the breast. *Int J Oncol* 51:281-288, 2017
186. Jung NY, Kim SH, Kim SH, et al: Effectiveness of Breast MRI and (18)F-FDG PET/CT for the Preoperative Staging of Invasive Lobular Carcinoma versus Ductal Carcinoma. *J Breast Cancer* 18:63-72, 2015
187. Ergul N, Kadioglu H, Yildiz S, et al: Assessment of multifocality and axillary nodal involvement in early-stage breast cancer patients using 18F-FDG PET/CT compared to contrast-enhanced and diffusion-weighted magnetic resonance imaging and sentinel node biopsy. *Acta Radiol* 56:917-23, 2015

188. Amornsiripanitch N, Bickelhaupt S, Shin HJ, et al: Diffusion-weighted MRI for Unenhanced Breast Cancer Screening. *Radiology* 293:504-520, 2019
189. Kang JW, Shin HJ, Shin KC, et al: Unenhanced magnetic resonance screening using fused diffusion-weighted imaging and maximum-intensity projection in patients with a personal history of breast cancer: role of fused DWI for postoperative screening. *Breast Cancer Res Treat* 165:119-128, 2017
190. Telegrafo M, Rella L, Stabile Ianora AA, et al: Unenhanced breast MRI (STIR, T2-weighted TSE, DWIBS): An accurate and alternative strategy for detecting and differentiating breast lesions. *Magn Reson Imaging* 33:951-5, 2015
191. Yabuuchi H, Matsuo Y, Sunami S, et al: Detection of non-palpable breast cancer in asymptomatic women by using unenhanced diffusion-weighted and T2-weighted MR imaging: comparison with mammography and dynamic contrast-enhanced MR imaging. *Eur Radiol* 21:11-7, 2011
192. Kazama T, Kuroki Y, Kikuchi M, et al: Diffusion-weighted MRI as an adjunct to mammography in women under 50 years of age: An initial study. *Journal of Magnetic Resonance Imaging* 36:139-144, 2012
193. Leithner D, Moy L, Morris EA, et al: Abbreviated MRI of the Breast: Does It Provide Value? *J Magn Reson Imaging* 49:e85-e100, 2019
194. Comstock CE, Gatsonis C, Newstead GM, et al: Comparison of Abbreviated Breast MRI vs Digital Breast Tomosynthesis for Breast Cancer Detection Among Women With Dense Breasts Undergoing Screening. *Jama* 323:746-756, 2020
195. Moschetta M, Telegrafo M, Rella L, et al: Abbreviated Combined MR Protocol: A New Faster Strategy for Characterizing Breast Lesions. *Clin Breast Cancer* 16:207-11, 2016
196. Kuhl CK, Schrading S, Strobel K, et al: Abbreviated breast magnetic resonance imaging (MRI): first postcontrast subtracted images and maximum-intensity projection-a novel approach to breast cancer screening with MRI. *J Clin Oncol* 32:2304-10, 2014

9. Papers

Paper I



Semi-automatic segmentation from intrinsically-registered 18F-FDG–PET/MRI for treatment response assessment in a breast cancer cohort: comparison to manual DCE–MRI

Maren Marie Sjaastad Andreassen¹ · Pål Erik Goa^{2,3} · Torill Eidhammer Sjøbakk¹ · Roja Hedayati^{4,5} · Hans Petter Eikesdal^{6,7} · Callie Deng¹ · Agnes Østlie³ · Steinar Lundgren^{4,5} · Tone Frost Bathen^{1,3} · Neil Peter Jerome^{1,3}

Received: 13 July 2019 / Revised: 27 August 2019 / Accepted: 16 September 2019 / Published online: 27 September 2019
© The Author(s) 2019

Abstract

Objectives To investigate the reliability of simultaneous positron emission tomography and magnetic resonance imaging (PET/MRI)-derived biomarkers using semi-automated Gaussian mixture model (GMM) segmentation on PET images, against conventional manual tumor segmentation on dynamic contrast-enhanced (DCE) images.

Materials and methods Twenty-four breast cancer patients underwent PET/MRI (following 18F-fluorodeoxyglucose (18F-FDG) injection) at baseline and during neoadjuvant treatment, yielding 53 data sets (24 untreated, 29 treated). Two-dimensional tumor segmentation was performed manually on DCE–MRI images (manual DCE) and using GMM with corresponding PET images (GMM–PET). Tumor area and mean apparent diffusion coefficient (ADC) derived from both segmentation methods were compared, and spatial overlap between the segmentations was assessed with Dice similarity coefficient and center-of-gravity displacement.

Results No significant differences were observed between mean ADC and tumor area derived from manual DCE segmentation and GMM–PET. There were strong positive correlations for tumor area and ADC derived from manual DCE and GMM–PET for untreated and treated lesions. The mean Dice score for GMM–PET was 0.770 and 0.649 for untreated and treated lesions, respectively.

Discussion Using PET/MRI, tumor area and mean ADC value estimated with a GMM–PET can replicate manual DCE tumor definition from MRI for monitoring neoadjuvant treatment response in breast cancer.

Keywords Breast cancer · Diffusion imaging · Mixture modelling · PET/MRI · Segmentation

Introduction

Breast cancer is the most frequent type of cancer in women worldwide [1], with a mean 5-year survival of 90.4% in Norway [2]. Patients diagnosed with locally advanced breast

cancer (LABC, stage 3), have a worse survival outcome (78.3%) [2]. They receive neoadjuvant chemotherapy treatment before surgery with the goal of complete pathological tumor regression, which correlates with improved survival and a reduced chance of breast cancer recurrence [3].

✉ Neil Peter Jerome
neil.p.jerome@ntnu.no

¹ Department of Circulation and Medical Imaging, NTNU, Norwegian University of Science and Technology, Trondheim, Norway

² Department of Physics, NTNU, Norwegian University of Science and Technology, Trondheim, Norway

³ Department of Radiology and Nuclear Medicine, St. Olav's University Hospital, Trondheim, Norway

⁴ Department of Clinical and Molecular Medicine, NTNU, Norwegian University of Science and Technology, Trondheim, Norway

⁵ Department of Oncology, St. Olav's University Hospital, Trondheim, Norway

⁶ Section of Oncology, Department of Clinical Science, University of Bergen, Bergen, Norway

⁷ Department of Oncology, Haukeland University Hospital, Bergen, Norway

Objective response evaluation during neoadjuvant therapy is important to assess treatment efficacy and to avoid unnecessary toxic side effects [4]. Radiologically, response evaluation has traditionally focused on measurements of tumor size [5], but several recent studies [6–10] have established functional imaging modalities as useful indicators of early response during neoadjuvant chemotherapy.

Diffusion-weighted magnetic resonance imaging (DWI) is a functional imaging modality with contrast arising from water molecule motion, and is, therefore, sensitized to tissue microstructure characteristics. DWI is most commonly utilized to assess tissue cellularity, where highly cellular tissues such as malignant tumors exhibit decreased diffusivity [11], quantified by calculation of an apparent diffusion coefficient (ADC). A robust empirical biomarker that is reduced in malignant tumors [12], ADC has shown higher specificity than conventional anatomical MRI for discriminating malignant and benign breast tumors [13].

Tumor ADC is commonly measured by the mean value of manually placed regions-of-interest (ROIs). There is no standard protocol for this tumor segmentation, and different approaches can significantly influence resulting ADC values [14]. Given that direct tumor segmentation of DWI may be confounded by noise and lack of conspicuity, tumor ROIs are commonly delineated on dynamic contrast-enhanced (DCE) images before being transferred to DWI. The definition of tumor on DCE images is thus governed by leakage of gadolinium contrast through pathological vessels and, therefore, linked to vascularity, whereas diffusion changes, reflecting cellularity, do not necessarily coincide [15].

Simultaneous positron emission tomography and magnetic resonance imaging (PET/MRI) is a recent technology with a significant potential in many aspects of breast cancer practice, including diagnostics, staging, and neoadjuvant response evaluation [16]. PET/MRI examinations allow simultaneous collection of structural, functional, and metabolic imaging properties in the same spatial and temporal domain. 18F-fluorodeoxyglucose (FDG)-PET visualizes upregulated glucose metabolism, while MRI reflects other hallmarks of cancer [17] including invasion and metastatic propensity (by ADC) and increased angiogenesis (DCE). Several studies report correlations between standardized uptake values (SUV) from FDG-PET and ADC in malignant tissue [18–20], indicating that intrinsically-registered 18F-FDG uptake may provide an alternative approach to manually drawn DCE-ROI delineation for use in DWI analysis [19]. FDG-PET is also known to outperform MRI tumor volume measurements in some cancers [21]. In this study, a simple, semi-automated Gaussian mixture model (GMM) segmentation algorithm was selected, to allow for heterogeneous FDG uptake across tumors and expected decline through treatment [22, 23].

The aim of the current study is to investigate the reliability of deriving lesion diffusion imaging characteristics from 18F-FDG uptake in invasive breast cancers > 4 cm or LABC (i.e., cT2-4N0-3) during neoadjuvant treatment. Specifically, we tested the reliability of deriving functional tumor area and ADC values in diffusion-weighted images from intrinsically-registered 18F-FDG-PET uptake using a semi-automated GMM segmentation algorithm in comparison with metrics derived from manually drawn DCE-ROIs.

Materials

Participants

This prospective study was approved by the Regional Committee for Medical and Health Research Ethics (REC) in western Norway (identifier 2015/1493). Informed consent was obtained from all individual participants included in the study. A total of 24 patients (median age 53 years, range 37–74) with biopsy-proven, invasive breast cancers > 4 cm or LABC (i.e., cT2-4N0-3). This minimum size was an inclusion criterion for recruitment to the phase II PETREMAC trial (Clinicaltrials.gov #NCT02624973), where lesions of this size are targets for neoadjuvant chemotherapy. The patients underwent individualized neoadjuvant therapy, based on tumor characteristics: estrogen (ER)/progesterone receptor (PgR), human epidermal growth factor-2 (HER2), and TP53 mutation status. The therapy used was primarily endocrine treatment (full details given in Table 1).

Patients were examined with 18F-FDG-PET/MRI scans, at baseline and up to four scanning sessions during neoadjuvant treatment (depending on trial progression and individual response). Two patients received neoadjuvant therapy 2 days prior to the baseline scan. The cohort scans are summarized in Fig. 1. All except three patients have undergone breast surgery (one patient dropped out, two scheduled after time of analysis). Tumor categorization was done by histopathologic analysis of core needle and open incisional biopsies.

Lesions with no remaining enhancement on DCE were excluded (8 data sets), resulting in 53 data sets overall: 24 untreated lesions, and 29 of treated lesions. Median number of scans was 2 (range 1–5), with mean intervals from baseline of 6, 12, 16, and 24 weeks. The mean time from study entry to surgery was 23 weeks. The two patients receiving neoadjuvant therapy 2 days prior to the baseline scan were considered untreated, as the lesions at this timepoint had undergone minimal treatment effect. This study did not explicitly consider clinical outcome or treatment effects, and therefore, this classification is predominantly to distinguish between lesions that have had the opportunity to undergo significant response.

Table 1 Clinical characteristics of patient cohort

Characteristic	All patients (<i>n</i> = 24)
Age (median, range), years	53 (37–74)
Height (median, range), m	1.65 (1.54–1.79)
Weight (median, range), kg	67 (50–100)
Tumor volume (median, range), cm ³	9.91 (2.88–60.56)
Histological type	
IDC	18
ILC	2
Other	4
Histological grade	
1	0
2	9
3	13
Unknown	2
Estrogen receptor (ER) status (%)	
Negative	8
≥ 1–10	1
≥ 10–50	0
> 50	15
Progesteron receptor (PgR) status (%)	
Negative	9
≥ 10–50	1
≥ 50	4
HER2 status	
Negative	15
Positive	7
Not applicable	1
Ki67 (%)	
< 30%	9
≥ 30%	15
Treatment	
Endocrine	11
Docetaxel and cyclophosphamid	1
Pertuzumab, trastuzumab and docetaxel/ cyclophosphamid	3
Pertuzumab, trastuzumab and docetaxel	5
Olaparib and carboplatin	4
Pathological response	
Complete response	8
Non-response	13
Not operated	3

Pathological characteristics are determined based on histopathologic analysis of pre-treatment core needle biopsy; for *n* = 3 patients, histological grade was determined from surgical specimen

Others (ICD and ILC (*n* = 1), poorly differentiated carcinoma (*n* = 1), carcinoma with medullary features (*n* = 2)

IDC invasive ductal carcinoma, ILC invasive lobular carcinoma

Methods

PET/MRI acquisition

All patients underwent simultaneous PET/MRI on a 3 T Biograph mMR scanner (Siemens Healthcare, Erlangen, Germany), 75 min after 18F-FDG injection (4 MBq/kg dose following 6 h fasting). The 18F-FDG was produced by the Norwegian Medical Cyclotron Center (Oslo, Norway). MRI acquisition utilized a designated 4-channel breast coil and included Dixon, T2-weighted, DWI, and DCE. DCE parameters included: 3D FLASH sequence, transverse orientation, TR/TE 5.88/2.21 ms, resolution 0.7 × 0.7 × 2.5 mm, 72 slices, flip angle 15°, 1 baseline, and 7 contrast sequences, time resolution 1 min. Multiple *b* value DWI parameters were: axial bilateral single-shot echo planar imaging, TR/TE 9000/77 ms, fat suppressed, *b* values = 0, 50, 120, 200, 400, 700 mm² s⁻¹, resolution 2 × 2 × 2.5 mm, 60 slices, and FoV 380 × 190 mm, with additional phase-reversed *b* = 0 mm² s⁻¹ (hereafter 'b0') image. Concurrent PET data were acquired at a bed position giving full breast region coverage, and reconstructed using a manufacturer-supplied algorithm (OSEM-PSF, 21 subsets, 3 iterations, and a 4 mm full-width-half-maximum Gaussian filter; Siemens, Erlangen). PET data concurrent with DCE acquisition were available for *n* = 31 data sets (16 untreated and 15 treated lesions).

Image preparation and manual segmentation (Manual DCE)

The lesion segmentation process is summarized in Fig. 2. DW images were distortion-corrected using phase-reversed b0 images [24]; dixon-based PET attenuation correction was performed on the scanner [25], and standardized uptake values (SUV) were normalized against body weight and dose. DCE and PET images were resampled using Elastix [26] to exactly match the resolution of the DWI images, and thus give direct voxel-to-voxel correspondence. Perfusion-insensitive ADC maps were calculated from DWI data (*b* ≥ 200 mm² s⁻¹) using a mono-exponential model:

$$S_b = S_{b=0} \cdot e^{-b \cdot ADC}$$

Manual DCE: manual segmentation of a single tumor region was performed by researcher (M.M.S.A.) on a single central slice of the enhancing solid tumor on DCE, ignoring satellite regions, with resulting ROIs supervised and approved by an expert radiologist (A.Ø.).

Fig. 1 Breast cancer patients ($n=24$) received one pretreatment baseline scan, and additional scans during neoadjuvant treatment prior to surgery. On average, scans during treatment were 6, 12, 16, and 24 weeks after baseline, and surgery was 23 weeks after baseline scan. Total data set included 53 scans: 24 from untreated, and 29 from treated lesions

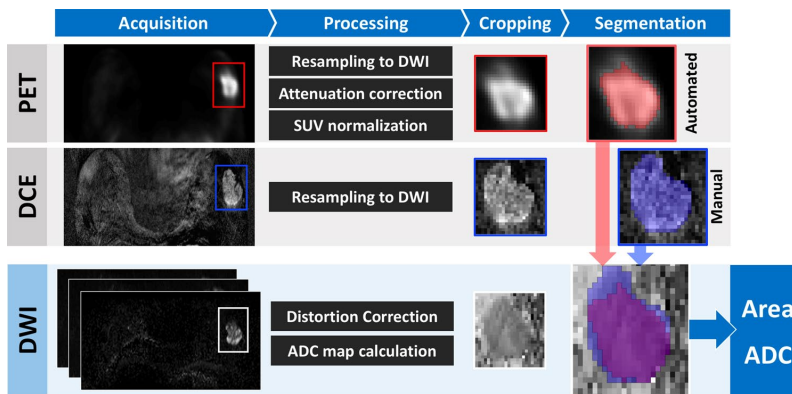
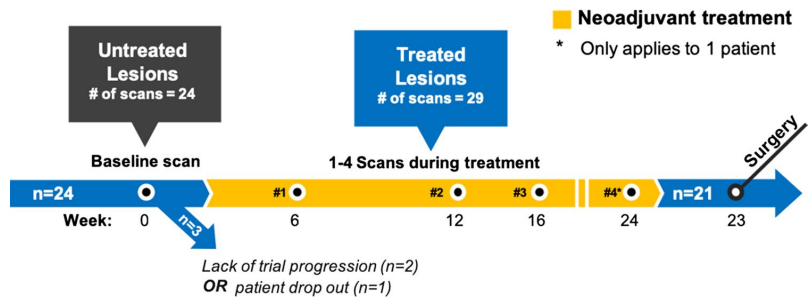


Fig. 2 All images were resampled to diffusion-weighted imaging (DWI) resolution. PET images were attenuation-corrected and SUV normalized. Apparent diffusion coefficient (ADC) maps were calculated from distortion-corrected diffusion images. Tumor segmenta-

tion was performed by semi-automated Gaussian mixture modelling (GMM) segmentation on cropped PET images, and manually on DCE images. Resulting regions-of-interest (ROIs) were transferred to the ADC maps for derivation of tumor area and mean ADC

Lesion cropping and Gaussian mixture modelling (GMM–PET)

A rectangular region containing the visible lesion was manually cropped from the SUV map (corresponding to the single central slice of enhancing tumor on DCE) for Gaussian mixture modelling (GMM–PET). An algorithm using default k-means++ [27] initialization (MATLAB; Mathworks, Natick, MA, USA) and an assumption of three Gaussian distribution classes were used, returning an assignment for each voxel based on highest probability [28] of belonging to each class: tumor (highest intensity), ‘non-tumor’ background (lowest intensity) and unknown (intermediate intensity). To compromise between accuracy and avoiding overestimation from partial volume effects, voxels classed as ‘unknown’ were considered non-tumor, defining the tumor class threshold as the intersection of tumor and unknown class distributions (Fig. 7 in Appendix). User input is thus limited to initial region cropping.

Two common simple thresholding-based PET segmentation methods, a fixed threshold of 2.5 ($SUV_{2.5}$) and 42% of the maximum SUV ($SUV_{42\%}$) [22], were also performed to provide comparison with GMM–PET (Fig. 7 in Appendix).

Derivation of DWI metrics from manual DCE and GMM–PET

ROIs, for the whole lesion within the chosen slice, derived from both manual DCE and from GMM–PET were transferred to ADC maps and used to calculate the tumor ROI area and the mean ADC value for the whole ROI.

Statistical analysis

Performance of the three PET segmentation techniques in reference to manual DCE–ROIs was measured using the Dice similarity coefficient, varying between 0 and 1

indicating degree of spatial overlap [29], and center-of-gravity displacement (CoG). CoG was normalized based on corresponding area DCE. Tumor area and ADC values from the different segmentation methods were compared using a paired *t* test, and Pearson’s test for correlation; relationship of these segmentation metrics with SUV_{2.5} and SUV_{42%} was also assessed. A two-sample *t* test was used to assess the difference between the untreated (*n*=24) and treated cohort (*n*=29) for all metrics. All *p* values were corrected for multiple testing with the Benjamini and Hochberg [30] approach, with values <0.05 considered statistically significant.

Results

Derived diffusion parameters (area, ADC) in GMM-PET versus manual DCE

DWI metrics for untreated, treated, and all lesions are given in Table 2, and show no significant differences. There were strong positive correlations between GMM-PET and manual

DCE for area and ADC for untreated and treated lesions, as shown for longitudinal scans of two patients receiving neo-adjuvant therapy in Fig. 3. GMM-PET successfully tracks the same changes in ADC and tumor area observed using the manual DCE, even when performance parameters to manual DCE are poor.

Spatial agreement of GMM-PET with manual DCE

Dice score [29] for GMM-PET was significantly higher, indicating better performance, than SUV_{42%} for untreated lesions (*p*=0.012) and higher than SUV_{2.5} for both untreated (*p*=0.024) and treated lesions (*p*<0.001) (Fig. 4a). CoG measurements were significantly lower for GMM-PET compared to SUV_{2.5} for treated lesions (*p*=0.002) (Fig. 4b). GMM-PET is able to successfully identify tumor tissue in untreated lesions where uptake is heterogeneous across the cohort, where SUV_{42%} and SUV_{2.5} over- and underestimate tumor areas, respectively, compared to the DCE definition. In 16 cases (3 untreated, 13 treated lesions), SUV_{2.5} could not define any tumor area, meaning that CoG measurements

Table 2 Values given as mean (range) and *p* values

	ADC mean ($\times 10^{-3} \text{ mm}^2 \text{ s}^{-1}$)			Tumor area (cm^2)		
	Manual DCE	GMM-PET	<i>p</i> value	Manual DCE	GMM-PET	<i>p</i> value
Untreated (<i>n</i> =24)	0.957 (0.3796)	0.964 (0.411)	0.930	6.189 (4.277)	5.923 (3.944)	0.899
Treated (<i>n</i> =29)	1.167 (0.392)	1.1701 (0.445)	0.930	4.076 (2.857)	4.147 (2.745)	0.930
All (<i>n</i> =53)	1.073 (0.397)	1.079 (0.439)	0.930	5.015 (3.677)	4.936 (3.416)	0.930

No significant difference between resulting parameters from manual DCE and GMM-PET

Fig. 3 Patient in **a** demonstrated good spatial overlay and excellent agreement of response parameters over time. The patient in **b** shows a patient with excellent spatial agreement for the untreated lesion, but for the treated lesion, the segmentation is offset, with corresponding poor performance parameters (low Dice score and high CoG). However, GMM-PET was still able to accurately assess parameter changes over time

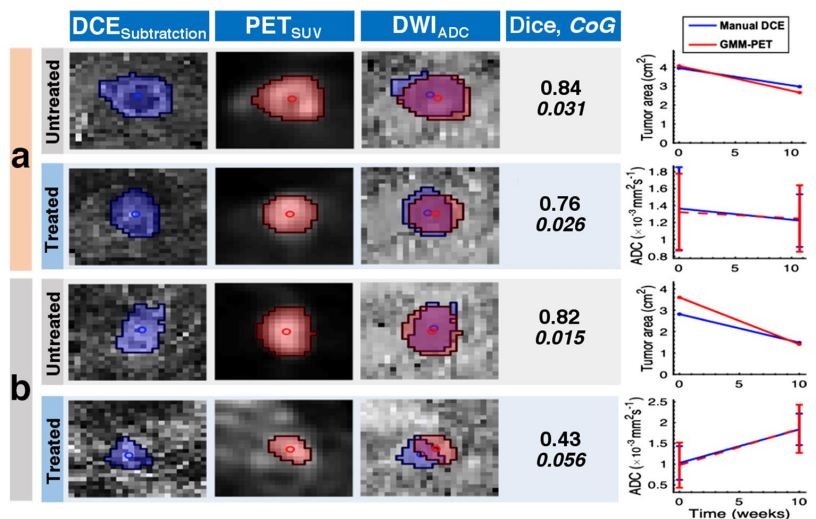
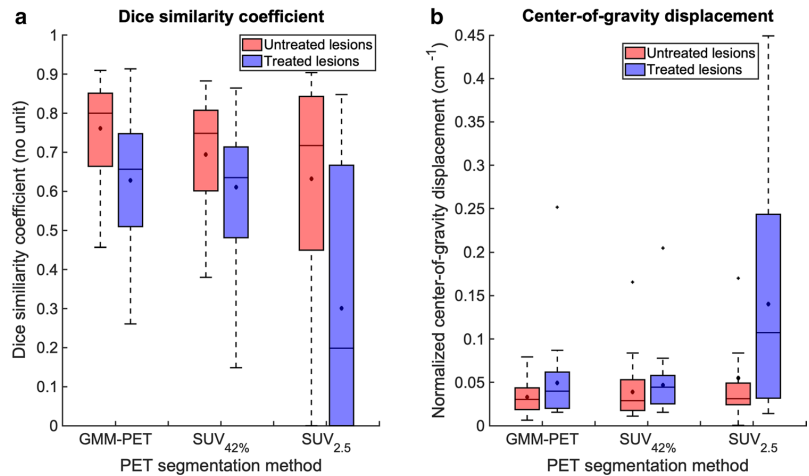


Fig. 4 **a** Dice similarity coefficient and **b** center-of-gravity displacement, normalized to manual DCE tumor area, from GMM, SUV_{42%}, and SUV_{2.5}. Median and mean values indicated by lines and asterisks; boxes show interquartile range, and whiskers show data range



were not applicable for these cases. GMM–PET and SUV_{2.5} performed significantly better in the treated lesions group compared to untreated lesions for both Dice score ($p=0.005$ and $p=0.002$) and CoG ($p=0.025$ and $p=0.005$), while SUV_{42%} only had significantly higher CoG ($p=0.002$).

Discussion

The main finding of the current breast cancer study is that functional tumor area and corresponding mean ADC values from GMM–PET ROIs matched those derived from manual DCE. As a superficial interpretation, these findings indicate that GMM–PET is a reliable technique to efficiently derive functional diffusion parameters for monitoring neoadjuvant treatment response in breast cancer. The segmentation is data driven, requiring minimal user input, and obviates the requirement for gadolinium contrast administration and, therefore, could have significant potential as an alternative objective evaluation method among the increasing number of breast cancer patients undergoing neoadjuvant treatment. At a deeper level, the results illuminate the concordance—and discordance—between ROIs derived from different imaging modalities, and as such allow interrogation of the spatial relationship existing between functional information arising from PET, diffusion, and DCE imaging, and ultimately the tissue characteristics these modalities are sensitized to.

Our study demonstrates a strong correlation between tumor ADC values derived from GMM–PET and manual DCE segmentation, in line with a previous study by Byun et al. [19] using a similar approach in breast carcinomas; our study utilizes the intrinsic voxel correspondence of simultaneous PET/MRI, thus avoiding the additional registration

required by sequential FDG–PET/CT and DWI and conferring greater confidence in the results. Notably, the calculated mean ADC from GMM–PET was not significantly different from mean ADC from manual DCE, despite ADC metrics having been shown to be significantly influenced by segmentation method [14, 31]. This suggests that GMM–PET may have value even while accurate assessment of ADC metrics is considered increasingly important in a neoadjuvant treatment response setting [6–8].

Conventional manual DCE segmentation means that diffusion measurements, reflecting cellularity [13, 32, 33], are drawn from areas defined by gadolinium contrast enhancement, which is not necessarily optimal and may introduce bias to functional biomarker measurements [15]. It can thus be argued that tumor definition for diffusion studies is better performed on another MR modality more closely related to cellularity. Several studies have described an underlying link between metabolism and cellularity, such as correlation between FDG uptake to cellularity [34, 35]. Consequently, a negative correlation should be expected between SUV and ADC, and it could be argued that GMM–PET would coincide better with changes in cellularity. However, the previous reports are contradictory with either negative [18–20] or no [36, 37] correlations between SUV and ADC, indicating that imaging metrics from DCE, DWI, and PET do not capture all relevant physiological properties, even when GMM–PET is able to localize tumors equivalent to DCE.

GMM–PET segmentation gives good spatial concordance with manual DCE for untreated breast cancer lesions, while the segmentation performance was significantly poorer for treated lesions, with lower Dice score and higher CoG. It is well known that therapy affects tumor vascularity [38], which may have influenced both manual DCE and

GMM–PET segmentation, as both modalities are dependent on sufficient blood flow for contrast and tracer uptake. However, DCE and PET reflect different physiological properties, and therefore, it would be of interest to observe if these have been altered differently during treatment. In addition, it should be noted that several treated lesions with poor overlap are cases where manual DCE segmentation was difficult due to low enhancement on DCE.

In this study, GMM–PET segmentation performed significantly better than the commonly used $SUV_{42\%}$ threshold in untreated lesions, and $SUV_{2.5}$ for both treated and untreated lesions in recapitulating manual DCE. Using GMM–PET, the tumor area is not underestimated in the cases of heterogeneous uptake (Fig. 5) or for tumors with high-intensity relative to their immediate surroundings, which is a well-known issue [39, 40]. However, as FDG uptake in the tumor decreases during treatment [23], GMM–PET did not perform better than $SUV_{42\%}$, which is known to give larger estimates of tumor size as SUV_{max} approaches background levels (Fig. 5), which is a limit of adaptive and data-driven algorithms that are sensitive to the FDG-uptake range [41, 42]. Other algorithm-based approaches such as gradient methods [40, 43] have also been recommended [22], although these require increased user input and were not investigated in this study (Fig. 6).

While the current findings suggest that GMM–PET segmentation can work as a proxy for manual DCE, we do not suggest that PET might replace manual DCE in today’s clinical context. Manual DCE is currently the most sensitive test for both breast cancer detection [44]

and monitoring treatment response in a neoadjuvant setting [45], although concerns regarding contrast allergy and potential brain deposition [46] of gadolinium create a setting for exploration of complementary techniques. The use of PET tracer comes with its own challenges, in handling and cost, and is neither available nor suitable in all contexts. Our study indicates that the use of PET data for tumor segmentation is more reliable in pre-treatment lesions; in cases where FDG uptake is substantially reduced by treatment the GMM–PET method becomes less effective, where the tumor may become more diffuse. In these cases, automated segmentation procedures will be more prone to variation. It is worth noting that this is not unique to the technique in this study; the reduction of DCE contrast in successfully treated tumors also makes tumor definition more challenging for the conventional approach. Thus, in a simple sense, PET data are able to act as a proxy for tumor definition using DCE, but are also more likely to become useful as an adjunct to DCE for deeper investigations of tumor characteristics in multimodality examinations. It would also be possible to examine other modality combinations, such as taking a PET ROI definition to derive quantitative DCE markers from a suitable protocol.

Benefits of a data-driven, semi-automated GMM–PET approach include reduced radiologist workload, faster segmentation processes, and reduced interobserver variability [47]. The major advantage of PET/MRI systems, exploited here, is intrinsic registration of simultaneously acquired PET and MR data, giving voxel-level correspondence, without additional registration processes that generally involve user

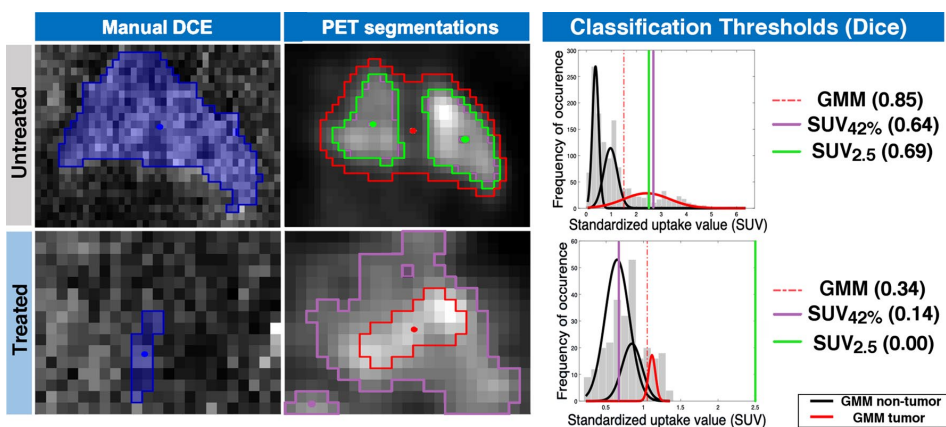
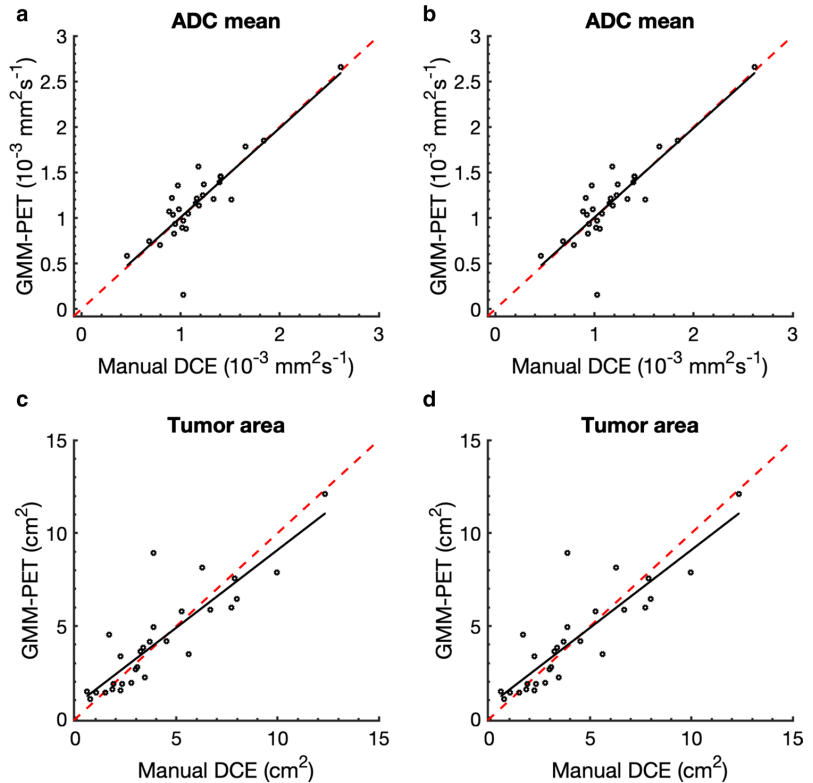


Fig. 5 Change in GMM–PET, $SUV_{42\%}$, and $SUV_{2.5}$ for an untreated (top row) and treated (bottom row) lesion from an illustrative patient, with corresponding histogram displays of SUV signal intensity and Dice similarity coefficient. GMM–PET is able to properly identify the whole tumor tissue of the heterogeneous untreated lesion, while

$SUV_{2.5}$ and $SUV_{42\%}$ give lower estimates. As SUV is reduced through treatment, $SUV_{2.5}$ cannot classify any tumor tissue, $SUV_{42\%}$ overestimates tumor area relative to DCE, while GMM–PET remains stable. Using DCE as a tumor definition standard becomes problematic when contrast leakage is reduced through treatment

Fig. 6 Relationship between the resulting metrics from manual DCE and GMM-PET for **a** ADC mean for untreated lesions ($r=0.866$, $p<0.001$) and **b** treated lesions ($r=0.895$, $p<0.001$) and **m** tumor area from **c** untreated ($r=0.870$, $p<0.0001$) and **d** treated ($r=0.928$, $p<0.001$) lesions. Red identity lines included show that area from GMM-PET is slightly smaller than from manual DCE



input or additional processing [48]. Further optimization of GMM-PET might include automated data-driven initialization and number of classes, with the goal of entirely eliminating manual input [49]. We illustrate the influence of lesion-region initialization, for which automation could be developed, in Appendix (Fig. 8). The number of voxels within the lesion is also a factor that will affect the performance of the GMM method, and is thus intrinsically tied to image resolution, and will ultimately limit use in smaller lesions.

One limitation to this methodology is that increased tracer uptake is less specific to disease than manual DCE [50], potentially introducing errors in the GMM-PET classification if not accounted for by appropriate selection of tumor-containing region. In addition, while the analysis in this study explicitly did not consider patient response from the clinical viewpoint, as well as other clinically relevant data such as hormone status, the variety of treatments and responses provided a suitably large range of situations in which to test the GMM-PET methodology, including cases where response included an almost total loss of detectable disease.

Conclusion

The potential implications of improved imaging technology in breast cancer are large, and PET/MRI is a unique tool to investigate links between increased metabolism (PET), perfusion (DCE), and decreased diffusion (DWI), without additional scan time or registration errors. The current findings show that PET/MRI, using a semi-automated GMM segmentation strategy, yields tumor area and mean ADC value estimates that can replicate today's gold standard of tumor definition of manual DCE from MRI. Furthermore, the GMM-PET method also captures tumor changes associated with response to neoadjuvant chemotherapy, which supplements today's gold standard which is manual DCE in the neoadjuvant setting. The potential benefits include a broader assessment of morphological and metabolic changes to guide clinical decisions regarding tumor operability, and thus to ensure a high probability of complete tumor regression, and subsequent cancer cure.

Acknowledgements We acknowledge support from the liaison Committee between the Central Norway Regional Health Authority and

the Norwegian University of Science and Technology (Project nr. 90065000).

Author contributions MMAA: acquisition of data, analysis and interpretation of data, drafting of manuscript, and critical revision. PEG: study conception and design, acquisition of data, and critical revision. TES: study conception and design, acquisition of data, and critical revision. RH: acquisition of data and critical revision. HPE: study conception and design, acquisition of data, and critical revision. CD: analysis and interpretation of data and critical revision. AØ: analysis and interpretation of data, critical revision. SL: study conception and design, acquisition of data, and critical revision. TFB: study conception and design, analysis and interpretation of data, and critical revision. NPJ: study conception and design, acquisition of data, analysis and interpretation of data, drafting of manuscript, and critical revision.

Funding We acknowledge support from the liaison Committee between the Central Norway Regional Health Authority and the Norwegian University of Science and Technology.

Compliance with ethical standards

Conflict of interest None of the authors of this work have any conflict of interest to declare

Ethical approval All procedures performed in studies involving human participants were in accordance with the ethical standards of the institutional and/or national research committee (Regional Committee for Medical and Health Research Ethics (REC) in western Norway, identifier 2015/1493) and with the 1964 Helsinki declaration and its later amendments or comparable ethical standards.

Open Access This article is distributed under the terms of the Creative Commons Attribution 4.0 International License (<http://creativecommons.org/licenses/by/4.0/>), which permits unrestricted use, distribution, and reproduction in any medium, provided you give appropriate credit to the original author(s) and the source, provide a link to the Creative Commons license, and indicate if changes were made.

Appendix

See Figs. 7 and 8.

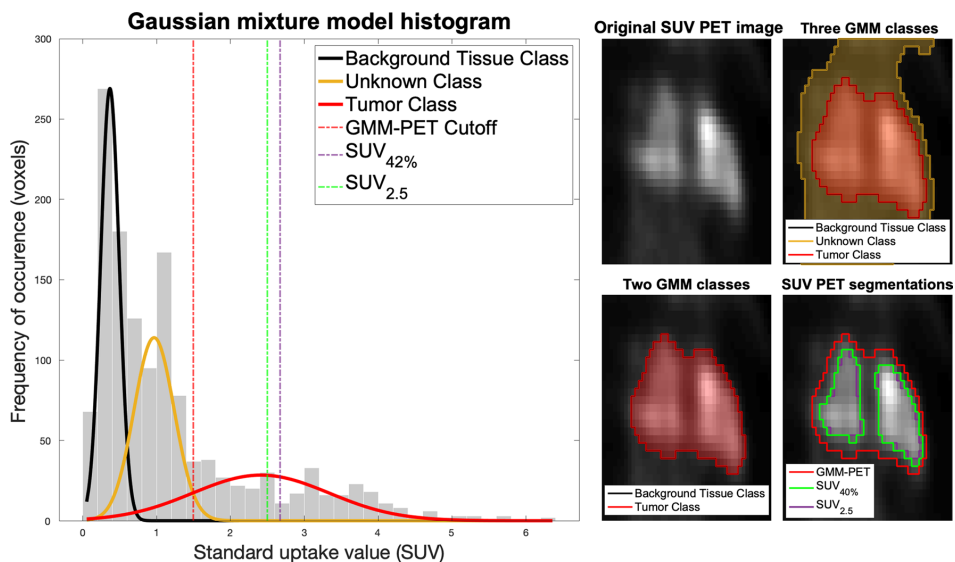
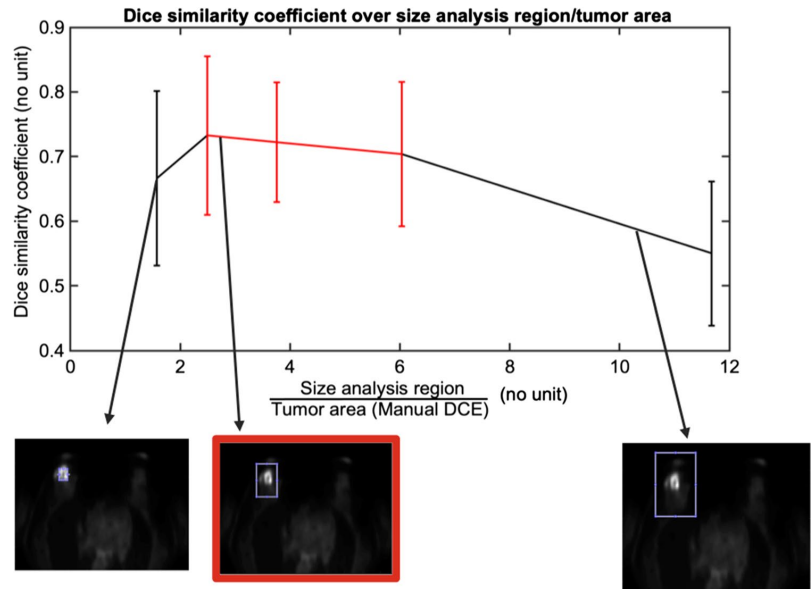


Fig. 7 Schematic illustration of the semi-automated Gaussian mixture model (GMM) segmentation performance, and the thresholding segmentation methods $SUV_{42\%}$ and $SUV_{2.5}$. **a** Histogram display of the three Gaussian distributions, together with $SUV_{42\%}$ and $SUV_{2.5}$ thresholds. **b** Cropped original PET image (upper), and resulting areas from GMM segmentation algorithm (lower) with three classes:

tumor (red), unknown (yellow), and background tissue (black) class. **c** GMM segmentation (red), $SUV_{42\%}$ (blue), and $SUV_{2.5}$ (green) ROIs overlaid on original PET image. For this example, $SUV_{42\%}$ is similar to GMM, but $SUV_{2.5}$ provides a much lower estimate of tumor volume

Fig. 8 Dice similarity coefficient (cohort mean \pm std) for Gaussian mixture model ROIs compared against manual dynamic contrast-enhanced (DCE) ROI. Indicated in red, the best results were given when the analysis regions were cropped at approximately 2–6 times the tumor area, and this was used in the study. This sensitivity would need to be accounted for in an automated cropping routine, as well as some sort of quality metric on the resulting ROI



References

1. Ferlay J EM, Lam F, Colombet M, Mery L, Piñeros M, Znaor A, Soerjomataram I, Bray F (2018) Global cancer observatory: cancer today. <https://gco.iarc.fr/today>. Accessed 29 Dec 2018
2. Cancer Registry of Norway (2018) Cancer in Norway 2017—cancer incidence, mortality, survival and prevalence in Norway. Accessed 10 Dec 2018
3. Cortazar P, Zhang L, Untch M, Mehta K, Costantino JP, Wolmark N, Bonnefoi H, Cameron D, Gianni L, Valagussa P, Swain SM, Prowell T, Loibl S, Wickerham DL, Bogaerts J, Baselga J, Perou C, Blumenthal G, Blohmer J, Mamounas EP, Bergh J, Semiglazov V, Justice R, Eidtmann H, Paik S, Piccart M, Sridhara R, Fasching PA, Slaets L, Tang S, Gerber B, Geyer CE Jr, Pazdur R, Ditsch N, Rastogi P, Eiermann W, von Minckwitz G (2014) Pathological complete response and long-term clinical benefit in breast cancer: the CTNeoBC pooled analysis. *Lancet* 384(9938):164–172
4. Thomas E, Holmes FA, Smith TL, Buzdar AU, Frye DK, Fraschini G, Singletary SE, Theriault RL, McNeese MD, Ames F, Walters R, Hortobagyi GN (2004) The use of alternate, non-cross-resistant adjuvant chemotherapy on the basis of pathologic response to a neoadjuvant doxorubicin-based regimen in women with operable breast cancer: long-term results from a prospective randomized trial. *J Clin Oncol* 22(12):2294–2302
5. Graham LJ, Shupe MP, Schneble EJ, Flynt FL, Clemenshaw MN, Kirkpatrick AD, Gallagher C, Nissan A, Henry L, Stojadinovic A, Peoples GE, Shumway NM (2014) Current approaches and challenges in monitoring treatment responses in breast cancer. *J Cancer* 5(1):58–68
6. Chu W, Jin W, Liu D, Wang J, Geng C, Chen L, Huang X (2018) Diffusion-weighted imaging in identifying breast cancer pathological response to neoadjuvant chemotherapy: a meta-analysis. *Oncotarget* 9(6):7088–7100
7. Partridge SC, Zhang Z, Newitt DC, Gibbs JE, Chenevert TL, Rosen MA, Bolan PJ, Marques HS, Romanoff J, Cimino L, Joe BN, Umphrey HR, Ojeda-Fournier H, Dogan B, Oh K, Abe H, Drukteinis JS, Esserman LJ, Hylton NM (2018) Diffusion-weighted MRI findings predict pathologic response in neoadjuvant treatment of breast cancer: the ACIN 6698 multicenter trial. *Radiology* 289(3):618–627
8. Pickles MD, Gibbs P, Lowry M, Turnbull LW (2006) Diffusion changes precede size reduction in neoadjuvant treatment of breast cancer. *Magn Reson Imaging* 24(7):843–847
9. Nilsen L, Fangberget A, Geier O, Olsen DR, Seierstad T (2010) Diffusion-weighted magnetic resonance imaging for pretreatment prediction and monitoring of treatment response of patients with locally advanced breast cancer undergoing neoadjuvant chemotherapy. *Acta Oncol (Stockholm, Sweden)* 49(3):354–360
10. Sharma U, Danishad KK, Seenu V, Jagannathan NR (2009) Longitudinal study of the assessment by MRI and diffusion-weighted imaging of tumor response in patients with locally advanced breast cancer undergoing neoadjuvant chemotherapy. *NMR Biomed* 22(1):104–113
11. Charles-Edwards EM, deSouza NM (2006) Diffusion-weighted magnetic resonance imaging and its application to cancer. *Cancer Imaging* 6(1):135–143
12. Sinha S, Lucas-Quesada FA, Sinha U, DeBruhl N, Bassett LW (2002) In vivo diffusion-weighted MRI of the breast: potential for lesion characterization. *J Magn Reson Imaging* 15(6):693–704
13. Guo Y, Cai Y-Q, Cai Z-L, Gao Y-G, An N-Y, Ma L, Mahankali S, Gao J-H (2002) Differentiation of clinically benign and malignant breast lesions using diffusion-weighted imaging. *J Magn Reson Imaging* 16(2):172–178
14. Bickel H, Pinker K, Polanc S, Magometschnigg H, Wengert G, Spick C, Bogner W, Bago-Horvath Z, Helbich TH, Baltzer P (2017) Diffusion-weighted imaging of breast lesions: region-of-interest placement and different ADC parameters influence apparent diffusion coefficient values. *Eur Radiol* 27(5):1883–1892
15. Kim TH, Yoon JK, Kang DK, Lee SJ, Jung YS, Yim H, An YS (2015) Correlation between F-18 fluorodeoxyglucose positron emission tomography metabolic parameters and dynamic contrast-enhanced MRI-derived perfusion data in patients with invasive ductal breast carcinoma. *Ann Surg Oncol* 22(12):3866–3872

16. Plecha DM, Faulhaber P (2017) PET/MRI of the breast. *Eur J Radiol* 94:A26–A34
17. Hanahan D, Weinberg RA (2011) Hallmarks of cancer: the next generation. *Cell* 144(5):646–674
18. Nakajo M, Kajiya Y, Kaneko T, Kaneko Y, Takasaki T, Tani A, Ueno M, Koriyama C, Nakajo M (2010) FDG PET/CT and diffusion-weighted imaging for breast cancer: prognostic value of maximum standardized uptake values and apparent diffusion coefficient values of the primary lesion. *Eur J Nucl Med Mol Imaging* 37(11):2011–2020
19. Byun BH, Noh WC, Lim I, Lee SS, Cho AR, Park JA, Kim KM, Kim HA, Kim EK, Kim BI, Choi CW, Lim SM (2013) A new method for apparent diffusion coefficient measurement using sequential (18)F-FDG PET and MRI: correlation with histological grade of invasive ductal carcinoma of the breast. *Ann Nucl Med* 27(8):720–728
20. Kitajima K, Yamano T, Fukushima K, Miyoshi Y, Hirota S, Kawana Y, Miya M, Doi H, Yamakado K, Hirota S (2016) Correlation of the SUVmax of FDG-PET and ADC values of diffusion-weighted MR imaging with pathologic prognostic factors in breast carcinoma. *Eur J Radiol* 85(5):943–949
21. Daisne JF, Duprez T, Weynand B, Lonnew M, Hamoir M, Reyckher H, Gregoire V (2004) Tumor volume in pharyngolaryngeal squamous cell carcinoma: comparison at CT, MR imaging, and FDG PET and validation with surgical specimen. *Radiology* 233(1):93–100
22. Im HJ, Bradshaw T, Solaiyappan M, Cho SY (2018) Current methods to define metabolic tumor volume in positron emission tomography: which one is better? *Nucl Med Mol Imaging* 52(1):5–15
23. Schelling M, Avril N, Nahrig J, Kuhn W, Romer W, Sattler D, Werner M, Dose J, Janicke F, Graeff H, Schwaiger M (2000) Positron emission tomography using [(18)F]Fluorodeoxyglucose for monitoring primary chemotherapy in breast cancer. *J Clin Oncol* 18(8):1689–1695
24. Holland D, Kuperman JM, Dale AM (2010) Efficient correction of inhomogeneous static magnetic field-induced distortion in Echo Planar Imaging. *Neuroimage* 50(1):175–183
25. Martinez-Moller A, Souvatzoglou M, Delso G, Bundschuh RA, Chef d'hotel C, Ziegler SI, Navab N, Schwaiger M, Nekolla SG (2009) Tissue classification as a potential approach for attenuation correction in whole-body PET/MRI: evaluation with PET/CT data. *J Nucl Med* 50(4):520–526
26. Klein S, Staring M, Murphy K, Viergever MA, Pluim JP (2010) Elastix: a toolbox for intensity-based medical image registration. *IEEE Trans Med Imaging* 29(1):196–205
27. Drzezga A, Souvatzoglou M, Eiber M, Beer AJ, Furst S, Martinez-Moller A, Nekolla SG, Ziegler S, Ganter C, Rummeny EJ, Schwaiger M (2012) First clinical experience with integrated whole-body PET/MR: comparison to PET/CT in patients with oncologic diagnoses. *J Nucl Med* 53(6):845–855
28. Geoff McLachlan DP (2000) Finite mixture models. Wiley series in probability and statistics. Applied probability and statistics. Wiley, New York
29. Dice LR (1945) Measures of the amount of ecologic association between species. *Ecology* 26(3):297–302
30. Benjamini Y, Hochberg Y (2000) On the adaptive control of the false discovery rate in multiple testing with independent statistics. *J Educ Behav Stat* 25(1):60–83
31. Nogueira L, Brandao S, Matos E, Nunes RG, Ferreira HA, Loureiro J, Ramos I (2015) Region of interest demarcation for quantification of the apparent diffusion coefficient in breast lesions and its interobserver variability. *Diagn Interv Radiol* 21(2):123–127
32. Nonomura Y, Yasumoto M, Yoshimura R, Haraguchi K, Ito S, Akashi T, Ohashi I (2001) Relationship between bone marrow cellularity and apparent diffusion coefficient. *J Magn Reson Imaging* 13(5):757–760
33. Yoshikawa MI, Ohsumi S, Sugata S, Kataoka M, Takashima S, Mochizuki T, Ikura H, Imai Y (2008) Relation between cancer cellularity and apparent diffusion coefficient values using diffusion-weighted magnetic resonance imaging in breast cancer. *Radiat Med* 26(4):222–226
34. Ito K, Kato T, Ohta T, Tadokoro M, Yamada T, Ikeda M, Nishino M, Ishigaki T, Gambhir S (1996) Fluorine-18 fluoro-2-deoxyglucose positron emission tomography in recurrent rectal cancer: relation to tumour size and cellularity. *Eur J Nucl Med* 23(10):1372–1377
35. Higashi T, Tamaki N, Torizuka T, Nakamoto Y, Sakahara H, Kimura T, Honda T, Inokuma T, Katsushima S, Ohshio G, Imamura M, Konishi J (1998) FDG uptake, GLUT-1 glucose transporter and cellularity in human pancreatic tumors. *J Nucl Med* 39(10):1727–1735
36. Choi BB, Kim SH, Kang BJ, Lee JH, Song BJ, Jeong SH, Yim HW (2012) Diffusion-weighted imaging and FDG PET/CT: predicting the prognoses with apparent diffusion coefficient values and maximum standardized uptake values in patients with invasive ductal carcinoma. *World J Surg Oncol* 10:126
37. Inglese M, Cavaliere C, Monti S, Forte E, Incoronato M, Nicolai E, Salvatore M, Aiello M (2019) A multi-parametric PET/MRI study of breast cancer: evaluation of DCE-MRI pharmacokinetic models and correlation with diffusion and functional parameters. *NMR Biomed* 32(1):e4026
38. Muz B, de la Puente P, Azab F, Azab AK (2015) The role of hypoxia in cancer progression, angiogenesis, metastasis, and resistance to therapy. *Hypoxia (Auckl)* 3:83–92
39. Daisne JF, Duprez T, Weynand B (2004) Tumor volume in pharyngolaryngeal squamous cell carcinoma: comparison at CT, MR imaging, and FDG PET and validation with surgical specimen. *Radiology* 233:93
40. Sridhar P, Mercier G, Tan J, Truong MT, Daly B, Subramaniam RM (2014) FDG PET metabolic tumor volume segmentation and pathologic volume of primary human solid tumors. *Am J Roentgenol* 202(5):1114–1119
41. Burger IA, Vargas HA, Apte A, Beattie BJ, Humm JL, Gonen M, Larson SM, Ross Schmidlein C (2014) PET quantification with a histogram derived total activity metric: superior quantitative consistency compared to total lesion glycolysis with absolute or relative SUV thresholds in phantoms and lung cancer patients. *Nucl Med Biol* 41(5):410–418
42. Burger IA, Casanova R, Steiger S, Husmann L, Stolzmann P, Huellner MW, Curioni A, Hillinger S, Schmidlein CR, Soltermann A (2016) 18F-FDG PET/CT of non-small cell lung carcinoma under neoadjuvant chemotherapy: background-based adaptive-volume metrics outperform TLG and MTV in predicting histopathologic response. *J Nucl Med* 57(6):849–854
43. Werner-Wasik M, Nelson AD, Choi W (2012) What is the best way to contour lung tumors on PET scans? Multiobserver validation of a gradient-based method using a NSCLC digital PET phantom. *Int J Radiat Oncol Biol Phys* 82:1164
44. Pinker K, Helbich TH, Morris EA (2017) The potential of multiparametric MRI of the breast. *Br J Radiol* 90(1069):20160715
45. Chen JH, Feig B, Agrawal G, Yu H, Carpenter PM, Mehta RS, Nalcioglu O, Su MY (2008) MRI evaluation of pathologically complete response and residual tumors in breast cancer after neoadjuvant chemotherapy. *Cancer* 112(1):17–26
46. Gulani V, Calamante F, Shellock FG, Kanal E, Reeder SB (2017) Gadolinium deposition in the brain: summary of evidence and recommendations. *Lancet Neurol* 16(7):564–570
47. Kim HR, Jung HK, Ko KH, Kim SJ, Lee KS (2016) Mammography, US, and MRI for preoperative prediction of extensive

- intraductal component of invasive breast cancer: interobserver variability and performances. *Clin Breast Cancer* 16(4):305–311
48. Riola-Parada C, García-Canamaque L, Perez-Duenas V, Garcerant-Tafur M, Carreras-Delgado JL (2016) Simultaneous PET/MRI vs PET/CT in oncology. A systematic review. *Rev Esp Med Nucl Imagen Mol* 35(5):306–312
49. Aristophanous M, Penney BC, Martel MK, Pelizzari CA (2007) A Gaussian mixture model for definition of lung tumor volumes in positron emission tomography. *Med Phys* 34(11):4223–4235
50. Adejolu M, Huo L, Rohren E, Santiago L, Yang WT (2012) False-positive lesions mimicking breast cancer on FDG PET and PET/CT. *Am J Roentgenol* 198(3):W304–W314

Publisher's Note Springer Nature remains neutral with regard to jurisdictional claims in published maps and institutional affiliations.



Correction to: Semi-automatic segmentation from intrinsically-registered 18F-FDG–PET/MRI for treatment response assessment in a breast cancer cohort: comparison to manual DCE–MRI

Maren Marie Sjaastad Andreassen¹ · Pål Erik Goa^{2,3} · Torill Eidhammer Sjøbakk¹ · Roja Hedayati^{4,5} · Hans Petter Eikesdal^{6,7} · Callie Deng¹ · Agnes Østlie³ · Steinar Lundgren^{4,5} · Tone Frost Bathen^{1,3} · Neil Peter Jerome^{1,3}

Published online: 29 October 2019
© The Author(s) 2019

Correction to:
Magnetic Resonance Materials in Physics, Biology and Medicine
<https://doi.org/10.1007/s10334-019-00778-8>

Open Access This article is distributed under the terms of the Creative Commons Attribution 4.0 International License (<http://creativecommons.org/licenses/by/4.0/>), which permits unrestricted use, distribution, and reproduction in any medium, provided you give appropriate credit to the original author(s) and the source, provide a link to the Creative Commons license, and indicate if changes were made.

The original version of this article unfortunately contained a mistake in Fig. 6.

The corrected Fig. 6 is placed in the following page.

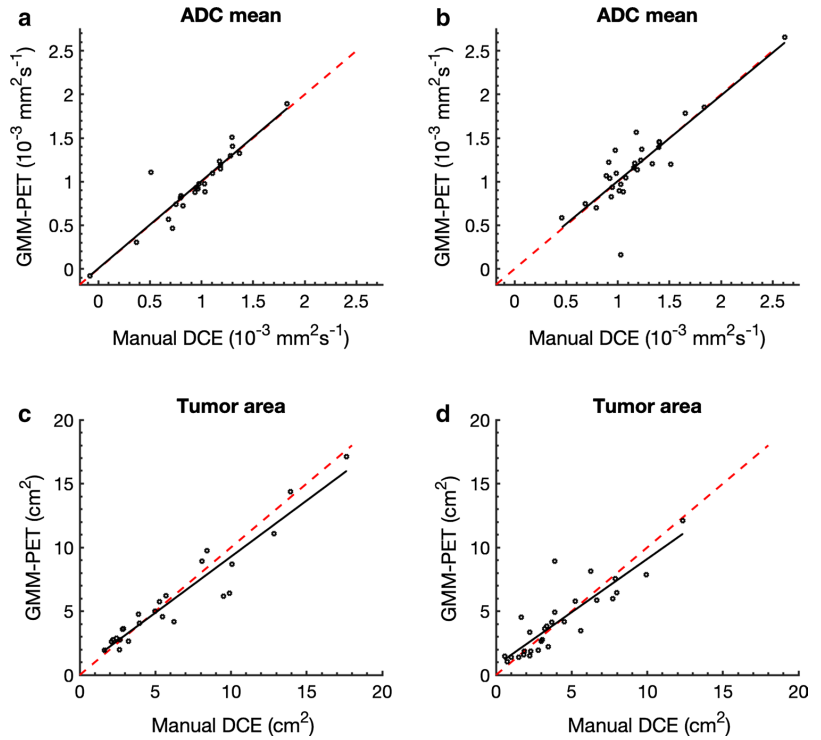
Publisher's Note Springer Nature remains neutral with regard to jurisdictional claims in published maps and institutional affiliations.

The original article can be found online at <https://doi.org/10.1007/s10334-019-00778-8>.

✉ Neil Peter Jerome
neil.p.jerome@ntnu.no




















- ¹ Department of Circulation and Medical Imaging, NTNU, Norwegian University of Science and Technology, Trondheim, Norway
- ² Department of Physics, NTNU, Norwegian University of Science and Technology, Trondheim, Norway
- ³ Department of Radiology and Nuclear Medicine, St. Olav's University Hospital, Trondheim, Norway
- ⁴ Department of Clinical and Molecular Medicine, NTNU, Norwegian University of Science and Technology, Trondheim, Norway
- ⁵ Department of Oncology, St. Olav's University Hospital, Trondheim, Norway
- ⁶ Section of Oncology, Department of Clinical Science, University of Bergen, Bergen, Norway
- ⁷ Department of Oncology, Haukeland University Hospital, Bergen, Norway

Fig. 6 Relationship between the resulting metrics from manual DCE and GMM-PET for **a** ADC mean for untreated lesions ($r=0.866$, $p<0.001$) and **b** treated lesions ($r=0.895$, $p<0.001$) and **m** tumor area from **c** untreated ($r=0.870$, $p<0.0001$) and **d** treated ($r=0.928$, $p<0.001$) lesions. Red identity lines included show that area from GMM-PET is slightly smaller than from manual DCE



Paper II

Characterization of the diffusion signal of breast tissues using multi-exponential models

Ana E. Rodríguez-Soto¹  | Maren M. Sjaastad Andreassen²  | Lauren K. Fang¹  | Christopher C. Conlin¹  | Helen H. Park³  | Grace S. Ahn³  | Hauke Bartsch¹  | Joshua Kuperman¹  | Igor Vidić⁴  | Haydee Ojeda-Fournier¹  | Anne M. Wallace¹  | Michael Hahn¹  | Tyler M. Seibert^{5,6}  | Neil Peter Jerome^{2,7}  | Agnes Østlie⁷ | Tone Frost Bathen^{2,7}  | Pål Erik Goa^{4,7}  | Rebecca Rakow-Penner^{1,6}   | Anders M. Dale¹ 

¹Department of Radiology, University of California San Diego, La Jolla, California, USA

²Department of Circulation and Medical Imaging, NTNU, Norwegian University of Science and Technology, Trondheim, Norway

³School of Medicine, University of California San Diego, La Jolla, California, USA

⁴Department of Physics, NTNU, Norwegian University of Science and Technology, Trondheim, Norway

⁵Department of Radiation Oncology, University of California San Diego, La Jolla, California, USA

⁶Department of Bioengineering, University of California San Diego, La Jolla, California, USA

⁷Department of Radiology and Nuclear Medicine, St. Olav's University Hospital, Trondheim, Norway

Correspondence

Rebecca Rakow-Penner, Department of Radiology, University of California San Diego, 9400 Campus Point Drive #7316, La Jolla, CA 92093, USA.
Email: rrakowpenner@health.ucsd.edu

Funding information

GE Healthcare; California Breast Cancer Research Program; Norges Forskningsråd; Fulbright Scholarship Program; National Institute of Biomedical Imaging and Bioengineering, Grant/Award Number: K08EB026503

Purpose: Restriction spectrum imaging (RSI) decomposes the diffusion-weighted MRI signal into separate components of known apparent diffusion coefficients (ADCs). The number of diffusion components and optimal ADCs for RSI are organ-specific and determined empirically. The purpose of this work was to determine the RSI model for breast tissues.

Methods: The diffusion-weighted MRI signal was described using a linear combination of multiple exponential components. A set of ADC values was estimated to fit voxels in cancer and control ROIs. Later, the signal contributions of each diffusion component were estimated using these fixed ADC values. Relative-fitting residuals and Bayesian information criterion were assessed. Contrast-to-noise ratio between cancer and fibroglandular tissue in RSI-derived signal contribution maps was compared to DCE imaging.

Results: A total of 74 women with breast cancer were scanned at 3.0 Tesla MRI. The fitting residuals of conventional ADC and Bayesian information criterion suggest that a 3-component model improves the characterization of the diffusion signal over a biexponential model. Estimated ADCs of triexponential model were $D_{1,3} = 0$, $D_{2,3} = 1.5 \times 10^{-3}$, and $D_{3,3} = 10.8 \times 10^{-3} \text{ mm}^2/\text{s}$. The RSI-derived signal contributions of the slower diffusion components were larger in tumors than in fibroglandular tissues. Further, the contrast-to-noise and specificity at 80% sensitivity of DCE and a subset of RSI-derived maps were equivalent.

Conclusion: Breast diffusion-weighted MRI signal was best described using a triexponential model. Tumor conspicuity in breast RSI model is comparable to that of DCE without the use of exogenous contrast. These data may be used as differential features between healthy and malignant breast tissues.

KEYWORDS

breast MRI, DWI, DW-MRI, restriction spectrum imaging, RSI

1 | INTRODUCTION

The American Cancer Society recommends that women at high risk for breast cancer receive both mammography and MRI exams yearly starting at age 30.¹ Breast MRI is also currently used for evaluating new breast cancer diagnosis² and response to neoadjuvant chemotherapy.³ Clinical breast MRI protocols include DCE-MRI, which requires intravenous administration of gadolinium-based contrast agents to visualize vascular patterns (i.e., tumor angiogenesis).⁴ Despite high sensitivity for breast cancer detection, DCE-MRI faces a number of challenges such as lengthy acquisition protocols, dependency on expert radiologist readers, and conflicting results regarding detection specificity.^{5–9} Further, such contrast agents have been linked to brain deposition with unknown sequelae,¹⁰ and some are contraindicated in patients with renal failure and pregnant women.¹¹ Hence, there is a need to develop highly specific and sensitive methods to improve breast cancer detection.

MRI has higher diagnostic accuracy compared to mammography and ultrasound in women at high risk for breast cancer or with dense breasts.¹² Breast MRI protocols typically consist of fat-suppressed T_2 -weighted imaging, pre- and multi-phased dynamic postcontrast T_1 -weighted imaging, and DWI.¹³ DW-MRI has been more recently introduced into breast MRI protocols as a promising screening tool for breast cancer. Conventional DW-MRI has demonstrated potential for discriminating predefined benign and malignant breast lesions.^{14–16} The combined use of DCE- and DW-MRI improves sensitivity and specificity in cancer detection compared to either technique individually.⁴

DW-MRI probes the diffusion of water in tissues, allowing for the characterization of tissue microstructure across different histologies.¹⁷ In fact, evidence suggests that cancers diagnosed with MRI are more likely to be invasive than those detected with mammography.¹⁸ Despite the quantitative nature of DW-MRI, resulting images are sometimes used to qualitatively inform clinical MRI exam interpretation.^{14,19} Cancer lesions are conspicuous on these images due to the combined effect of

lengthened T_2 and the shift in the relative size between slow- and fast-water diffusion components in neoplasms compared to fibroglandular tissue.^{19,20} This effect is enhanced by the fact that breast DW-MRI data are typically fat-suppressed,¹³ thereby further increasing tumor-to-background contrast. However, inadequate fat suppression and the presence of additional ongoing biological processes (e.g., edema or lactation) may affect the extracted diffusion estimates and image interpretation.^{21,22} Thus, there is a need for DW-MRI models that fully capture and allow for the differentiation of breasts complex tissue microstructure.

Restriction spectrum imaging (RSI) is an advanced DW-MRI technique that has previously demonstrated potential in improving tumor conspicuity when evaluating disease severity and response to treatment in brain^{23,24} and prostate.^{25,26} In RSI, an advanced linear mixture model is used to decompose the DW-MRI signal into separate water diffusion components such as restricted, hindered, and free water pools. Changes in the signal intensity between voxels is considered to result from changes in the relative size of these intravoxel water compartments. Further, the RSI model does not normalize by signal at $b = 0$ s/mm², as it is done in conventional DW-MRI estimates. As a result, RSI outputs display the joint effect of changes in diffusion properties and T_2 due to the presence of cancer in tissues microenvironment. For different organs, the number of discernable diffusion components and their corresponding diffusion coefficients have been determined empirically and theoretically.²⁷

Previously, Vidić et al. demonstrated that a normalized biexponential model was able to discriminate between predefined regions of interest (ROIs) of benign and malignant breast lesions but did not explore additional diffusion components or assess optimal diffusion coefficients for both cancer and healthy breast tissues.²⁸ Considering the complex tissue microenvironment in the breast, we hypothesized that the RSI framework will be helpful in improving tumor conspicuity. Thus, the purpose of this work was to determine the optimal number of RSI diffusion components and their corresponding apparent diffusion coefficients (ADCs) for breast tissues.

2 | METHODS

2.1 | Subjects

Patients from 2 different institutions (sites) with known breast lesions were invited to participate in this study before receiving treatment, and they underwent a breast MRI at 3.0 Tesla (T) before treatment began. Only patients with malignant lesions confirmed by histopathologic analysis were included in this study. This study was approved by the institutional review boards from both sites. All participants provided both oral and written consent.

Patients were from 2 sites: 57 women from site 1 and 25 women from site 2 were enrolled in this study. From site 1, a total of 8 participants were excluded from the study: 6 women had contralateral cancer or mastectomy, and in 2 cases DW-MRI data were of low quality.

2.2 | MRI data collection

Data from 2 sites were used to increase the applicability of the model across acquisition protocols and vendors. Data at site 1 were collected using a 3T MR750 scanner (DV25-26, GE Healthcare, Milwaukee, WI) and an 8-channel breast array coil. Pulse sequence parameters were *axial DCE-MRI 3D fast spoiler gradient-recalled acquisition*: TE = 2.6 ms, TR = 5.4 ms, flip angle = 10°, FOV = 320 × 320 mm², acquisition matrix 512 × 406, reconstruction matrix 512 × 512, and voxel size 0.625 × 0.625 × 2.4 mm³; *axial T₂ fat suppressed fast spin echo*: TE/TR = 107/4520 ms, flip angle = 111°, FOV = 320 × 320 mm², acquisition matrix 512 × 320, and voxel size = 0.625 × 0.625 × 5 mm³; *axial reduced-FOV EPI DW-MRI*: TE/TR = 82/9000 ms, *b* values (number of diffusion directions) = 0, 500 (6), 1500 (6), and 4000 (15) s/mm², FOV = 160 × 320 mm², acquisition matrix 48 × 96, voxel size = 2.5 × 2.5 × 5 mm³, spectral attenuated inversion recovery fat suppression, phase-encoding direction anteroposterior, and no parallel imaging.

Data at site 2 were collected using a 3T Skyra scanner (VD13-VE11, Siemens, Erlangen, Germany) and 16-channel breast array coil. Pulse sequence parameters were *sagittal DCE-MRI 3D FLASH acquisition*: unilateral sagittal plane, TE/TR = 2.2/5.8 ms, flip angle = 15°, FOV = 180 × 180 mm², acquisition matrix 256 × 256, reconstruction matrix 256 × 256, voxel size 0.7 × 0.7 × 2.5 mm³, and GRAPPA with acceleration factor of 2 and 36 reference lines; *sagittal T₂ fast spin echo*: unilateral sagittal plane, TE/TR = 118/5500 ms, flip angle = 120°, FOV = 180 × 180 mm², acquisition matrix 256 × 256, and voxel size = 0.7 × 0.7 × 2.5 mm³; *sagittal EPI DW-MRI*: unilateral sagittal plane, TE = 88 ms, TR = 10,600 ms for 15 participants and TR = 11,800 ms for 10 participants, *b* values = 0, 200 (6), 600 (6),

1200 (6), 1800 (6), 2400 (6), and 3000 (6) s/mm², FOV = 180 × 180 mm², acquisition matrix 90 × 90, and voxel size = 2.0 × 2.0 × 2.5 mm³. Spectral fat saturation in strong mode was used on 15 participants, and spectral attenuated inversion recovery fat suppression was used on 10 participants, phase-encoding direction anteroposterior, GRAPPA with acceleration factor of 2 and 24 reference lines.

The *b* = 0 s/mm² volumes at both sites were collected in the anteroposterior and posteroanterior phase-encoding directions to correct DW-MRI data for geometric and intensity distortions due to B₀ inhomogeneities using the reverse polarity gradient method.²⁹

2.3 | DW-MRI data preprocessing

Analyses were performed using MatLab R2016b (MathWorks, Natick, MA). The noise probability density function of MRI data when using multiple-receiver coils and sum of squares reconstruction is a noncentral chi distribution.³⁰ Thus, the noise floor was estimated by first masking out all voxels within the body, and the average of the peak corresponding to the background signal was found as determined from the histogram of the DW-MRI data at the maximum *b* value. Diffusion-weighted data were noise corrected by subtracting the noise floor value from all voxels. In order to evaluate data quality before fitting, the SNR was estimated as average signal within cancer or fibroglandular ROIs divided by the SD of a background ROI at each *b* value.

All diffusion directions for a determined *b* value were averaged. Data were then normalized by the 98th percentile signal intensity value in *b* = 0 s/mm² volume. In contrast to conventional ADC estimation, in RSI the DW-MRI signal is not divided by *b* = 0 s/mm², thus preserving T₂ information. The following volumetric ROIs were manually drawn on the resulting images, informed by all available data in the exam protocol (including DCE and T₂-weighted images): (i) control regions including either the cancer-free contralateral breast (site 1) or regions without cancer in the ipsilateral breast at least 10 mm away from the cancer lesion (site 2), (ii) whole-volume cancer lesions, and (iii) background regions. Control ROIs excluded the axillary region, large cysts (>2.5 cm), and susceptibility artifacts (e.g., from surgical clips). Control ROIs were initially drawn as boxes and were masked using binarized T₂-weighted images, resampled to DW-MRI space, to remove the background from the ROI. Volumetric cancer ROIs were manually drawn on the averaged DW images. All cancer ROIs were validated by a breast radiologist at each site (R.R.P. and A.Ø.). Examples of these ROIs are shown in Supporting Information Figures S1 and S2. In order to

investigate the differences in RSI estimates between cancer and noncancerous tissues in breast, fibroglandular tissue, and fatty tissue ROIs were generated by thresholding the $b = 0$ s/mm² volume. The threshold was determined (using MatLab graythresh function) within the initial control ROI in the $b = 0$ s/mm² volume.

2.4 | RSI modeling

In RSI, the diffusion signal was modeled as the linear combination of multiple exponential decays:

$$S_{diff}(b, N) = \sum_{i=1}^N C_{i,N} e^{-bD_{i,N}} = S_0 \sum_{i=1}^N e^{-bD_{i,N}}, \quad (1)$$

where N is the total number of exponential decays (here 2 and 3); $C_{i,N}$ are the signal contributions of each exponential component; b are the b values; $D_{i,N}$ are the apparent diffusion coefficients of each exponential component; and $D_{1,N} < D_{2,N} < D_{3,N}$. Note that in RSI, $D_{i,N}$ are fixed to allow for comparison of signal contributions $C_{i,N}$ across different tissues. The signal contributions $C_{i,N}$ include information on the proton density and T_2 properties of each voxel, which are contained in the $b = 0$ s/mm² volume, S_0 . The fractional contributions, $f_{i,N}$, of each signal component $C_{i,N}$ were also estimated as:

$$S_{diff}(b, N) = S_0 \sum_{i=1}^N f_{i,N} \text{ and } f_{i,N} = \frac{C_{i,N}}{\sum_i C_{i,N}}. \quad (2)$$

In order to determine the apparent diffusion coefficients ($D_{i,N}$) to describe breast tissues, global fittings of bi- and triexponential models to DW-MRI data from cancer and control ROIs were performed. A simplex search was performed using the built-in MatLab R2016b (MathWorks) function `fminsearch` to minimize the sum-of-squared difference between the observed and fitted signal values across all voxels. A nonnegative least squares fit of the current estimates for $D_{i,N}$ was used to estimate the fitted $C_{i,N}$ values at each iteration of the minimization. To enforce nonnegativity on $D_{i,N}$ for each compartment, this optimization procedure was performed on the $\log(D_{i,N})$ values, which were then exponentiated afterwards. No upper bounds were imposed on the possible values for $D_{i,N}$.²⁷ After $D_{i,N}$ were determined, maps of the signal contributions of each exponential component $C_{i,N}$ were estimated via nonnegative least-squares fitting of the model to the signal versus b value curve from each voxel.²⁷

The relative-fitting residual and relative Bayesian information criterion (BIC) were calculated for both bi- and triexponential models. Relative-fitting residual was calculated as the difference between observed and predicted

diffusion-weighted signal divided by the observed signal in all ROIs, as well as for conventional ADC maps of b values $\leq 1,500$ s/mm². The BIC was used because it penalizes the model's likelihood for increasing the number of estimated parameters.³¹ Lower BIC values denote improved model fitting. However, absolute BIC values are arbitrary; therefore, we report the difference in BIC ($\Delta\text{BIC} = \text{BIC}_{\text{bi}} - \text{BIC}_{\text{tri}}$).

In order to compare tumor conspicuity on RSI outputs ($C_{i,N}$) to the gold standard and other conventional DW-MRI methods, the contrast-to-noise (CNR) ratio was approximated as the average signal of tumor divided by the average signal of fibroglandular tissue. The CNR was estimated for $C_{i,N}$, conventional ADC and DCE.

2.5 | Statistical analysis

Statistical analyses were performed using SPSS statistics software (version 26 for Mac OS X, IBM Corp., Armonk, NY). All signal contributions are reported as median, interquartile range, and range values. Kolmogorov-Smirnov test was used to examine data normality, and related-samples Friedman's 1-way analysis of variance by ranks tests were used to identify differences in $C_{i,N}$ and $f_{i,N}$ signal contributions and CNR across diffusion components and tissues (cancer vs. fibroglandular tissue). The threshold for significance (α) was set at 0.05 for all analyses. In order to investigate the robustness of RSI to SNR, we performed our fitting analysis using only data of b values $\leq 1,500$ s/mm² and found that the estimated $D_{i,N}$ values were the same as those in the original analysis. The area under the curve (AUC) of receiver operating characteristic curves was used to evaluate the diagnostic value of normalized and non-normalized RSI outputs, DCE, and ADC. The specificity of each parameter at 80% specificity is also reported.

3 | RESULTS

Demographic information can be found in Table 1. Representative images of both sites are shown in Figure 1. The diffusion signals of control and tumor ROIs were then fitted by bi- and triexponential models to estimate fixed ADCs.

3.1 | SNR in cancer and fibroglandular tissue ROIs

The SNR of data from site 2 was lower than that from site 1. In general, SNR was higher at low non-zero b values than at $b = 0$ s/mm² for both cancer and fibroglandular tissue ROIs (Table 2). This was due to the averaging of

Characteristics	Site 1	Site 2
Number of lesions	50	25
Average patient age, years (range)	47.6 ± 11.5 (27–73)	52.8 ± 11.2 (29–75)
Histological type		
Carcinoma with medullary features		3
DCIS	1	1
IDC	42	17
ILC	4	1
Metaplastic carcinoma	2	
Mixed IDC and ILC	1	
Mucinous carcinoma		1
Papillary carcinoma		1
Tubular carcinoma		1

TABLE 1 Demographic information of participants

Abbreviations: DCIS, ductal carcinoma in situ; IDC, invasive ductal carcinoma; ILC, invasive lobular carcinoma.

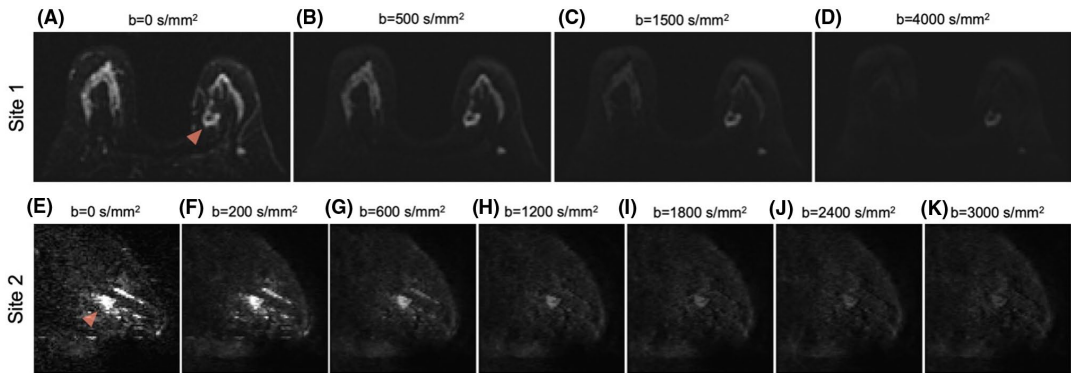


FIGURE 1 Images from DW-MRI were averaged over all diffusion directions for each b value and noise-corrected. Representative images at different b values and for both sites (top and bottom rows) are shown. DW, diffusion-weighted

Site	B value (s/mm^2)	Median Cancer SNR (IQR)	Median FBG Tissue SNR (IQR)	Median Fat SNR (IQR)
1	0	88.7 (82.6)	51.5 (48.5)	9.8 (7.0)
	500	119.6 (111.0)	52.7 (47.3)	15.2 (7.7)
	1500	65.6 (61.8)	18.5 (13.0)	11.1 (4.7)
	4000	39.8 (46.3)	13.6 (11.3)	13.5 (8.5)
2	0	57.1 (18.8)	10.6 (10.5)	8.6 (5.7)
	200	84.8 (49.3)	15.7 (13.0)	13.0 (6.6)
	600	59.2 (24.5)	11.6 (6.5)	10.3 (5.5)
	1200	39.6 (18.7)	9.7 (4.7)	9.1 (4.2)
	1800	29.5 (12.3)	8.8 (4.1)	8.7 (3.0)
	2400	22.6 (8.5)	8.5 (4.5)	8.0 (3.1)
	3000	19.1 (6.3)	8.2 (3.2)	7.6 (3.7)

TABLE 2 SNR for cancer and FBG ROIs after noise correction and averaging over diffusion directions of the same b value for each site

Abbreviations: FBG, fibroglandular; IQR, interquartile range.

diffusion directions at non-zero b values. As expected, the SNR became progressively lower at higher b values. The lowest median SNR was 19.1 (interquartile range 6.3) and 8.2 (interquartile range 3.2) for cancer and fibroglandular tissue, respectively.

3.2 | RSI model for breast

The relative-fitting residuals of conventional ADC and of bi- and triexponential models in control ROIs were 2.1%, 1.6%, and 1.0% of the overall signal value, whereas the residuals for the cancer ROIs were 3.3%, 1.0%, and 0.3%, respectively. Residuals were considerably smaller for the triexponential model. Similarly, a Δ BIC of 74 was estimated between the bi- and triexponential models, indicating that a triexponential model further improves the fitting of breast DW-MRI data.

Estimated diffusion coefficients using the biexponential model were $D_{1,2} = 2.8 \times 10^{-5}$ and $D_{2,2} = 2.4 \times 10^{-3}$ mm²/s; and $D_{1,3} = 1.6 \times 10^{-17}$, $D_{2,3} = 1.5 \times 10^{-3}$, and $D_{3,3} = 10.8 \times 10^{-3}$ mm²/s for the triexponential model (Table 3). The determined diffusion coefficients for each site were $D_{1,2} = 4.8 \times 10^{-5}$ and $D_{2,2} = 2.2 \times 10^{-3}$ mm²/s and $D_{1,2} = 8.6 \times 10^{-7}$ and $D_{2,2} = 2.9 \times 10^{-3}$ mm²/s for site 1 and site 2, respectively. Similarly, when using 3 exponentials, we calculated the diffusion coefficients to be $D_{1,3} = 6.5 \times 10^{-6}$, $D_{2,3} = 1.2 \times 10^{-3}$, and $D_{3,3} = 4.6 \times 10^{-3}$ mm²/s for site 1; and $D_{1,3} = 2.1 \times 10^{-18}$, $D_{2,3} = 1.9 \times 10^{-3}$, and $D_{3,3} = 16.5 \times 10^{-3}$ mm²/s for site 2. In all cases, for the triexponential model the slowest diffusion coefficients $D_{1,3}$ is far smaller than can be quantified accurately. Thus, in this RSI model for breast $D_{1,3}$ was set to 0 mm²/s, replacing the slowest diffusion component with a constant offset term ($C_{1,3}$).

The signal contributions $C_{i,N}$ for cancer and fibroglandular tissue ROIs were not significantly different ($P > 0.05$) when estimated using $D_{1,3} = 1.6 \times 10^{-17}$ mm²/s and $D_{1,3} = 0$ mm²/s for the triexponential model. The diffusion

signal of all tissues was then described with the following 3-component model:

$$S_{diff}(b) = C_{1,3} + C_{2,3}e^{-b \cdot 1.5 \times 10^{-3}} + C_{3,3}e^{-b \cdot 10.8 \times 10^{-3}}$$

Because the magnitudes of $D_{1,N}$ were so small, we investigated if the source of this restricted diffusion was the fatty tissue voxels in control ROIs. Thus, we performed the same RSI model fitting, excluding fatty tissue voxels, and found that $D_{1,N}$ were very similar to those from the original analysis, including fatty tissue in control ROI (see Table 3, last column).

3.3 | RSI estimates in breast cancer and fibroglandular tissue

The signal contributions of RSI $C_{i,N}$ and $f_{i,N}$ and estimated conventional ADC values within cancer and fibroglandular ROIs are shown in Table 4. The ADC values between tumor and fibroglandular tissue were not statistically different from each other; however, they displayed a trend toward statistical difference ($p = 0.065$) (Figure 2A).

Median cancer and fibroglandular tissue signal contributions ($C_{i,N}$) for biexponential and 3-component models are shown in Figure 2B. The signal contribution attributed to the slowest diffusion compartments from the biexponential model ($C_{1,2}$) was different ($p < 0.05$) between cancer and fibroglandular tissues. Similarly, the signal contribution of the 2 slowest components derived from the 3-component model ($C_{1,3}$ and $C_{2,3}$) were also different between tumor and fibroglandular tissue ROIs ($p < 0.05$). In terms of the normalized signal contributions, the biexponential model $f_{1,2}$, $f_{2,2}$, and $f_{1,3}$ were higher ($p < 0.05$) in cancer ROIs than in fibroglandular tissue (Figure 2C) (Table 4). In contrast, $f_{3,3}$, the compartment attributed to the fastest diffusion, was higher ($p < 0.05$) in fibroglandular tissue than in cancer tissues.

TABLE 3 Diffusion coefficients of RSI bi- and triexponential breast model estimated for each site and together

Model	Parameter	Site 1 (mm ² /s)	Site 2 (mm ² /s)	Joint Model (mm ² /s)	Joint Model Excluding fat (mm ² /s)
Biexponential	$D_{1,2}$	4.8×10^{-5}	8.6×10^{-7}	2.8×10^{-5}	5.8×10^{-5}
	$D_{2,2}$	2.2×10^{-3}	2.9×10^{-3}	2.4×10^{-3}	2.3×10^{-3}
Three-component	$D_{1,3}$	6.5×10^{-6}	2.1×10^{-18}	1.6×10^{-17}	9.8×10^{-7}
	$D_{2,3}$	1.2×10^{-3}	1.9×10^{-3}	1.5×10^{-3}	1.4×10^{-3}
	$D_{3,3}$	4.6×10^{-3}	16.5×10^{-3}	10.8×10^{-3}	7.2×10^{-3}

Abbreviation: RSI, restriction spectrum imaging.

TABLE 4 Average signal contribution of the FBG tissue and cancer ROIs for biexponential and 3-component models

Model	Parameter	Cancer		FBG Tissue		P Value
		Median (range)	IQ Range	Median (range)	IQ Range	
Conventional ADC (mm ² /s)	ADC (×10 ⁻³)	0.93	0.30	1.1	1.1	<i>p</i> > 0.05
Biexponential	C _{1,2}	1.43	1.76	0.51	0.30	<i>p</i> < 0.05*
	C _{2,2}	5.25	6.16	3.11	3.70	<i>p</i> > 0.05
	f _{1,2}	0.31	0.21	0.14	0.18	<i>p</i> < 0.05*
	f _{2,2}	0.69	0.21	0.86	0.17	<i>p</i> < 0.05*
Three-component	C _{1,3}	1.02	1.15	0.37	0.19	<i>p</i> < 0.05*
	C _{2,3}	5.17	6.89	2.52	3.42	<i>p</i> < 0.05*
	C _{3,3}	0.31	0.52	1.01	1.10	<i>p</i> > 0.05
	f _{1,3}	0.22	0.20	0.10	0.17	<i>p</i> < 0.05*
	f _{2,3}	0.72	0.27	0.62	0.26	<i>p</i> > 0.05
	f _{3,3}	0.09	0.11	0.25	0.17	<i>p</i> < 0.05*

Signal contributions C_{i,N} are in arbitrary units, and f_{i,N} are normalized.

Abbreviation: ROIs, regions of interest.

In order to understand the relationship of the multiple signal contributions in the 3-component model, the average values for each subject were plotted between tissues (Figure 3). These plots showed that tumor ROIs present larger signal in both C_{1,3} and C_{2,3} compared to fibroglandular tissue. Further, given that data were collected with fat suppression, the signal contributions in fatty tissue were minimal.

To test the generality of the 3-component model, we compared the signal contributions in cancer ROIs across models determined with data from each site and together (Supporting Information Table S1). We found that in cancer tissues, the signal contributions C_{3,3} and f_{3,3} generated from the individual site models were different (*p* < 0.05) from each other. Similarly, in fibroglandular tissue, the fractional signal contribution f_{3,3} was different (*p* < 0.05) across individual site models.

3.4 | CNR between cancer lesions and fibroglandular tissue

Results of CNR between tumor and fibroglandular tissue are shown in Table 5 (and Supporting Information Figure S3). Compared to DCE, the CNR of all DW-MRI estimates was lower (*p* < 0.05), with the exception of signal contributions of the slowest compartments in RSI models C_{1,3} and C_{2,3}, and f_{1,3}. Further, the CNR of conventional ADC was lower (*p* < 0.05) than that of DCE and of C_{1,2}, C_{1,3}, and f_{1,3} RSI signal contributions. In contrast, the CNR of C_{3,3} and f_{3,3} was higher (*p* < 0.05) than that of ADC. This means that RSI signal contributions C_{2,2}, C_{2,3}, f_{1,2}, and f_{2,2} yielded similar CNR to that of conventional ADC (Figure 4).

3.5 | Performance of DCE, ADC and RSI to differentiate cancer lesions from fibroglandular tissue

The AUCs of DCE and ADC were 0.79 and 0.46, respectively (Table 5). The AUCs of the 2 slowest compartments of the non-normalized RSI outputs C_{1,2}, C_{2,2}, C_{1,3}, and C_{2,3} were comparable or higher than those of DCE (0.94, 0.77, 0.90, and 0.84, respectively). The AUC of C_{3,3} was 0.36. Of the normalized RSI outputs, f_{2,3} had the highest AUC (0.78), whereas the rest were much lower (f_{1,2} = 0.54, f_{2,2} = 0.46, f_{1,3} = 0.51, and f_{3,3} = 0.26). The specificity of DCE at 80% sensitivity was of 81% in this cohort, whereas that of conventional ADC was only 34.3%. The 3 RSI outputs with the highest specificity were C_{1,2} (90.8%), C_{1,3} (82.2%), and C_{2,3} (73.5%).

4 | DISCUSSION

In the RSI framework, the diffusion-weighted MR signal is fit to an organ-specific multi-exponential model containing fixed ADCs. By doing so, direct comparison of the signal from each model component (attributed to different water pools) can be performed across tissues. The RSI framework is also characterized by the inclusion of signal from all relevant tissues, including cancer lesions, into an organ-specific model. This strategy has been shown to improve tumor conspicuity in prostate and brain applications.^{27,32} Here, we determined the RSI model parameters for breast and compared lesion conspicuity across RSI-derived maps, conventional ADC, and the clinical standard DCE.

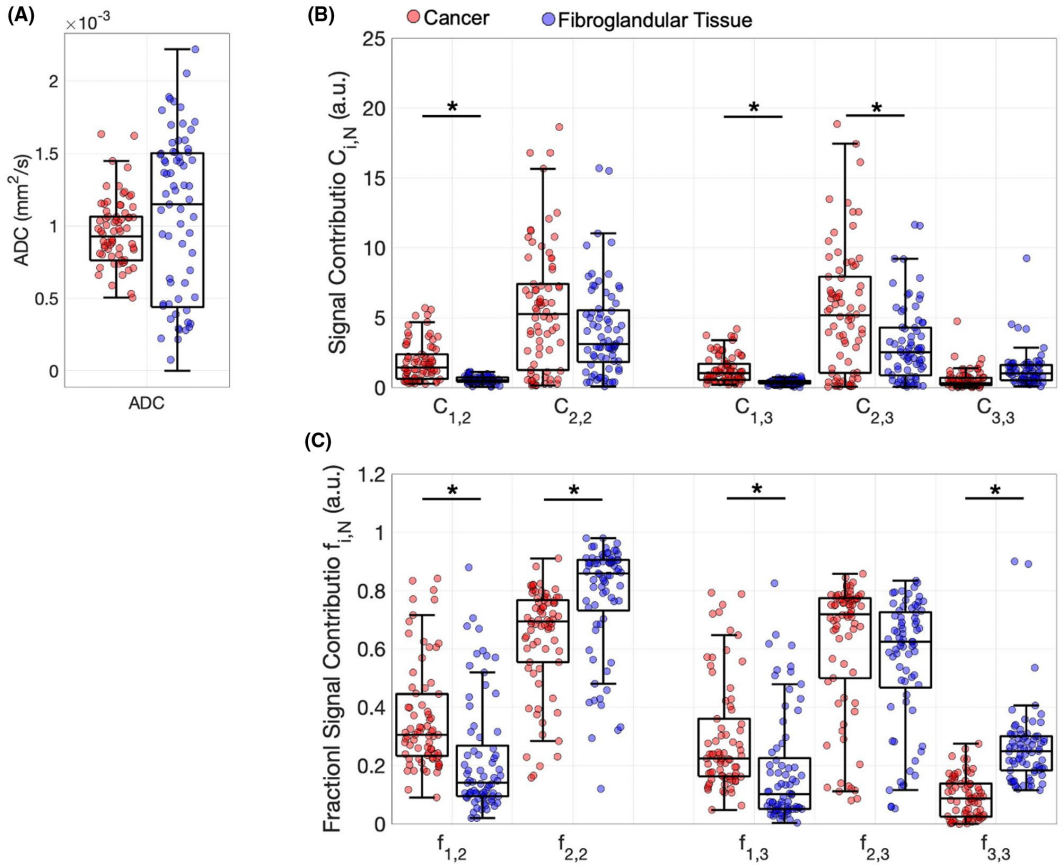


FIGURE 2 Boxplot of (A) conventional ADC, (B) median signal contributions of the components of the biexponential and 3-component model, and (C) median fractional signal contributions within cancer (red) and control (blue) ROIs. In both models, the magnitude of the components of cancer and control ROIs were statistically different ($p < 0.05$, horizontal bars). ADC, apparent diffusion coefficients; ROIs, regions of interest

DW-MRI data at high b values are strongly affected by the presence of noise, which has a distribution that depends on the utilized coils and reconstruction methods.³³ In RSI, data are inherently noisy due to the use of high b values. We found that the median SNR within cancer lesions and fibroglandular tissue ROIs was ≥ 20 and ≥ 8 , respectively. Although no consensus has been reached as to the necessary SNR to accurately estimate conventional DW-MRI estimates for breast applications,³⁴ an SNR >20 has been suggested to be adequate.³⁵ However, these SNR guidelines were made for voxel-wise quantitative DW-MRI, whereas in RSI all voxels are fit simultaneously. Our results suggests that that the SNR requirements for RSI modeling are more lenient than those for conventional DWI estimates.

In the present work, we used 2 and 3 diffusion components to describe the diffusion signal of breast tissues

and determine the corresponding diffusion coefficients of each exponential component. The ΔBIC ($BIC_{bi} - BIC_{tri}$) results suggest that a 3-component model improves the characterization of the diffusion signal over a biexponential model. Further, the relative-fitting residuals when using a 3-component model are 2 and 10 times smaller in control and cancer ROIs, respectively, compared to conventional ADC.

In the present study, DW-MRI data acquisition differed between sites. The rationale to include data from different protocols, MRI scanners, and vendors was to increase the generalizability of the models determined here. A limitation of this setup may be the difference in TEs of DW-MRI data between sites (82 and 88 msec). However, given the TEs used and T₂ values of fibroglandular and cancer tissues (46 and 68 msec, respectively) at 3T,²⁰ the expected signal decay due to T₂

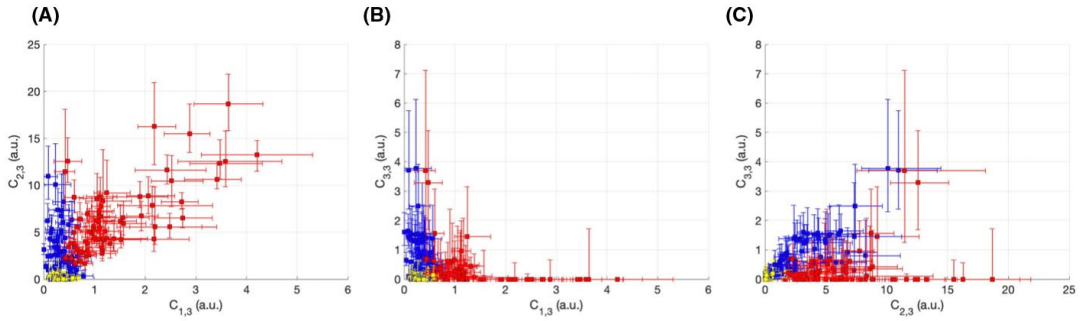


FIGURE 3 $D_{i,N}$ of a 3-component model ($S_{diff}(b) = C_{1,3} + C_{2,3}e^{-bD_{2,3}} + C_{3,3}e^{-bD_{3,3}}$) were determined by simultaneously fitting both control and cancer ROIs of both sites. Values of $D_{i,N}$ were then fixed ($D_{2,3} = 1.4 \times 10^{-3} \text{ mm}^2/\text{s}$, and $D_{3,3} = 10.2 \times 10^{-3} \text{ mm}^2/\text{s}$) and used to estimate the $C_{i,N}$. Two-dimensional plots of the magnitude of (A) $C_{1,3}$ versus $C_{2,3}$, (B) $C_{1,3}$ versus $C_{3,3}$, and (C) $C_{2,3}$ and $C_{3,3}$ are shown for fibroglandular tissue (blue circles), fatty tissue (yellow squares), and cancer (red squares) ROIs. Circles and bar represent the $C_{i,N}$ ROI median and 25th and 75th percentiles for each subject. $C_{i,N}$, signal contribution of each component; $D_{i,N}$, fixed apparent diffusion coefficients of each component

Parameter	Median CNR	CNR Interquartile range (range)	AUC	Specificity at 80% Sensitivity (%)
DCE	5.1	4.5 (0.7–17.8) †	0.79	81.0
ADC	0.8	1.0 (0.3–11.4) ‡	0.46	34.3
$C_{1,2}$	2.8	3.1 (0.6–11.9) ‡†	0.94	90.8
$C_{2,2}$	1.3	2.0 (0–22.0) ‡	0.77	61.6
$C_{1,3}$	2.9	3.2 (0.5–48.5) †	0.90	82.2
$C_{2,3}$	1.6	3.0 (0.1–39.0)	0.84	73.5
$C_{3,3}$	0.5	0.7 (0–3.1) ‡†	0.36	*
$f_{1,2}$	2.2	2.1 (0.3–41.3) ‡	0.54	44.2
$f_{2,2}$	0.8	0.2 (0.2–2.6) ‡	0.46	35.2
$f_{1,3}$	2.2	3.5 (0.3–45.2) †	0.51	40.4
$f_{2,3}$	1.1	0.4 (0.2–5.9) ‡	0.78	66.4
$F_{3,3}$	0.3	0.5 (0–1.2) ‡†	0.26	*

Abbreviations: AUC, area under the curve; CNR, contrast-to-noise ratio.

‡Statistical difference compared to DCE.

†Statistical difference compared to ADC.

*Maximum sensitivity of 44% and corresponding specificity of 25%.

effects is somewhat similar (~70%–85%) across sites for both tissues. The RSI model parameters estimated from each site revealed that the estimated ADCs of the faster compartments (for both bi- and triexponential models) are larger in data from site 2. This is attributed to both the differences in TE between sites and the inclusion of more b values, which improve the characterization of the diffusion-weighted signal curve between zero and $500 \text{ s}/\text{mm}^2$. Similarly, the estimated diffusion coefficient of the slowest component of the RSI 3-component model appears to be driven by the data from site 2. However, the diffusion coefficients of both sites are smaller than what can be accurately quantified in studies using

clinical scanners. Importantly, the signal contributions within tumor ROIs were overall not different when estimated using the models determined from each site independently. Thus, suggesting that the joint RSI breast model established here may be applied to data acquired with different parameters within a certain range. Future work will focus on testing the validity and limitations of this model on an independent sample.

Control ROIs included fatty tissue voxels because in breast RSI the tissues that are not cancer are considered background and are included in the model fitting process. The definition of the control ROI used to determine the RSI model directly impacts the estimated ADC values.

TABLE 5 Median CNR, AUC, and specificity at 80% sensitivity between cancer and FBG tissues extracted from RSI-derived maps and compared to DCE MRI and conventional ADC

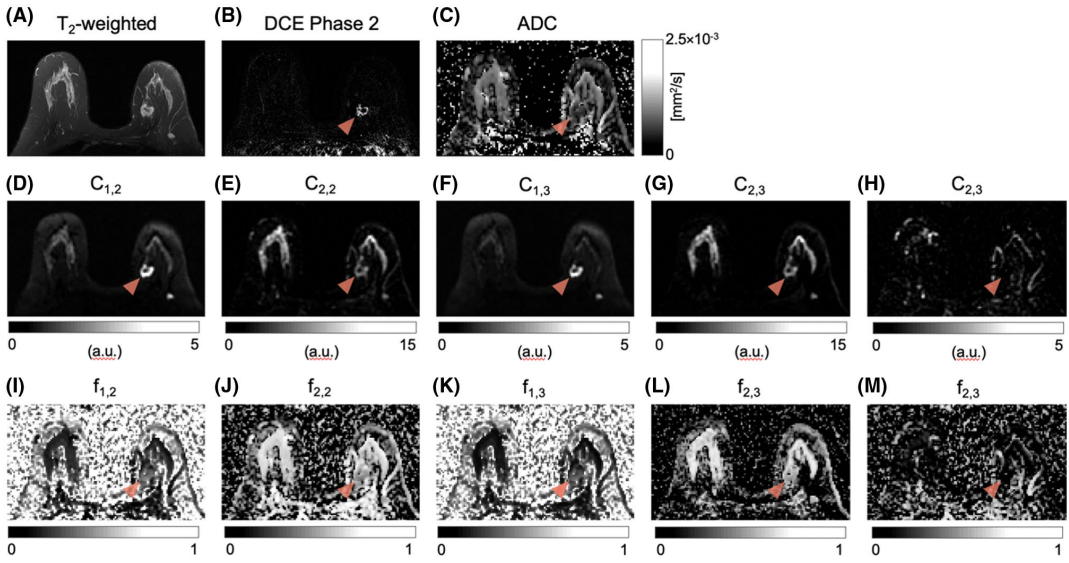


FIGURE 4 Processed images from patient from site 1 in Figure 1, including images from site 1 such as (A) T₂-weighted and (B) DCE images, (C) conventional apparent diffusion coefficient map, and the signal contributions (C_{i,N}) of biexponential (D-E) and 3-component (F-H) models. The fractional signal contributions are also shown for biexponential (I-J) and 3-component (K-M) models. Arrowheads indicate tumor location. Signal contribution in tumors was higher than surrounding tissues in both C_{1,N} and C_{2,N} in both models. The compartment C_{3,3} displays vascular flow information

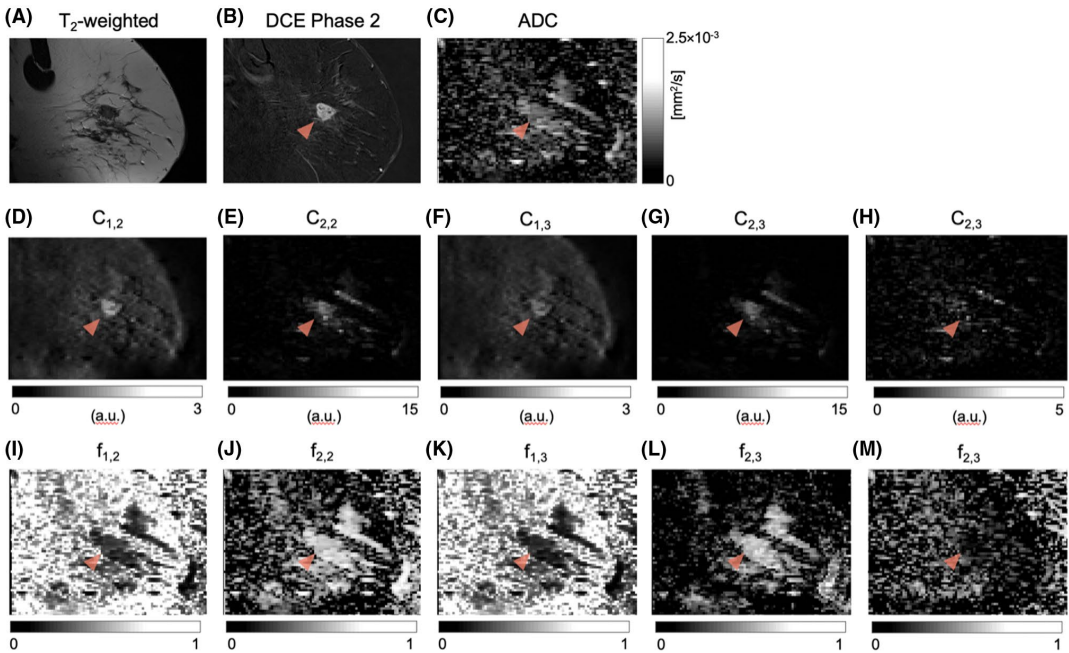


FIGURE 5 Processed images from patient from site 2 in Figure 1, including (A) T₂-weighted and (B) DCE images, (C) conventional apparent diffusion coefficient map, and the signal contributions (C_{i,N}) of biexponential (D-E) and 3-component (F-H) models. The fractional signal contributions are also shown for biexponential (I-J) and 3-component (K-M) models. Arrowheads indicate tumor location

Thus, we excluded fatty tissue from the RSI breast model fitting process and found that the main difference between RSI models was in $D_{3,3}$ (excluding fatty tissue $D_{3,3} = 7.2 \times 10^{-3} \text{ mm}^2/\text{s}$ vs. including fatty tissue $D_{3,3} = 10.8 \times 10^{-3} \text{ mm}^2/\text{s}$). These results indicate that by removing fatty tissue from the analysis, the component attributed to pseudo-diffusion evolves at a slower rate due to the exclusion of low signal in fatty tissue. Finally, these data suggest that water in both cancer and fibroglandular tissue also experiences restricted diffusion. The amount of water molecules experiencing restricted diffusion appears to be higher in tumor tissues (Figure 3A).

Representative DW-MRI-derived maps for each site are shown in Figures 4 and 5, together with T_2 -weighted and DCE images as well as conventional ADC (b values $\leq 1,500 \text{ s/mm}^2$) maps (Figures 4A–C and 5A–C). Tumor signal contributions in RSI outputs $C_{1,2}$ and $C_{1,3}$ (Figures 4D,F and 5D,F) displayed higher intensities than in fibroglandular tissues, whereas signals of both tumors and fibroglandular tissues were similar in $C_{2,2}$ and $C_{2,3}$ (Figures 4E,G and 5E,G). Thus, $C_{1,3}$ and $C_{2,3}$ signals were attributed to hindered and restricted diffusion. High signal intensities observed in $C_{3,3}$ correspond to the location of vessels; therefore, we hypothesized that this compartment contains information pertaining to vascular flow (Figures 4H and 5H). In the biexponential model, flow information appears to be contained in the fast signal contributions $C_{2,2}$ (Figures 4C and 5C).

The bottom rows of Figures 4 and 5 show maps of the normalized RSI signal contributions. It can be observed that the CNR between tumor and fibroglandular tissue is similar to that of ADC. Even though we found that the CNR of $f_{1,3}$ (Figures 4L and 5L) was statistically higher, the contrast between cancer and fibroglandular tissues is visually very similar. In contrast, in non-normalized 3-component RSI model outputs, the CNR between tumor and fibroglandular tissues is similar to that of DCE (Table 5) (Supporting Information Figure S3). More importantly, the specificity of RSI $C_{1,2}$ and $C_{1,3}$ at 80% sensitivity is comparable or higher (90.8% and 82.2%) than that of DCE (81.0%) — without the use of exogenous contrast. In the RSI outputs, T_2 information is preserved, which increases tumor conspicuity with respect to healthy breast tissues and background. In our data, the differences magnitude in signal intensity between fibroglandular and cancer tissues due to T_2 effects is approximately 13% (assuming T_2 values of 47 and 68 msec, respectively²⁰) with the TEs used here. In contrast, the signal difference due to diffusion (assuming ADC values of 0.93×10^{-3} and $1.1 \times 10^{-3} \text{ mm}^2/\text{s}$, from our results) is about 5% for b values of 500 and $1,500 \text{ s/mm}^2$ and 1%–2% for b value of $4,000 \text{ s/mm}^2$ between these tissues. The effect of TEs and T_2 values of tissues on RSI outputs will be evaluated in future work.

Several studies have used multi-compartment models to characterize the diffusion properties of cancer and healthy breast tissues.^{19,36–40} The most commonly used multi-compartment model in breast is intravoxel incoherent motion imaging, which uses a biexponential decay with 2 different ADCs.⁴¹ The slow ADC (D) describes water diffusion in the tissue, whereas the fast ADC (D_p) is associated with perfusion in capillaries. The percent of voxel-wise signal in the capillaries is described via the perfusion fraction f . The values of D_p in breast tumors (mostly ductal) estimated at 3T range between $10.0 \pm 10.1 \times 10^{-3} \text{ mm}^2/\text{s}$ ⁴⁰ and $21.7 \pm 11.0 \times 10^{-3} \text{ mm}^2/\text{s}$,³⁸ whereas the values of f range between $16.5 \pm 13.2\%$ ⁴⁰ and $6.4 \pm 3.1\%$.³⁸ The magnitude of the fast diffusion compartment ($D_{3,3} = 10.8 \times 10^{-3} \text{ mm}^2/\text{s}$) of the RSI breast model determined here is in good agreement with the values reported for breast tumors. However, the fractional signal contribution of this compartment ($f_{3,3} = 22\%$, interquartile range = 20%) is somewhat higher than those extracted using the intravoxel incoherent motion model. A source of this discrepancy may be the different number of exponential components. Finally, the intravoxel incoherent motion perfusion fraction and RSI fractional signal contribution ($f_{3,3}$) of fibroglandular tissue are both lower than that of tumor tissues.³⁸

As described above, intravoxel incoherent motion aims to separate water diffusion in the tissue from that in the capillaries (pseudo-diffusion). Moreover, multi-compartmental models have been developed to further characterize water diffusion within tissues. The breast RSI model presented here appears to isolate the signal from pseudo-diffusion ($D_{3,3}$) and to decompose the diffusion-weighted signal from within breast tissues into hindered ($D_{2,3}$) and restricted ($D_{1,3}$) components. The persistent signal at high b values in cancerous tissue, as well as the fact that $D_{1,3}$ was set to $0 \text{ mm}^2/\text{s}$, suggests that the diffusion in this compartment was too slow to be accurately measured with our experimental setup (i.e., long diffusion time⁴²). Thus, we hypothesize that the biophysical origin of the slowest compartment is restricted diffusion of intracellular water wherein the water molecules reflect off relatively impermeable cellular membranes,⁴³ whereas less confined water molecules in the extracellular space experience hindered diffusion.⁴⁴ Histological analysis will be used to test this hypothesis in future work.

The diffusion-weighted MR signal of breast lesions collected at high b values (up to $2,500 \text{ s/mm}^2$) was previously fit to bi- and triexponential models by Nakagawa et al. to simultaneously characterize perfusion and diffusion properties of cancer lesions.⁴⁵ The authors reported a correlation between the triexponential model-derived fast diffusion coefficient (D_p , attributed to perfusion) and tumor enhancement derived from DCE-MR. In addition, the slowest (D_s) and fastest

(D_p) diffusion coefficients (attributed to restricted diffusion and perfusion, respectively) were statistically different between malignant and benign breast lesions. Direct comparison between the results of the present study and that by Nakagawa et al. is not possible due to the differences in diffusion models and lesions examined. However, results from both studies demonstrate the relevance of multi-component models in breast DW-MRI and indicate their potential in clinical applications.

Other multi-compartmental models have been developed to probe properties of tissue-specific microstructure. For example, in prostate, Panagiotaki et al. developed the vascular, extracellular and restricted diffusion for cytometry in tumors (VERDICT) model.⁴⁶ Similarly, Gilani et al developed a model that distinguishes between the vascular, ductal, and cellular compartments.⁴⁷ In both cases, the researchers demonstrated an association between estimates from multi-compartmental models and physiological parameters such as intra- and extracellular volumes, lumen radius, and vascular fraction.^{46,47} These 2 models and RSI are different multicompartmental approaches for describing DW-MRI signal that vary mainly in whether the compartmental diffusion coefficients are fixed between voxels. In practice, however, the diffusion coefficients are fixed in VERDICT as well as in RSI.⁴⁸ Fixed diffusion coefficients enable meaningful comparisons of the volume parameters (C or f) between voxels. If the diffusion coefficients are voxel-wise independent, the volume parameters of each voxel would likely be derived using different diffusion coefficients, which would confound comparisons across voxels.

Similarly, in rat brain tissue, White et al. demonstrated an association between volume fractions and orientation distribution of neurites and RSI outputs.²⁴ In its current form, the RSI breast model does not utilize orientation information, which may be helpful in determining the different constituents of cancerous or fibroglandular tissues. In the present work, notably, most of the cancer lesions were IDC; therefore, the resulting model may be biased towards identification of such cancers. Future work will focus on increasing the number of other breast cancer types and incorporating orientation information to evaluate the ability of RSI to identify aggressive tumors and evaluate response to treatment.

5 | CONCLUSION

The overarching goal of this work was to generate quantitative maps in which tumor conspicuity is maximized without the use of exogenous contrast agents. Signal contributions $C_{1,3}$ and $C_{2,3}$ (Figure 4) generated from the 3-component RSI model have similar CNR between cancer and fibroglandular tissues to the clinical standard DCE. However, visual inspection (Figures 4 and 5)

reveals that this may not be in fact the case. Based on the plots from biexponential and 3-component models in Figure 2B, it becomes evident that $C_{1,3}$ has a higher tumor conspicuity compared to $C_{2,3}$. Combination of multiple RSI outputs is ongoing work in our laboratory and has shown potential for accurate automatic classification of breast lesions.⁴⁹ Future work includes the use of RSI-derived signal contributions and advanced computer algorithms to evaluate the diagnostic value of multi-exponential models in an independent cohort. Altogether, these data may be used to aid in radiological differentiation between benign tissues and malignant breast lesions without the use of intravenous contrast agents.


ACKNOWLEDGMENT


The authors A.E.R.S and M.M.S.A share first authorship. The senior authors R.R.P and A.M.D. share last authorship.


CONFLICT OF INTEREST


Two of the authors of this manuscript have conflicts of interest that they would like to disclose: Dr. Anders Dale is a Founder of and holds equity in CorTechs Labs, Inc., and serves on its Scientific Advisory Board. He is a member of the Scientific Advisory Board of Human Longevity, Inc. He receives funding through research grants from GE Healthcare to the University of California San Diego (UCSD). Similarly, Dr. Rebecca Rakow-Penner is a consultant for Human Longevity, Inc. She also receives funding through research grants from GE Healthcare to UCSD. The terms of these arrangements have been reviewed by and approved by UCSD in accordance with its conflict-of-interest policies.

ORCID

Ana E. Rodriguez-Soto  <https://orcid.org/0000-0002-9544-547X>

Maren M. Sjaastad Andreassen  <https://orcid.org/0000-0002-2581-7135>

Lauren K. Fang  <https://orcid.org/0000-0003-3072-9276>

Christopher C. Conlin  <https://orcid.org/0000-0003-4509-8702>

Helen H. Park  <https://orcid.org/0000-0002-1006-7028>


Grace S. Ahn  <https://orcid.org/0000-0001-6141-589X>


Hauke Bartsch  <https://orcid.org/0000-0003-1486-4128>





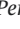

Joshua Kuperman  <https://orcid.org/0000-0002-7890-4785>

Igor Vidić  <https://orcid.org/0000-0001-6610-1187>


Haydee Ojeda-Fournier  <https://orcid.org/0000-0003-3773-0050>

Anne M. Wallace  <https://orcid.org/0000-0003-2919-2491>

Michael Hahn  <https://orcid.org/0000-0002-8323-8174>

Tyler M. Seibert  <https://orcid.org/0000-0002-4089-7399>
 Neil Peter Jerome  <https://orcid.org/0000-0002-9556-5930>
 Tone Frost Bathen  <https://orcid.org/0000-0002-8582-6965>
 Pål Erik Goa  <https://orcid.org/0000-0002-6866-6111>
 Rebecca Rakow-Penner  <https://orcid.org/0000-0002-2566-1978>
 Anders M. Dale  <https://orcid.org/0000-0002-6126-2966>

TWITTER

Rebecca Rakow-Penner  @RakowPenner

REFERENCES

- Lee CH, Dershaw DD, Kopans D, et al. Breast cancer screening with imaging: recommendations from the Society of Breast Imaging and the ACR on the use of mammography, breast MRI, breast ultrasound, and other technologies for the detection of clinically occult breast cancer. *J Am Coll Radiol*. 2010;7:18-27.
- Orel SG, Schnall MD. MR imaging of the breast for the detection, diagnosis, and staging of breast cancer. *Radiology*. 2001;220:13-30.
- Sentis M. Imaging diagnosis of young women with breast cancer. *Breast Cancer Res Treat*. 2010;123:11-13.
- Zhang L, Tang M, Min Z, Lu J, Lei X, Zhang X. Accuracy of combined dynamic contrast-enhanced magnetic resonance imaging and diffusion-weighted imaging for breast cancer detection: a meta-analysis. *Acta Radiol*. 2016;57:651-660.
- Kuhl CK, Schrading S, Leutner CC, et al. Mammography, breast ultrasound, and magnetic resonance imaging for surveillance of women at high familial risk for breast cancer. *J Clin Oncol*. 2005;23:8469-8476.
- Kriege M, Brekelmans CTM, Boetes C, et al. Efficacy of MRI and mammography for breast-cancer screening in women with a familial or genetic predisposition. *N Engl J Med*. 2004;351:427-437.
- Leach MO, Boggis CR, Dixon AK, et al. Screening with magnetic resonance imaging and mammography of a UK population at high familial risk of breast cancer: a prospective multicentre cohort study (MARIBS). *Lancet*. 2005;365:1769-1778.
- Peters NH, Borel Rinkes IH, Zuihthoff NP, Mali WP, Moons KG, Peeters PH. Meta-analysis of MR imaging in the diagnosis of breast lesions. *Radiology*. 2008;246:116-124.
- Saadatmand S, Geuzinge HA, Rutgers EJT, et al. MRI versus mammography for breast cancer screening in women with familial risk (FaMRIsc): a multicentre, randomised, controlled trial. *Lancet Oncol*. 2019;20:1136-1147.
- Kanda T, Ishii K, Kawaguchi H, Kitajima K, Takenaka D. High signal intensity in the dentate nucleus and globus pallidus on unenhanced T1-weighted MR images: relationship with increasing cumulative dose of a gadolinium-based contrast material. *Radiology*. 2014;270:834-841.
- Weinreb JC, Rodby RA, Yee J, et al. Use of intravenous gadolinium-based contrast media in patients with kidney disease: consensus statements from the American College of Radiology and the National Kidney Foundation. *Radiology*. 2021;298:28-35.
- Ko ES, Morris EA. Abbreviated magnetic resonance imaging for breast cancer screening: concept, early results, and considerations. *Korean J Radiol*. 2019;20:533-541.
- Partridge SC, McDonald ES. Diffusion weighted magnetic resonance imaging of the breast: protocol optimization, interpretation, and clinical applications. *Magn Reson Imaging Clin N Am*. 2013;21:601-624.
- Kuroki-Suzuki S, Kuroki Y, Nasu K, Nawano S, Moriyama N, Okazaki M. Detecting breast cancer with non-contrast MR imaging: combining diffusion-weighted and STIR imaging. *Magn Reson Med Sci*. 2007;6:21-27.
- Partridge SC, Amornsiripanitch N. DWI in the assessment of breast lesions. *Top Magn Reson Imaging*. 2017;26:201-209.
- Woodhams R, Ramadan S, Stanwell P, et al. Diffusion-weighted imaging of the breast: principles and clinical applications. *Radiographics*. 2011;31:1059-1084.
- Stejskal EO, Tanner JE. Spin diffusion measurements: spin echoes in the presence of a time-dependent field gradient. *J Chem Phys*. 1965;42:288-292.
- Sung JS, Stamler S, Brooks J, et al. Breast cancers detected at screening MR imaging and mammography in patients at high risk: method of detection reflects tumor histopathologic results. *Radiology*. 2016;280:716-722.
- Tamura T, Usui S, Murakami S, et al. Comparisons of multi b-value DWI signal analysis with pathological specimen of breast cancer. *Magn Reson Med*. 2012;68:890-897.
- Chen Y, Panda A, Pahwa S, et al. Three-dimensional MR fingerprinting for quantitative breast imaging. *Radiology*. 2019;290:33-40.
- Partridge SC, Nissan N, Rahbar H, Kitsch AE, Sigmund EE. Diffusion-weighted breast MRI: clinical applications and emerging techniques. *J Magn Reson Imaging*. 2017;45:337-355.
- Nogueira L, Brandão S, Nunes RG, Ferreira HA, Loureiro J, Ramos I. Breast DWI at 3 T: influence of the fat-suppression technique on image quality and diagnostic performance. *Clin Radiol*. 2015;70:286-294.
- Kothari PD, White NS, Farid N, et al. Longitudinal restriction spectrum imaging is resistant to pseudoresponse in patients with high-grade gliomas treated with bevacizumab. *AJNR Am J Neuroradiol*. 2013;34:1752-1757.
- White NS, Leergaard TB, D'Arceuil H, Bjaalie JG, Dale AM. Probing tissue microstructure with restriction spectrum imaging: histological and theoretical validation. *Hum Brain Mapp*. 2013;34:327-346.
- McCammack KC, Schenker-Ahmed NM, White NS, et al. Restriction spectrum imaging improves MRI-based prostate cancer detection. *Abdom Radiol*. 2016;41:946-953.
- Yamin G, Schenker-Ahmed NM, Shabaik A, et al. Voxel level radiologic-pathologic validation of restriction spectrum imaging cellularity index with Gleason grade in prostate cancer. *Clin Cancer Res*. 2016;22:2668-2674.
- Conlin CC, Feng CH, Rodriguez-Soto AE, et al. Improved characterization of diffusion in normal and cancerous prostate tissue through optimization of multicompartmental signal models. *J Magn Reson Imaging*. 2021;53:628-639.
- Vidić I, Egnell L, Jerome NP, et al. Modeling the diffusion-weighted imaging signal for breast lesions in the b = 200 to 3000 s/mm² range: quality of fit and classification accuracy for different representations. *Magn Reson Med*. 2020;84:1011-1023.
- Holland D, Kuperman JM, Dale AM. Efficient correction of inhomogeneous static magnetic field-induced distortion in Echo Planar Imaging. *NeuroImage*. 2010;50:175-183.

30. Dietrich O, Raya JG, Reeder SB, Ingrisch M, Reiser MF, Schoenberg SO. Influence of multichannel combination, parallel imaging and other reconstruction techniques on MRI noise characteristics. *Magn Reson Imaging*. 2008;26:754-762.
31. Saritas EU, Cunningham CH, Lee JH, Han ET, Nishimura DG. DWI of the spinal cord with reduced FOV single-shot EPI. *Magn Reson Med*. 2008;60:468-473.
32. White NS, McDonald CR, Farid N, Kuperman JM, Kesari S, Dale AM. Improved conspicuity and delineation of high-grade primary and metastatic brain tumors using "restriction spectrum imaging": quantitative comparison with high B-value DWI and ADC. *Am J Neuroradiol*. 2013;34:958-964.
33. Dikaos N, Punwani S, Hamy V, et al. Noise estimation from averaged diffusion weighted images: can unbiased quantitative decay parameters assist cancer evaluation? *Magn Reson Med*. 2014;71:2105-2117.
34. Baltzer P, Mann RM, Iima M, et al. Diffusion-weighted imaging of the breast—a consensus and mission statement from the EUSOBI international breast diffusion-weighted imaging working group. *Eur Radiol*. 2020;30:1436-1450.
35. Celik A. Effect of imaging parameters on the accuracy of apparent diffusion coefficient and optimization strategies. *Diagn Interv Radiol*. 2016;22:101-107.
36. Sigmund EE, Cho GY, Kim S, et al. Intravoxel incoherent motion imaging of tumor microenvironment in locally advanced breast cancer. *Magn Reson Med*. 2011;65:1437-1447.
37. Liu C, Wang K, Chan Q, et al. Intravoxel incoherent motion MR imaging for breast lesions: comparison and correlation with pharmacokinetic evaluation from dynamic contrast-enhanced MR imaging. *Eur Radiol*. 2016;26:3888-3898.
38. Bokacheva L, Kaplan JB, Giri DD, et al. Intravoxel incoherent motion diffusion-weighted MRI at 3.0 T differentiates malignant breast lesions from benign lesions and breast parenchyma. *J Magn Reson Imaging*. 2014;40:813-823.
39. Iima M, Yano K, Kataoka M, et al. Quantitative non-Gaussian diffusion and intravoxel incoherent motion magnetic resonance imaging: differentiation of malignant and benign breast lesions. *Invest Radiol*. 2015;50:205-211.
40. Song SE, Cho KR, Seo BK, et al. Intravoxel incoherent motion diffusion-weighted MRI of invasive breast cancer: correlation with prognostic factors and kinetic features acquired with computer-aided diagnosis. *J Magn Reson Imaging*. 2019;49:118-130.
41. Le Bihan D, Breton E, Lallemand D, Grenier P, Cabanis E, Laval-Jeantet M. MR imaging of intravoxel incoherent motions: application to diffusion and perfusion in neurologic disorders. *Radiology*. 1986;161:401-407.
42. Hope TR, White NS, Kuperman J, et al. Demonstration of non-Gaussian restricted diffusion in tumor cells using diffusion time-dependent diffusion-weighted magnetic resonance imaging contrast. *Front Oncol*. 2016;6:179.
43. Le Bihan D. Molecular diffusion, tissue microdynamics and microstructure. *NMR Biomed*. 1995;8:375-386.
44. Nicholson C. Diffusion and related transport mechanisms in brain tissue. *Rep Prog Phys*. 2001;64:815-884.
45. Nakagawa M, Miyati T, Hayashi T, et al. Triexponential diffusion analysis in invasive ductal carcinoma and fibroadenoma. *Nihon Hoshasen Gijutsu Gakkai Zasshi*. 2014;70:199-205.
46. Panagiotaki E, Walker-Samuel S, Siow B, et al. Noninvasive quantification of solid tumor microstructure using VERDICT MRI. *Can Res*. 2014;74:1902-1912.
47. Gilani N, Malcolm P, Johnson G. A model describing diffusion in prostate cancer. *Magn Reson Med*. 2017;78:316-326.
48. Panagiotaki E, Chan RW, Dikaos N, et al. Microstructural characterization of normal and malignant human prostate tissue with vascular, extracellular, and restricted diffusion for cytometry in tumours magnetic resonance imaging. *Invest Radiol*. 2015;50:218-227.
49. Andreassen MMS, Rodríguez-Soto AE, Conlin CC, et al. Discrimination of breast cancer from healthy breast tissue using a three-component diffusion-weighted MRI model. *Clin Cancer Res*. 2021;27:1094-1104.

SUPPORTING INFORMATION

Additional supporting information may be found in the online version of the article at the publisher's website.

FIGURE S1 Example images of A) dynamic contrast-enhanced (DCE) MRI, B) DCE pre/post contrast subtraction, C) T_2 -weighted, and D) DW-MRI $b=0$ s/mm² volumes from site 1. Overlaid regions of interest (ROIs) are control (blue), cancer (red), and noise (grey), respectively

FIGURE S2 Example images of A) dynamic contrast-enhanced (DCE) MRI, B) DCE pre/post contrast subtraction, C) and E) T_2 -weighted, and F) and D) DW-MRI $b=0$ s/mm² volumes from site 2. Overlaid regions of interest (ROIs) are control (blue), cancer (red), and noise (grey), respectively. Note that control ROIs were placed on a different image to avoid inclusion of tumor tissue/peritumor infiltration in the control ROI

FIGURE S3 Median contrast-to-noise ratio (CNR), area under the curve (AUC) and specificity at 80% sensitivity between cancer and fibroglandular tissues extracted from RSI-derived maps and compared to dynamic contrast-enhanced (DCE) MRI and conventional apparent diffusion coefficient (ADC)

TABLE S1 Signal contributions of cancer for data from both sites estimated using individual site models

How to cite this article: Rodríguez-Soto AE, Andreassen MMS, Fang LK, et al. Characterization of the diffusion signal of breast tissues using multi-exponential models. *Magn Reson Med*. 2022;87:1938–1951. doi:[10.1002/mrm.29090](https://doi.org/10.1002/mrm.29090)

Paper III

Discrimination of Breast Cancer from Healthy Breast Tissue Using a Three-component Diffusion-weighted MRI Model



Maren M. Sjaastad Andreassen¹, Ana E. Rodríguez-Soto², Christopher C. Conlin², Igor Vidić⁸, Tyler M. Seibert^{2,4,5}, Anne M. Wallace⁶, Somaye Zare³, Joshua Kuperman², Boya Abudu⁷, Grace S. Ahn⁷, Michael Hahn², Neil P. Jerome^{1,8}, Agnes Østlie¹, Tone F. Bathen^{1,9}, Haydee Ojeda-Fournier², Pål Erik Goa^{8,9}, Rebecca Rakow-Penner², and Anders M. Dale^{2,10}

ABSTRACT

Purpose: Diffusion-weighted MRI (DW-MRI) is a contrast-free modality that has demonstrated ability to discriminate between predefined benign and malignant breast lesions. However, how well DW-MRI discriminates cancer from all other breast tissue voxels in a clinical setting is unknown. Here we explore the voxelwise ability to distinguish cancer from healthy breast tissue using signal contributions from the newly developed three-component multi-b-value DW-MRI model.

Experimental Design: Patients with pathology-proven breast cancer from two datasets ($n = 81$ and $n = 25$) underwent multi-b-value DW-MRI. The three-component signal contributions C_1 and C_2 and their product, C_1C_2 , and signal fractions F_1 , F_2 , and F_1F_2 were compared with the image defined on maximum b-value (DWI_{max}), conventional apparent diffusion coefficient (ADC), and apparent diffusion kurtosis (K_{app}). The ability to discriminate between cancer and healthy breast tissue was

assessed by the false-positive rate given a sensitivity of 80% (FPR_{80}) and ROC AUC.

Results: Mean FPR_{80} for both datasets was 0.016 [95% confidence interval (CI), 0.008–0.024] for C_1C_2 , 0.136 (95% CI, 0.092–0.180) for C_1 , 0.068 (95% CI, 0.049–0.087) for C_2 , 0.462 (95% CI, 0.425–0.499) for F_1F_2 , 0.832 (95% CI, 0.797–0.868) for F_1 , 0.176 (95% CI, 0.150–0.203) for F_2 , 0.159 (95% CI, 0.114–0.204) for DWI_{max} , 0.731 (95% CI, 0.692–0.770) for ADC, and 0.684 (95% CI, 0.660–0.709) for K_{app} . Mean ROC AUC for C_1C_2 was 0.984 (95% CI, 0.977–0.991).

Conclusions: The C_1C_2 parameter of the three-component model yields a clinically useful discrimination between cancer and healthy breast tissue, superior to other DW-MRI methods and obviating predefining lesions. This novel DW-MRI method may serve as noncontrast alternative to standard-of-care dynamic contrast-enhanced MRI.

1

This paper is not included due to copyright restrictions

Paper IV

Restriction Spectrum Imaging with elastic image registration for automated evaluation of early response to neoadjuvant therapy in breast cancer

Maren M. Sjaastad Andreassen^{1,2}, Michelle Tong³, Stephane Loubrie³, Lauren Fang³, Tyler M. Seibert^{3,4,5}, Anne M. Wallace⁶, Somaye Zare⁷, Haydee Ojeda-Fournier³, Joshua Kuperman³, Michael Hahn³, Neil P. Jerome^{1,9}, Tone F. Bathen^{1,10}, Ana E. Rodríguez-Soto³, Anders M. Dale^{2,3} and Rebecca Rakow-Penner^{3,5}

¹Department of Circulation and Medical Imaging, Norwegian University of Science and Technology, Trondheim, Norway

²Department of Research and Innovation, Vestre Viken, Drammen, Norway

³Department of Radiology, University of California, San Diego. La Jolla, CA, USA

⁴Department of Radiation Medicine and Applied Sciences, University of California, San Diego. La Jolla, CA, USA

⁵Department of Bioengineering, University of California, San Diego. La Jolla, CA, USA

⁶Department of Surgery, University of California, San Diego. La Jolla, CA, USA

⁷Department of Pathology, University of California, San Diego. La Jolla, CA, USA

⁸School of Medicine, University of California, San Diego. La Jolla, CA, USA

⁹Department of Physics, Norwegian University of Science and Technology, Trondheim, Norway

¹⁰Department of Radiology and Nuclear Medicine, St. Olav's University Hospital, Trondheim, Norway

Corresponding author

Rebecca Rakow-Penner, M.D., Ph.D.

Department of Radiology,

University of California, San Diego.

9452 Medical Center Dr, La Jolla, CA 92037, USA.

Phone: (650) 269-7132, Fax: (858) 534-1078.

Email: rrakowpenner@health.ucsd.edu

Dr. Dale reports that he was a Founder of and holds equity in CorTechs Labs, Inc., and serves on its Scientific Advisory Board. He is a member of the Scientific Advisory Board of Human Longevity, Inc. He receives funding through research grants from GE Healthcare to UCSD. Dr. Rakow-Penner is a consultant for Human Longevity, Inc., has equity interest in CorTechs Labs, Inc. and receives funding through research grants from GE Healthcare and NIH R37CA249659. The terms of these arrangements have been reviewed by and approved by UCSD in accordance with its conflict of interest policies. Dr. Seibert reports honoraria from Varian Medical Systems and WebMD; he has an equity interest in CorTechs Labs, Inc. and serves on its Scientific Advisory Board. These companies might potentially benefit from the research results. The terms of this arrangement have been reviewed and approved by the University of California San Diego in accordance with its conflict-of-interest policies.

Abstract

Purpose: Dynamic contrast-enhanced MRI (DCE) and apparent diffusion coefficient (ADC) are currently used to evaluate treatment response of breast cancer. The purpose of the current study was to evaluate a novel diffusion-weighted MRI (DWI) based tumor classification method (restriction spectrum imaging, RSI) combined with elastic image registration to automatically monitor breast tumor size throughout treatment.

Experimental design: Breast cancer patients ($n=27$) underwent multi-parametric 3T MRI at four time points during treatment. Longitudinally-registered DWI was used to generate an automatic RSI response classifier, assessed against manual DCE size measurements and mean ADC values. Predictions of treatment response (pathological complete response, pCR) and residual tumor burden post-treatment using the RSI classifier were assessed.

Results: Ten patients experienced pCR. ROC AUC (95% CI) was most significant at the early-treatment time point 0.73 (0.48-0.97) for the RSI classifier, compared to 0.64 (0.36-0.91) for DCE and 0.56 (0.27-0.85) for ADC. Sensitivity for detection of residual disease post-treatment tumor size were 0.71 (0.44-0.90) for the RSI classifier compared to 0.88 (0.64-0.99) for DCE classifier and 0.71 (0.44-0.90) for ADC. Specificity were 0.90 (0.56-1.00) for the RSI classifier compared to 0.70 (0.35-0.93) for DCE classifier and 0.50 (0.19-0.81) for ADC.

Conclusions: The RSI classifier with elastic image registration was able to predict response to treatment already after 3 weeks, and showed comparable accuracy to DCE for assessment of residual tumor post-therapy. This can be important for cost-efficient evaluation of neoadjuvant breast cancer treatment and improved clinical decision-making to enable tailored treatment regimens.

Introduction

Neoadjuvant therapy of breast cancer is used to enable breast-conserving surgery, to provide an *in vivo* drug-sensitivity test bed^{1,2}, and provide short- and long-term prognostic information. The goal of neoadjuvant therapy is pathological complete response (pCR), defined as no remaining tumor tissue in breast and lymph nodes as measured by post-surgical pathology, which is associated with prognostic benefits such as improved survival and reduced recurrence rates³. Early assessment of treatment response is important for tailoring treatment regimens for the best patient outcome.

Change in tumor size on dynamic contrast-enhanced MRI (DCE), manually assessed by the longest diameter in three dimensions⁴, is the current gold standard for neoadjuvant treatment response assessment in breast cancer. Changes in size may take several weeks before being detected by DCE, however, potentially delaying critical clinical decisions, as well as requiring the administration of Gadolinium-based exogenous contrast agents. Furthermore, DCE-based manual measurements have conflicting results regarding residual cancer detection specificity⁵ and require expert radiologist readers to delineate tumor tissue at each time point. One contrast-free MRI modality is diffusion-weighted MRI (DWI), which is a functional measurement and known to be sensitive to early treatment-induced changes⁶. However, quantitative analysis of lesions using the clinical standard DWI biomarker apparent diffusion coefficient (ADC) is normally predicated on time-consuming manual tumor delineation, most commonly on DCE images,⁷ and may be confounded by treatment-related changes such as edema⁸. This calls for exploration of alternative techniques that maximize the potential of DWI as an adjunct or alternative to DCE methods.

Restriction spectrum imaging (RSI) is a multi-component modelling framework that uses DWI signal over broad ranges of diffusion weightings (*b*-values) to capture the restricted diffusion of intracellular water, which is increased in highly cellular lesions^{9,10}. RSI estimates of cellularity are shown to be directly related to histopathological tumor cellularity in preclinical models^{11,12} and in the human prostate¹³⁻¹⁵. Additionally, RSI is effective for treatment response assessment for glioma^{11,16}. In the breast, a three-component RSI model (RSI_{3C}) has been shown to discriminate untreated breast cancer from healthy breast^{17,18}, but has not yet been evaluated for treatment response assessment. The aim of this study was therefore to assess the ability of RSI_{3C} to detect lesion tissue, without user input, applied over longitudinal data both to assess detection of early response to treatment, and to assess detection of post-therapy residual cancer compared to conventional methods such as manual DCE delineation, and subsequent DWI quantitation using ADC, both of which rely on extensive radiologist input.

Methods

Subject Eligibility

Twenty-seven breast cancer patients (median age 47 years, range 20-68) were included in this retrospective analysis from participants in a prospective phase II clinical trial. Written informed consent was obtained from all patients. The studies were approved by local institutional review boards and conducted in accordance with the Declaration of Helsinki. Criteria for inclusion in the trial included biopsy-proven unilateral invasive breast cancer ≥ 2.5 cm (defined on imaging/clinical examination) with indication for neoadjuvant therapy. We included all participants ($n=31$) from the University of California San Diego (UCSD) site who underwent multi- b -value DWI acquisition between December 2015 and June 2019. Four patients were excluded from further analyses due to poor image quality for DCE ($n=3$) and DWI ($n=1$).

Patients underwent MRI at four time points to evaluate response to treatment: pre-treatment, early-treatment (3 weeks), mid-treatment (12 weeks), and post-treatment (Figure 1). Seventeen patients received all four scans; for three patients, scans at specific time points were excluded due to major patient movement ($n=1$) and poor DWI image quality ($n=2$). This led to the following numbers available for analysis; pre-treatment ($n=27$), early-treatment ($n=22$), mid-treatment ($n=19$) and post-treatment imaging ($n=27$) (Figure 1). For five patients, surgery was performed directly after the 12 week scan, and this was thus categorized as post-treatment scan rather than mid-treatment. The pre-treatment scans ($n=27$) were previously used for development of RSI_{3c} in two studies^{17,19}.

MRI Acquisition and Image Preprocessing

MRI data were acquired on a 3T GE scanner (MR750, DV25-26, GE Healthcare, Milwaukee, US) and an 8-channel breast array coil with a bilateral axial imaging plane. The MRI protocol included Gadolinium DCE (Gadovist or MultiHance), non-fat-saturated T_1 , and multi- b -value DWI acquisition. DCE acquisition parameters included TE = 2.6 ms, TR = 5.4 ms, flip angle = 10° , acquisition matrix 512 x 406, reconstruction matrix 512 x 512, and voxel size 0.625 x 0.625 (in-plane) x 2.4 (slice) mm³. DWI was performed using reduced field of view (FOV) echo-planar imaging (EPI) including the following parameters: spectral attenuated inversion recovery (SPAIR) fat suppression, TE = 82 ms, TR = 9000 ms, b -values (number of diffusion directions) = 0, 500 (6), 1500 (6), and 4000 (15) s/mm², FOV = 160 x 320 mm², acquisition matrix = 48 x 96, reconstruction matrix = 128 x 128, voxel size = 2.5 x 2.5 x 5.0 mm³, phase-encoding (PE) direction anterior to posterior (A/P).

All data analysis was performed using MATLAB 2020b (MathWorks, Natick, MA). DWI data were averaged across diffusion directions for each b -value, corrected for eddy current artifacts, motion⁹ and geometric distortion²⁰, and resampled to match the geometry of the DCE images.

Fast longitudinal image registration (FLIRE)²¹ was used to co-register DWI data to non-fat-saturated T_1 and to longitudinally register all images and ROIs to the pre-treatment time point. FLIRE is based on a well-established non-rigid deformable brain registration technique²², which when optimized for the breast has been shown in preliminary studies to outperform existing registration methods, with significantly reduced run time²¹.

Tumor Assessment by DCE

To provide standard-of-care response assessment, the longest diameter of cancer in any plane (in cm) was manually defined on post-contrast DCE by a breast radiologist (RRP) for each individual time point. For cases with several cancer lesions, the largest conglomerate of connected lesions was used as the definition of the cancer.

Automatic Tissue Classification and Tumor Measurement using RSI

Full-lesion cancer and control regions of interest (ROIs) were manually defined at the pre-treatment time point on DWI images, validated by a breast radiologist (RRP) as described in prior publications^{17,19}. Cancer ROIs were drawn for the lesions corresponding to pathology-proven cancer; for cases with several cancer lesions, the largest conglomerate of connected lesions was defined as the cancer ROI. Control ROIs were defined using a semi-automatic approach with the aim to include all representative healthy breast tissue; first, a rectangular box was placed around the entire healthy contralateral breast (only unilateral breast cancer was included in this study), then the background was masked using intensity thresholding and 3D connected components.

The DWI signal for all voxels across all available b -values was fitted to a previously-developed RSI_{3c} model^{17,19}, given as:

$$S_{DWI}(b) = C_1 \exp(-b \cdot ADC_1) + C_2 \exp(-b \cdot ADC_2) + C_3 \exp(-b \cdot ADC_3)$$

where S_{DWI} is the diffusion signal in arbitrary units, b is the b -value in s/mm^2 , and C_i denotes the voxel-wise, unit-less signal contribution of each component. The apparent diffusion coefficient (ADC_i) values, given in mm^2/s , were fixed as previously reported in Rodríguez-Soto et al¹⁷. The data were normalized to the 95th percentile of intensity of the computed geometric mean of C_1 and C_2 of the control ROI for each patient.

To create a global RSI tissue classifier applicable across patients and time points, the first two components of RSI_{3c} (C_1 and C_2) were selected, as these have demonstrated excellent discrimination of cancer from healthy breast tissue¹⁶. Joint C_1 and C_2 probability density functions (PDFs) for voxels in the cancer and control ROIs were calculated for all patients simultaneously at the pre-treatment time point, generating a lookup table of posterior probability of cancer, given C_1 and C_2 measurements for any voxel. This was used to create voxel-wise probability maps for each individual patient at each time point.

To estimate the longest tumor dimension after voxel classification, the defined cancer ROI at the pre-treatment time point was uniformly expanded by 1 cm to generate a 'tumor-containing region' and used for analysis on the voxel-wise probability maps (Figure 2). The largest single connected component within the tumor-containing region on the voxel-wise probability maps was identified and the longest diameter (in cm) was automatically calculated. To account for any tumor growth outside of the tumor-containing region, any components connected to the tumor-containing region above a threshold of 0.4 on voxel-wise probability maps were included in the tumor-containing region in analysis. For two cases, any enhancement from the skin was masked as the focus of this study was the primary tumor. The tumor-containing region at pre-treatment was applied for all time points, thus limiting manual definition of cancer ROI and semi-automatic definition of control ROI to the pre-treatment time point.

Diffusion quantification using ADC

Conventional apparent diffusion coefficient (ADC) maps were calculated as described by Jensen et al²² using b -values < 1000 s/mm^2 taken from the multi- b -value RSI acquisition. The mean ADC value was assessed within the pre-treatment cancer ROI, applied to each successive time point, was used to assess treatment response. This approach thus avoids the time-consuming and technically difficult manual delineation of a tumor undergoing treatment.

Clinical response definition

The primary endpoint was pathological complete response (pCR), defined as no residual invasive disease with or without ductal carcinoma *in situ* in either breast or axillary lymph nodes after neoadjuvant therapy (ypT0/is, ypN0) ²³. Assessment of pCR was performed on the post-surgical histological specimen, and patients were categorized into pCR and non-pCR groups. The post-treatment size and residual tumor cellularity of the post-surgical specimen were recorded.

Assessment of Treatment Response by Imaging Metrics

The tumor size from DCE and RSI measurements, as well as ADC values, were analysed for all patients ($n=27$) at the post-treatment time point. In addition, for the patients who underwent all four scans ($n=17$), response to treatment during the course of treatment was assessed using the relative change in measured diameter sizes (Δ RSI, Δ DCE) and change in mean ADC (Δ ADC) from pre-treatment to each of the early, mid, and post-treatment time points.

In addition, a radiological response endpoint, early imaging response, was assessed. We defined early imaging response as a $\geq 30\%$ decrease in diameter size (Δ RSI, Δ DCE) at the early-treatment time point, when validated by a corresponding $\geq 30\%$ decrease at the mid-treatment time point.

Statistical analysis

For cases with all four scans ($n=17$), the receiver operating characteristics (ROC) area under the curve (AUC) was assessed for the ability of Δ RSI, Δ DCE, Δ ADC to predict non-pCR at the early, mid, and post-treatment imaging time points. Additionally, ROC curves were calculated for all cases ($n=27$) at the post-treatment time point. Absolute values were used for DCE, RSI, and ADC at the post-treatment time point. At the post-treatment time point, our DCE and RSI measures examined the ability to detect residual tumor tissue (i.e. positive was defined as a patient with remaining tumor tissue, meaning non-pCR, and so accurate detection of pCR corresponded to a negative classification in the imaging). We used an *a priori* assumption that an increase in mean ADC ^{6,7,24-27} and a decrease in RSI and DCE size represents response to treatment, in line with previous experience. The classification thresholds, as well as ROC metrics accuracy, specificity and sensitivity were calculated. Diagnostic sensitivity and specificity between techniques was compared by McNemar's test, while DeLong's test was used to compare ROC curves. Alpha was set to 0.025 due to correction for two primary outcomes (AUC and sensitivity/specificity).

Results

After post-surgical histology, 10/27 (37%) patients were classified as showing pCR. Of the 17 non-pCR patients, the RSI classifier correctly identified 12 using a threshold of 0.87 cm for non-pCR definition, with 5 false negatives that showed generally small remaining tumor size and varied cellularity (Figure 3A). Correspondingly, the DCE classifier correctly classified 15 non-pCR patients, with only 2 false negatives (using a threshold 0.60 cm for non-pCR definition). Example classifications are shown in Figure 3B.

Full ROC metrics for the post-treatment time point are given in Table 2. Sensitivity, specificity, and accuracy for absolute post-treatment tumor size were 0.88, 0.70, and 0.81 for the DCE classifier, and were 0.71, 0.90, and 0.78 for the RSI classifier, and ADC at post-treatment gave 0.71, 0.50 and 0.63. The corresponding ROC AUCs were 0.79 for DCE, 0.79 for RSI, and 0.53 for ADC.

McNemar's test for comparison of sensitivity and specificity did not show significant differences for comparison between any modalities.

ROC AUC for change in measured tumor size from pre-treatment for early-treatment, mid-treatment, and post-treatment time points were 0.64, 0.71 and 0.80 for the Δ DCE classifier; 0.73, 0.62 and 0.76 for the Δ RSI classifier; and 0.56, 0.39 and 0.44 for Δ ADC (under the assumption of ADC increase with response). DeLong's test for comparison of ROC curves for early-treatment time point resulted in p-values throughout: Δ DCE vs. Δ RSI p=0.55, Δ DCE vs. Δ ADC p=0.71, Δ RSI vs. Δ ADC p=0.48, mid-treatment time point: Δ DCE vs. Δ RSI p=0.54, Δ DCE vs. Δ ADC p=0.19 and Δ RSI vs. Δ ADC p=0.21, and post-treatment: Δ DCE vs. Δ RSI p=0.66, Δ DCE vs. Δ ADC p=0.08, and Δ RSI vs. Δ ADC p=0.08.

With the observation of ADC data giving ROC AUC < 0.5, closer examination indicated that the ADC classification improved if the assumption increasing diffusion with response was reversed, contrary to expectation; the AUCs then became 0.47 for the post-Tx (n=27) cohort (sensitivity, specificity, accuracy: 1.00, 0.20, 0.71; threshold $0.8 \times 10^{-3} \text{ mm}^2/\text{s}$), and for the early-, mid-, and post-Tx cohort (n=17) these became 0.44 (0.73, 0.5, 0.65; 0.1), 0.61 (0.82, 0.5, 0.71; 0), and 0.56 (1.00, 0.17, 0.71; -0.32) respectively.

The early imaging response criteria identified manual DCE and RSI classifiers correctly captured early treatment response in 2/10 and 7/10 cases, respectively, with accuracy of 0.67 and 0.74 (Figure 5).

Discussion

Our study shows that the classifier based on automatic cancer tissue detection using restriction spectrum imaging (RSI), has some ability to predict early response to treatment with significant changes detected after only three weeks of neoadjuvant breast cancer therapy. In the later phase of treatment, the automatic RSI classifier showed approximately the same accuracy as manual tumor measurement on DCE. In contrast to DCE, which requires manual user input in the form of ROIs or tumor diameter measurement, the RSI classifier is automatic beyond the pre-treatment MRI scan. In addition to classification at the post-treatment stage, the RSI classifier appeared more sensitive at the early time point when compared to DCE, classifying more tumors as early responders according to the -30% imaging criterion size decrease imaging criterion, and giving a threshold of more than 50% decrease for most accurate classification using ROC analysis compared to a small (7%) decrease in the corresponding DCE analysis. The development of advanced DWI classifiers such as in this study lays the foundation for a quantitative, easily implemented, and cost-efficient response assessment framework that may complement standard DCE in evaluation of neoadjuvant breast cancer treatment in both early and late-phase treatment and improve clinical decision-making to enable tailored treatment regimens.

The improved predictive performance at the early treatment time point is probably due to the RSI classifier's quantification reflecting tumor cellularity, rather than tumor vascular perfusion as in DCE. The RSI classifier is sensitive to slow diffusion within hypercellular tumors while simultaneously suppressing signal from healthy fatty and fibroglandular breast tissue¹⁷. It is expected that the RSI classifier reflects the decrease in cellularity through the course of neoadjuvant therapy, consistent with RSI's known estimation of tumor cellularity across organs¹¹⁻¹⁵. This might reflect the mechanism of action of the primary chemotherapy used in this study, Taxol, which arrests cells in mitosis^{4,25} and thus leads to cell death. This may help resolve early-phase diagnostic challenges of tumors that regress with diffuse cell loss, observable in functional measurements such as DWI, rather than with direct tumor shrinkage, meaning little or no change in overall tumor size on DCE.

Assessment of treatment response at an early time point is important for clinical decision-making and enables tailored treatment regimens. The current findings of accurate response assessment after only three weeks by the RSI classifier (both pathological and imaging response) yields valuable information of *in vivo* treatment efficacy. Thus, establishing early response status may allow for non-responding patients in adaptive treatment regimens to switch to alternative treatment regimens pre-surgery. This allows for planning of additional systemic therapy for non-responders, which is known to improve survival^{28,29}. On the other hand, establishing early complete responders may facilitate deescalated treatment strategies such as shortened treatment regimens³⁰, thus avoiding unnecessary chemotherapy with toxic side-effects.

The RSI classifier is also informative of tumor cellularity in later phases of therapy, which is important as post-therapy cellularity is associated with overall patient survival²⁹. However, RSI did not reflect post-therapy size as well as conventional DCE measures. This may have contributed to the low sensitivity for detection of remaining tumor tissue post-therapy. Thus, DCE-based methods still have a more prominent role than the RSI classifier in the context of surgical planning after neoadjuvant therapy. The RSI classifier may have a role in complementing DCE in this setting, as suggested by the (although non-significant) in this work) higher specificity than DCE post-therapy.

Our ADC results were generally poorer than might be expected from the literature^{6,7,24-27}. It is worth noting that there are conflicting results in the literature regarding the predictive value of ADC; while several single-center trials have reported that ADC is predictive of response in

the early phase,^{6,26 27} the multi-center I-SPY trial⁷, and a recent study by Almutlaq et al.²⁴ show low predictive value of ADC at this time point. Unexpectedly, we observed a ROC AUC < 0.5, indicating a superior classification performance associated with the reverse hypothesis (decrease in ADC equals response to treatment) at the mid and post-treatment time points (although not at the pre-treatment time point). This behavior is unexpected and is not seen in other literature, and indicates that the results for ADC in this study may not provide useful information. The ROI definition in our study may be a source of this unexpected behavior, where the same cancer ROI, defined on the first time point, was used for all subsequent time points. This differs from conventional analysis, where cancer ROIs normally are manually defined for each time point. The rationale for this approach was to avoid time-consuming and technically difficult manual delineation of a tumor undergoing treatment. However, this approach necessarily creates some uncertainty of the nature of the tissue in the ROI, which would include some surrounding healthy tissue if the tumor decreases in size. ADC mean in this study is therefore influenced by the diffusion properties of the surrounding tissue, in addition to tumor-related necrosis. In addition, the choice of *b*-values will influence ADC values, and our study was not optimized for ADC estimation. Since our dataset focused on high *b*-values acquired for RSI, only 0 and 500 s/mm² were available for ADC calculation, and not a range of several low *b*-values as in comparable studies⁷. These methodological factors in our ADC analysis, differing from more conventional ADC analysis, indicate that it is difficult to determine if RSI performs better than ADC based on our study.

The RSI classifier is able to automatically estimate tumor volume following a single cancer ROI definition, which is an advantage compared to conventional DWI that requires manually-defined regions for every time point. Automatic assessment is particularly useful in the treatment setting, as defining tumor volume is especially difficult when the tumor shrinks in size and may be affected by treatment- and procedure-related changes. These results also add to current literature demonstrating that DWI-based response assessment may precede changes in tumor size measured by DCE⁶. In another directly comparable I-SPY trial²⁵, RSI performed better than the longest diameter of manual DCE, which had an AUC of predicting pCR at the early time point of 0.64; AUC increased to 0.70 using a threshold-based DCE model (functional tumor volume, FTV).

The RSI classifier may bring about a computationally efficient and standardized framework for breast cancer treatment response assessment. The RSI classifier is based on the multi-component RSI model that uses globally-determined, fixed component ADCs, thus allowing rapid fitting of the diffusion signal suitable for application as a turn-key processing stream on multiple MRI platforms¹⁷. Furthermore, the RSI classifier uses an effective rapid longitudinal registration²¹ incorporating the pre-treatment MRI scan which automates the response evaluation and requires no user-input. These factors are important for implementing RSI in standard-of care breast MRI.

There were some limitations to our study. Most notably, the sample size of this longitudinal study was small. There were 27 patients included, where 17 had all four scans in the study protocol, and this limits the generalisability of the conclusions. Also, in this study we did not correct for overall differences in DWI signal intensity for the RSI classifier across time points, which could be expected to affect resulting tumor detection and is therefore an area of interest for future method development. One minor limitation of the RSI classifier method is the remaining requirement for user input for generating the pre-treatment ROI, although tumors that receive neoadjuvant chemotherapy are generally large (> 4 cm) and relatively easy to detect on pre-treatment MRI scans, whereas the more challenging task of delineating tumors that are affected by treatment is avoided. Lastly, as discussed above, the ADC value appeared to associate a decrease in ADC with response for the mid and post-treatment time points; this behavior was unexpected and should be investigated further in a larger cohort to understand its origin.

In conclusion, our study demonstrates that the RSI classifier, an automatic quantification procedure based on the three-component RSI DWI model and incorporating elastic image registration, showed promising ability to assess response to treatment after only three weeks of neoadjuvant breast cancer therapy. The classifier eliminates the need for pre-defined lesions for each imaging time point that is required for conventional DWI and DCE. We propose that the RSI classifier is a novel response biomarker that can work as a diagnostic tool in both early and late-phase of treatment, and shows highly promising diagnostic properties which warrant large-scale studies for validation in routine breast cancer detection and follow-up in comparison to DCE and ADC metrics.

Acknowledgements

Thank you to Dr. Sherin Hashem for providing pathological images. We would like to acknowledge the financial support from the California Breast Cancer Research Program Early Career Award 25IB-0056 (Rakow-Penner R.), Krueger v. Wyeth Settlement research grant (Rakow-Penner R.), GE Healthcare (Rakow-Penner R., Dale A.M.), NIH/NIBIB grant no. K08EB026503 (Seibert T.M.), the Prostate Cancer Foundation (Seibert T.M.), and the liaison Committee between the Central Norway Regional Health Authority and the Norwegian University of Science and Technology project no. 90065000 (Bathen T.F., Jerome N.P, Andreassen M.M.S).

Tables

Table 1

No. Patients	27
Median patient age, years (range)	47 (20-68)
Lesion type mass (mass vs. NME)	
Mass	24
Mass + NME	3
Histologic type	
NST	24
Metaplastic carcinoma	2
Mixed IDC/ILC	1
MBR score	
1	1
2	11
3	15
ER status	
Positive	15
Negative	12
PR status	
Positive	13
Negative	14
HER2 status	
Positive	3
Negative	23
Not analyzed	1
pCR status	
pCR	10
non-pCR	17
Median time from therapy start to MRI scan, days (range)	
Early-treatment	19 (15-26)
Mid-treatment	81 (48-94)
Post-treatment	147 (98-190)

Table 2

Sensitivity, specificity and accuracy for prediction of non-pCR for dynamic contrast-enhanced MRI (DCE) classifier, restriction spectrum imaging (RSI) classifier and the mean apparent diffusion coefficient (ADC) after all neoadjuvant therapy prior to surgical intervention (post-Tx time point).

	DCE classifier	RSI classifier	ADC classifier
Threshold value	0.60 cm	0.87 cm	1.5×10^{-3} mm ² /s
Sensitivity (95% CI) Post-Tx	0.88 (0.64-0.99)	0.71 (0.44-0.90)	0.71 (0.44-0.90)
Specificity (95% CI) Post-Tx	0.70 (0.35-0.93)	0.90 (0.56-1.00)	0.50 (0.19-0.81)
Accuracy (95% CI) Post-Tx	0.81 (0.61-0.94)	0.78 (0.58-0.91)	0.63 (0.42-0.81)
ROC AUC	0.79	0.79	0.53

pCR = pathological complete response, Tx = treatment.

Table 3

ROC AUC performance of Δ DCE classifier, Δ RSI classifier and Δ ADC for prediction of non-pCR at each time point. Note that post-Tx time point is after all neoadjuvant therapy prior to surgical intervention. Threshold values are unitless multiplication factors.

		Δ DCE classifier	Δ RSI classifier	Δ ADC classifier (\uparrow = response)
Early-Tx (3 weeks)	AUC (95%CI)	0.64 (0.36-0.91)	0.73 (0.48-0.97)	0.56 (0.27-0.85)
	Sens.	0.54	0.91	0.82
	Spec.	1.00	0.50	0.50
	Accu.	0.71	0.76	0.71
	Thresh.	-0.07	-0.58	0.36
Mid-Tx (12 weeks)	AUC (95%CI)	0.71 (0.45-0.96)	0.62 (0.34-0.90)	0.39 (0.10-0.69)
	Sens.	0.91	0.45	1.00
	Spec.	0.33	1.00	0.17
	Accu.	0.71	0.65	0.71
	Thresh.	-0.73	-0.06	0.98
Post-Tx	AUC (95%CI)	0.80 (0.59-1.00)	0.76 (0.52-0.99)	0.44 (0.14-0.74)
	Sens.	0.73	0.64	0.91
	Spec.	0.83	1.00	0.17
	Accu.	0.76	0.76	0.65
	Thresh.	-0.72	-0.78	0.94

Area under the receiver operating curve = AUC, pCR = pathological complete response, Tx = treatment, Δ DCE classifier = change in size from pre-treatment time point for dynamic contrast-enhanced MRI, Δ RSI classifier = change in size from pre-treatment time point for Restriction Spectrum Imaging, Δ ADC = change in mean value from pre-treatment time point for apparent diffusion coefficient.

Figures

Figure 1

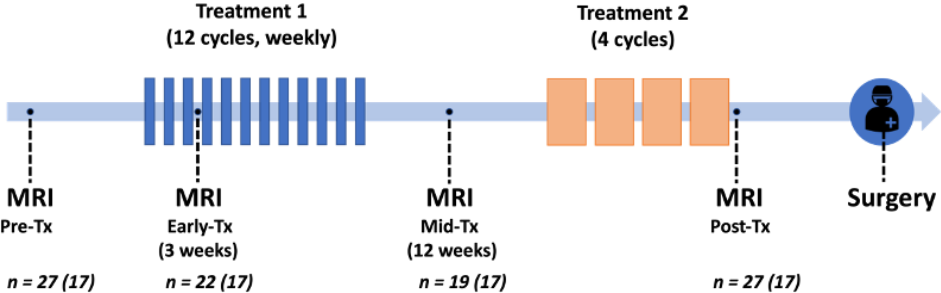


Figure 1: Trial schematic showing neoadjuvant treatments in relation to pre-treatment, early-treatment, mid-treatment and post-treatment MRI, followed by surgery. 17 patients were scanned at all four time points.

Figure 2

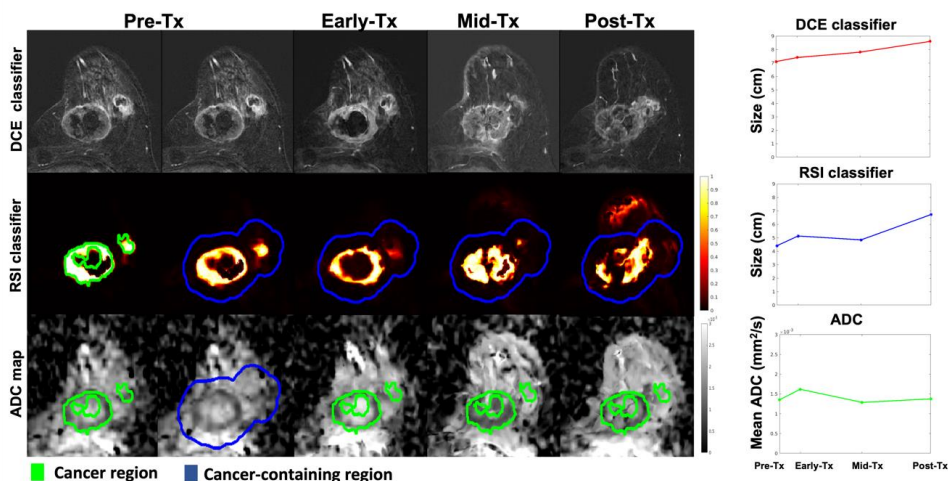


Figure 2: DCE classifier, RSI classifier, and ADC maps with corresponding size (DCE and RSI) and mean calculation (ADC) for all four time points for a non-responding case with invasive carcinoma of no special type measuring 7.5 cm on final post-surgical pathology. The cancer region (green outline) at the pre-treatment time point was uniformly expanded by 1 cm to generate a cancer-containing region (blue outline). The longest diameter of cancer (in cm) was manually defined on post-contrast DCE for each individual time point. As demonstrated for this case, the largest conglomerate of connected lesions was defined as cancer (ie. both lesions were included). For the RSI classifier, the largest single connected component within the cancer-containing region was identified and the longest diameter (in cm) was automatically assessed. To account for tumor growth outside of the tumor-containing region, any components connected to the tumor-containing region above a threshold of included 0.4 were included in analysis. The tumor-containing region at pre-treatment was applied for all time points. Also note that the RSI classifier is well-defined within the cancer ROI (region outline) at the pre- treatment time point. The mean ADC was calculated within the cancer region (green outline) for each time point.

Tx = treatment, DCE = dynamic contrast-enhanced MRI, RSI = Restriction Spectrum Imaging, ADC = apparent diffusion coefficient.

Figure 3

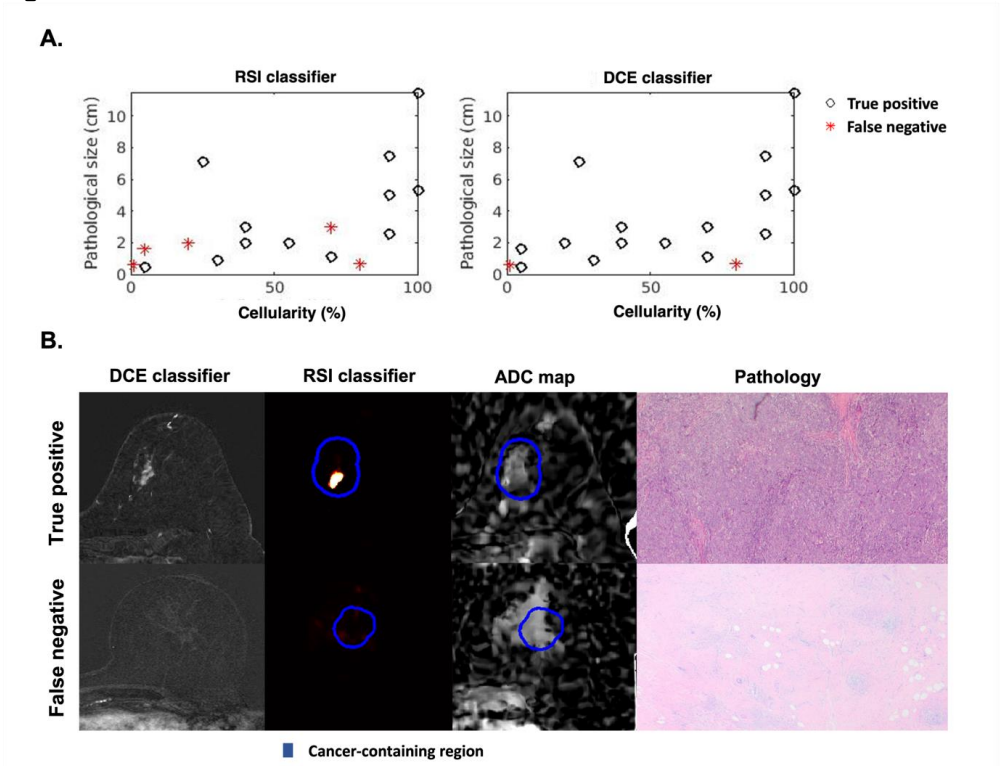


Figure 3: A. Cases with remaining tumor tissue on final post-surgical pathology are included for RSI and DCE classifier. RSI classifier has more false negative plots, which were associated with low pathological size. **B.** Two example cases, where (upper row) a true positive case for both RSI (1.5 cm) and DCE classifier (2.0 cm) had corresponding high cellularity of 70% (size 1.1 x 0.6 cm) on final post-surgical pathology, while (lower row) a false negative for RSI (0 cm) and DCE classifier (0 cm) had low cellularity of 1% and similar size (0.6 x 0.5 cm) on final post-surgical pathology.

Figure 4

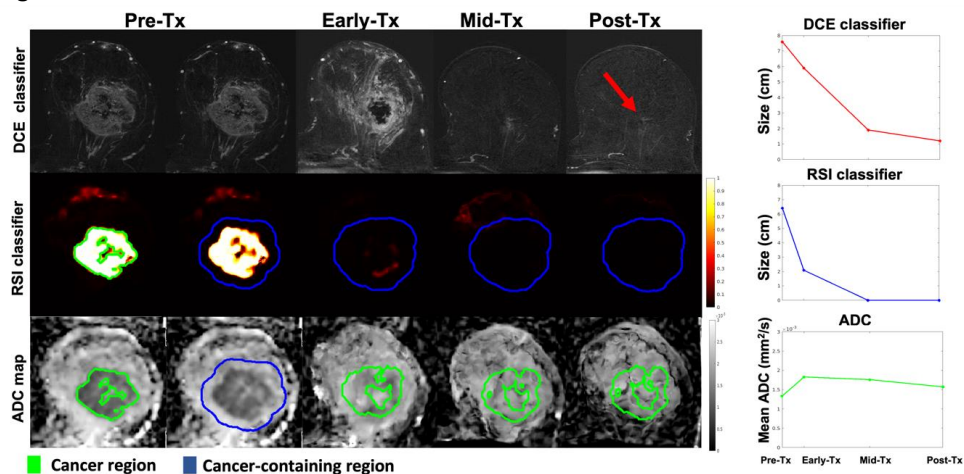


Figure 4: DCE classifier, RSI classifier, and ADC maps with corresponding size (DCE and RSI) and mean calculation (ADC) for all four time points for a subject with no remaining tumor tissue on final post-surgical pathology. The RSI classifier shows a more pronounced size decrease at the early-treatment time point compared to the DCE classifier. The RSI classifier was more specific at the post-treatment time point, while there was still some remaining tumor left within the tumor bed at the post-treatment time point for the DCE classifier (red arrow). Also note that the RSI classifier is well-defined within the cancer ROI at the pre-treatment time point (green outline).

Tx = treatment, DCE = dynamic contrast-enhanced MRI, RSI = Restriction Spectrum Imaging, ADC = apparent diffusion coefficient.

Figure 5

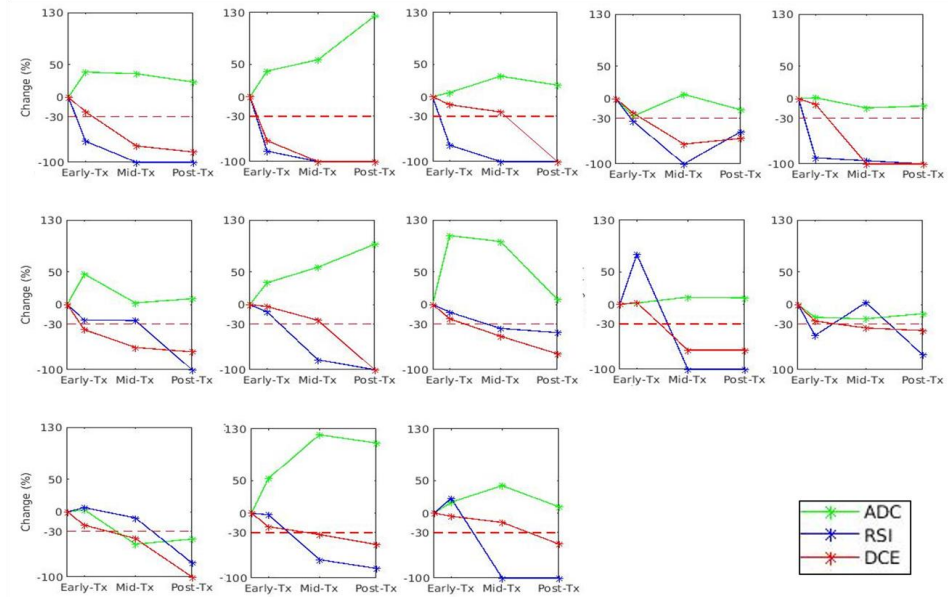


Figure 5: Early imaging response were identified for all cases with a $\geq 30\%$ decrease in size at the mid-treatment time point on RSI classifier ($n=10$) or DCE classifier ($n=10$). Change in tumor size from the pre-treatment time point by longest tumor diameter by the DCE classifier (red) and RSI classifier (blue) for imaging responders ($\geq 30\%$ decrease in size from pre-treatment time point was considered response to treatment). The RSI classifier identifies early responders in five out of ten cases, while the DCE classifier identifies early responders in two out of ten cases. Change in mean ADC (green) are plotted for reference, where an increase in ADC represents response to treatment. Note that for graph 9, there was a post-biopsy hematoma connected to the tumor gave an increase in size at the Early-Tx time point for RSI.

Tx = treatment, DCE = dynamic contrast-enhanced MRI, RSI = Restriction Spectrum Imaging, ADC = apparent diffusion coefficient.

References

1. Makhoul I, Kiwan E: Neoadjuvant systemic treatment of breast cancer. *J Surg Oncol* 103:348-57, 2011
2. Miller E, Lee HJ, Lulla A, et al: Current treatment of early breast cancer: adjuvant and neoadjuvant therapy. *F1000Res* 3:198, 2014
3. Cortazar P, Zhang L, Untch M, et al: Pathological complete response and long-term clinical benefit in breast cancer: the CTNeoBC pooled analysis. *Lancet* 384:164-72, 2014
4. Reig B, Lewin AA, Du L, et al: Breast MRI for Evaluation of Response to Neoadjuvant Therapy. *Radiographics* 41:665-679, 2021
5. Gu YL, Pan SM, Ren J, et al: Role of Magnetic Resonance Imaging in Detection of Pathologic Complete Remission in Breast Cancer Patients Treated With Neoadjuvant Chemotherapy: A Meta-analysis. *Clin Breast Cancer* 17:245-255, 2017
6. Pickles MD, Gibbs P, Lowry M, et al: Diffusion changes precede size reduction in neoadjuvant treatment of breast cancer. *Magn Reson Imaging* 24:843-7, 2006
7. Partridge SC, Zhang Z, Newitt DC, et al: Diffusion-weighted MRI Findings Predict Pathologic Response in Neoadjuvant Treatment of Breast Cancer: The ACRIN 6698 Multicenter Trial. *Radiology* 289:618-627, 2018
8. White NS, McDonald CR, Farid N, et al: Improved conspicuity and delineation of high-grade primary and metastatic brain tumors using "restriction spectrum imaging": quantitative comparison with high B-value DWI and ADC. *AJNR Am J Neuroradiol* 34:958-64, s1, 2013
9. White NS, McDonald CR, Farid N, et al: Diffusion-weighted imaging in cancer: Physical foundations and applications of restriction spectrum imaging. *Cancer Research* 74:4638-4652, 2014
10. Rakow-Penner RA, White NS, Parsons JK, et al: Novel technique for characterizing prostate cancer utilizing MRI restriction spectrum imaging: proof of principle and initial clinical experience with extraprostatic extension. *Prostate Cancer Prostatic Dis* 18:81-5, 2015
11. White NS, McDonald C, Farid N, et al: Diffusion-weighted imaging in cancer: physical foundations and applications of restriction spectrum imaging. *Cancer Res* 74:4638-52, 2014
12. Hope TR, White NS, Kuperman J, et al: Demonstration of Non-Gaussian Restricted Diffusion in Tumor Cells Using Diffusion Time-Dependent Diffusion-Weighted Magnetic Resonance Imaging Contrast. *Front Oncol* 6:179, 2016
13. Liss MA, White NS, Parsons JK, et al: MRI-Derived Restriction Spectrum Imaging Cellularity Index is Associated with High Grade Prostate Cancer on Radical Prostatectomy Specimens. *Front Oncol* 5:30, 2015
14. McCammack KC, Schenker-Ahmed NM, White NS, et al: Restriction spectrum imaging improves MRI-based prostate cancer detection. *Abdom Radiol (NY)* 41:946-53, 2016
15. Yamin G, Schenker-Ahmed NM, Shabaik A, et al: Voxel Level Radiologic-Pathologic Validation of Restriction Spectrum Imaging Cellularity Index with Gleason Grade in Prostate Cancer. *Clin Cancer Res* 22:2668-74, 2016
16. Daghighi S, Bahrami N, Tom WJ, et al: Restriction Spectrum Imaging Differentiates True Tumor Progression From Immune-Mediated Pseudoprogression: Case Report of a Patient With Glioblastoma. *Front Oncol* 10:24, 2020

17. Andreassen MMS, Rodríguez-Soto AE, Conlin CC, et al: Discrimination of breast cancer from healthy breast tissue using a three-component diffusion-weighted MRI model. *Clin Cancer Res*, 2020
18. Rodríguez-Soto AE, Andreassen MMS, Fang LK, et al: Characterization of the diffusion signal of breast tissues using multi-exponential models. *Magn Reson Med*, 2021
19. Rodríguez-Soto AE, Andreassen MMS, Conlin CC, et al: Characterization of the Diffusion Signal of Breast Tissues using Multi-exponential Models. *medRxiv:2020.04.27.20082271*, 2020
20. Holland D, Kuperman JM, Dale AM: Efficient correction of inhomogeneous static magnetic field-induced distortion in Echo Planar Imaging. *Neuroimage* 50:175-83, 2010
21. Tong M, Rodríguez-Soto AE, Andreassen MMS, et al: Fast Longitudinal Image REgistration (FLIRE) for Breast MRI, International Society of Magnetic Resonance Medicine Vancouver, Canada 2021
22. Holland D, Brewer JB, Hagler DJ, et al: Subregional neuroanatomical change as a biomarker for Alzheimer's disease. *Proceedings of the National Academy of Sciences of the United States of America* 106:20954-20959, 2009
23. U.S. Food and Drug Administration (FDA) . Guidance for industry: pathological complete response in neoadjuvant treatment of high-risk early-stage breast cancer: use as an endpoint to support accelerated approval.,
24. Almutlaq ZM, Wilson DJ, Bacon SE, et al: Evaluation of Monoexponential, Stretched-Exponential and Intravoxel Incoherent Motion MRI Diffusion Models in Early Response Monitoring to Neoadjuvant Chemotherapy in Patients With Breast Cancer-A Preliminary Study. *J Magn Reson Imaging*, 2022
25. Hylton NM, Blume JD, Bernreuter WK, et al: Locally advanced breast cancer: MR imaging for prediction of response to neoadjuvant chemotherapy--results from ACRIN 6657/I-SPY TRIAL. *Radiology* 263:663-672, 2012
26. Jensen LR, Garzon B, Heldahl MG, et al: Diffusion-weighted and dynamic contrast-enhanced MRI in evaluation of early treatment effects during neoadjuvant chemotherapy in breast cancer patients. *J Magn Reson Imaging* 34:1099-109, 2011
27. Bedair R, Priest AN, Patterson AJ, et al: Assessment of early treatment response to neoadjuvant chemotherapy in breast cancer using non-mono-exponential diffusion models: a feasibility study comparing the baseline and mid-treatment MRI examinations. *Eur Radiol* 27:2726-2736, 2017
28. Masuda N, Lee SJ, Ohtani S, et al: Adjuvant Capecitabine for Breast Cancer after Preoperative Chemotherapy. *N Engl J Med* 376:2147-2159, 2017
29. von Minckwitz G, Huang CS, Mano MS, et al: Trastuzumab Emtansine for Residual Invasive HER2-Positive Breast Cancer. *N Engl J Med* 380:617-628, 2019
30. van der Voort A., Image-guided de-escalation of neo-adjuvant chemotherapy in HER2-positive breast cancer: the TRAIN-3 study (TRAIN-3). *ClinicalTrials.gov Identifier: NCT03820063*.<https://clinicaltrials.gov/ct2/show/NCT03820063>
Date accessed: October 1, 2021

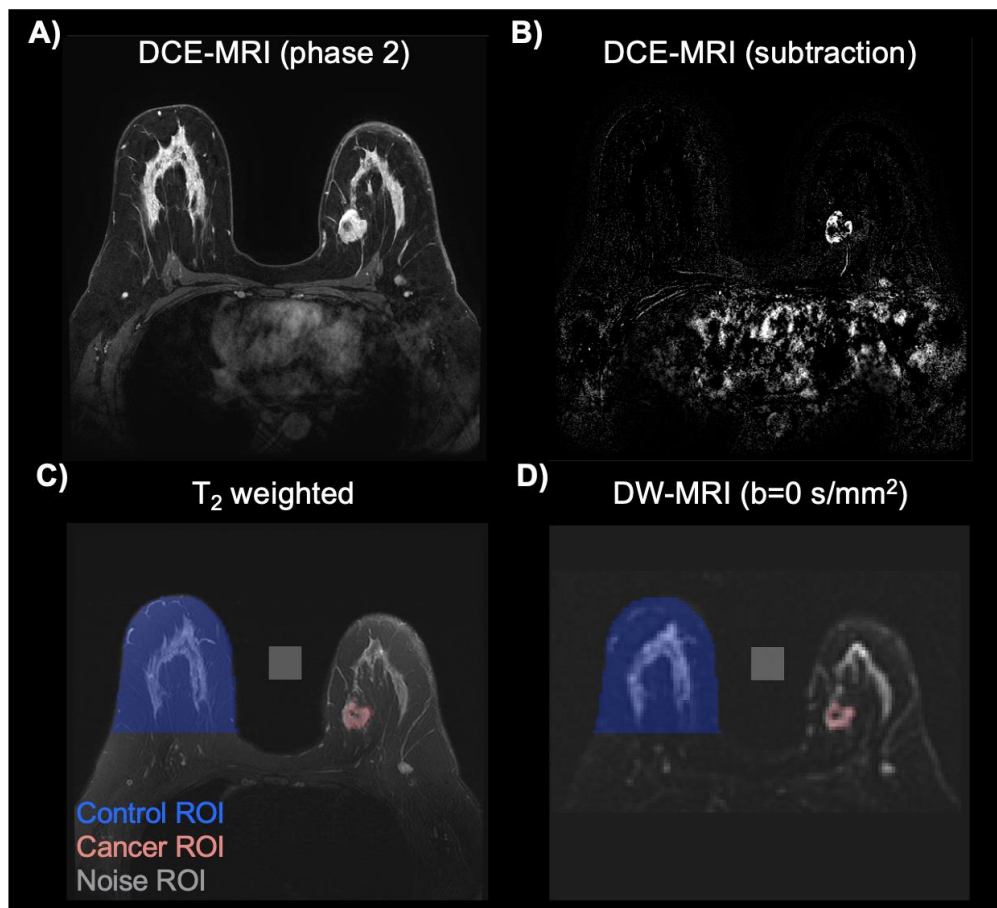
Supplementary Materials Paper II

Supporting Information

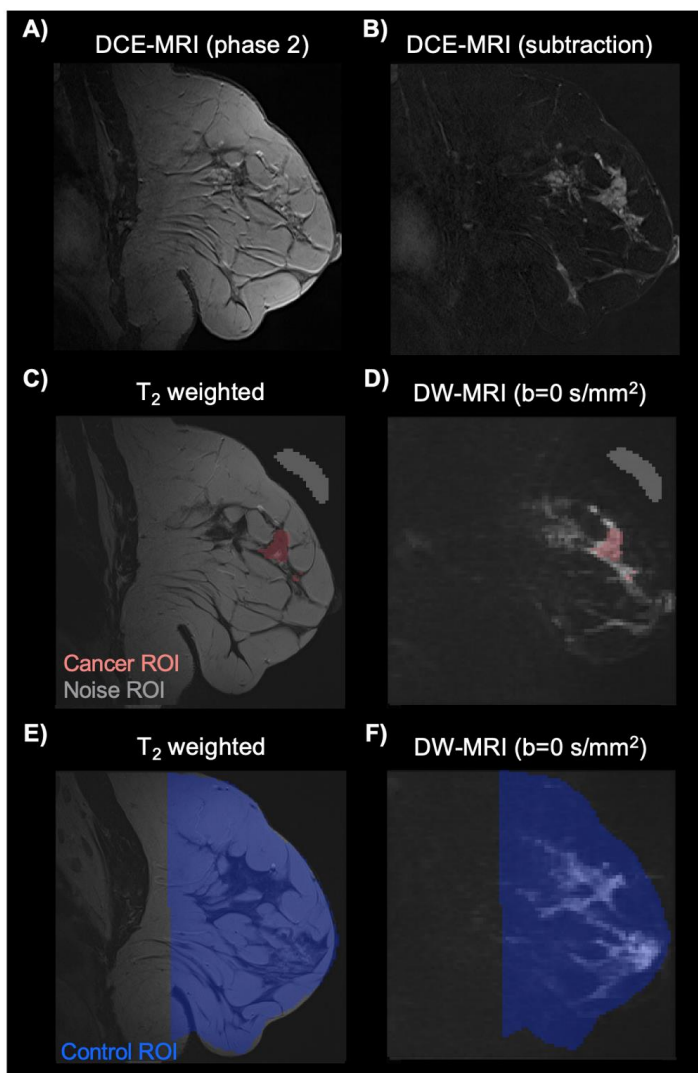
Supporting Information Table S1. Signal contributions of cancer for data from both sites estimated using individual site models.

Model	Parameter	Site 1		Site 2		p-value
		Median (range)	IQ Range	Median (range)	IQ Range	
Bi-exponential	C _{1,2}	1.42	1.77	1.50	1.79	p>0.05
	C _{2,2}	1.71	2.12	1.76	2.04	p>0.05
	f _{1,2}	0.31	0.23	0.31	0.19	p>0.05
	f _{2,2}	0.69	0.23	0.69	0.19	p>0.05
Three-component	C _{1,3}	0.89	1.01	1.19	1.35	p>0.05
	C _{2,3}	4.61	6.44	5.44	6.98	p>0.05
	C _{3,3}	0.73	1.27	0.16	0.24	p<0.05*
	f _{1,3}	0.19	0.20	0.25	0.20	p>0.05
	f _{2,3}	0.65	0.34	0.72	0.26	p>0.05
	f _{3,3}	0.16	0.16	0.03	0.09	p<0.05*

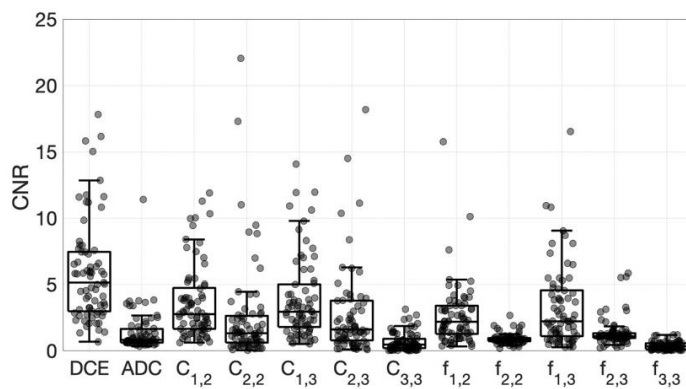
Supporting Information Figure S1. Example images of A) dynamic contrast-enhanced (DCE) MRI, B) DCE pre/post contrast subtraction, C) T₂-weighted, and D) DW-MRI $b=0$ s/mm² volumes from site 1. Overlaid regions of interest (ROIs) are control (blue), cancer (red), and noise (grey), respectively.



Supporting Information Figure S2. Example images of A) dynamic contrast-enhanced (DCE) MRI, B) DCE pre/post contrast subtraction, C) and E) T₂-weighted, and F) and D) DW-MRI b=0 s/mm² volumes from site 2. Overlaid regions of interest (ROIs) are control (blue), cancer (red), and noise (grey), respectively. Note that control ROIs were placed on a different image to avoid inclusion of tumor tissue/peritumor infiltration in the control ROI.



Supporting Information Figure S3. Median contrast-to-noise ratio (CNR), area under the curve (AUC) and specificity at 80% sensitivity between cancer and fibroglandular tissues extracted from RSI-derived maps and compared to dynamic contrast-enhanced (DCE) MRI and conventional apparent diffusion coefficient (ADC).



Supplementary Materials Paper III

Supplementary Materials I

Supplementary Table 1: Data are mean (95% CI) for the US dataset.

ADC, conventional apparent diffusion coefficient; AUC, area under the curve; C, signal contribution; DWI_{max} , image defined on maximum b-value; F, signal fraction; FPR_{80} , false positive rate given sensitivity of 80%; K_{app} , apparent diffusion kurtosis; ROC, receiver operating curve; S_0 , signal at b-value = 0 s/mm².

	ROC AUC	SENSITIVITY	SPECIFICITY	ACCURACY	FPR_{80}
C_1C_2	0.984 (0.976 - 0.991)	0.974 (0.965 - 0.983)	0.965 (0.952 - 0.977)	0.969 (0.960 - 0.979)	0.017 (0.007 - 0.027)
C_1	0.914 (0.883 - 0.945)	0.903 (0.868 - 0.937)	0.876 (0.835 - 0.917)	0.889 (0.861 - 0.918)	0.138 (0.088 - 0.188)
C_2	0.949 (0.934 - 0.964)	0.957 (0.944 - 0.969)	0.894 (0.870 - 0.917)	0.925 (0.910 - 0.940)	0.072 (0.051 - 0.093)
F_1F_2	0.617 (0.581 - 0.653)	0.938 (0.925 - 0.951)	0.448 (0.404 - 0.492)	0.693 (0.673 - 0.713)	0.492 (0.450 - 0.533)
F_1	0.250 (0.206 - 0.294)	0.970 (0.950 - 0.991)	0.145 (0.101 - 0.188)	0.557 (0.540 - 0.575)	0.817 (0.775 - 0.859)
F_2	0.868 (0.848 - 0.888)	0.936 (0.921 - 0.950)	0.765 (0.735 - 0.796)	0.850 (0.832 - 0.868)	0.192 (0.163 - 0.222)
DWI_{MAX}	0.889 (0.851 - 0.926)	0.915 (0.885 - 0.945)	0.827 (0.776 - 0.879)	0.871 (0.839 - 0.903)	0.176 (0.119 - 0.233)
ADC	0.402 (0.359 - 0.446)	0.946 (0.932 - 0.959)	0.232 (0.184 - 0.280)	0.589 (0.569 - 0.609)	0.713 (0.667 - 0.759)
K_{APP}	0.437 (0.407 - 0.468)	0.884 (0.851 - 0.917)	0.334 (0.290 - 0.377)	0.609 (0.595 - 0.623)	0.671 (0.642 - 0.700)
$S_0F_1F_2$	0.976 (0.967 - 0.986)	0.952 (0.937 - 0.967)	0.956 (0.944 - 0.968)	0.954 (0.942 - 0.966)	0.028 (0.014 - 0.042)
S_0F_1	0.920 (0.890 - 0.949)	0.909 (0.878 - 0.940)	0.879 (0.839 - 0.918)	0.894 (0.866 - 0.921)	0.128 (0.080 - 0.175)
S_0F_2	0.948 (0.933 - 0.963)	0.957 (0.946 - 0.968)	0.890 (0.865 - 0.915)	0.924 (0.908 - 0.939)	0.074 (0.053 - 0.096)

Supplementary Table 2: Data are mean (95% CI) for the European dataset.

ADC, conventional apparent diffusion coefficient; AUC, area under the curve; C, signal contribution; DWI_{max} , image defined on maximum b-value; F, signal fraction; FPR_{80} , false positive rate given sensitivity of 80%; K_{app} , apparent diffusion kurtosis; ROC, receiver operating curve; S_0 , signal at b-value = 0 s/mm².

	ROC AUC	SENSITIVITY	SPECIFICITY	ACCURACY	FPR_{80}
C_1C_2	0.985 (0.971 - 1.000)	0.980 (0.965 - 0.996)	0.968 (0.947 - 0.990)	0.974 (0.960 - 0.989)	0.012 (-0.003 - 0.026)
C_1	0.907 (0.851 - 0.962)	0.839 (0.780 - 0.897)	0.905 (0.854 - 0.955)	0.872 (0.830 - 0.914)	0.129 (0.030 - 0.227)
C_2	0.961 (0.927 - 0.995)	0.980 (0.970 - 0.989)	0.917 (0.866 - 0.969)	0.949 (0.920 - 0.977)	0.054 (0.011 - 0.096)
F_1F_2	0.723 (0.658 - 0.788)	0.907 (0.885 - 0.929)	0.582 (0.507 - 0.657)	0.745 (0.706 - 0.783)	0.365 (0.290 - 0.439)
F_1	0.151 (0.084 - 0.219)	0.989 (0.979 - 1.000)	0.077 (0.018 - 0.135)	0.533 (0.506 - 0.560)	0.883 (0.819 - 0.947)
F_2	0.909 (0.863 - 0.955)	0.970 (0.960 - 0.981)	0.823 (0.757 - 0.890)	0.897 (0.861 - 0.933)	0.124 (0.064 - 0.183)
DWI_{MAX}	0.929 (0.898 - 0.959)	0.858 (0.827 - 0.889)	0.887 (0.849 - 0.924)	0.873 (0.843 - 0.902)	0.104 (0.052 - 0.156)
ADC	0.293 (0.219 - 0.368)	0.944 (0.914 - 0.973)	0.167 (0.090 - 0.245)	0.555 (0.526 - 0.585)	0.788 (0.718 - 0.857)
K_{APP}	0.303 (0.259 - 0.348)	0.949 (0.926 - 0.972)	0.229 (0.183 - 0.275)	0.589 (0.573 - 0.605)	0.728 (0.688 - 0.768)
$S_0F_1F_2$	0.979 (0.958 - 0.999)	0.959 (0.932 - 0.985)	0.961 (0.932 - 0.991)	0.960 (0.936 - 0.984)	0.031 (-0.010 - 0.071)
S_0F_1	0.911 (0.858 - 0.965)	0.848 (0.790 - 0.905)	0.904 (0.857 - 0.951)	0.876 (0.835 - 0.917)	0.120 (0.023 - 0.218)
S_0F_2	0.961 (0.927 - 0.995)	0.978 (0.968 - 0.989)	0.918 (0.867 - 0.969)	0.948 (0.919 - 0.977)	0.054 (0.011 - 0.097)

Supplementary Table 3: Data are median (interquartile range) for average signal of the cancer and control regions of interest (ROIs) for both datasets combined. All cancer and control regions were significantly different ($p < 1 \times 10^{-9}$).

ADC, conventional apparent diffusion coefficient; Au, arbitrary unit, C, signal contribution; DWI_{\max} , image defined on maximum b-value; F, signal fraction; K_{app} , apparent diffusion kurtosis

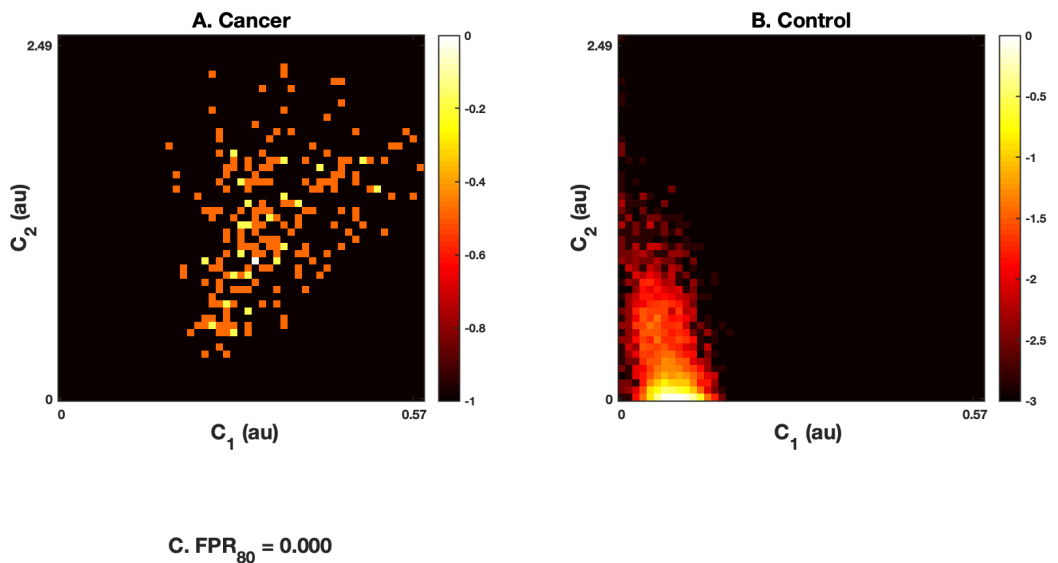
	Cancer	Control
C_1C_2 [au]	0.264 (0.608)	0.013 (0.015)
C_1 [au]	0.252 (0.257)	0.104 (0.086)
C_2 [au]	1.039 (0.856)	0.152 (0.111)
F_1F_2 [au]	0.144 (0.061)	0.102 (0.040)
F_1 [au]	0.208 (0.102)	0.513 (0.216)
F_2 [au]	0.731 (0.074)	0.359 (0.185)
DWI_{\max} [au]	0.238 (0.232)	0.131 (0.103)
ADC [$\text{mm}^2/\text{s} \times 10^{-3}$]	1.052 (0.412)	0.710 (0.388)
K_{app} [au]	1.105 (0.300)	2.437 (1.449)

Supplementary Materials II

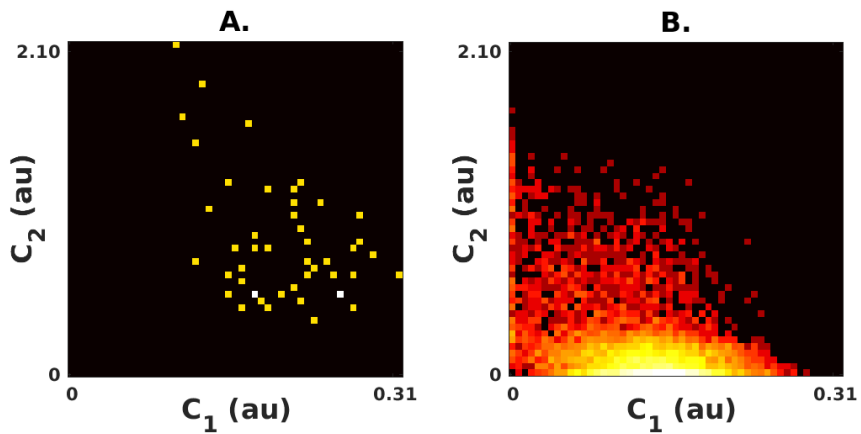
Supplementary Figure 1-106:

Probability density colormaps for the three-component model given C_1 and C_2 for all voxels per patient for all 81 cases from the US dataset (Supplementary Figure 1-81) and 25 cases from the European dataset (Supplementary Figure 82-106) and are given for (A.) cancer (cancer ROI) and (B.) healthy breast tissue (control ROI). The discriminatory performance between cancer and healthy breast tissue is given by FPR_{80} for each case (C.). Colormaps are given on a logarithmic scale normalized to the maximum probability density value. Y- and x-axis are defined by the maximum value for each case. Color bars are identical for all figures and given for the first (Supplementary Figure 1) only. Au, arbitrary unit; C, signal contribution; FPR_{80} , false positive rate given sensitivity of 80%.

Supplementary Figure 1

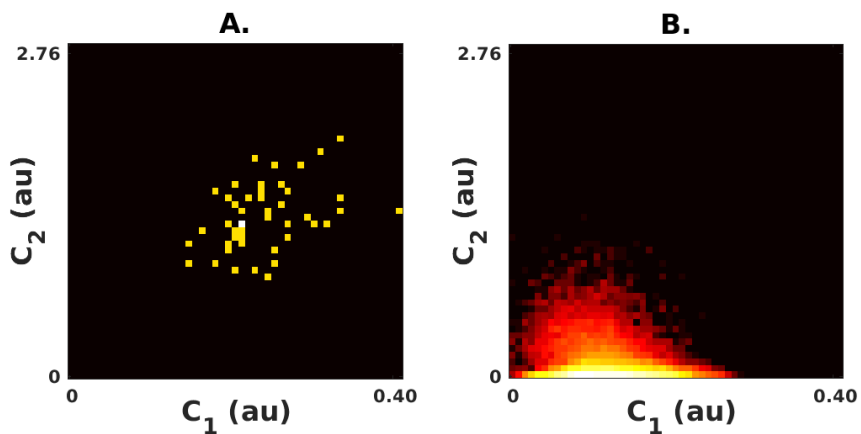


Supplementary Figure 2



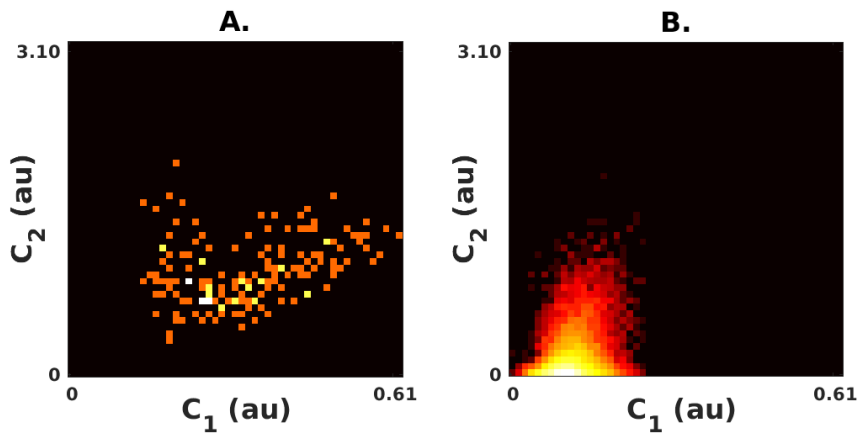
C. $FPR_{80} = 0.012$

Supplementary Figure 3



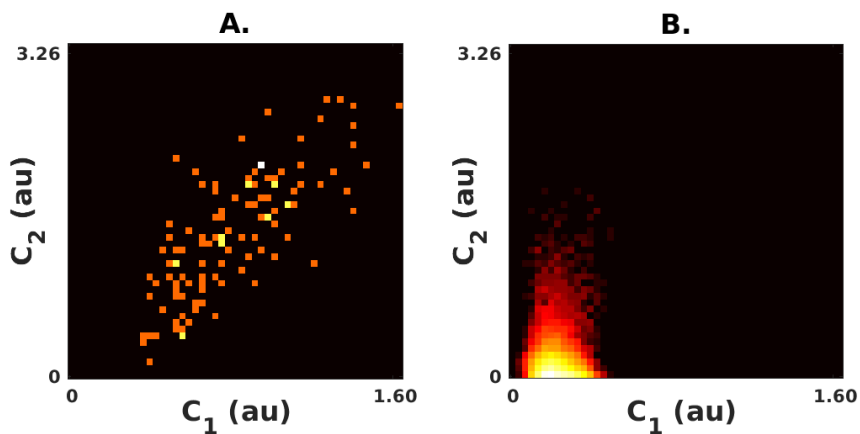
C. $FPR_{80} = 0.000$

Supplementary Figure 4



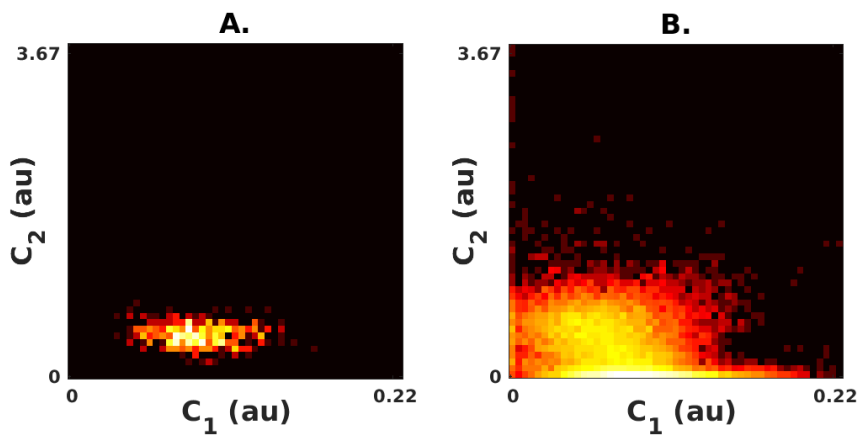
C. $FPR_{80} = 0.008$

Supplementary Figure 5



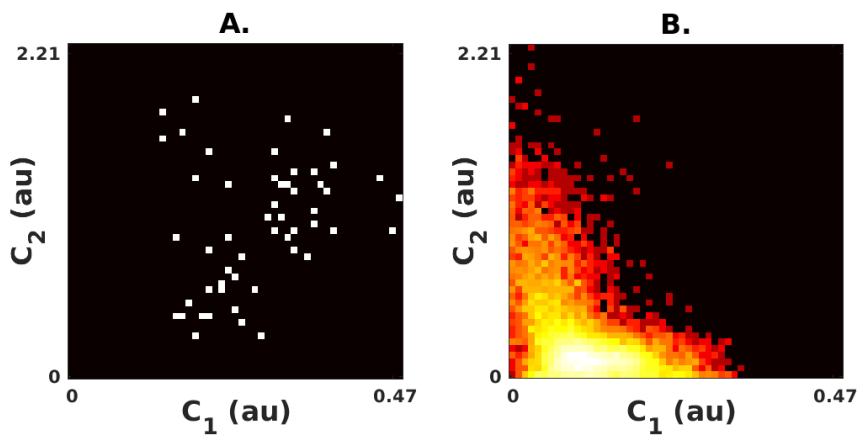
C. $FPR_{80} = 0.007$

Supplementary Figure 6



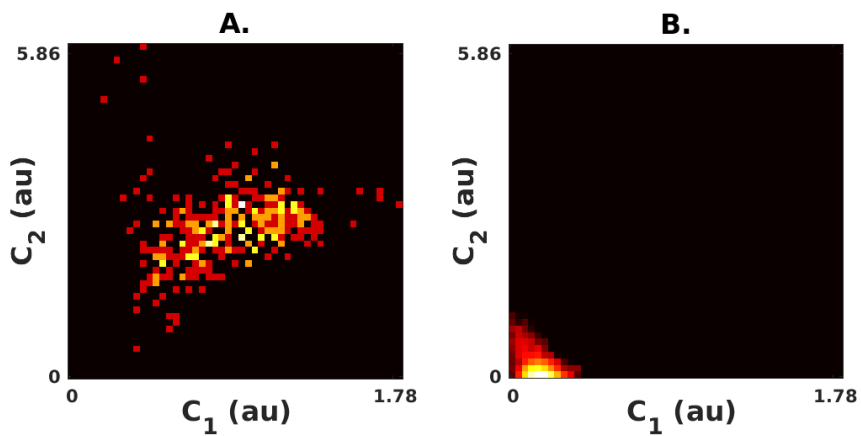
C. $FPR_{80} = 0.249$

Supplementary Figure 7



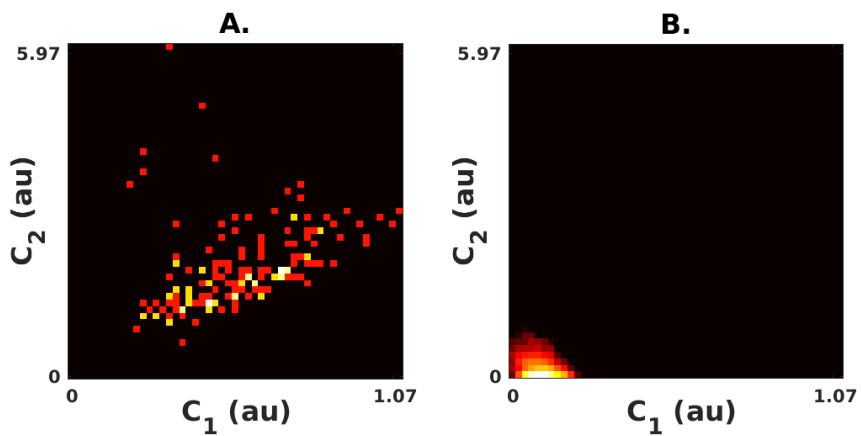
C. $FPR_{80} = 0.002$

Supplementary Figure 8



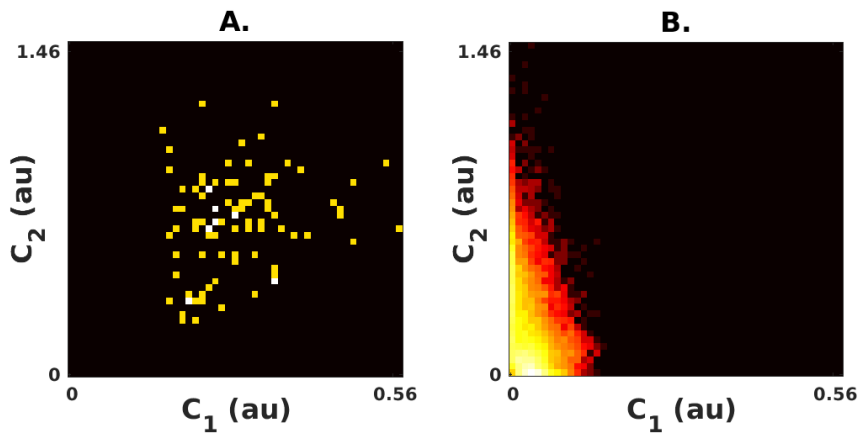
C. $FPR_{80} = 0.000$

Supplementary Figure 9



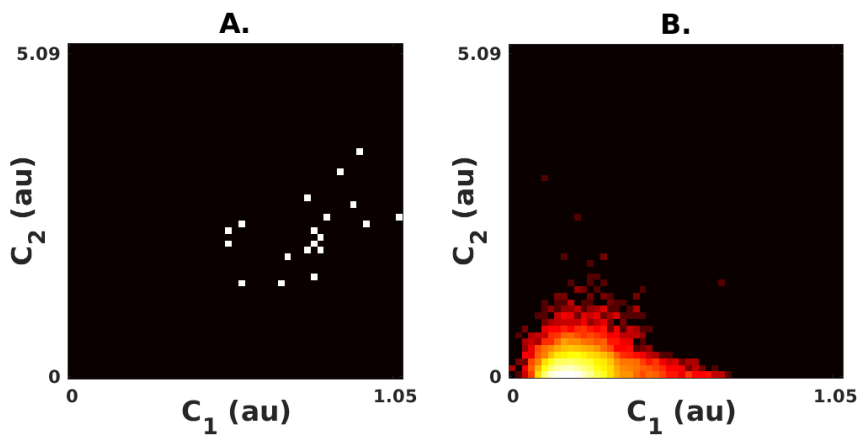
C. $FPR_{80} = 0.000$

Supplementary Figure 10



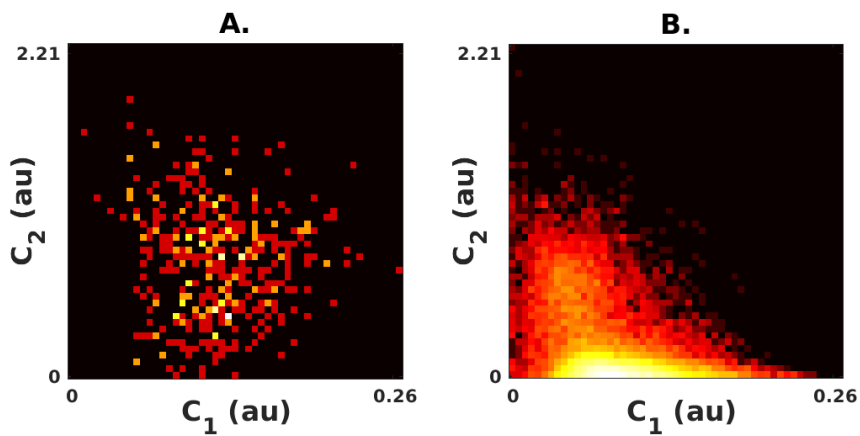
C. $FPR_{80} = 0.000$

Supplementary Figure 11



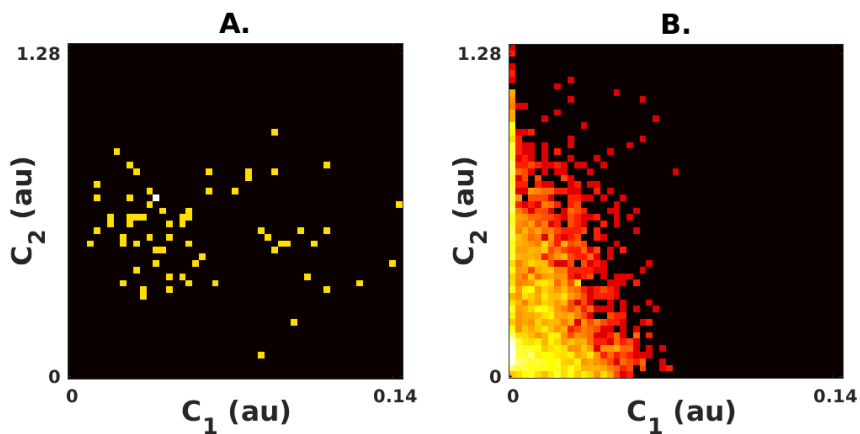
C. $FPR_{80} = 0.000$

Supplementary Figure 12



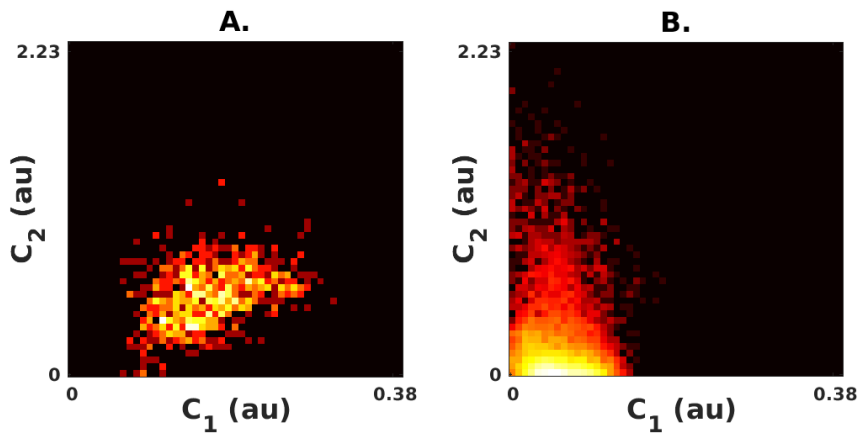
C. $FPR_{80} = 0.031$

Supplementary Figure 13



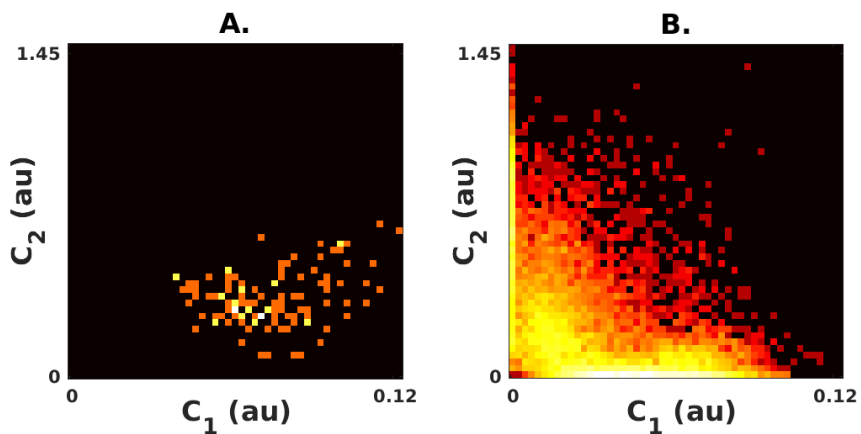
C. $FPR_{80} = 0.038$

Supplementary Figure 14



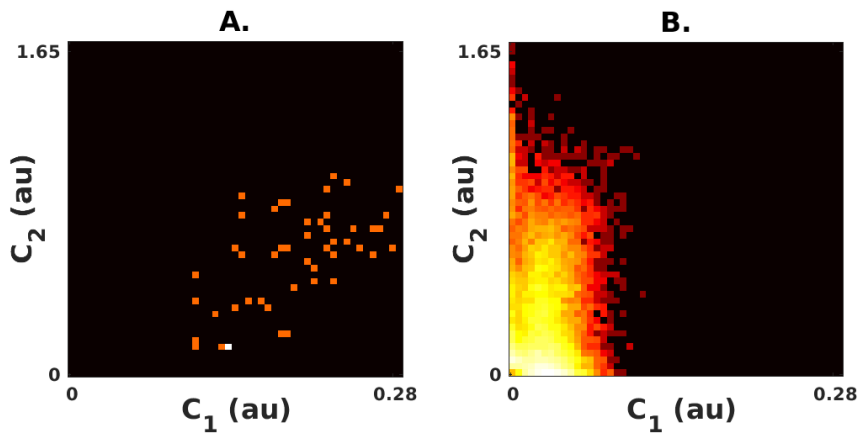
C. $FPR_{80} = 0.027$

Supplementary Figure 15



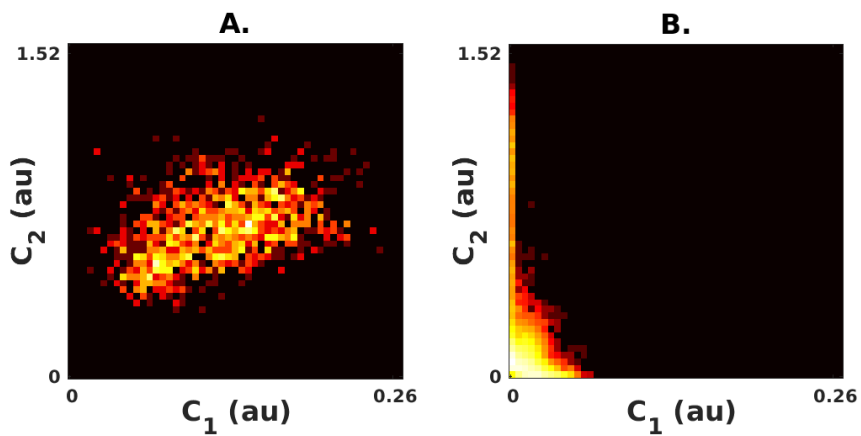
C. $FPR_{80} = 0.032$

Supplementary Figure 16



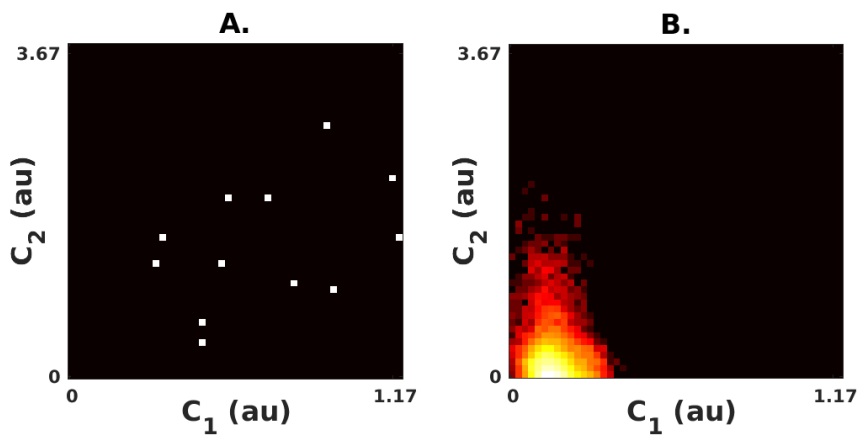
C. $FPR_{80} = 0.020$

Supplementary Figure 17



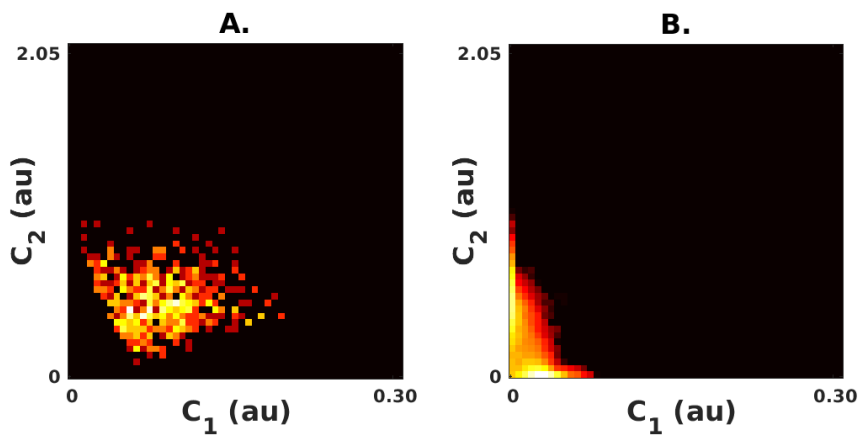
C. $FPR_{80} = 0.000$

Supplementary Figure 18



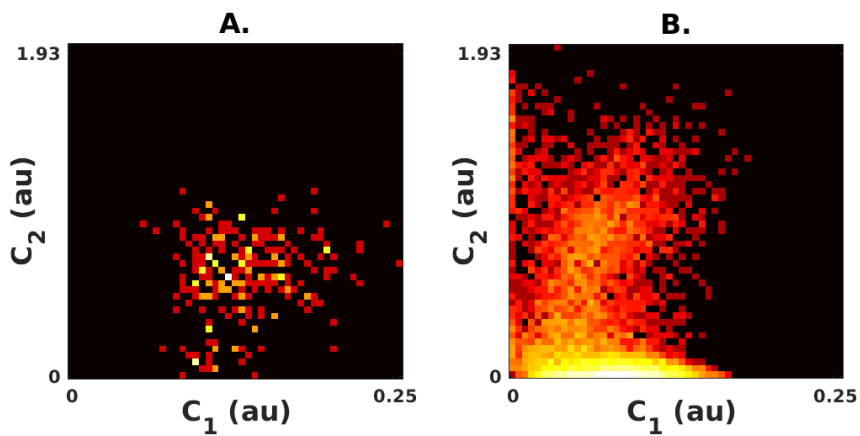
C. $FPR_{80} = 0.001$

Supplementary Figure 19



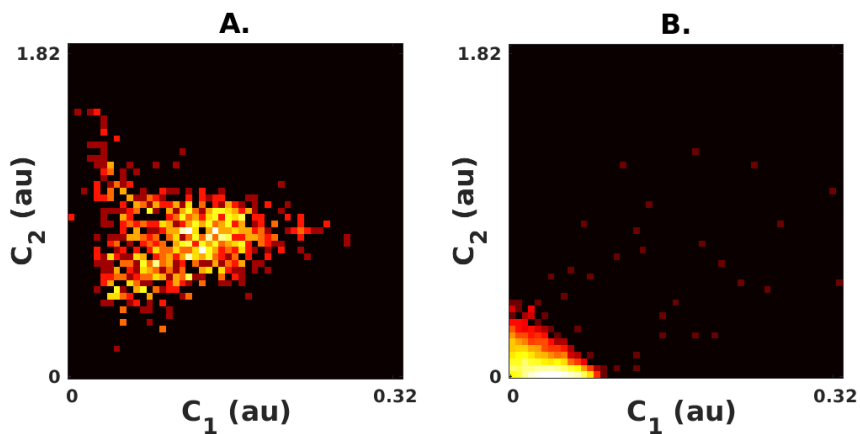
C. $FPR_{80} = 0.000$

Supplementary Figure 20



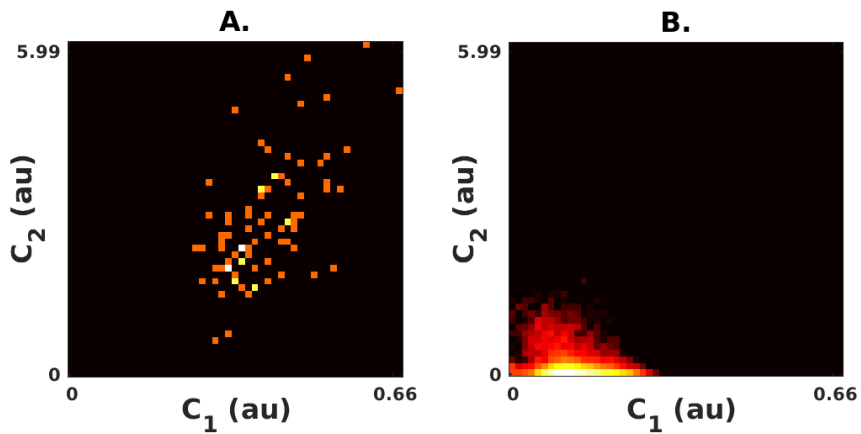
C. $FPR_{80} = 0.120$

Supplementary Figure 21



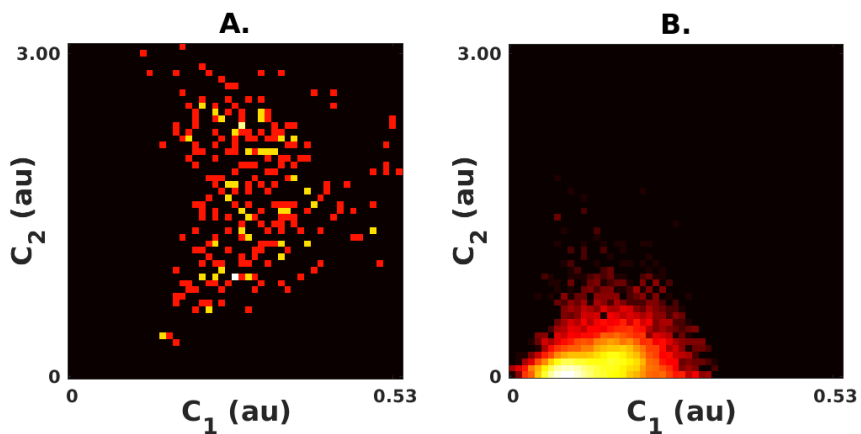
C. $FPR_{80} = 0.003$

Supplementary Figure 22



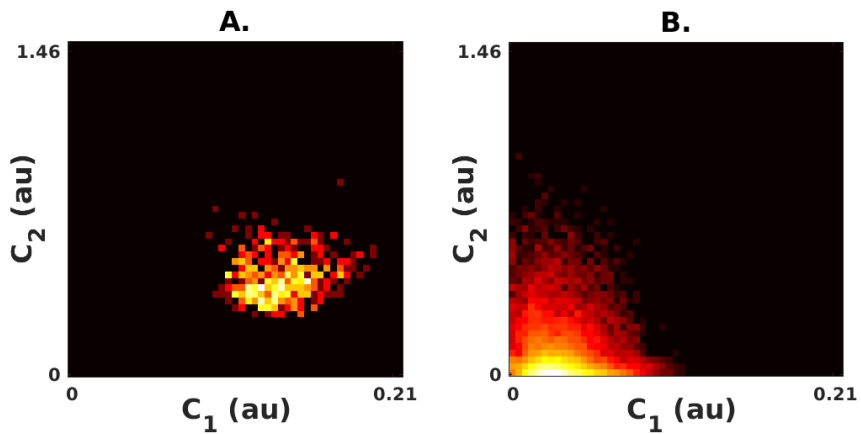
C. $FPR_{80} = 0.000$

Supplementary Figure 23



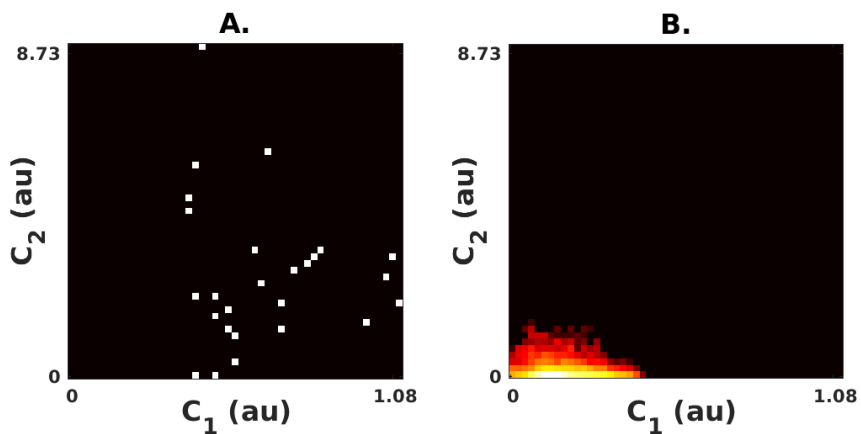
C. $FPR_{80} = 0.000$

Supplementary Figure 24



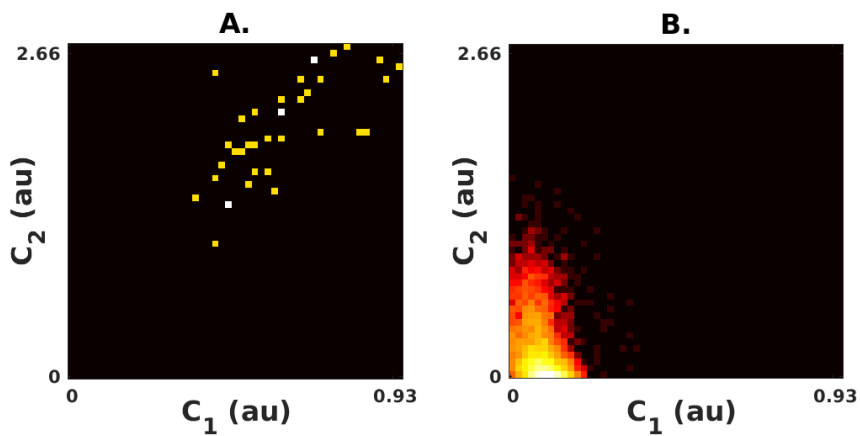
C. $FPR_{80} = 0.001$

Supplementary Figure 25



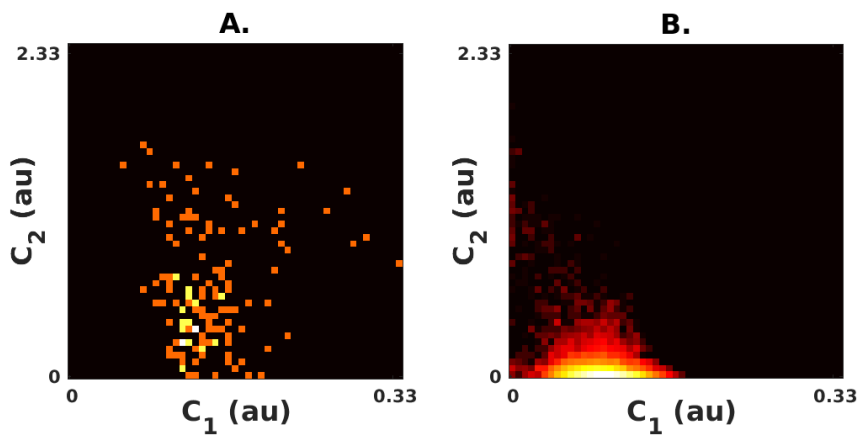
C. $FPR_{80} = 0.000$

Supplementary Figure 26



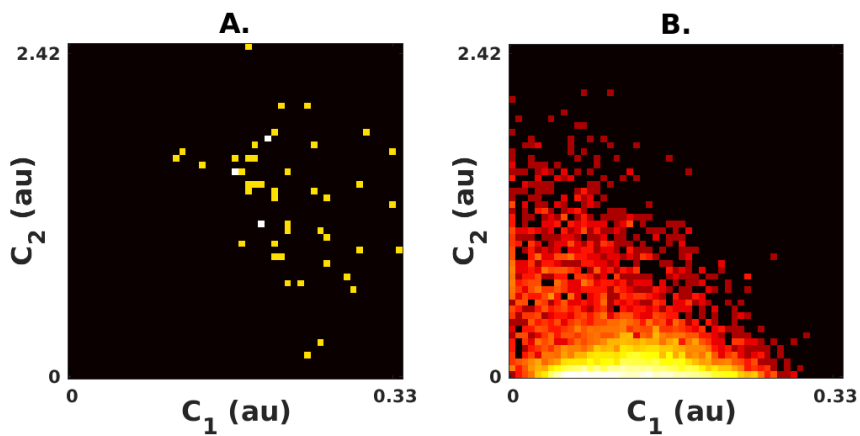
C. $FPR_{80} = 0.000$

Supplementary Figure 27



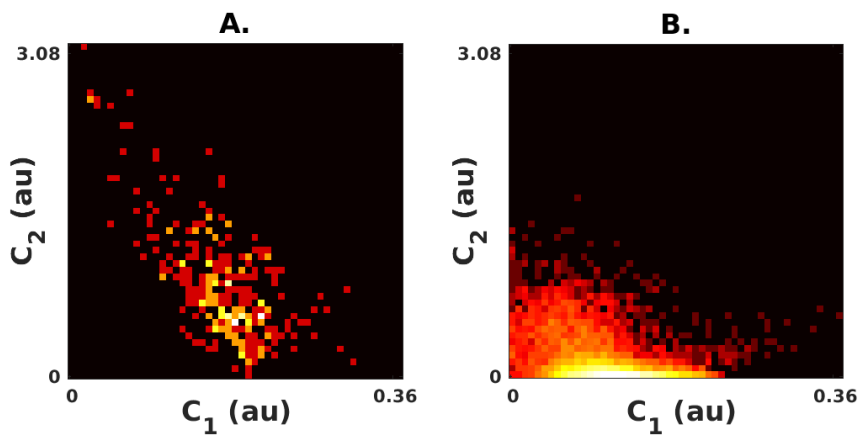
C. $FPR_{80} = 0.017$

Supplementary Figure 28



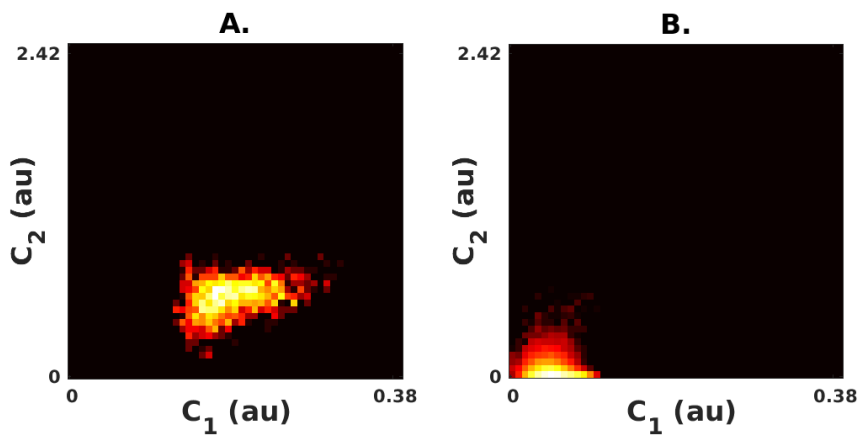
C. $FPR_{80} = 0.001$

Supplementary Figure 29



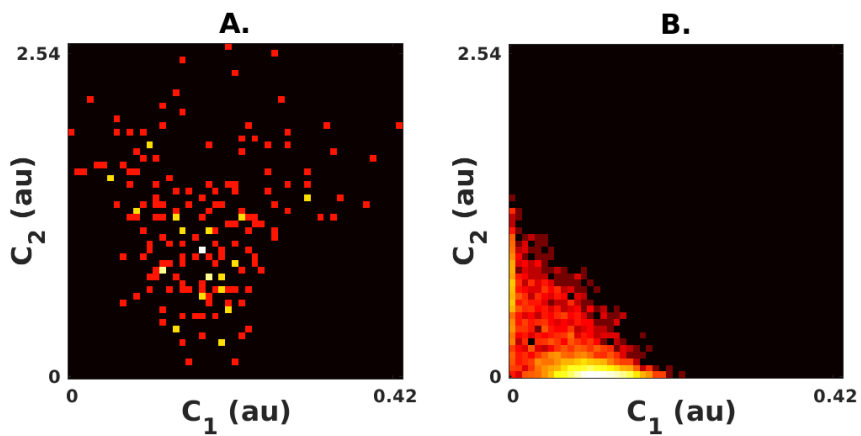
C. $FPR_{80} = 0.009$

Supplementary Figure 30



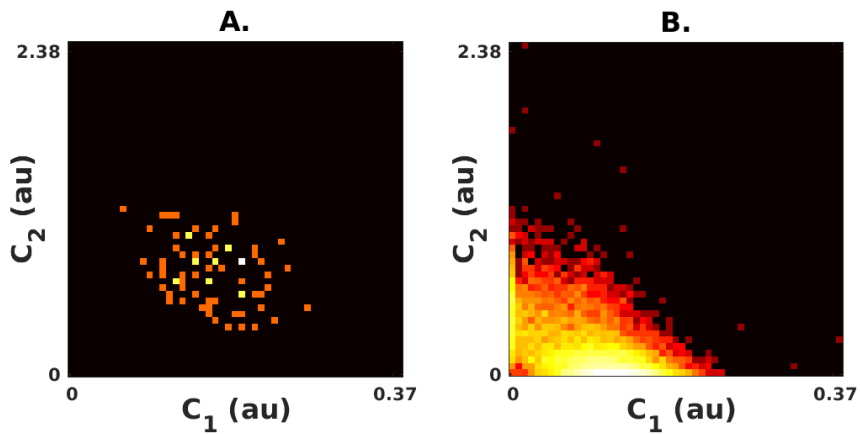
C. $FPR_{80} = 0.000$

Supplementary Figure 31



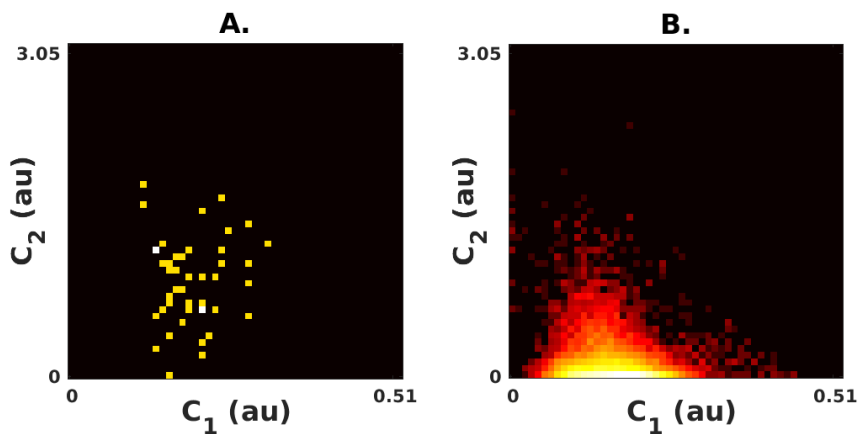
C. $FPR_{80} = 0.000$

Supplementary Figure 32



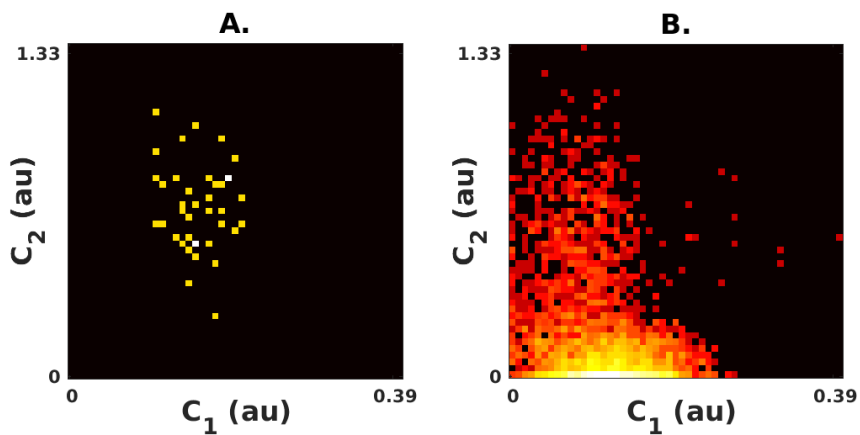
C. $FPR_{80} = 0.003$

Supplementary Figure 33



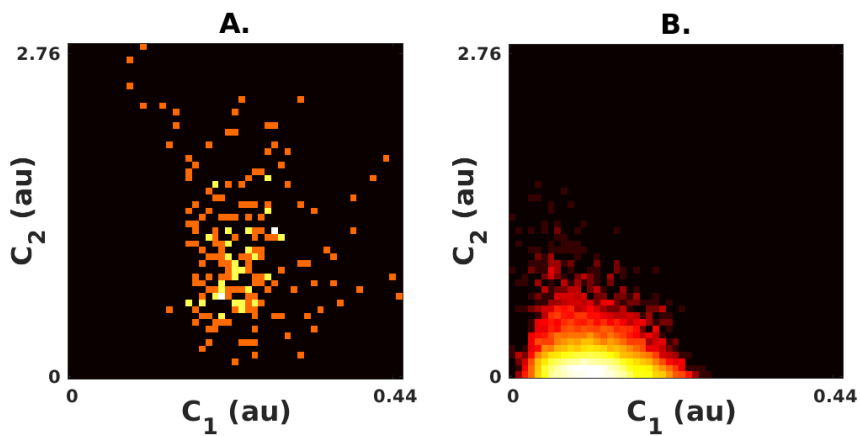
C. $FPR_{80} = 0.039$

Supplementary Figure 34



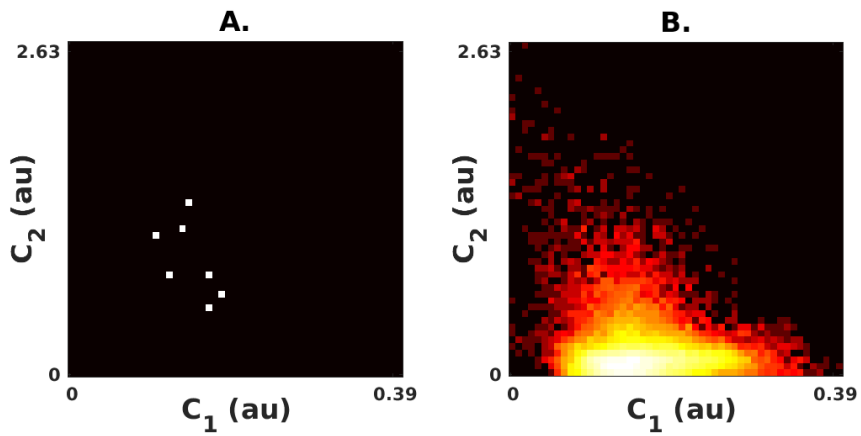
C. $FPR_{80} = 0.025$

Supplementary Figure 35



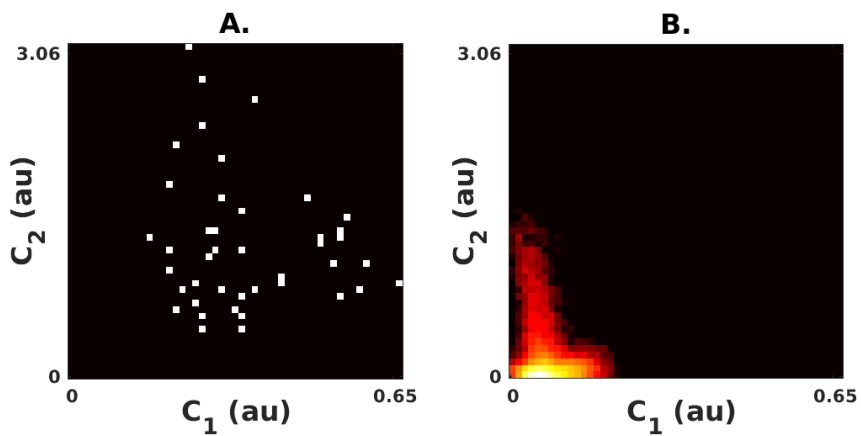
C. $FPR_{80} = 0.000$

Supplementary Figure 36



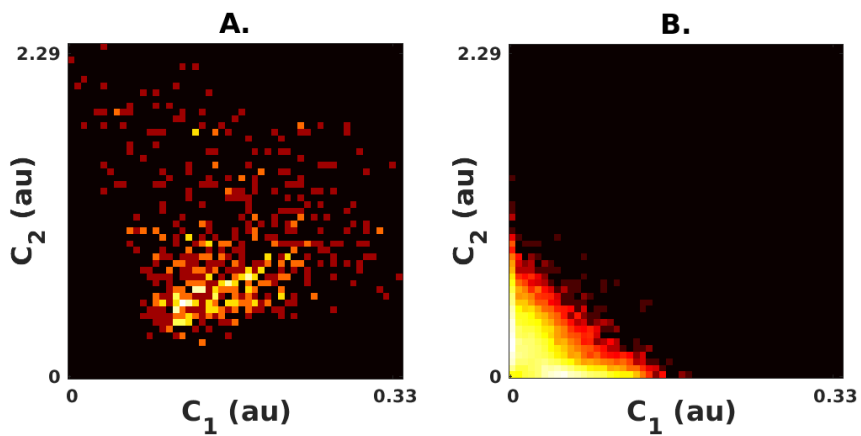
C. $FPR_{80} = 0.027$

Supplementary Figure 37



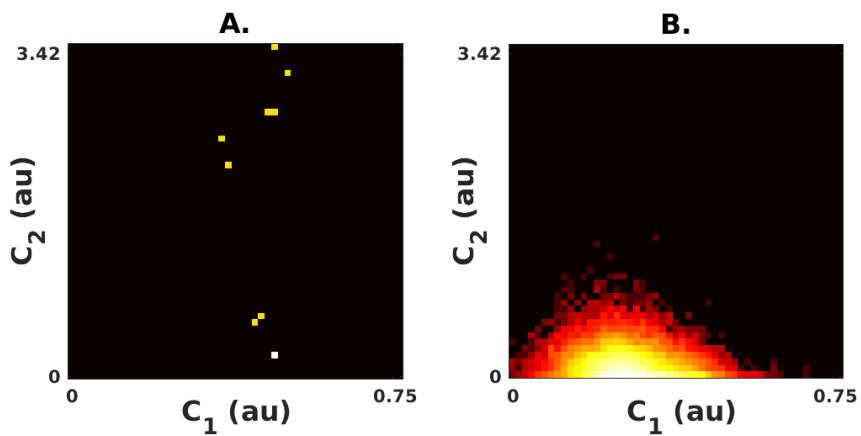
C. $FPR_{80} = 0.000$

Supplementary Figure 38



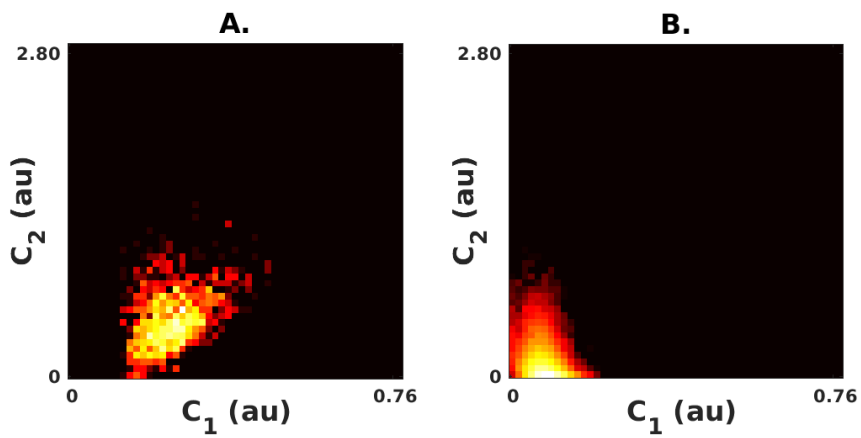
C. $FPR_{80} = 0.000$

Supplementary Figure 39



C. $FPR_{80} = 0.041$

Supplementary Figure 40



C. $FPR_{80} = 0.004$

Supplementary Materials III

Supplementary Figure 1-106:

Probability density colormaps for the three-component model given C_1 and C_2 for all voxels per patient for all 81 cases from the US dataset (Supplementary Figure 1-81) and 25 cases from the European dataset (Supplementary Figure 82-106) and are given for (A.) cancer (cancer ROI) and (B.) healthy breast tissue (control ROI). The discriminatory performance between cancer and healthy breast tissue is given by FPR_{80} for each case (C.). Colormaps are given on a logarithmic scale normalized to the maximum probability density value. Y- and x-axis are defined by the maximum value for each case. Color bars are identical for all figures and given for the first (Supplementary Figure 1) only. Au, arbitrary unit; C, signal contribution; FPR_{80} , false positive rate given sensitivity of 80%.

Supplementary Figure 41

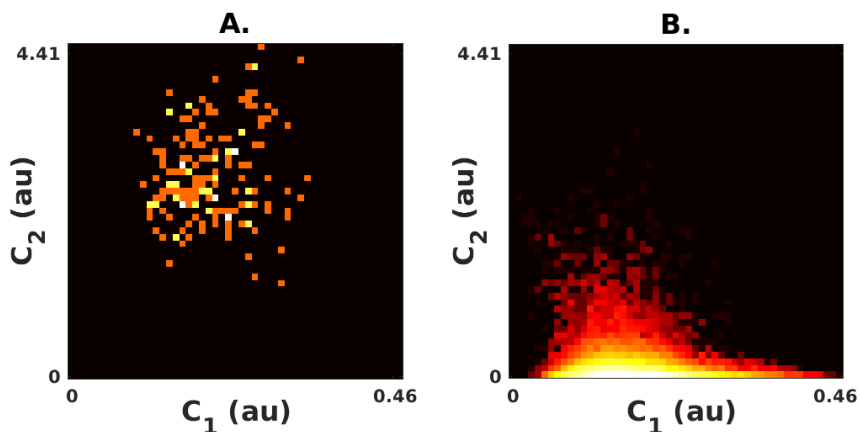
This material is not included in NTNU Open

Supplementary Materials IV

Supplementary Figure 1-106:

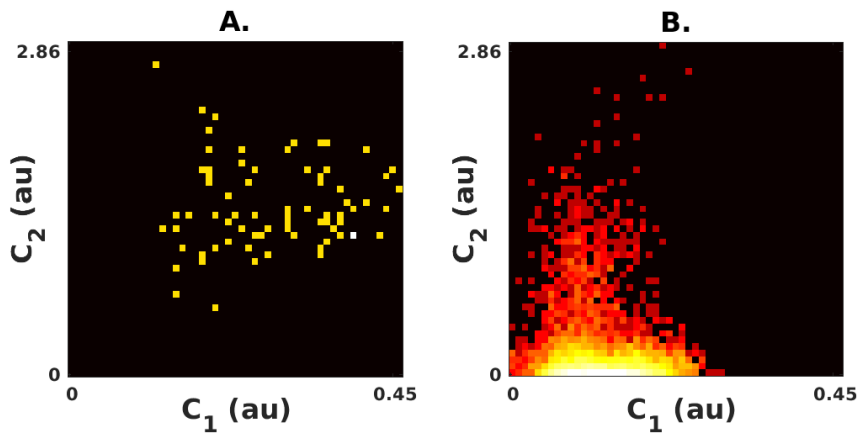
Probability density colormaps for the three-component model given C_1 and C_2 for all voxels per patient for all 81 cases from the US dataset (Supplementary Figure 1-81) and 25 cases from the European dataset (Supplementary Figure 82-106) and are given for (A.) cancer (cancer ROI) and (B.) healthy breast tissue (control ROI). The discriminatory performance between cancer and healthy breast tissue is given by FPR_{80} for each case (C.). Colormaps are given on a logarithmic scale normalized to the maximum probability density value. Y- and x-axis are defined by the maximum value for each case. Color bars are identical for all figures and given for the first (Supplementary Figure 1) only. Au, arbitrary unit; C, signal contribution; FPR_{80} , false positive rate given sensitivity of 80%.

Supplementary Figure 71



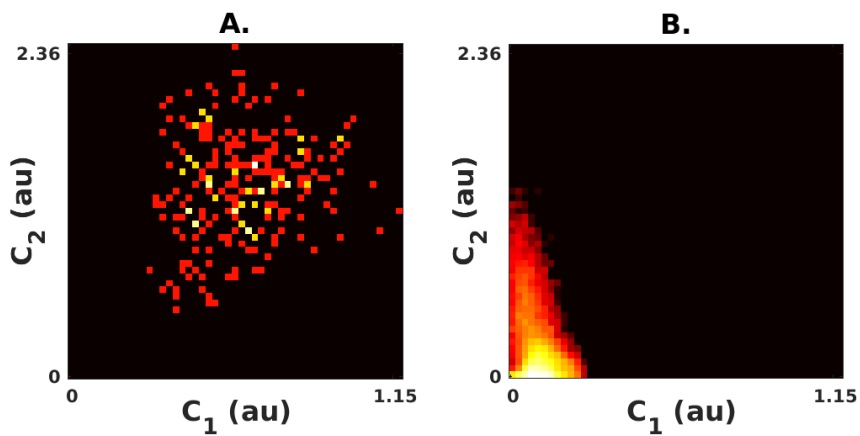
C. $FPR_{80} = 0.001$

Supplementary Figure 72



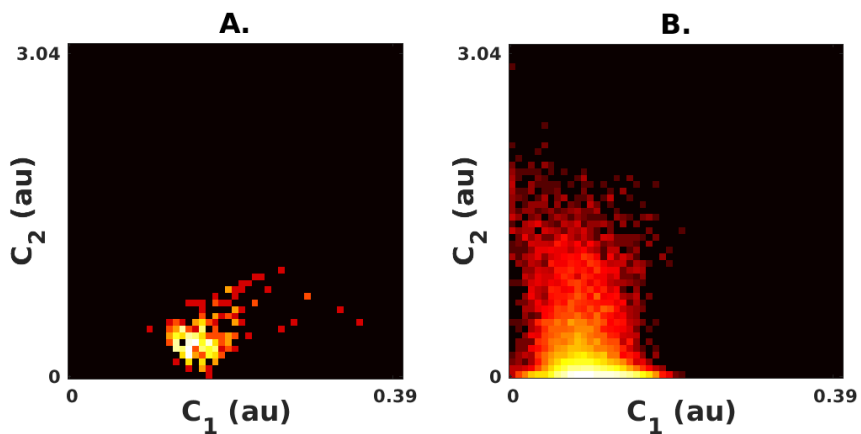
C. $FPR_{80} = 0.002$

Supplementary Figure 73



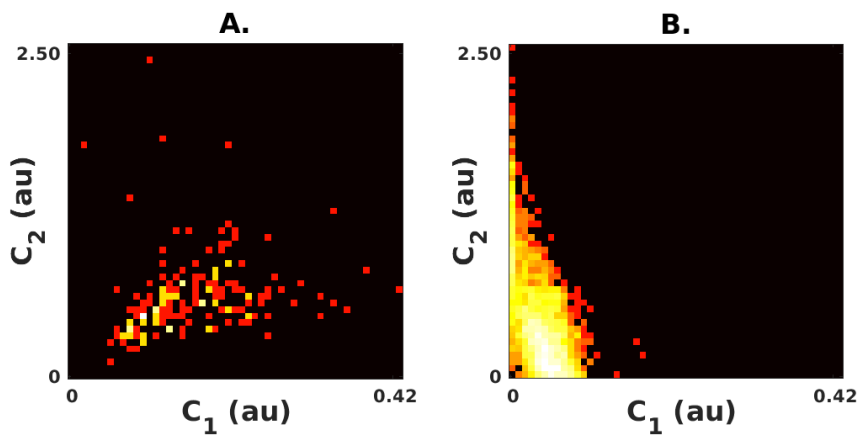
C. $FPR_{80} = 0.000$

Supplementary Figure 74



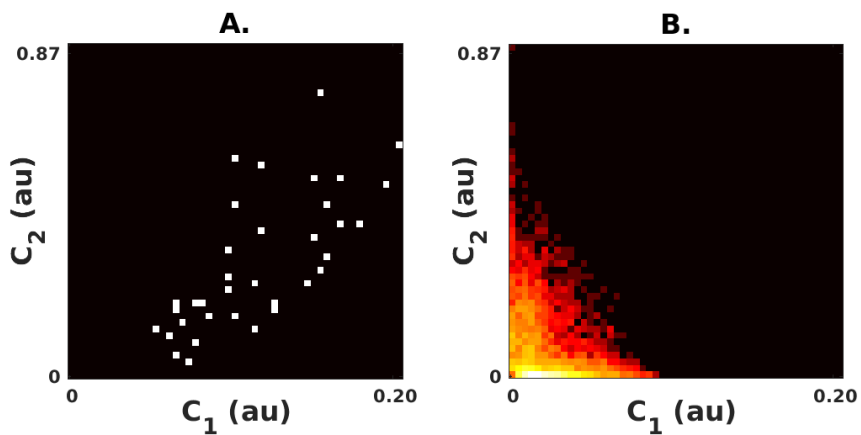
C. $FPR_{80} = 0.146$

Supplementary Figure 75



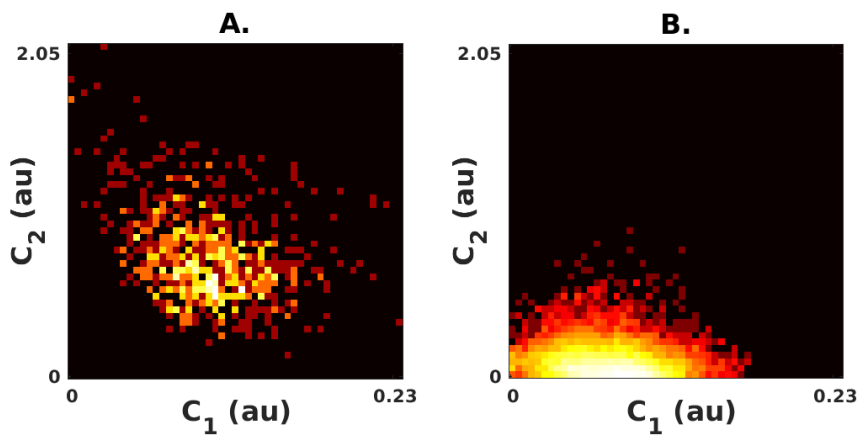
C. $FPR_{80} = 0.005$

Supplementary Figure 76



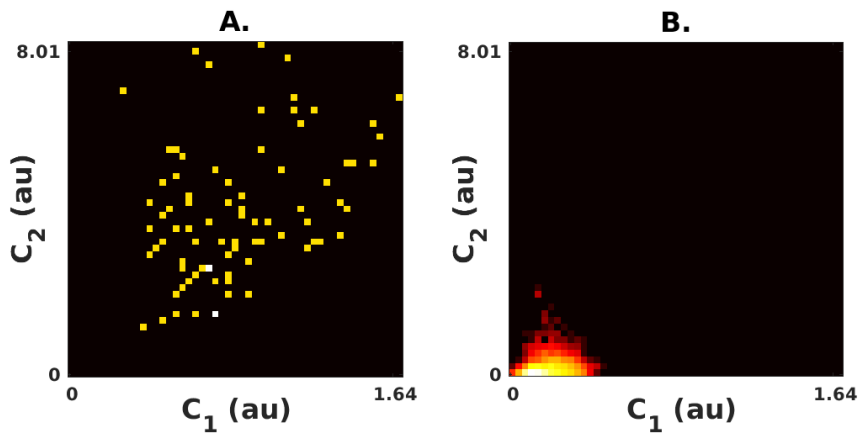
C. $FPR_{80} = 0.001$

Supplementary Figure 77



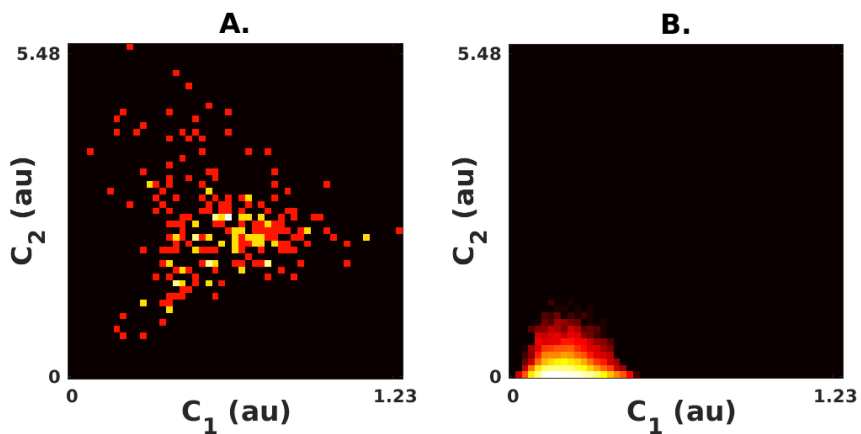
C. $FPR_{80} = 0.002$

Supplementary Figure 78



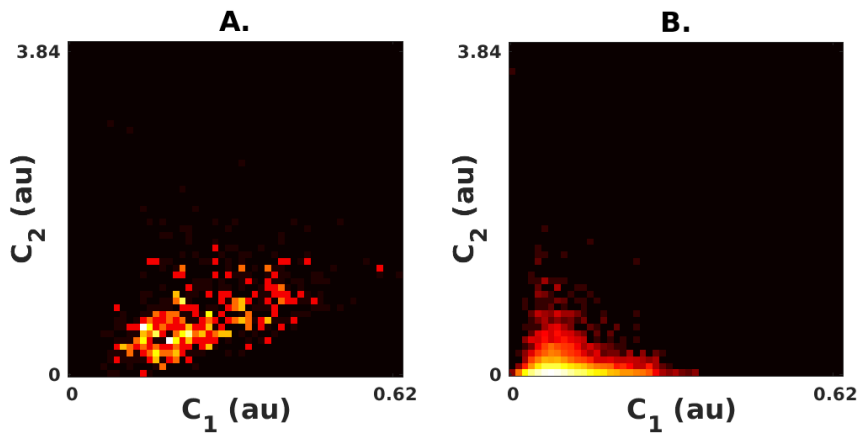
C. $FPR_{80} = 0.000$

Supplementary Figure 79



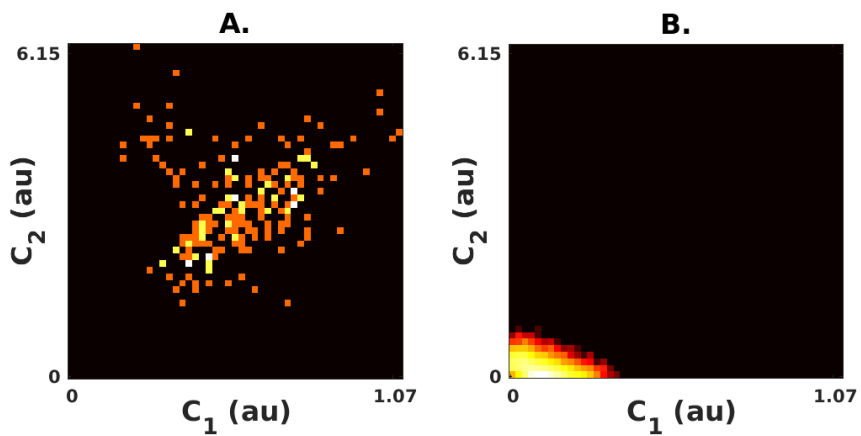
C. $FPR_{80} = 0.000$

Supplementary Figure 80



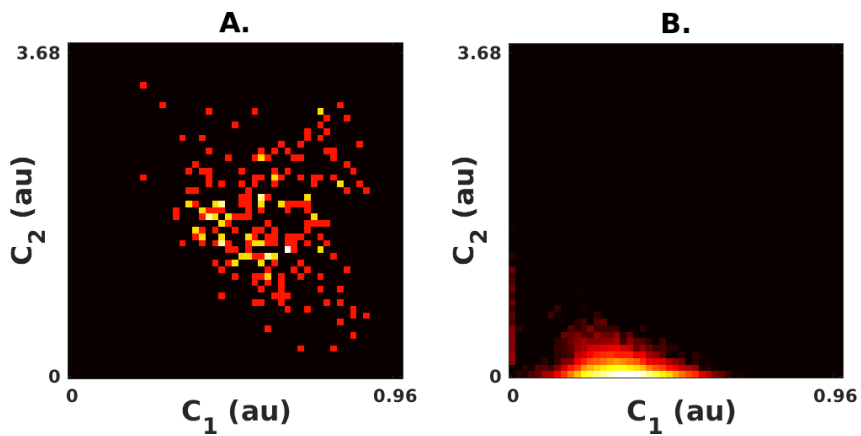
C. $FPR_{80} = 0.017$

Supplementary Figure 81



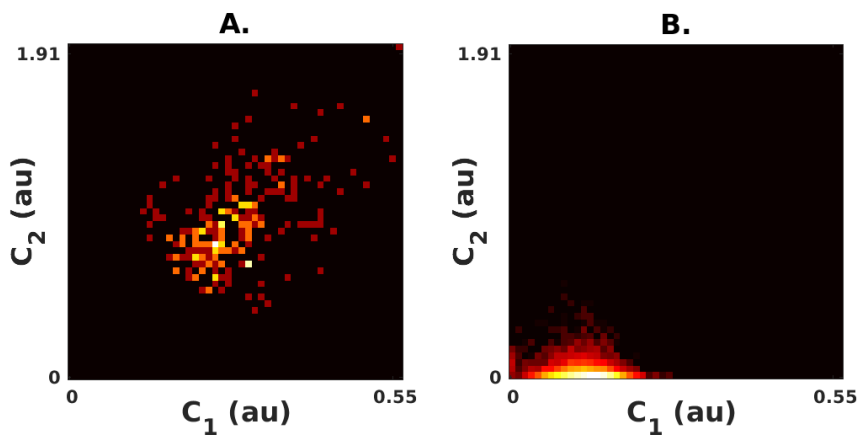
C. $FPR_{80} = 0.000$

Supplementary Figure 82



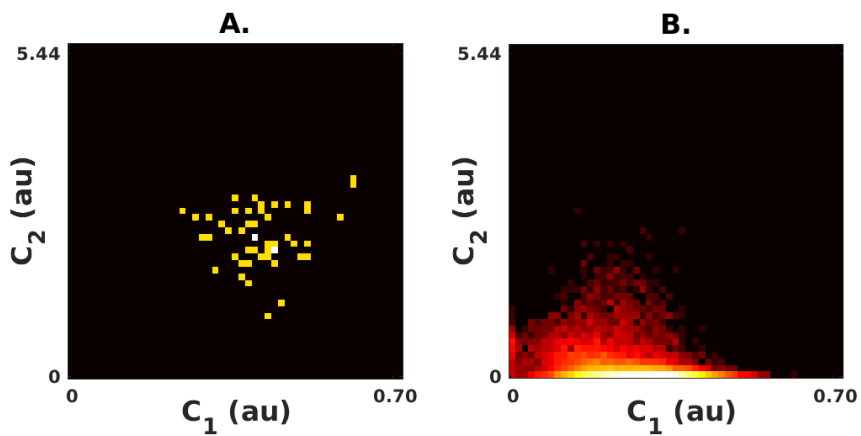
C. $FPR_{80} = 0.000$

Supplementary Figure 83



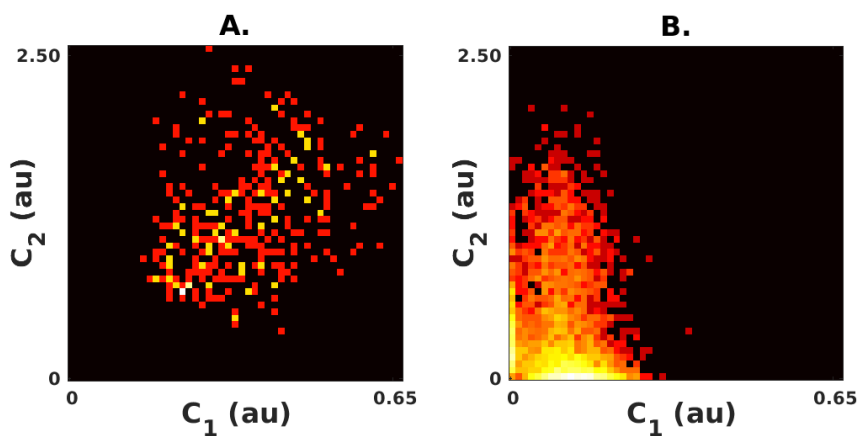
C. $FPR_{80} = 0.000$

Supplementary Figure 84



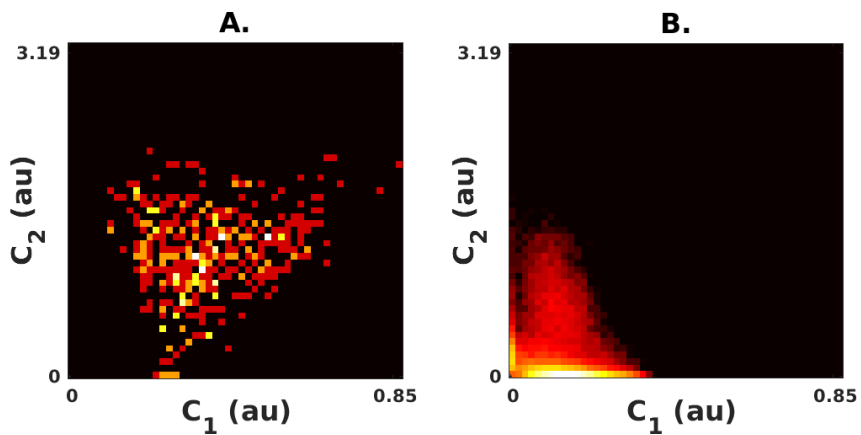
C. $FPR_{80} = 0.002$

Supplementary Figure 85



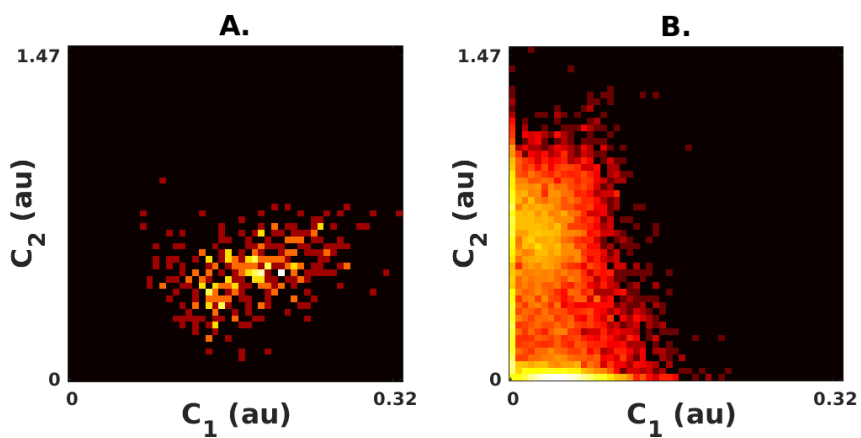
C. $FPR_{80} = 0.004$

Supplementary Figure 86



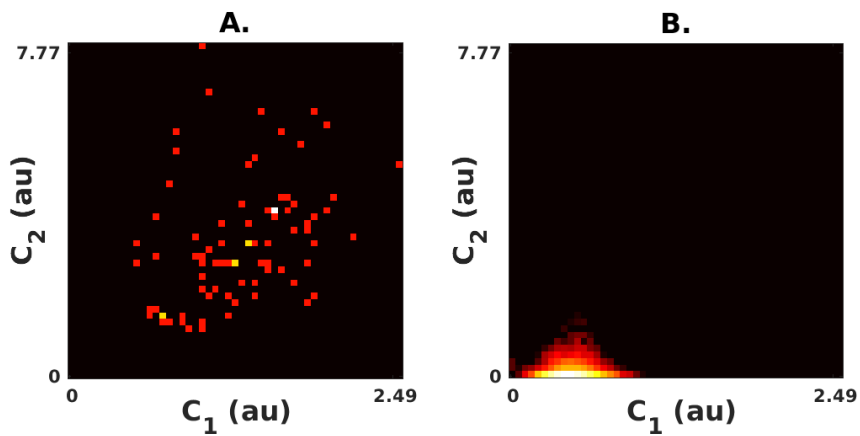
C. $FPR_{80} = 0.002$

Supplementary Figure 87



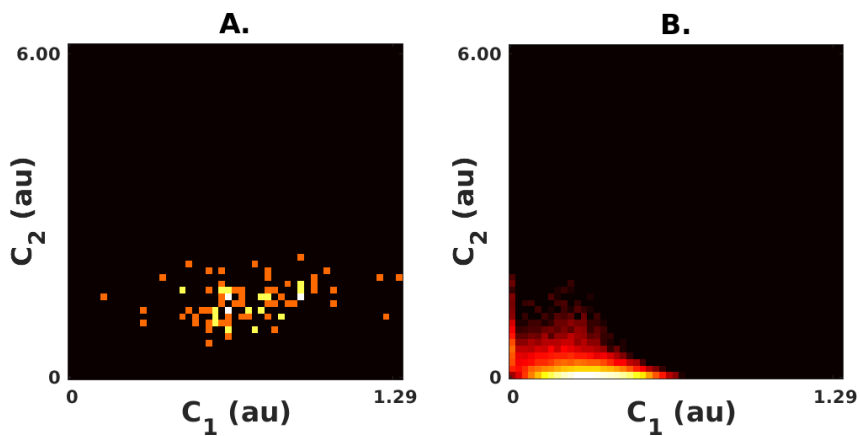
C. $FPR_{80} = 0.037$

Supplementary Figure 88



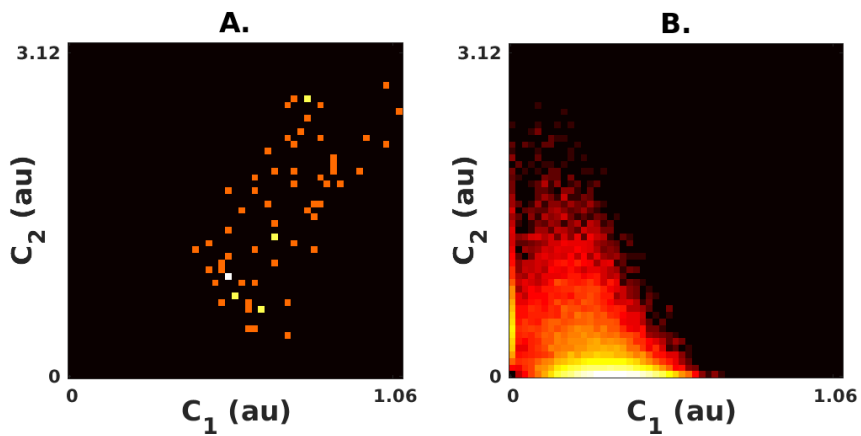
C. $FPR_{80} = 0.000$

Supplementary Figure 89



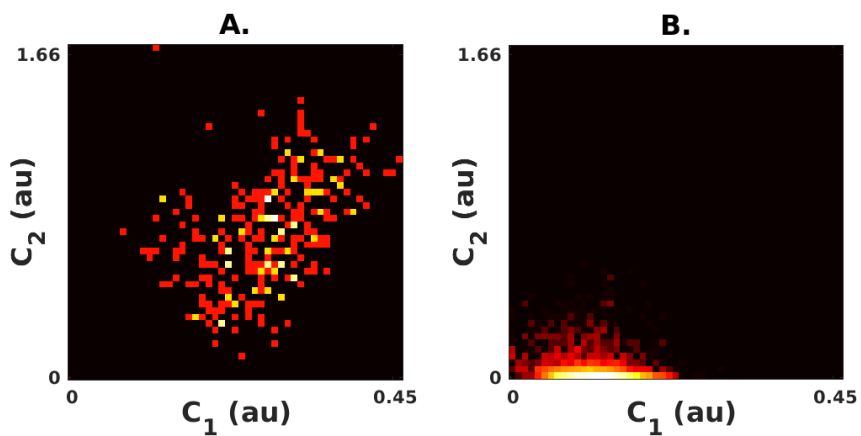
C. $FPR_{80} = 0.001$

Supplementary Figure 90



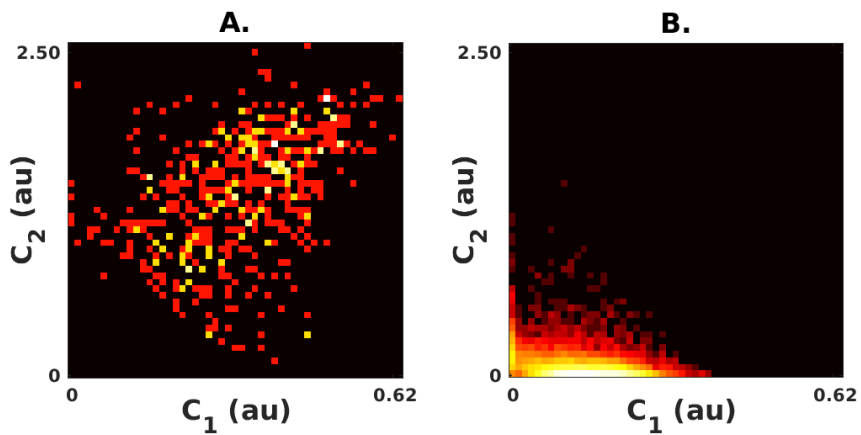
C. $FPR_{80} = 0.002$

Supplementary Figure 91



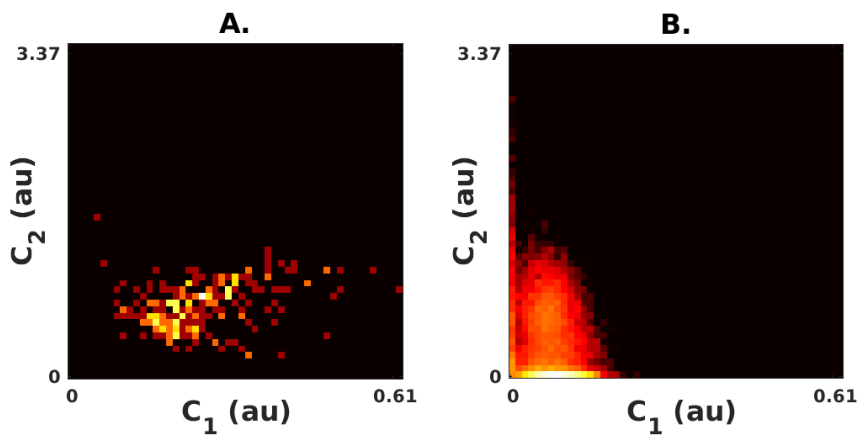
C. $FPR_{80} = 0.000$

Supplementary Figure 92



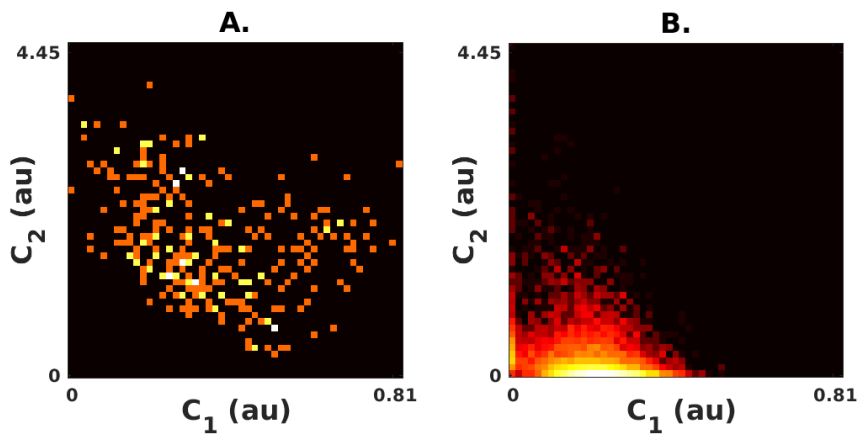
C. $FPR_{80} = 0.000$

Supplementary Figure 93



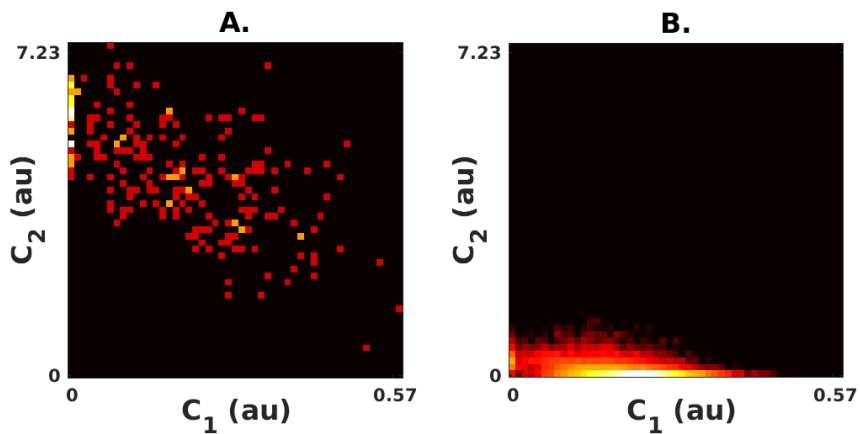
C. $FPR_{80} = 0.015$

Supplementary Figure 94



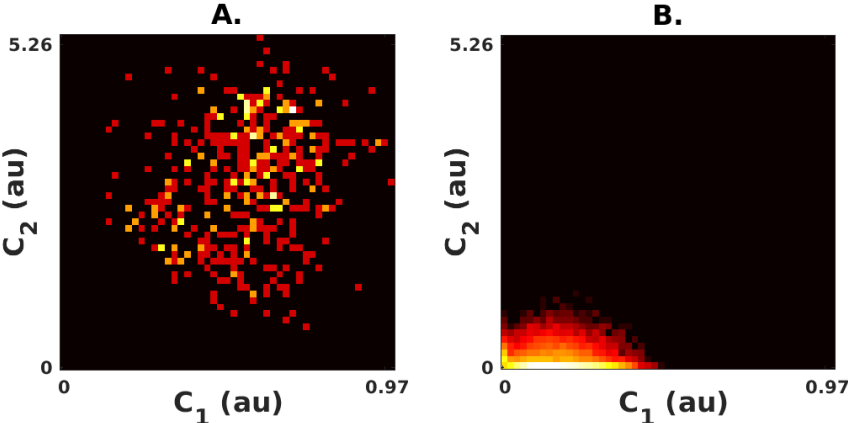
C. $FPR_{80} = 0.004$

Supplementary Figure 95



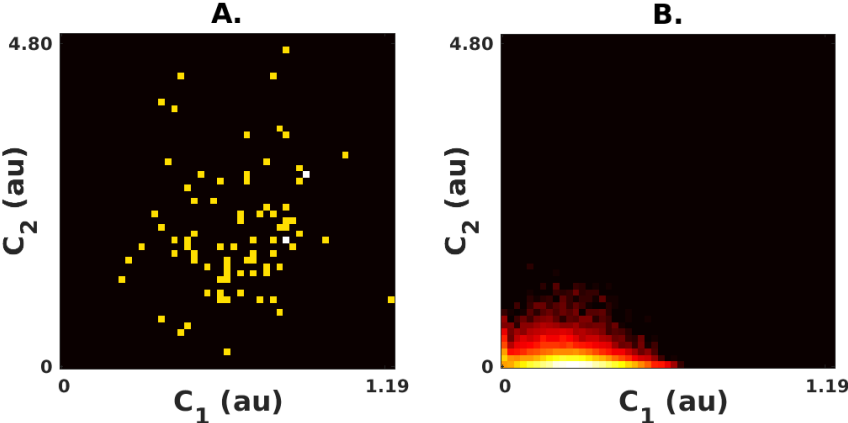
C. $FPR_{80} = 0.002$

Supplementary Figure 96



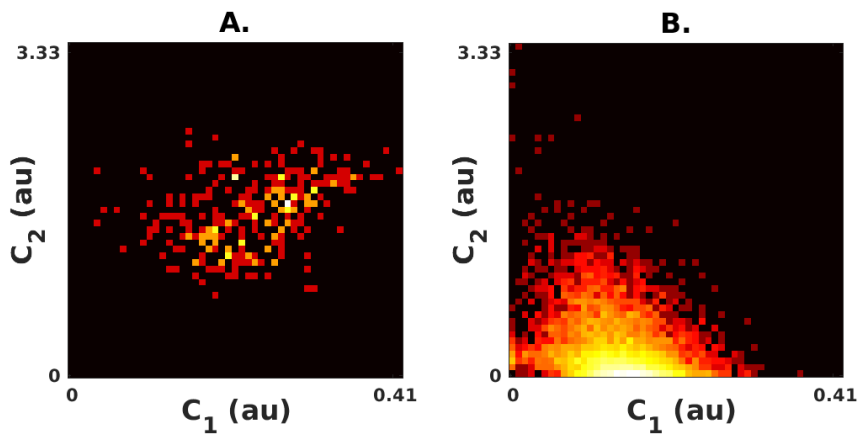
C. $FPR_{80} = 0.000$

Supplementary Figure 97



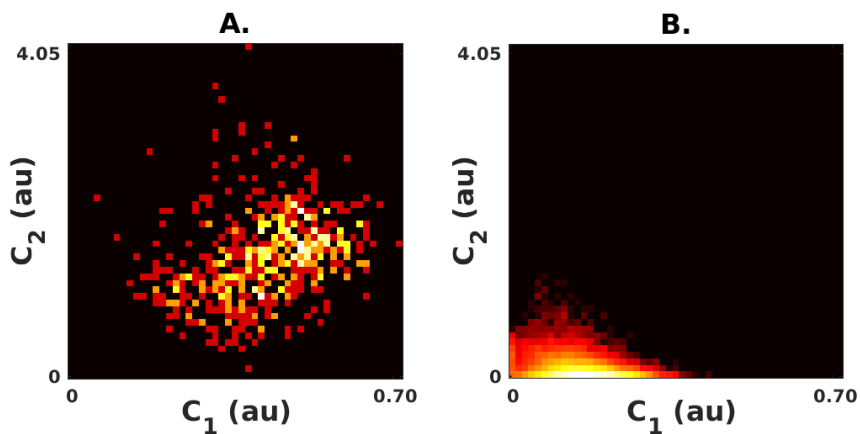
C. $FPR_{80} = 0.000$

Supplementary Figure 98



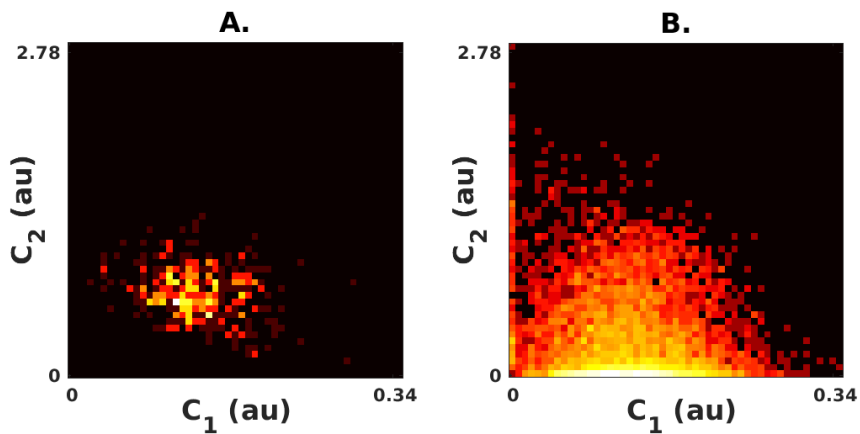
C. $FPR_{80} = 0.001$

Supplementary Figure 99



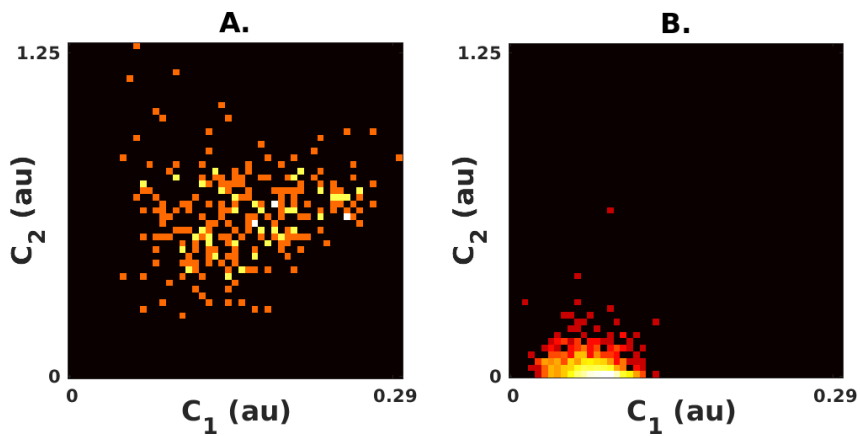
C. $FPR_{80} = 0.000$

Supplementary Figure 100



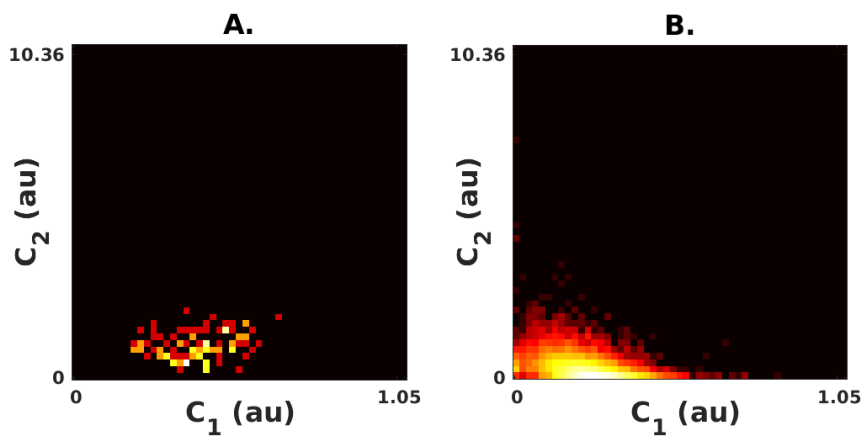
C. $FPR_{80} = 0.175$

Supplementary Figure 101



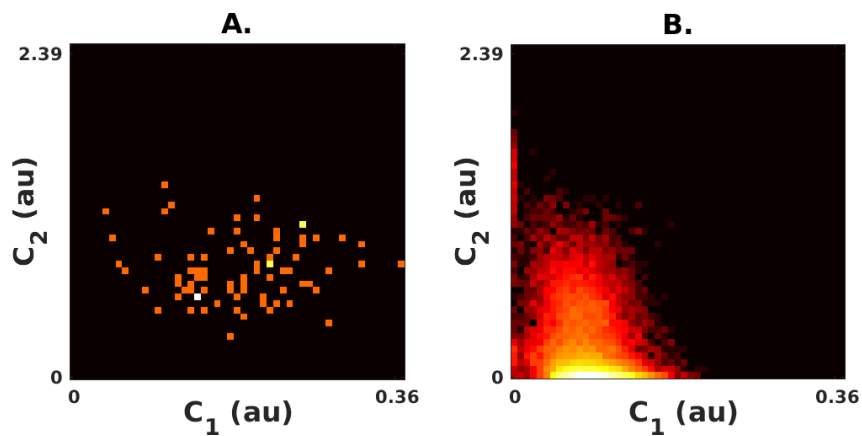
C. $FPR_{80} = 0.000$

Supplementary Figure 102



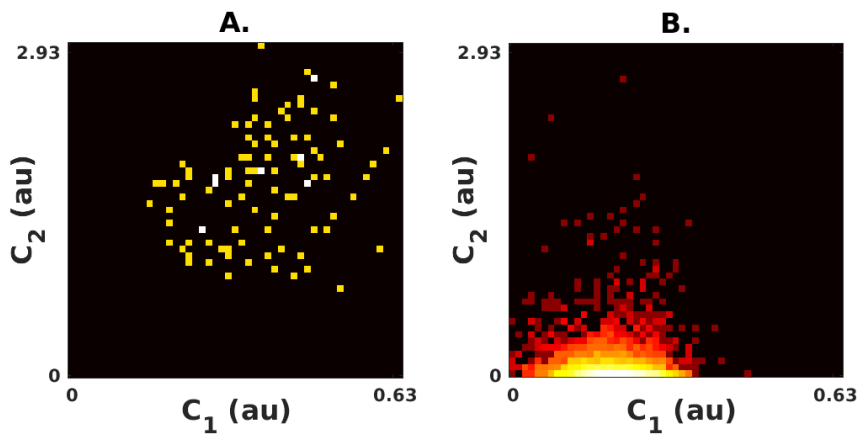
C. $FPR_{80} = 0.029$

Supplementary Figure 103



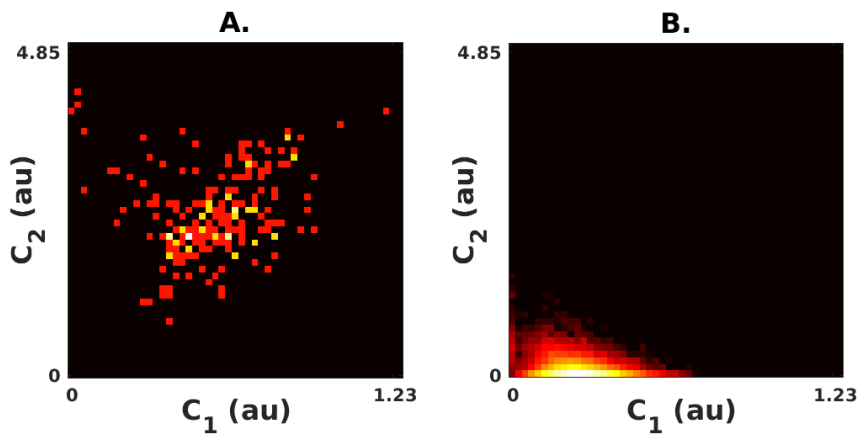
C. $FPR_{80} = 0.015$

Supplementary Figure 104



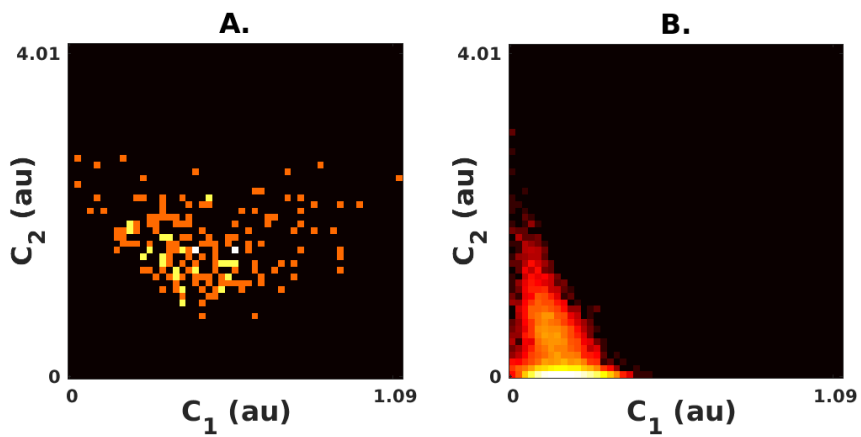
C. $FPR_{80} = 0.001$

Supplementary Figure 105



C. $FPR_{80} = 0.000$

Supplementary Figure 106



C. $FPR_{80} = 0.000$

ISBN 978-82-326-5677-6 (printed ver.)
ISBN 978-82-326-5933-3 (electronic ver.)
ISSN 1503-8181 (printed ver.)
ISSN 2703-8084 (online ver.)